



## Composite Membranes for HighTemperature Polymer Electrolyte Membrane Fuel Cells

Chen, Yongfang

*Publication date:*  
2021

*Document Version*  
Publisher's PDF, also known as Version of record

[Link back to DTU Orbit](#)

*Citation (APA):*  
Chen, Y. (2021). *Composite Membranes for HighTemperature Polymer Electrolyte Membrane Fuel Cells*. DTU Energy.

---

### General rights

Copyright and moral rights for the publications made accessible in the public portal are retained by the authors and/or other copyright owners and it is a condition of accessing publications that users recognise and abide by the legal requirements associated with these rights.

- Users may download and print one copy of any publication from the public portal for the purpose of private study or research.
- You may not further distribute the material or use it for any profit-making activity or commercial gain
- You may freely distribute the URL identifying the publication in the public portal

If you believe that this document breaches copyright please contact us providing details, and we will remove access to the work immediately and investigate your claim.

# Composite Membranes for High-Temperature Polymer Electrolyte Membrane Fuel Cells

---

A PhD thesis by

**Yongfang Chen**

May 2021

Principal Supervisor: Professor Qingfeng Li

Co-supervisor: Associate Professor Wenjing(Angela) Zhang

Anker Engelunds Vej, Building 310  
DK - 2800 Kgs. Lyngby  
Denmark  
[www.energy.dtu.dk](http://www.energy.dtu.dk)

Technical University  
of Denmark





# Acknowledgements

---

The work was carried out from February 2018 to May 2021 at Section of Electrochemistry (formerly known as Section of Proton Conductors), Department of Energy Conversion and Storage, Technical University of Denmark, with Professor Qingfeng Li as the principal supervisor and associate Professor Wenjing Zhang as the co-supervisor.

First and foremost, I would like to thank Professor Li for giving me the opportunity for this Ph.D. study. Professor Li has spent lots of his treasured hours and patience in discussions, from which I have learned the scientific disciplines and technical proficiencies of doing research. Professor Li has always showed up in time whenever I need help. What impressed me the most is that professor Li appears and guides me in person when I am stuck by my experiment in the laboratory. The guidance is truly priceless and an irreplaceable part of this project. Similar gratitude goes to Associate Professor Zhang who has initialized this project by helping me in the application for the scholarship from China Scholarship Council. She has guided and supported me to the core part of this research on electrospinning experiments.

My thanks go to Professor Jens Oluf Jensen, Senior researcher Dr. David Aili and associate Professor Lars Nilausen Cleemann. Professor Jensen has provided great assistance during my scholarship application. He is not on my supervisor list for administrative reasons but has followed and helped me throughout the project. Dr. Aili shares his precious working experience in polymers and membranes. Associate Professor Cleemann is always ready and available for any help from office to laboratory and from administration to science.

I thank my colleagues and technicians in the Section who have always been around when I need help. Dr. Mikkel Rykær Kraglund has kept the new electrochemistry lab functional while Sanser Celenk maintains the fuel cell test stations. Chao Pan provides all kinds of practical support in the sample preparation, characterization and cell testing. Larisa Seerup is of great help with microscopy characterization, XRD and ion milling. Claus Burke Mortensen is skillful in design and processing of auxiliary setups. Thamis Maria Lindorff has introduced and helped me in membrane preparation in Building 375.

During the COVID-19 pandemic, I have spent my external stay at Danish Power Systems Aps (DPS, now Blue World Technologies) where I have achieved an important part of results on thin membranes. More important for me is the professional training in handling membranes and MEAs and fuel cell tests. For this should my thanks go to Drs. Hans Aage Hjuler, Søren Primdahl, Kobra Azizi, and other DPS colleagues for their encouragement, enthusiasm, and patience during my stay.

My colleagues in the electrochemistry lab, Dr. Yang Hu, Dr. Xuan Liu, Dr. Hongying Tang, Quan Zhou, Jianan Yu and in the electrospinning group, Yibo Dou, Dan Zhao, Apiwat Dankeaw, Iram Aziz, Tian Tian, have kindly shared their precious lab experience. Of them has Eftychia Bompolaki shared with me her sadness in failure and happiness in success in electrospinning

as well as the early morning hours in the car from Lyngby to Risø.

I own my deepest thanks to my family: my parents for supporting and encouraging me, their love gives me the strength and determination to never give up; my beloved husband Xiaofeng for love, patience, support, and accompany in the past three years, not only in life but also in fuel cell work.

Finally, I thank the China Scholarship Council and DTU Energy for providing the scholarship in my study period otherwise this project is impossible.

Yongfang Chen

Kgs. Lyngby, Denmark

May 31<sup>st</sup> 2021

High temperature proton exchange membrane fuel cell (HT-PEMFC) is one of the promising technologies for power generation in an efficient and environmentally friendly way. The major obstacles for the large-scale commercialization of the technology are performance, cost, and durability, which are expected to improve by the development of key materials and components include the membrane. The most commonly used membrane in HT-PEMFCs is based on phosphoric acid doped polybenzimidazole (PBI). One of the major membrane issues is the relatively large ohmic resistance primarily due to the thick membranes used. The present project is attempted to address this issue by developing PBI composite membranes with reduced thickness and thus improved cell performance. Compared with conventional membranes, a thinner membrane may face challenges: 1) reduced mechanical stability and 2) increased crossover of reactants, which may result in formation of additional hydrogen peroxide and hence exaggerated oxidative degradation of the polymer.

The strategy of the project is to prepare the electrospun PBI fiber mats, which after crosslinking are insoluble in organic solvents and less swollen in phosphoric acid. The PBI fiber mats are then used as reinforcement of PBI membranes. The reinforcement fiber mat and the bulk membrane are made of the same polymer to improve the compatibility of the two phases.

This thesis consists of seven chapters. **Chapter 1** gives an introduction of principles and constructions of the fuel cells, with special emphasis on the PEMFC technology working at high temperatures (above 100 °C).

**Chapter 2** is a detailed literature review on high temperature polymer membrane electrolytes and associated technologies. The state of the art and updated progress of the HT-PEMs are presented, based on which the focus and methodologies of the present project are justified.

The experimental part of this thesis has focused on the development and characterization of thin membranes and composite membranes. The most frequently recurring experimental methods and techniques are described in **Chapter 3** while the experimental details for specific tasks be introduced in other chapters.

Experimental results of the project are presented in **Chapters 4-6**. Thin PBI membranes with thicknesses from 10 to 40 (standard)  $\mu\text{m}$  are first benchmarked in association with development of characterization protocols and techniques. The results are summarized in **Chapter 4**. High molecular weight polymer membranes with thickness of 10-20  $\mu\text{m}$  at a normal acid doping level of 11-12 mol  $\text{H}_3\text{PO}_4$  have been implemented in fuel cells with an MEA active area of 21  $\text{cm}^2$  and tested at 160 °C under operation with hydrogen and air. The hydrogen crossover rate is sufficiently low and as a result the open circuit voltages of fuel cells are typically above 0.95V. Decreased ohmic resistance and improved I-V performance are observed for thin membranes based MEAs. The total acid inventory in thin membranes is however an issue when part of the doping acid is transferred from the membrane to the catalyst layer.

PBI fiber mats have been successfully prepared by electrospinning after optimization of parameters including temperature, polymer concentration, spinning voltage, and collection distance (**Chapter 5**). The mat typically consists of fibers less than 200 nm diameter and has been fabricated in an upscaled size of 50x100 cm<sup>2</sup>. The PBI fibers are thermally crosslinked by curing at temperatures of 390-450 °C for 10 min under an inert atmosphere. Attempt is also made to introduce crosslinkers in the precursor solution before electrospinning and activate the covalent crosslinking by heat treatment at 280 °C of the electrospun fibers. Thus obtained PBI fibers are insoluble in hot (80 °C) dimethylacetamide, the typical solvent of PBI, and show limited swelling in hot phosphoric acid (85% at 80 °C), essential for reinforcement of the composite membranes.

Composite membranes are prepared from the bulk PBI matrix reinforced by the crosslinked PBI fiber mat (**Chapter 6**). As a result of the phase compatibility, dense and robust membranes are obtained from solution casting, as indicated by the low hydrogen permeability and high mechanical strength measured for the acid-doped composite membranes. The membranes exhibit anisotropic swelling during the acid doping. The composite membranes show slightly higher elastic modulus compared to that of pristine PBI membranes at similar acid doping levels. All MEAs with composite membranes exhibit high open circuit voltage of 0.95-1.00 V in H<sub>2</sub>-Air fuel cells at 160 °C. The composite membranes show a hydrogen permeability coefficient of the 10<sup>-11</sup> mol cm<sup>-1</sup> s<sup>-1</sup> bar<sup>-1</sup> level. A weak correlation of the fuel cell OCV with the hydrogen crossover and membrane thickness is observed for both pure and composite PBI membranes.

Conclusions and perspectives are given in **Chapter 7**.

# Table of Contents

---

<b>Acknowledgements</b> .....	<b>I</b>
<b>Abstract</b> .....	<b>III</b>
<b>Table of Contents</b> .....	<b>V</b>
<b>List of Figures</b> .....	<b>IX</b>
<b>List of Tables</b> .....	<b>XIII</b>
<b>List of Abbreviations</b> .....	<b>XV</b>
<b>Chapter 1 Introduction of fuel cells</b> .....	<b>1</b>
1.1 General introduction.....	1
1.2 History of fuel cells .....	1
1.3 Classification of fuel cells .....	2
1.3.1 Alkaline fuel cells (AFCs) .....	3
1.3.2 Phosphoric acid fuel cells (PAFCs) .....	3
1.3.3 Molten carbonate fuel cells (MCFCs).....	4
1.3.4 Solid oxide fuel cells (SOFCs) .....	4
1.3.5 Proton exchange membrane fuel cells (PEMFCs).....	4
1.4 Proton exchange membrane fuel cells.....	5
1.4.1 Principle and construction of PEMFC .....	5
1.4.2 Catalysts, electrodes, and gas diffusion layers.....	6
1.4.3 Bipolar plates .....	7
1.4.4 Proton exchange membranes (PEMs).....	7
1.4.5 Membrane electrode assemblies (MEAs) .....	7
1.5 Perfluorosulfonic acid membranes .....	8
1.5.1 Water uptake and swelling .....	11
1.5.2 Proton conductivity and electro-osmotic drag of water.....	12
1.5.3 Short side-chain PFSA membranes.....	12
1.5.4 PFSA composite membranes .....	13
1.5.5 Alternative membranes based on hydrocarbon polymers .....	15
1.6 High temperature PEMs .....	16
1.6.1 Why high temperatures .....	16
1.6.2 Types of HT-PEMs.....	17
<b>Chapter 2 High temperature proton exchange membranes</b> .....	<b>19</b>
2.1 Approaches to higher operating temperatures .....	19
2.2 Synthesis of PBI .....	20
2.2.1 Structure and applications of polybenzimidazoles .....	20
2.2.2 Polymer synthesis .....	20
2.3 Phosphoric acid and doped membrane fabrication.....	22
2.3.1 Phosphoric acid and doping chemistry .....	22
2.3.2 Direct casting by the PPA process.....	23

2.3.3 Post doping of DMAc membranes.....	23
2.4 Properties of acid doped PBI membranes .....	26
2.4.1 Proton conductivity.....	26
2.4.2 Electro-osmotic water drag coefficient.....	27
2.4.3 Thermal and oxidative stability.....	28
2.4.4 Mechanical strength.....	29
2.4.5 Gas permeability .....	30
2.5 PBI variants and crosslinking.....	31
2.5.1 Synthesis of modified PBI .....	31
2.5.2 Crosslinking .....	32
2.6 Inorganic-organic composites .....	35
2.6.1 Types of inorganic fillers .....	35
2.6.2 Methods of composite preparation.....	36
2.6.3 Composite membranes containing oxides and phosphates.....	37
2.6.4 Composite membranes containing phosphates and heteropolyacids.....	37
2.6.5 Composite membranes containing carbon based fillers.....	38
2.6.6 PBI composite containing ionic liquids .....	39
2.7 Electrospun nanofiber based composite membranes.....	40
2.7.1 Electrospinning technique.....	40
2.7.2 PBI nanofiber mat/ionomer matrix .....	42
2.7.3 Crosslinked or inorganic fibers/PBI matrix .....	42
2.8 Challenges of PBI membranes .....	44
2.8.1 Acid loss and inventory in MEAs .....	44
2.8.2 Importance of the membrane thickness .....	45
2.9 Approaches and scope of the thesis .....	47
<b>Chapter 3 Experimental .....</b>	<b>49</b>
3.1 Preparation of membranes.....	49
3.2 Preparation of fiber reinforced composite membranes .....	49
3.2.1 Electrospun fiber preparation.....	49
3.2.2 Upscale of electrospun mats .....	50
3.2.3 Thermal treatment.....	50
3.2.4 Crosslinked fibers .....	51
3.2.5 Fabrication of composite membranes .....	51
3.3 Thermogravimetric Analyses.....	52
3.4 Scanning electron microscope.....	52
3.5 Acid doping and swellings .....	53
3.6 Mechanical strength .....	53
3.7 Fuel cell test.....	54
3.7.1 21 cm <sup>2</sup> cell.....	54
3.7.2 1 cm <sup>2</sup> cell.....	55
3.7.3 Electrochemical impedance spectroscopy .....	55
3.7.4 Hydrogen crossover .....	57

<b>Chapter 4 Thin membranes .....</b>	<b>59</b>
4.1 Introduction .....	59
4.2 Experimental .....	61
4.2.1 Membrane casting.....	61
4.2.2 Acid doping and tensile strength measurement .....	61
4.2.3 MEA fabrication and fuel cell tests.....	61
4.3 Results and discussion.....	62
4.3.1 Preparation and acid doping of thin membranes.....	62
4.3.2 Mechanical strengthen .....	63
4.3.3 Analysis of I-V data .....	64
4.3.4 Break-in under constant current.....	66
4.3.5 Polarization curves of varied membrane thicknesses .....	68
4.3.6 Effect of acid inventory .....	69
4.3.7 OCV loss.....	71
4.3.8 Hydrogen permeability .....	72
4.3.9 Thermally cured and covalently crosslinked membranes .....	74
4.4 Conclusions .....	76
<b>Chapter 5 Fabrication of electrospun PBI nanofibers and mats.....</b>	<b>79</b>
5.1 Introduction .....	79
5.1.1 Basic setup and working parameters.....	80
5.1.2 Applications .....	80
5.1.3 Electrospun PBI nanofibers .....	80
5.2 Experimental .....	81
5.2.1 Fiber preparation by Linari electrospinninger .....	81
5.2.2 Upscaled fiber preparation by Naospider electrospinninger.....	82
5.2.3 Thermal curing of fiber mats .....	82
5.2.4 Covalent crosslinking of fiber mats .....	82
5.2.5 Solubility and swelling test.....	82
5.2.6 ATR-FTIR characterization.....	84
5.3 Results and discussion.....	84
5.3.1 Solution parameters .....	84
5.3.2 Processing parameters.....	86
5.3.3 Summary and characterization of PBI fiber mats .....	90
5.3.4 Crosslinking chemistry and thermogravimetric analysis .....	91
5.3.5 ATR-FTIR charaterization of thermally cured membranes .....	92
5.3.6 Solubility of thermally cured and covalently crosslinked fibers in DMAc .....	93
5.3.7 Swelling of thermal cured fiber mats in PA.....	95
5.3.8 Upscaled electrospinning .....	97
5.3.9 Morphology characterization of upscaled PBI fiber mats .....	98
5.4 Conclusions .....	99
<b>Chapter 6 Composite membranes .....</b>	<b>101</b>
6.1 Introduction .....	101

6.1.1 Thin membranes for LT- and HT-PEMFCs.....	101
6.1.2 PTFE-PFSA composite membranes.....	102
6.1.3 PTFE-PBI composite membranes.....	102
6.2 Experimental .....	103
6.2.1 Fabrication of composite membranes .....	103
6.2.2 Redissolution of composite membranes .....	104
6.2.3 Acid doping and tensile strength measurement .....	104
6.2.4 MEA, fuel cell test, and H <sub>2</sub> crossover measurement .....	104
6.3 Results and discussion.....	104
6.3.1 Composite membrane casting.....	104
6.3.2 Mat content and residue after redissolution test .....	106
6.3.3 Acid swelling of composite membranes .....	107
6.3.4 Mechanical strength.....	109
6.3.5 Open circuit voltage and hydrogen crossover.....	111
6.3.6 Polarization curves.....	112
6.4 Conclusions .....	114
<b>Chapter 7 Conclusions and perspectives .....</b>	<b>117</b>
7.1 Conclusions .....	117
7.2 Perspectives .....	119
<b>Bibliography .....</b>	<b>121</b>

# List of Figures

---

Figure 1.1 Schematic illustration of principle and construction of proton exchange membrane fuel cells. ....	6
Figure 1.2 Schematic of transport processes in electrodes. ....	8
Figure 1.3 The chemical structures of poly(perfluorosulfonic acid) membranes. ....	10
Figure 1.4 Schematic illustration of hydrated PFSA structure. ....	11
Figure 1.5 (a) Heat of fusion and (b) water uptake of Aquivion® and Nafion® membranes..	13
Figure 1.6 Structures of polymers.....	15
Figure 1.7 Polarization and power density curves at (a) 160 °C and (b) 180 °C.....	17
Figure 2.1 Structure of poly 2,2'-(phenylene)-5,5'-bibenzimidazole (meta-PBI or m-PBI)..	20
Figure 2.2 Schematic of the two-stage process for PBI synthesis. ....	21
Figure 2.3 Schematic of the single-stage process for PBI synthesis.....	21
Figure 2.4 Schematic of the PPA process for PBI synthesis. ....	21
Figure 2.5 State diagram of the PPA process. ....	23
Figure 2.6 H <sub>3</sub> PO <sub>4</sub> sorption isotherm at room temperature for m-PBI as a function of H <sub>3</sub> PO <sub>4</sub> concentration at equilibrium. ....	24
Figure 2.7 Conductivity mechanism of phosphoric acid doped polybenzimidazoles. ....	26
Figure 2.8 Proton conductivity of 100% phosphoric acid, Aquivion S98-09S and acid doped PBI membranes. ....	27
Figure 2.9 Membrane degradation in 3% H <sub>2</sub> O <sub>2</sub> .....	29
Figure 2.10 Tensile strength of DMAc-cast PBI membranes as a function of acid doping level at different temperatures. . ....	29
Figure 2.11 Possible reaction mechanism between benzimidazole and benzoxazine . ....	35
Figure 2.12 Schematic representation of the synthesis of IL@SNR ionogels.....	39
Figure 2.13 Number of research articles concerning electrospun nanofiber applications in fuel cells and electrolyte membranes published between 2010 and 2021 .....	41
Figure 2.14 Schematic illustration of a typical electrospinning set-up and the Taylor cone .....	41
Figure 2.15 Types of membrane architectures based on PBI materials.. ....	42
Figure 2.16 (a) Stress-strain curves; (b) Temperature-dependent proton conductivity of nanofiber-reinforced PBI composite membranes. ....	44
Figure 2.17 Estimations and measurements of acid loss carried by gas flow and the extrapolation of acid vapor pressure. ....	45
Figure 2.18 Conductivity data for phosphoric acid doped m-PBI prepared by casting from	

DMAc. . . . .	46
Figure 3.1 Nozzle-less electrospinning. . . . .	50
Figure 3.2 Schematic diagram of thermal treatment in Ar atmosphere. . . . .	51
Figure 3.3 Mat edge fixed with metal sticks during the composite casting process. . . . .	52
Figure 3.4 Types of interactions between electrons and a sample. . . . .	52
Figure 3.5 EIS spectra of a HT-PEMFC. . . . .	57
Figure 4.1 Photo of pure membranes. . . . .	62
Figure 4.2 Stress-strain curves at room temperature and atmospheric humidity of membranes with different thickness. . . . .	64
Figure 4.3 Polarization curve of a PBI cell obtained by linear scan voltammetry. . . . .	66
Figure 4.4 Cell voltages as a function of time for membranes. . . . .	67
Figure 4.5 (a) Polarization data (symbols) and the iR-free fitting curves and (b) the fitted area specific resistance of PBI-10 . . . . .	68
Figure 4.6 Polarization curve at 160 °C. . . . .	69
Figure 4.7 Nyquist of PBI-20 membrane with different acid doping level. . . . .	70
Figure 4.8 Hydrogen crossover current density of membrane. . . . .	72
Figure 4.9 Chronoamperograms for the hydrogen permeability measurements at 160 °C. ....	73
Figure 4.10 Schematic of thermal curing heating process . . . . .	74
Figure 4.11 Photos of thermal cured and crosslinked membranes. . . . .	75
Figure 4.12 Acid doping level of thermal cured and crosslinked membranes at different temperatures. . . . .	75
Figure 5.1 SEM images of samples obtained from solution with different concentration. ....	85
Figure 5.2 SEM images of samples obtained from solution with LiCl. . . . .	86
Figure 5.3 The average fiber diameter as a function of the LiCl content in the polymer solutions. . . . .	86
Figure 5.4 SEM images of electrospun PBI fibers obtained from solution A4. . . . .	87
Figure 5.5 SEM images of electrospun fibers obtained from solution A5-14%PBI at different collect distances and flow rates. . . . .	88
Figure 5.6 SEM images of samples collected with brown paper and Aluminium foil. . . . .	89
Figure 5.7 Photo of PBI fibers collected with brown paper. . . . .	90
Figure 5.8 Chemistry of PBI crosslinking by DBpX (a) and thermal curing (b). . . . .	91
Figure 5.9 (a) TGA and (b) DTA data of the pristine PBI mat and cured mats. . . . .	92
Figure 5.10 ATR-FTIR spectra of pristine membrane and thermally cured membrane. . . . .	93
Figure 5.11 Solubility of thermally cured fibers and covalently crosslinked fibers in DMAc at 80 °C. . . . .	94
Figure 5.12 Solubility of thermally cured PBI membranes in DMAc at 80 °C. . . . .	95
Figure 5.13 Area swelling of PBI fiber mats after immersion in phosphoric acid at 80 °C. ....	96

Figure 5.14 SEM images and fiber diameter distribution of thermal cured fibers in PA. ....	97
Figure 5.15 Photos of PBI fiber mats prepared by Nanospider. ....	98
Figure 5.16 SEM images of electrospun PBI fiber mats.. ....	99
Figure 6.1 Schematic illustration of the fabrication of the fiber-reinforced PBI composite membranes. ....	103
Figure 6.2 Photos of composite membranes.. ....	105
Figure 6.3 Photos of composite samples containing thermal cured (a and c) and covalently crosslinked (b and d) fiber mat immersion before (a and c) and after being immersed in DMAc 80 °C for 24 h.....	107
Figure 6.4 Volume (a), area (b) and thickness (c) swelling of PBI reference and composite membranes at different acid doping level. ....	108
Figure 6.5 Illustration of anisotropic swelling of PBI reference and composite membranes. ....	109
Figure 6.6 Typical stress-strain curves for PBI and fiber mat reinforced composite membranes at ambient temperature and relative humidity. ....	110
Figure 6.7 Correlation of open circuit voltages with hydrogen crossover current density and thickness of pure and composite membranes.....	112
Figure 6.8 Polarization curves (as measured), iR-free fitting curves and the fitted area specific resistance of fuel cells based on four composite membranes. ....	113
Figure 6.9 I-Vcurve of composite membranes with acid doping levels of 11.9 and 15.6 mol H <sub>3</sub> PO <sub>4</sub> /PRU. ....	114



# List of Tables

---

Table 1.1 Types of fuel cells. ....	3
Table 1.2 Summary of fundamental requirements on the proton exchange membrane material.....	9
Table 1.3 Some properties of Nafion 117 membranes measured at 23 °C and 50% RH after conditioning by water soaking at 100 °C.....	10
Table 1.4 Characteristic data of Gore-select® membranes compared with Nafion® 117.....	14
Table 1.5 Challenges for LT-PEMFCs that can be addressed by development of HT-PEM. ..	17
Table 2.1 Properties of PBI membranes synthesized by PPA process. ....	25
Table 2.2 Properties of PBI membranes (DMAc-cast) before and after acid doping. ....	31
Table 2.3 Examples of common derivatives of PBI membranes. ....	32
Table 2.4 List of example crosslinkers. ....	34
Table 2.5 Selected inorganic-organic composite membranes. ....	36
Table 2.6 Ionic liquids/PBI composite membranes. ....	40
Table 2.7 Overview of PBI nanofiber mat/ionomer matrix. ....	43
Table 2.8 Overview of proton conducting membranes of crosslinked electrospun polymer mat/ionomer or inert matrix. ....	44
Table 3.1 H <sub>2</sub> and air flow rate for measurements of I-V curves at fixed stoichiometries.....	55
Table 4.1 A set of parameters of Nafion, Nation/PTFE composite and PA-doped PBI membranes at specified temperatures.....	60
Table 4.2 Summary of acid doping level, swelling, and mechanical data at room temperature. ....	63
Table 4.3 Summary of cell performance at 160 °C with membranes of different thicknesses.....	69
Table 4.4 Properties of PBI-20 with different ADLs .....	70
Table 4.5 Summary of hydrogen permeability for thin PBI membranes at different acid doping levels.....	72
Table 4.6 Summary of cell performance of thermal cured and crosslinked membranes operated at 160 °C. ....	76
Table 5.1 Summary of experiments for PBI nanofiber preparation under various solution and electrospinning parameters.....	83
Table 5.2 Summary of prepared PBI fiber mat samples for further characterization .....	90

Table 5.3 Summary of solution and electrospinning parameters for upscaled PBI nanofibers. ....	98
Table 5.4 Estimated properties of PBI nanofiber mats .....	99
Table 6.1 Summary of composite membrane samples and estimated properties. ....	105
Table 6.2 Results of the re-dissolution test of the composite membranes in hot DMAc.....	106
Table 6.3 Summary of the thickness, acid doping level, area swelling, and the mechanical data of doped composite membranes. ....	110
Table 6.4 Summary of fuel cell open circuit voltages and H <sub>2</sub> crossover for PBI composite membranes.....	111
Table 6.5 Summary of cell performances of composite membranes with cured mats at 160 °C.....	113

## List of Abbreviations

---

<b>2,5-py PBI</b>	2,5-pyridinedicarboxylic acid polybenzimidazole
<b>2OH-PBI</b>	Poly(2,20-(2,5-dihydroxy-1,4-phenylene) 5,50-bibenzimidazole)
<b>3,5-py PBI</b>	3,5-pyridinedicarboxylic acid polybenzimidazole
<b>ADL</b>	Acid doping level
<b>AFC</b>	Alkaline fuel cell
<b>AS</b>	Area swelling
<b>ASR</b>	Area specific resistance
<b>ATR-FTIR</b>	Attenuated Total Reflectance Fourier Transform Infrared spectroscopy
<b>BPP</b>	Bipolar plate
<b>CHP</b>	Co-generation of heat and power
<b>CL</b>	Catalyst layer
<b>DABA</b>	3,4-diaminobenzoic acid
<b>DBpX</b>	$\alpha,\alpha$ -dibromo-p-xylene
<b>DMAc</b>	Dimethylacetamide
<b>DMF</b>	N,N-dimethylformamide
<b>DMFC</b>	Direct methanol fuel cell
<b>DMSO</b>	Dimethylsulfoxide
<b>DPIP</b>	Diphenyl isophthalate
<b>DTA</b>	Differential thermal analysis
<b>EGDE</b>	Ethylene glycol diglycidyl ether
<b>EIS</b>	Electrochemical impedance spectroscopy
<b>EW</b>	Equivalent weight
<b>F6-PBI</b>	Fluorinated polybenzimidazole
<b>FCEV</b>	Fuel cell electric vehicle
<b>FEP</b>	Poly(tetrafluoroethylene-co-hexafluoropropylene)
<b>GC</b>	Gas chromatography
<b>GDL</b>	Gas diffusion layer
<b>GO</b>	Graphite oxide
<b>HOR</b>	Hydrogen oxidation reaction
<b>HPA</b>	Heteropolyacid
<b>HT-PEMFC</b>	High temperature polymer electrolyte membrane fuel cell
<b>ICE</b>	Ion exchange capacity
<b>IL</b>	Ionic liquid
<b>IPA</b>	Isophthalic acid
<b>LSC</b>	Long side chain
<b>LSV</b>	Linear scan voltammetry
<b>LT-PEMFC</b>	Low temperature polymer electrolyte membrane fuel cell

<b>MCFC</b>	Molten carbonate fuel cell
<b>MD</b>	Machine direction
<b>MEA</b>	Membrane-electrode assembly
<b>m-PBI / PBI</b>	Poly 2,2'-(m-phenylene)-5,5'-bibenzimidazole / Polybenzimidazole
<b>MPL</b>	Microporous layer
<b>MS</b>	Mass spectrometry
<b>MSA</b>	Methane sulfonic acid
<b>NMP</b>	N-methyl-2-pyrrolidone
<b>OCV</b>	Open circuit voltage
<b>ORR</b>	Oxygen reduction reaction
<b>PA</b>	Phosphoric acid
<b>PAFC</b>	Phosphoric acid fuel cell
<b>P(ara)-PBI</b>	Poly(2,2'-(1,4-phenylene)5,5'-bibenzimidazole)
<b>PEEK</b>	Poly(ether ether ketone)
<b>PEG</b>	Poly(ethylene glycol)
<b>PEM</b>	Proton exchange membrane
<b>PEMFC</b>	Polymer electrolyte membrane fuel cell
<b>PFSA</b>	Perfluorosulfonic acid
<b>PIL</b>	Polymeric ionic liquid
<b>PPA</b>	Polyphosphoric acid
<b>PRU</b>	Polymer repeating unit
<b>PSU</b>	Poly(ether sulfone)
<b>PTFE</b>	Polytetrafluoroethylene
<b>PVDF</b>	Poly(vinylidene fluoride)
<b>RH</b>	Relative humidity
<b>SEM</b>	Scanning electron microscope
<b>SOFC</b>	Solid oxide fuel cell
<b>s-PBI</b>	Sulphonated polybenzimidazole
<b>SSC</b>	short side-chain
<b>TAB</b>	Tetraaminobiphenyl
<b>TCDA</b>	Tetracarboxylic dianhydride
<b>TD</b>	Transverse direction
<b>TGA</b>	Thermogravimetric analysis
<b>TPAH</b>	Terephthaldehyde
<b>VRFB</b>	Vanadium redox flow battery
<b>VS</b>	Volume swelling

# CHAPTER 1

## Introduction of fuel cells

---

### 1.1 General introduction

Growing concerns about the depletion of fossil fuels and environmental issues have forced society to look for clean and renewable energy technologies. Many forms of renewable energies (e.g., solar energy, wind power, and hydropower) are directly or indirectly derived from the sun. Utilization of renewable power in a grid requires some back-up storage of the energy for a shorter or longer period due to the intermittent nature of the renewable energy sources. Water electrolysis, among others, offers a practical way of storing energy from renewable sources via hydrogen. Hydrogen can be stored as compressed gas, liquid, or in a variety of metal hydrides. An alternative way of hydrogen storage is via synthesis of chemical compounds such as methanol, ethanol or hydrocarbons. Whenever electrical power is needed, hydrogen can be efficiently converted via an electrochemical energy conversion device - fuel cells. The hydrogen route of renewable energy storage and its combination with fuel cells have been recognized as a reliable, secure, and clean energy technology in future renewable energy systems.

### 1.2 History of fuel cells

The history of fuel cells can be dated back to about 200 years ago. The first battery, a galvanic cell for electrical power generation was invented by A. Volta in 1800, called the voltaic pile, which enabled the immediate discovery by Carlisle and Nicholson[1] that electricity could decompose water into hydrogen and oxygen.

In 1838 British physicist Sir William Robert Grove reported the very first fuel cell, which named “Gaseous Voltaic Battery”, showing that the electrochemical dissociation of water was almost reversible using platinized platinum (Pt) electrodes in dilute sulfuric acid [2]. A similar experiment was carried out at about the same time by German-Swiss chemist Christian Friedrich Schönbein [3]. In 1889, Ludwig Mond and Carl Langer developed Grove’s device using coal gas as a fuel, and they coined the term ‘fuel cell’ [4].

Different types of fuel cells were invented and developed for practical applications in the twentieth century. In 1932, Cambridge engineering professor Francis Bacon modified Mond's and Langer's device to develop the first alkaline fuel cell (AFC). In 1958, Bacon demonstrated a practical 5 kW fuel cell system [5]. Soon after the demonstration the Bacon-type fuel cells were fitted and tested in driving tractors, forklift trucks, and golf carts. By the end of the 1950s National Aeronautics and Space Administration (NASA), US, developed fuel cells for space

missions. Willard Thomas Grubb and Leonard Niedrach designed the first polymer electrolyte membrane fuel cell (PEMFC), used by NASA in the Gemini space program, while a 1.5 kW AFC was applied in Apollo space missions, providing the astronauts both power and drinking water and a 12 kW AFC has been applied in a space shuttle [6].

Efforts to develop fuel cells for application in transportation and stationary power generation were motivated after the oil crisis in the 1970s. In particular, General Electric and other vehicle manufacturers embarked on the research and development of fuel cell electric vehicles (FCEVs). In 1983 the Canadian company Ballard began working on PEMFC and since then has been a major player in the manufacturing of stacks and systems[7]. The renaissance of FCEVs was symbolized by the collaboration between Ballard and Daimler-Benz for development of compact and high power density PEMFC stacks for automobile applications in early 1990s. At the same time, development of PEMFC and solid oxide fuel cell (SOFC) technologies was started for residential co-generation of heat and power (CHP) applications. Meanwhile, the molten carbonate fuel cell (MCFC) technology made substantial commercial advances for large stationary applications. In the 2000s, the first 700 bar compressed hydrogen tanks were demonstrated for an extended driving range. Today three major types of fuel cell cars are on the market from Hyundai, Toyota, and Honda. By May 2020, there were more than 15,000 hydrogen fuel cell vehicles on roads worldwide [8].

Government and private funding for fuel cell research and development has increased markedly in the 2000s. There has been a renewed focus on fundamental research to achieve breakthroughs in cost reduction and operational performance to make fuel cells competitive with conventional energy conversion technologies. The major European, North American, and Asian countries are all engaged in high-profile demonstration projects of stationary and transport fuel cells and the associated fuelling infrastructure. The clean urban transport for Europe (CUTE) program initiated 27 fuel cell buses in 9 European countries in the early 2000s. Fuel cell buses, running on fixed routes and fueling at fixed sites, were seen as an early market for fuel cell applications due to their combination of high efficiency and zero emissions. The end of 2020 saw an estimated 115 fuel cell buses in operation in Europe[8].

From 2010 to now, growth in shipments of fuel cells has accelerated rapidly as various applications have become commercial. Shipments in the portable sector were also augmented by the launch of Toshiba's Dynario fuel cell battery charger in 2009. In 2020, the fuel cell industry finally shipped 82,500 power units in the total power of 1.32 gigawatt (GW). Of the fuel cell types, PEMFC dominates shipments both in power unit number (65%) and in capacity (78%). SOFC is the second in terms of unit numbers mainly for stationary power and particularly domestic CHP [8].

### 1.3 Classification of fuel cells

All fuel cells are constructed using two electrodes separated by the electrolyte that carries electrically charged particles between them. Catalysts are often used to accelerate the reactions at both electrodes. Fuel cell types are generally classified according to the electrolyte they use.

The electrolytes used as well as the mobile ions and operating temperatures for each type of fuel cells are given in Table 1.1 [9, 10].

Table 1.1 Types of fuel cells.

Fuel cells types		Electrolyte	Mobile ion	Operating temperature (°C)
Alkaline fuel cell (AFC)		KOH	OH <sup>-</sup>	50-200
Proton exchange membrane fuel cell (PEMFC)	LT-PEMFC	Perfluorosulfonic acid	H <sub>3</sub> O <sup>+</sup>	60-80
	HT-PEMFC	H <sub>3</sub> PO <sub>4</sub> doped PBI	H <sup>+</sup>	120-200
Phosphoric acid fuel cell (PAFC)		H <sub>3</sub> PO <sub>4</sub>	H <sup>+</sup>	150-200
Molten carbonate fuel cell (MCFC)		(Li/Na/K) <sub>2</sub> CO <sub>3</sub>	CO <sub>3</sub> <sup>2-</sup>	650
Solid oxide fuel cell (SOFC)		Ceramics	O <sup>2-</sup>	500-1000

### 1.3.1 Alkaline fuel cells (AFCs)

The alkaline fuel cell was proved to be viable power units by Sir Francis Bacon [5, 6]. In the mid of 1960s, AFCs have been used by NASA in the Apollo and Space Shuttle programs with a high electrical efficiency of nearly 70% [5]. A key advantage of the AFCs is the low overpotential of the oxygen reduction reaction enabling the use of non-noble catalysts at the cathode and thus reducing the capital cost of the stack. AFCs are intolerant towards CO<sub>2</sub> as it reacts with KOH of the electrolyte forming solid carbonates, which dictates the use of high purity hydrogen and CO<sub>2</sub>-scrubbed air. Any precipitation of carbonates will not only block the porous electrodes but also reduce the conductivity of the electrolyte, increase its viscosity and decrease the oxygen solubility, which in turn decreases cell performance[9]. The liquid electrolyte is either immobilized in a matrix or circulated, which is a big issue for the AFC system. In the last ten years, AFCs are attracting much attention because of the development and application of alkaline anion exchange membrane [11, 12].

### 1.3.2 Phosphoric acid fuel cells (PAFCs)

The phosphoric acid fuel cell is one of the most mature cell types and it is the first commercialized technology since the 1990s. PAFCs use concentrated phosphoric acid as electrolyte. The acid is absorbed in a Teflon-bonded silicon carbide (SiC) matrix. This type of cell normally operates at 150-220 °C, as phosphoric acid is a thermally stable triprotic inorganic acid with low vapor pressure and high proton conductivity at temperatures up to 200 °C. One advantage of PAFCs is that the anode can be fed with hydrocarbon fuel reformat containing up to 25% CO<sub>2</sub> and 3% CO that can be tolerated by the platinum-based electrocatalysts. Thermal management is relatively simple and the waste heat from PAFCs can be used for CHP. However, the strong adsorption of dissociated phosphoric acid on the platinum surface reduces the kinetic rate of the oxygen reduction reaction (ORR) at the cathode and therefore the fuel cell performance. In addition, the high corrosion rate of the carbon catalyst support as well as

other construction materials limits the long-term lifetime of the technology. Pure phosphoric acid has a freezing point of 42 °C, therefore PAFC stacks are usually kept at an elevated temperature after commissioning to avoid stress development due to freezing and thawing of the acid. Even though the vapour pressure of phosphoric acid is low, acid is lost over time, reducing the electrolyte conductivity.

### 1.3.3 Molten carbonate fuel cells (MCFCs)

Molten carbonate fuel cells are high-temperature fuel cells that operate at temperatures around 650 °C. A molten and corrosive mixture of carbonate salts of alkali metals (lithium, sodium, and potassium) is used as the electrolyte, which is retained in a ceramic matrix of  $\text{LiAlO}_3$ . The high operating temperature makes MCFC possible to use non-precious metal-based catalysts i.e. nickel and its alloys as the anode catalysts and nickel oxide (NiO) as cathode catalysts. The efficiency of MCFCs is approaching 60%. Better utilization of waste heat is optional for further improvement of the overall efficiency. Natural gas, biogas, and coal gas can be used as fuel without external reformer [13]. At the cathode, oxygen is reduced and combined with carbon dioxide to carbonate (mobile ion). Stainless steel can be used as construction materials. The primary limitation of MCFCs is the insufficient durability as the high operating temperature accelerates component corrosion. Therefore, the recent effort has been devoted to exploring corrosion-resistant materials for MCFCs [14].

### 1.3.4 Solid oxide fuel cells (SOFCs)

The SOFC is a complete solid-state device that uses oxide ion-conducting ceramic materials, typically sintered yttria, yttria-stabilized zirconia, or scandia stabilized zirconia, as the electrolyte. The operating temperature of SOFCs is high, from 500 to 1000 °C. The feeding fuels can be hydrogen [15, 16],  $\text{NH}_3$  [17] as well as various hydrocarbon-based compounds such as natural gas [18], biogas [19], and alcohols [20]. Currently, much research effort is devoted to reducing the operating temperature in order to allow a broader choice of materials, reduce startup time and minimize degradation of cell and stack components.

### 1.3.5 Proton exchange membrane fuel cells (PEMFCs)

Proton exchange membrane fuel cell has a polymeric proton conductor as electrolyte to separate the anode and cathode. PEMFC can be classified into two categories by its range of working temperature. The LT-PEMFC operates around 60 to 80 °C while the HT-PEMFC operates above 120 °C up to 200 °C.

At low working temperatures (below 100 °C), the startup is easy, the gases need not be preheated, the selection of construction materials is wide, and degradation processes are generally slower. High fuel cell performance in terms of power density has been achieved for LT-PEMFC which has stimulated the automobile and portable power applications [21, 22]. Toyota started selling their hydrogen fuel cell car ‘Mirai’ while other automotive companies such as Hyundai (Tucson), Honda (Clarity), Mercedes (B-Class) are also in the same focus on

manufacturing their own fuel cell electric vehicles. PEMFCs for buses, which use compressed hydrogen for fuel, can operate at up to 40% efficiency. Generally PEMFCs are implemented on buses over smaller cars because of the available volume to house the system and store the fuel. Technical issues for transportation involve incorporation of PEMs into current vehicle technology and updating energy systems. Full fuel cell vehicles are not advantageous if hydrogen is sourced from fossil fuels; however, they become beneficial when implemented as hybrids. There is potential for PEMFCs to be used for stationary power generation as well, however, they run into competition with other types of fuel cells e.g. SOFCs and MCFCs which can run on methane instead of high purity hydrogen with also much better value of waste heat to recover [23].

Technically some issues of LT-PEMFC are pending to improve. First of all, the anode catalyst of LT-PEMFC is very sensitive to CO down to a level of 10-20 ppm, which limits the use of fuel to high purity hydrogen. The mobile ions in PEM are not bare protons ( $H^+$ ) but hydrated protons (e.g.  $H_3O^+$ ), which means that the management of water balance is always needed to consider in the stack design of the LT-PEMFC. If there is too little water supplied with feeding air and hydrogen, the membrane will sooner or later be drying out and the cell resistance will increase significantly, the overall power and efficiency of the system will be affected. If there is an excessive amount of water supplied with the feeding gases, the electrodes may be flooded and the transportation of reactants (hydrogen and oxygen) will be restricted [24].

Both CO poisoning and humidification issues can be minimized by increasing the operating temperature of PEMFC. At working temperatures above 100 °C, only one phase of water i.e. the water vapor needs to handle and the CO tolerance can be significantly enhanced. In addition, the electrode reaction rates are expected to be increased. The main challenge for PEMFCs to operate at higher temperatures is the membrane electrolyte materials. It has been discovered that a polybenzimidazole (PBI) membrane doped with phosphoric acid (PA) as the proton conductor can operate at temperatures up to 200 °C. Much research work focused on the membrane properties, lifetime of the component, and system design [25]. More detail is discussed in the next section.

## 1.4 Proton exchange membrane fuel cells

### 1.4.1 Principle and construction of PEMFC

The construction of a single fuel cell using a proton conducting electrolyte is depicted as an exploded view in Figure 1.1. The electrolyte is, in addition to the functionality of proton conduction, an electronically insulating and gas tight material, employed to separate the anode and the cathode. Water is the only product of the reaction when hydrogen is used as fuel and oxygen is used as oxidant. The oxidation of the fuel happens on the anode where a hydrogen molecule is oxidized to two protons by releasing two electrons. The protons can pass across the electrolyte to the cathode while the generated electrons flow from the anode to the cathode through an external circuit. The reduction of the oxidant happens at the cathode where oxygen is combined with protons and electrons to form  $H_2O$ . The electrochemical reaction on anode

and cathode are as follows:

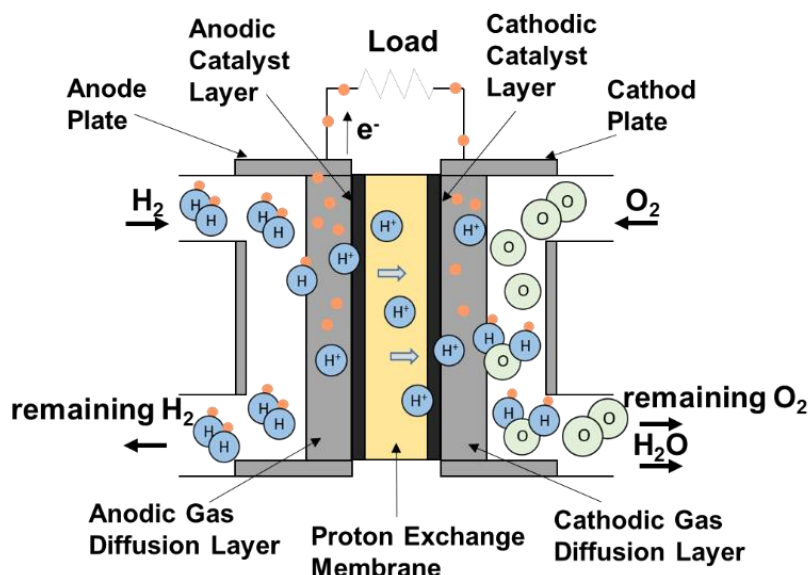
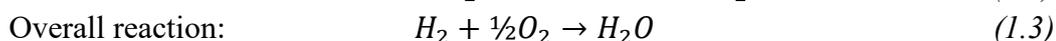
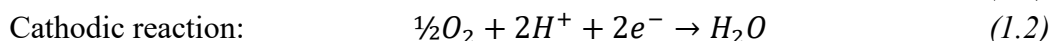
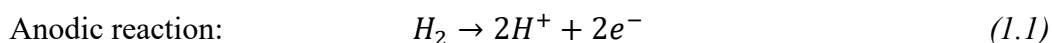


Figure 1.1 Schematic illustration of principle and construction of proton exchange membrane fuel cells.

#### 1.4.2 Catalysts, electrodes, and gas diffusion layers

In PEMFC, both the cathode oxygen reduction reaction (ORR) and hydrogen oxidation reaction (HOR) are facilitated by the use of highly active catalysts. The kinetics of the ORR, as expressed by the exchange current density, is six or more orders of magnitude slower than the HOR and thus limits the fuel cell performance. Platinum supported on carbon has been the most effective catalyst for both the HOR and ORR. The slow reaction rate at the cathode generally requires a higher loading of Pt of the cathode catalyst. The carbon used as the catalyst support serves not only to disperse the active metal nanoparticles but also to provide good electronic conductivity to enable a high current to be drawn from the fuel cell [26].

The electrodes are comprised of several layers, each with its own functionality. Closest to the membrane is the catalyst layer (CL), consisting of a mixture of the proton conducting electrolyte and electronically conducting catalyst material. The electrode is a porous structure in which the triple phase boundary is formed at the catalyst and membrane interface. Maximizing the triple phase boundary area has a tremendous positive effect on the performance of the fuel cell. On the outside of the electrode, there is the gas diffusion layer (GDL) which consists of carbon cloth or paper, made up of carbon fibers, and is usually treated with polytetrafluoroethylene (PTFE, Teflon®) to make the layer hydrophobic in order to facilitate water removal from the catalyst layer. As the name implies, the GDL is responsible for the diffusion of the reactant gases to the catalyst layer. At the same time, the GDL also serves as

an electron conductor and provides physical support, as it is the most rigid part of the membrane-electrode assembly (MEA). It is a common practice that the GDL is coated with a mixture of PTFE and carbon black, which ensures a smooth surface, on which the catalyst layer is applied. This is called the microporous layer (MPL), as it is highly porous to allow gas diffusion to and from the catalyst layer. The carbon black component ensures electronic conductivity between the catalyst and gas diffusion layers.

### 1.4.3 Bipolar plates

When multiple cells are piled together in a stack, a plate is needed between every two cells in order to connect the anode of one cell to the cathode of the next. Such a plate is called a bipolar plate (BPP) which provides a pathway for the electrons and ensures no mixing of the anode and cathode gases. The requirements for the bipolar plates are quite demanding – they must be electrically and thermally conductive, impermeable to gasses, mechanically strong, and lightweight, as they provide structural support to the stacking. The common materials for BPPs used in PEMFCs include high density graphite, metals (stainless steel often with surface coatings), and polymer composites (metal-polymer composites and carbon-polymer composites) [27].

### 1.4.4 Proton exchange membranes (PEMs)

Proton exchange membranes (PEMs) as the electrolyte play an important role in conducting protons, separating reactants i.e. the fuel and oxidant, and insulating the electron conduction between the anode and cathode. PEMs can be made from either pure polymer membranes or from composite membranes [28], where other materials are embedded in a polymer matrix. One of the most common and commercially available PEM materials is perfluorosulfonic acid (PFSA) (Nafion<sup>®</sup>, DuPont Company). PFSA is chemically inert in both oxidizing and reducing atmospheres because of its perfluorinated carbon backbone. Nafion membranes are highly acidic, have proton conductivity above  $10^{-1} \text{ S cm}^{-1}$  at 80 °C under full hydration i.e. around 100% relative humidity [29]. Alternative membranes have also been developed including partially fluorinated and nonfluorinated hydrocarbons. Details of the PEM materials will be introduced in Section 1.5.

### 1.4.5 Membrane electrode assemblies (MEAs)

The membrane electrode assembly is the heart of the cell and it consists of the proton exchange membrane (PEM) together with the catalyst layers and eventually the gas diffusion layers depending on the specific engineering of the electrodes [30].

The interface between the catalyst layer and the membrane is generally of rather complex structure [31], the so-called triple-phase boundary where a protonic conducting phase intersects with gas filled pores that are in direct contact with catalytically active sites on the surface of catalyst particles. To maximize the electrochemically active surface area per mass unit of the noble metal, the diameter of the catalyst particles is optimized to be in a range of 2-5 nm [32]. The gas diffusion layer and the catalyst layer must provide good electronic conductivity in the

electrode to ensure that electrons can effectively be transported to and from the catalytically active sites. A certain amount of the proton conducting polymer is also required in the catalyst layers to ensure that the protons can be effectively transported between the bulk membrane and the catalytically active sites in the electrodes. Additionally, the catalyst layers have to be highly porous in order to facilitate efficient and rapid transport of gaseous or liquid reactants and products to and from the electrochemically active sites of the catalyst particles.

Figure 1.2 schematically shows the transport processes in the cathode triple-phase boundary for the oxygen reduction reaction [30] i.e., (1) protons from the membrane to the catalyst; (2) electrons from the gas diffusion layer; and (3) reactant (oxygen) to and product (water) from the catalyst layer and the gas channels.

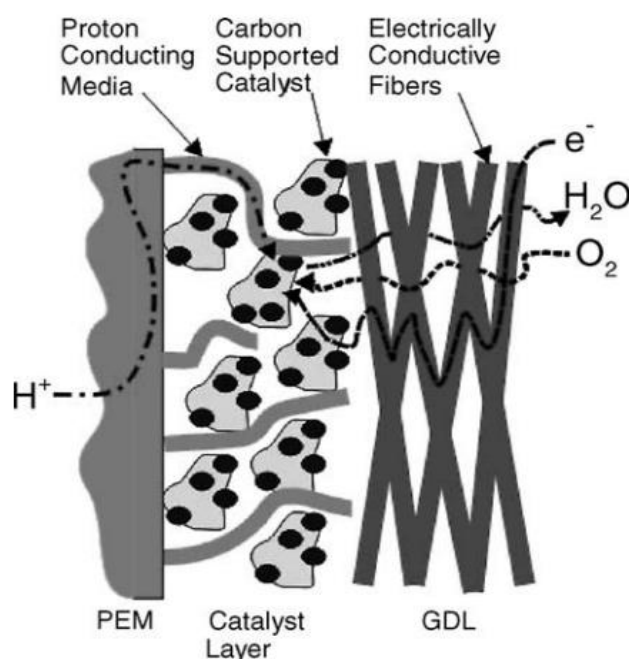


Figure 1.2 Schematic of transport processes in electrodes [30].

## 1.5 Perfluorosulfonic acid membranes

Proton exchange membrane (PEM) is one of the key materials in the PEMFC that partly determines the overall efficiency, cost and lifetime of the system. A PEM functions as (i) a separator to prevent mixing of reactants; (ii) a conductor for protons from anode to cathode; and (iii) an electrical insulator to drive electrons through an external path to the cathode. To be applied in PEMFCs, the advanced membrane materials should meet some requirements, as summarized in Table 1.2 below.

In 1959, PEMFCs were invented by General Electric (GE) [33]. Initially, GE was using membranes made from polystyrene sulfonic acid polymer (sulfonated polystyrene–divinylbenzene) as the electrolyte in these fuel cells. However, these fuel cells were failing prematurely because the membranes were chemically unstable to the oxidative environment of the fuel cell. The membrane was soon replaced by perfluorosulfonic acid polymer (PFSA) e.g. Nafion<sup>®</sup> [29, 34].

*Table 1.2 Summary of fundamental requirements on the proton exchange membrane material [35, 36]*

<b>Requirement</b>	<b>Motivation</b>
High proton conductivity	Proton conductivity above $10^{-2}$ S cm <sup>-1</sup> is required in order to minimize the ohmic voltage losses, especially at high current densities.
Negligible electronic conductivity	The membrane has to be electronically insulating in order to avoid short circuit of the cell.
Low reactant permeability	The membrane has to be a good barrier for the reactants. Reactant cross-over results in poor fuel utilization and voltage losses in fuel cells. High cross-over rate might also be connected with safety issues due to the formation of explosive gas mixtures.
Mechanical strength and flexibility	The mechanical strength and the flexibility of the membrane are important parameters in the membrane processing and production of MEAs. Thermal cycling of the electrochemical cell will induce stresses in contact points between different cell components, which ultimately might lead to physical membrane failures.
Durability	The membrane has to be tolerant to the harsh oxidative conditions in the operating cell. For example the polymer matrix has to withstand aggressive radicals, high potentials, extreme pH and eventually high temperatures.
Fast electrode kinetics	The proton conductor is part of electrode-membrane interface where electrode reactions take place and therefor needs to allow for good reaction kinetics.
Availability	In order to reach widespread commercial utilization of the PEM technology, the cost of the membrane material has to be minimized.

The PFSA membrane, represented by Nafion<sup>®</sup> (DuPont), is the most commonly used PEM and has served as benchmarks for membrane performances because of its excellent chemical and electrochemical stabilities as well as outstanding proton conductivity [37]. PFSA membranes have ionic groups that are covalently bonded to the polymer backbone as pendant group moieties and are called ionomers. Figure 1.3 shows examples of these ionomers commercialized by DuPont, 3M, and Aquivion. The structures vary slightly in the length of the backbones but mainly in the length of the sulfonic acid terminated side chains. Nafion<sup>®</sup> is called the long side chain (LSC) while the 3M and Aquivion membranes are called the short side chain (SSC) membranes.

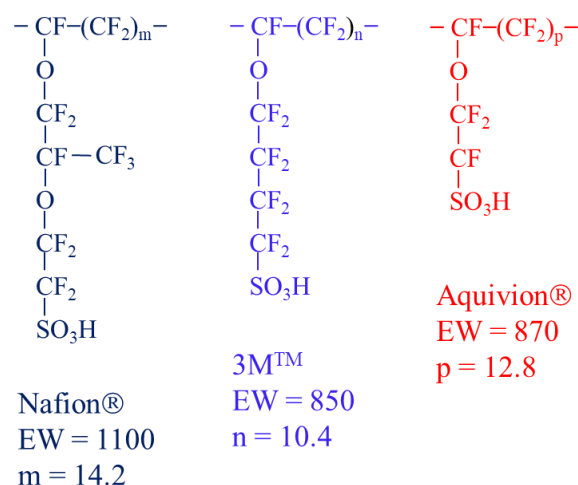


Figure 1.3 The chemical structures of poly(perfluorosulfonic acid) membranes.

Ion exchange capacity (IEC) is defined as the number of active sites or functional groups responsible for ion exchange per unit mass of the dry polymer, usually expressed as milli-moles per gram ( $\text{mmol g}^{-1}$ ). In polymer chemistry another relevant term often used is the equivalent weight (EW) which is the inverse of the ion exchange capacity (IEC) i.e. the mass of the polymer containing one mole of functional groups. Typical PFSA membranes e.g. Nafion 117 has an EW  $1100 \text{ g mol}^{-1}$ . Table 1.3 summarizes the properties of typical Nafion and Aquivion membranes.

Table 1.3 Some properties of Nafion 117 membranes measured at 23 °C and 50% RH after conditioning by water soaking at 100 °C.

Properties	Nafion® 117
Equivalent weight (g/mol)	1100
Thickness ( $\mu\text{m}$ )	183
Density ( $\text{g/cm}^3$ )	1.98
Specific Weight ( $\text{g/m}^2$ )	360
Tensile Modulus (MPa):	
- at 23 °C, 50%RH	249
- Water soaked at 100 °C	64
Max. Tensile Strength (MD/TD, MPa):	
- at 23 °C, 50%RH	43/32
- Water soaked at 100 °C	25/24
Elongation at Break (MD/TD, %):	
- at 23 °C, 50%RH	225/310
- Water soaked at 100 °C	180/240
Conductivity ( $\text{S cm}^{-1}$ ), 80 °C, 100%HR	0.12
Water uptake (wt%):	
- From dry to 23 °C, 50%RH	5
- From dry to water soaked at 100 °C	38

### 1.5.1 Water uptake and swelling

The water uptake and swelling of PFSA membranes are essential to achieve proton conductivity. The water uptake behavior and ionic clustering structure of the perfluorinated ionomer membranes are well understood in the literature. It has a hydrophobic phase that functions as the continuous phase for the structural integrity of the membrane, as well as a sulfonic acid group that acts as a hydrophilic phase for the water uptake [38].

The absorbed water solvates the protons and enables the proton conductivity. Between the ion clusters are some cylindrical channels, allowing for hydrodynamic permeability of charged as well as uncharged species through a membrane. On a microscopic scale, this is schematically illustrated in Figure 1.4. The scale bar to the left indicates, from top to bottom, the increase in hydrophobicity and therefore water content with accompanying transition from crystalline, amorphous to ionic phases.

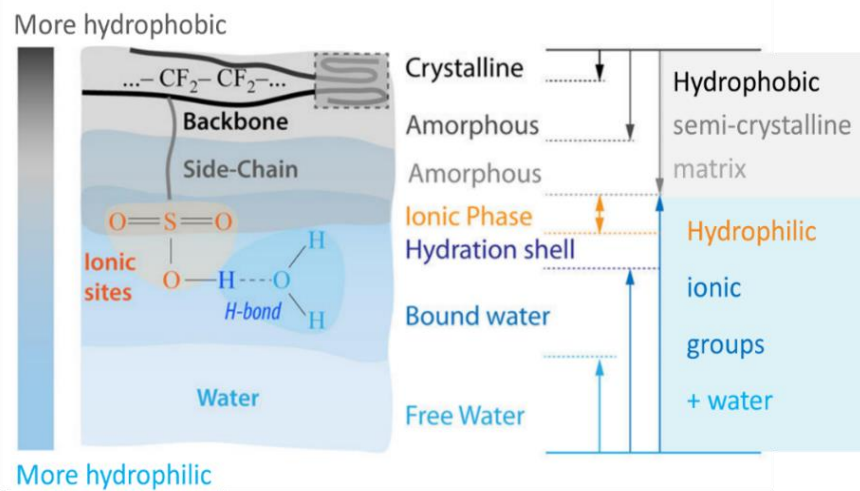


Figure 1.4 Schematic illustration of hydrated PFSA structure with separation of the hydrophobic backbone and hydrophilic pendant ionic domain as well as bound hydration water. Modified from ref [39].

The water uptake of a membrane is the weight percent of absorbed water by the dry polymer, which is often normalized and expressed as hydration number,  $\lambda$ , defined as the number of water molecules per sulfonic acid group.

$$\lambda = \frac{\text{Molar number of } H_2O}{\text{Molar number of } -SO_3H} = \frac{\text{Weight of } H_2O (g) / 18 \text{ g/mol}}{\text{Weight of dry ionomer (g)} / EW \text{ g/mol}} \quad (1.4)$$

For Nafion 117 membranes, for example,  $\lambda = 21-22$  after equilibrium in liquid water at room temperature, *i.e.*, around each sulfonic acid group there are about 21 water molecules absorbed. This corresponds to a water uptake of 34-36 wt% on basis of the dry polymer weight. This water uptake level approximately results in 15-20% increase in the dry thickness, *e.g.*, the typical wet thickness of Nafion 117 membranes is about 200-210  $\mu\text{m}$ .

### 1.5.2 Proton conductivity and electro-osmotic drag of water

Typical PFSA membranes in the  $H^+$  form *e.g.*, Nafion exhibit an ionic conductivity of about  $0.05\text{--}0.06\text{ S cm}^{-1}$  at room temperature, which is increased to above  $0.1\text{ S cm}^{-1}$  at about  $80\text{ }^\circ\text{C}$  and  $100\%\text{RH}$ . When the temperature approaches the boiling point of water, the proton conductivity declines as water evaporates.

Conduction of protons through PEMs is a thermally activated process and the temperature dependence of the conductivity follows the Arrhenius equation as shown below:

$$\sigma = A \text{ Exp}\left(-\frac{E_a}{RT}\right) \quad (1.5)$$

$$\text{or } \sigma = \frac{\sigma_0}{T} \text{ Exp}\left(-\frac{E_a}{RT}\right) \quad (1.6)$$

where  $E_a$  is the activation energy for the proton conduction,  $R$  the gas constant,  $T$  is the absolute temperature, and  $\sigma_0$  or  $A$  is the pre-exponential coefficient. The activation energy of conductivity can be obtained by plotting the logarithm of the conductivity ( $\text{S cm}^{-1}$ ) against the inverse absolute temperature [ $1/T, \text{K}^{-1}$ ] in an Arrhenius plot. In literature the reported activation energy is in a range of  $10\text{--}20\text{ kJ mol}^{-1}$ , depending very much on the humidity. Based on data at temperatures from  $25$  to  $90\text{ }^\circ\text{C}$  and varied hydrations, Springer et al. suggested the following expression of conductivity for Nafion 117 membranes [40]:

$$\sigma \text{ (S/cm)} = (0.5139 \times \lambda - 0.326) \exp\left[1268\left(\frac{1}{303} - \frac{1}{T}\right)\right] \quad (1.7)$$

It is seen that the conductivity is a linear function of hydration number  $\lambda$ . For the membrane to exhibit a minimum conductivity,  $\lambda$  should be higher than  $0.6$ , *i.e.*,  $0.6$  water molecules per sulfonic acid site.

It is the water molecules that solvate the protons from the sulfonic acid groups, forming hydrated complexes such as hydronium cations ( $H_3O^+$ ), Zundel cations ( $H_5O_2^+$ ) or Eigen cations ( $H_9O_4^+$ ). These proton containing charge carriers are mobile and involved in the charge transport, *i.e.*, *via* the vehicle mechanism. This means that water migrates through the membrane during fuel cell operation. The water movement due to the proton transport is called the electroosmotic drag and therefore dependent on the current passing through the membrane. An electroosmotic drag coefficient of water is defined as the molar ratio of water moved with each proton in the absence of a concentration gradient. For liquid water equilibrated Nafion membranes at room temperature, a coefficient of  $2.5\text{--}3.0\text{ H}_2\text{O}/H^+$  has been reported. For water vapor equilibrated membranes with low water content, however, the coefficient is between  $1.0$  and  $1.4\text{ H}_2\text{O}/H^+$ , varying with the water vapor activity.

### 1.5.3 Short side-chain PFSA membranes

For a fuel cell with an electrolyte with a certain conductivity, the area specific resistance increases with increasing distance between the electrodes. The ohmic loss of a PEM fuel cell can thus be lowered by reducing the thickness of the membrane. Another advantage of using thinner membranes is the improved water transport via electroosmotic migration and diffusion, which is an issue when operating at higher current densities. The mechanical strength can be

improved by modifying the side chain structures of the membranes. This was the initial motivation for the development of the short side-chain (SSC) membranes. The short side-chain PFSA membranes were intensively developed by Dow Chemical in the early 1990s and later on by Solvay Solexis. The SSC PFSA membrane provided by Solvay is under a trade name of Aquivion®.

The short side-chain PFSA materials have a high concentration of sulfonic acid groups and therefore proton conductivity. At the same time, the materials have a high degree of crystallinity within the hydrophobic regions, as indicated by the high heat values of fusion, compared with Nafion (Figure 1.5a). In addition, the short side-chain PFSA membranes show better hydration characteristics than Nafion® type membranes. Figure 1.5b shows the water uptake in liquid water at 100 °C, which is considerably higher than that for the long side-chain (Nafion®) membrane at a given EW.

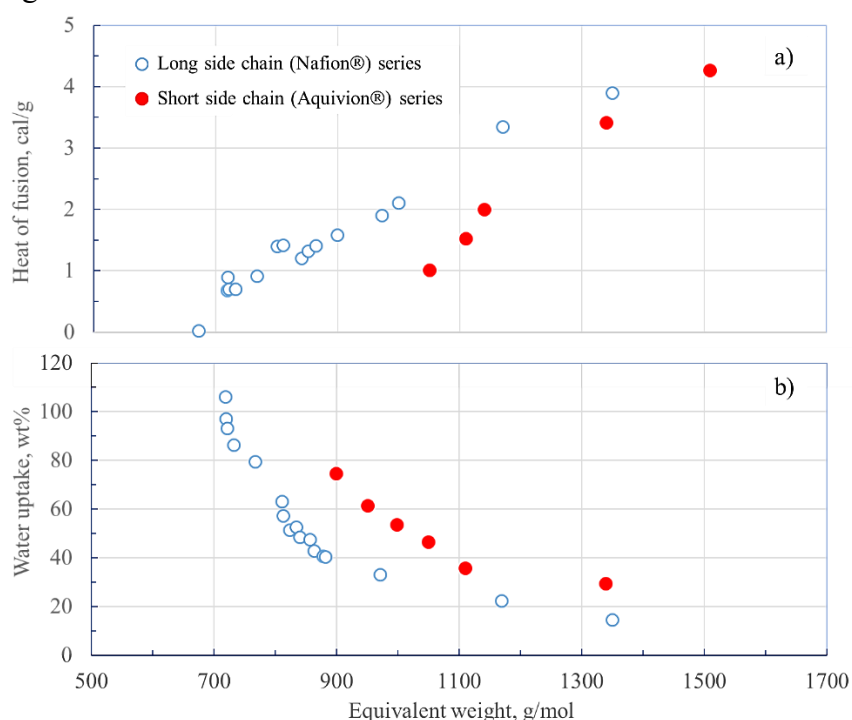


Figure 1.5 (a) Heat of fusion and (b) water uptake of Aquivion® and Nafion® membranes as a function of equivalent weight. The water uptake was measured from liquid water at 100 °C. Replotted from [41].

As a result, the SSC membranes have a higher softening temperature, *e.g.* *ca.* 100 °C for Nafion® and *ca.* 140 °C for Aquivion® membranes. In addition to the improved thermal stability, the SSC membranes exhibit better hydration characteristics and therefore higher proton conductivity due to the high concentration of highly hydrophilic sulfonic acid groups.

#### 1.5.4 PFSA composite membranes

A thin and robust membrane is desirable to reduce the area specific resistance. Due to the effective back diffusion of water from the cathode to the anode side through such thin membranes, water management and therefore the average conductivity can also be improved.

A challenge for thin membranes is the reduced mechanical strength, especially under swelling. This has been addressed by development of composite membranes. Briefly speaking there are two types of composite PFSA membranes, reinforced by PTFE fibers or inorganic fillers.

#### 1.5.4.1 Reinforced composite membranes

In the early 1980s, reinforced PFSA membranes were first developed for chlor-alkali electrolysis cells where PTFE woven fabrics were embedded in composite membranes typically of 200 - 300  $\mu\text{m}$  thickness. In 1990s, W.L. Gore & Associates commercialized composite membranes (Gore-select®) using thin PTFE porous sheets impregnated with PFSA ionomer from both sides. Reinforced membranes by dispersion of the PTFE fibrils such as Flemion® have also been prepared by extrusion. Today very thin membranes of 5 - 20  $\mu\text{m}$  thick are commercially available. A set of data of Gore-select® membranes and Nafion 117 are compared in Table 1.4. The reinforced membranes are characterized by small thickness (5-20  $\mu\text{m}$ ) and excellent mechanical properties. The mechanical stability in terms of shrinkage upon dehydration, defined as dry dimension relative to the fully hydrated dimension, is also much better for the reinforced thin membranes (-2.9% for 20  $\mu\text{m}$ ) than for Nafion 117 (ca. 10-11%). The composite membranes often exhibit lower conductivity than Nafion®. By taking the thickness into account, the reinforced membranes have a significantly higher conductance, which is defined as the reciprocal of the area specific resistance (ASR) or the ratio of the membrane thickness to its conductivity in  $\text{S cm}^{-2}$ .

Table 1.4 Characteristic data of Gore-select® membranes compared with Nafion® 117[42].

Properties	Gore-select®	Gore-select®	Nafion®-117
Thickness ( $\mu\text{m}$ )	5	20	200
Equivalent weight ( $\text{g mol}^{-1}$ )	1100	1100	1100
Water uptake (wt%)	33	32	32-34
Conductivity in 1M $\text{H}_2\text{SO}_4$ at 25°C ( $\text{S cm}^{-1}$ )	0.03	0.05	0.10-0.14
Conductance ( $\text{S cm}^{-2}$ )	56	26	5-7
Tensile strength (fully hydrated, MPa)			
- Machine direction (MD)*	-	32.4	15.9
- Transverse direction (TD)*	-	17.7	10.8
Water vapor transmission rates in 24 h ( $\text{kg m}^{-2}$ )	-	25.0	23.6
Shrinkage upon dehydration (%)			
- Machine direction (MD)*	-	-2.9	-10.5
- Transverse direction (TD)*	-	-2.9	-11.8

\* PFSA membranes are fabricated by extrusion cast and the mechanical behaviors of the membrane are anisotropic along with the machine and transverse directions.

## 1.5.4.2 Inorganic filler based composite membranes

Another important type of composite membrane is based on inorganic fillers. There are various techniques to fabricate metal oxides based composite membranes such as casting and *in situ* sol-gel reaction. The casting method is the most simple one by which nano-sized inorganic particles are blended uniformly with PFSA ionomers to form nanocomposite membranes. The commonly used inorganic fillers are hygroscopic oxides (e.g., silica (SiO<sub>2</sub>), titanium oxide (TiO<sub>2</sub>), and zirconia (ZrO<sub>2</sub>)), and proton conductors (e.g., zirconium hydrogen phosphates, phosphotungstic acid, and silicotungstic acid). The hygroscopic oxides are assumed to improve the water retention characteristics. As a result, improved conductivity at lower water contents has been reported when the inorganic fillers have functionalities adding to the total ion exchange capacity of the membrane. The elastic modulus of the membrane can also be enhanced especially at temperatures close to the softening temperatures of the ionomers. Most importantly for direct methanol fuel cells (DMFCs), incorporation of inorganic particles within the polymer matrix gives a reduced permeability of reactants, *i.e.*, methanol.

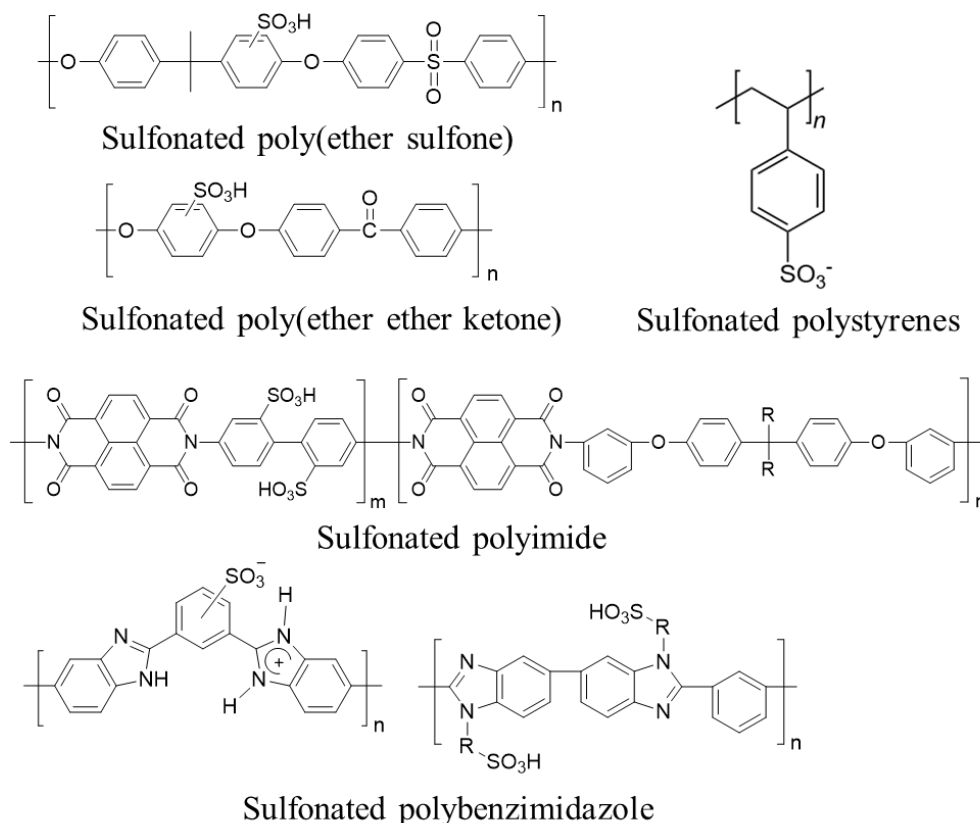


Figure 1.6 Structures of sulfonated poly(ether sulfone), polystyrene, poly(ether ether ketone), polyimide and polybenzimidazole.

## 1.5.5 Alternative membranes based on hydrocarbon polymers

High price and significant performance loss at elevated temperature and low relative humidity impedes the development of PEMFC systems using PFSA electrolytes. A large number of

alternative membranes, mostly hydrocarbons based, have been developed and studied. Sulfonated polystyrenes are one of the polymers investigated in the early years of PEMFCs. To improve their stability, partially fluorinated polystyrenes have been investigated by sulfonation of membranes based on  $\alpha$ ,  $\beta$ ,  $\beta$ -trifluoro-styrene monomers. Many aromatic structures are also known to exhibit excellent chemical stability. Much research effort has been devoted to the development of sulfonic acid functionalized systems, especially homopolymers and different copolymers based on poly(arylene ether)s, *e.g.*, poly(ether sulfone) (PSU) and poly(ether ether ketone) (PEEK). Sulfonated polyimides, especially the six-membered ring derivatives have been thoroughly studied as polymer electrolyte membranes with high proton conductivities and promising durability. Polybenzimidazoles are aromatic engineering plastics that can be sulfonated to give materials with sufficient proton conductivity. Figure 1.6 shows some typical alternative sulfonated PEMs for fuel cells.

## 1.6 High temperature PEMs

### 1.6.1 Why high temperatures

PFSA membranes have high conductivity, excellent chemical stability, mechanical strength and flexibility. PEMFCs based on perfluorosulfonic acid type membrane are well developed technologies. The shortcomings of current LT-PEMFC technology are obvious as well.

Typically, the LT-PEMFC operates at temperatures below 100 °C. Nafion is sensitive to changes in the hydration level, water is required as the charge carrier for the proton conductivity inside the Nafion membrane. Therefore, the membrane must always be kept in a hydrated condition to maintain optimal performance. At such low temperatures, the ORR has slow reaction kinetics and the overpotential at the cathode is hence leading to a large cell voltage loss. The platinum used as the catalyst to improve the electrochemical reaction has a significant affinity for carbon monoxide (CO). Traces of CO at 10 ppm level deteriorate the anode performance since CO strongly adsorbs onto the platinum surface and prevents the hydrogen molecules from access to the active sites [43]. Many efforts have been made to mitigate the CO effect, including the feeding of oxidants (O<sub>2</sub>) into the fuel and using more CO-tolerant catalysts (*e.g.*, PtRu/C). Even with these measures, when reformat hydrogen fuel is used, bulky and complex reformer units are still needed in order to remove CO down to 100 ppm level. Cooling is another issue for LT-PEMFC when the difference between the fuel cell stack and ambient temperatures is very small. In addition, the waste heat from the fuel cell stack is of little value because of its low temperature.

Most of these shortcomings of the current LT-PEMFC technology are associated with the PFSA membranes, which operate only under a highly hydrated state and therefore are limited to below 100 °C under ambient pressure. Elevating the operating temperature of PEMFCs to a range of 120–180 °C is a potential solution to these issues. The lower temperature of 120 °C is recommended to avoid the formation of liquid water while the upper boundary level of 180 °C is to avoid unnecessary material degradation. The resistance of the charge transfer at electrodes will be reduced as the temperature increases, which will result in better performance of fuel cells[44]. Moreover, at higher temperatures above 140 °C, the CO tolerance is significantly

increased [45-47] as shown in Figure 1.7, where the CO adsorption on Pt is associated with a high negative entropy [48]. At such temperatures, the CO tolerance is raised from 100 ppm to over 30,000 ppm, depending on the temperature and the catalyst loading [46], which enables direct use of reformed hydrogen from e.g. a methanol reformer without further CO cleanup. This discussion is summarized in Table 1.5.

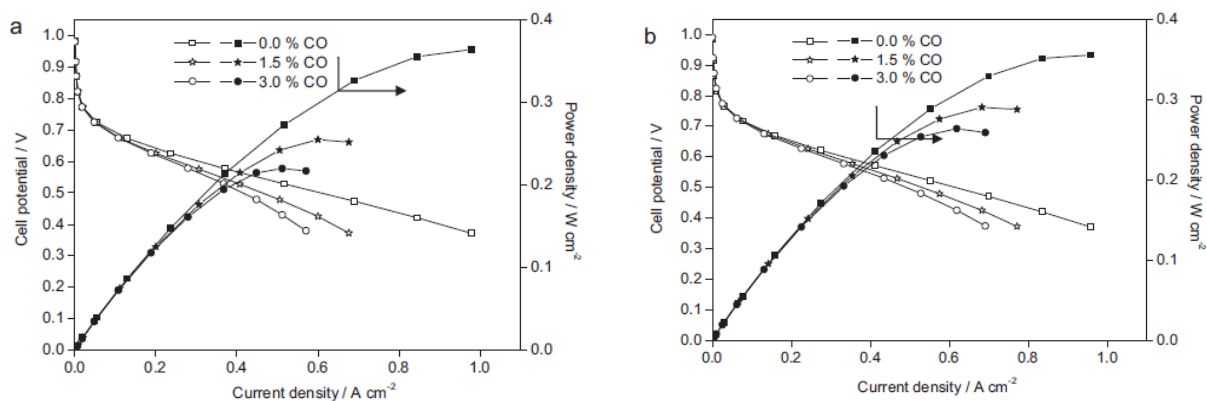


Figure 1.7 Polarization and power density curves at (a) 160 °C and (b) 180 °C for three different anode fuels: 0.0% of CO, 1.5% of CO and 3.0% of CO [46].

Table 1.5 Challenges for LT-PEMFCs that can be addressed by development of HT-PEM.

Challenges for LT-PEMFCs	Expected advantages of HT-PEMFC
(1) Slow kinetics for the ORR	(1) Faster kinetics of both electrodes
(2) Critical water management at temperatures close to the boiling point	(2) Above the boiling point of water, only a single phase of water is handled i.e. the water vapor.
(3) Poor catalyst tolerance to e.g. CO, which results in bulky methanol reformer due to CO cleanup	(3) Much enhanced CO tolerance and therefore simplified reforming unit
(4) Intensive cooling especially when it operates at high loads	(4) More efficient cooling due to the large difference between stack and ambient temperatures
(5) Little value of the heat recovery	(5) The heat can be recovered and therefore higher system efficiency

### 1.6.2 Types of HT-PEMs

As mentioned above, PFSA membranes have been modified by introducing inorganic fillers to achieve higher operating temperature. The most effective approach is by acid-base

complexation of a basic polymer with a doping acid. Polymers bearing basic sites such as ether, alcohol, imine, amide, or imide groups react with strong acids. The basicity of polymers enables the establishment of hydrogen bonds with the acid. In other words, the basic polymers act as a solvent in which the acid undergoes in some extent dissociation. When an amphoteric acid, e.g. phosphoric acid is used for doping a basic polymer, the resulting acid-base blends constitute a class of proton conducting membranes with high conductivity even in the anhydrous state. A breakthrough was achieved when polybenzimidazole (PBI) was first doped with phosphoric acid in 1995 [49]. In the past 25 years, much research has been carried out on exploring the fuel cell application of acid-doped PBI membranes [35, 49-51]. Fuel cells and related technologies have since then been developed, as well reviewed [52-54]. The state-of-the-art PBI membranes will be described in Chapter 2. This thesis is devoted to further development of advanced membranes based on PBI.

## CHAPTER 2

# High temperature proton exchange membranes

---

### 2.1 Approaches to higher operating temperatures

PEMFCs operating at high temperatures have been recognized as a promising pathway to meet the challenges faced by PFSA-based technologies. The term high temperature refers to a temperature range from 120 to 200 °C, relative to the well-developed PEMFC technology typically operating at 80 °C. Operating at temperatures above 100 °C is indeed a challenge for proton conducting polymers. First, the temperature stresses polymer membranes in terms of thermal, chemical, and mechanical stabilities. Secondly, the proton conductivity usually involves water molecules as the proton carriers, which are also a product of fuel cells. Above 100 °C water evaporates under ambient pressure. To keep water inside a membrane as a liquid needs to pressurize the power unit which increases the system complexity. To mitigate the water management at elevated temperatures the proton conducting membrane need to have an alternative mechanism that is less dependent on the presence of water. Great efforts have been made in the last more than 20 years to develop proton conducting membranes and relative materials for operation at temperatures above 100 °C [53]. Membranes under active development can be classified into the following groups and have been well-reviewed in recent years: (1) modified perfluorosulphonic acid (PFSA) membranes [55]; (2) alternative membranes based on partially fluorinated or aromatic hydrocarbon polymers [36]; (3) inorganic (acidic salts [56] and pyrophosphates [57] and their polymer composites [58]; (4) acid-base polymer membranes [54].

The most successful approach to achieve HT-PEMFCs is the development of acid-base polymer membranes. Polybenzimidazoles have been the most investigated polymer in this connection, whereas the widely used doping acid is phosphoric acid. Acid-doped polybenzimidazole (PBI) membrane was first reported as electrolyte materials in 1995 [49], and since then membranes of this type have been developed and characterized [35, 43, 44, 50, 51, 59-67]. The proton conduction mechanism of the acid doped PBI membranes is, in contrast to the conventional PFSA membranes, not dependent on the presence of water molecules within the membrane matrix. The acid doped PBI can therefore operate in the temperature range of 120-200 °C under anhydrous conditions. The HT-PEMFCs and related technologies have been developed with operating features including elimination of the need for humidification, effective cooling, high CO tolerance and therefore simpler integration with e.g, methanol reformer. As the focus of this thesis detailed discussion will be given in the following sections.

## 2.2 Synthesis of PBI

### 2.2.1 Structure and applications of polybenzimidazoles

The polybenzimidazoles are a family of thermally stable and oxidation resistant engineering plastics. The first polybenzimidazoles were described and patented by DuPont de Nemours in 1959 [68]. In a paper published in 1961, Vogel and Marvel [69] reported synthetic routes to a wide range of different polybenzimidazoles accompanied by systematic and extensive physiochemical characterization of the novel materials. Figure 2.1 shows the structure of the most studied PBI, poly 2,2'-(phenylene)-5,5'-bibenzimidazole (m-PBI), a commercial product under the trademark Celazole®.

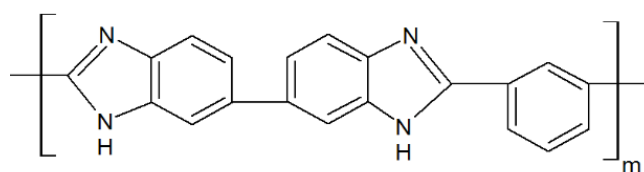


Figure 2.1 Structure of poly 2,2'-(*m*-phenylene)-5,5'-bibenzimidazole (*m*-PBI)

As an amorphous thermoplastic polymer, the aromatic nuclei of PBI provide the polymer high thermal stability (glass transition temperature,  $T_g = 425\text{--}436\text{ }^\circ\text{C}$ ), excellent chemical resistance, retention of stiffness and toughness, however, with poor processability, as reviewed previously [50]. Primarily used in textile fibers, the selection of *m*-PBI as the commercial product was made based on its good fiber properties, availability of monomers and identification of suitable solvents for fiber extrusion. As a specialty polymer PBI has also been used as compression moulding resin, electrically conductive materials, casting films and coatings for liquid, gas and other separation purposes.

### 2.2.2 Polymer synthesis

Polybenzimidazoles can be prepared by polymerization of the corresponding diamines and carboxylic acids in solid-state melts or in polyphosphoric acid (PPA).

#### 2.2.2.1 Heterogeneous molten/solid state synthesis

Vogel and Marvel [69] synthesized a variety of polybenzimidazoles by melt polycondensation of suitable aromatic tetraamines and aromatic dicarboxylic acids. Based on it, a two-stage process was developed to produce PBI with tetraaminobiphenyl (TAB) and diphenyl isophthalate (DPIP) as monomers [70], as shown in Figure 2.2. The first step is carried out at about  $270\text{ }^\circ\text{C}$  to produce the low molecular weight prepolymer in form of voluminous foams. The prepolymer is then pulverized and further heat-treated at temperatures of up to  $360\text{ }^\circ\text{C}$  to increase the molecular weight of the polymer by further polymerization. In general, this is an inconvenient process as the prepolymer has to be discharged and pulverized before the second step. By replacing DPIP with isophthalic acid (IPA) in the presence of organophosphorus and

silicon compounds as catalysts, Choe [71, 72] developed a single-stage method to synthesize high molecular PBI (Figure 2.3).

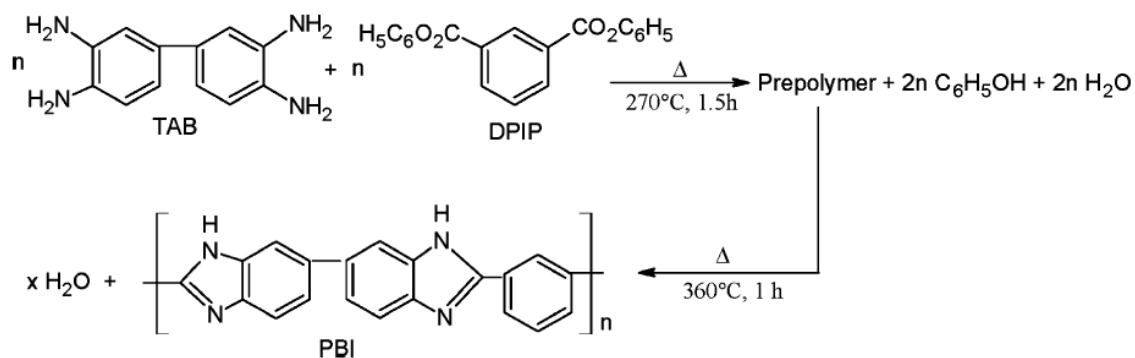


Figure 2.2 Schematic of the two-stage process for PBI synthesis [73].

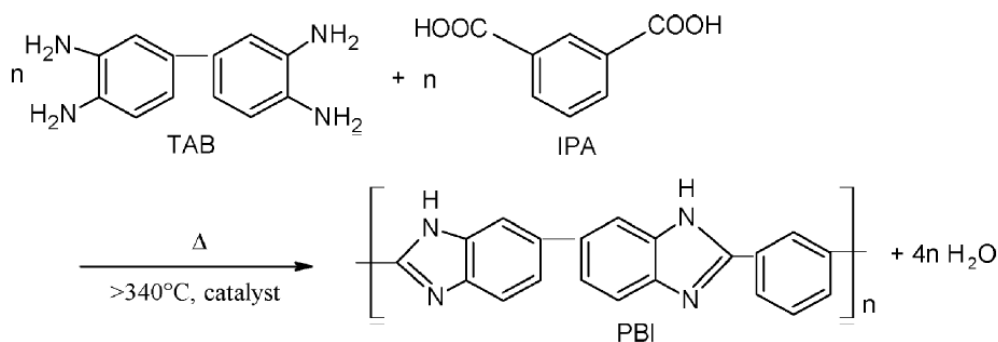


Figure 2.3 Schematic of the single-stage process for PBI synthesis [73].

### 2.2.2.2 Homogeneous solution synthesis

PBI can also be synthesized in homogeneous solutions with solvents such as polyphosphoric acid (PPA) [74, 75] (Figure 2.4). The homogeneous solution polymerization in PPA at 170–200 °C gives better control of the reaction, which also results in a more well defined polymer in terms of reduced polydispersity index as well as minimized side reactions such as branching and/or crosslinking.

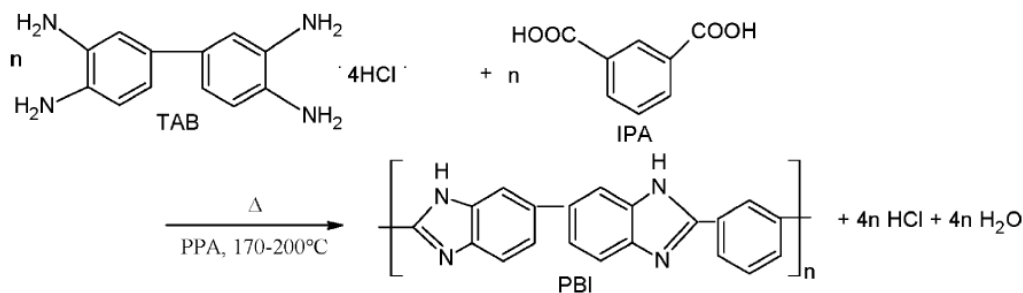


Figure 2.4 Schematic of the PPA process for PBI synthesis [74].

The synthesized polymer is usually characterized in terms of molecular weight by measurement of the inherent viscosity ( $\eta_{IV}$ , in dL/g) of a polymer solution, *e.g.*, 0.5 g polymer in 100 ml 96 wt% H<sub>2</sub>SO<sub>4</sub> at room temperature. The viscosity of polymer solutions can be measured with an Ubbelohde viscometer and is related to the weight averaged molecular weight ( $M_w$ , in g/mol) of the polymer by the Mark-Houwink-Sakurada equation:

$$\eta_{IV} = 1.94 \times 10^{-4} \times M_w^{0.79} \quad (2.1)$$

The commercially available polymer (Celazole<sup>®</sup>) has a relatively low molecular weight to avoid the polymer insolubility, with  $M_w = 23,000$  to  $37,000$  g/mol or an inherent viscosity of  $\eta_{IV} = 0.55 - 0.8$  dL/g. Using the polyphosphoric acid method of synthesis at a solid concentration of 3-5% and temperature of 195-220 °C the synthesized polymers may exhibit an inherent viscosity up to 1.5 dL/g as measured in sulfuric acid, which corresponds to a weight average molecular weight of over 100,000 g/mol.

## 2.3 Phosphoric acid and doped membrane fabrication

### 2.3.1 Phosphoric acid and doping chemistry

Orthophosphoric acid (H<sub>3</sub>PO<sub>4</sub>, PA) is a medium-strong acid, which dissociates in water according to the reaction:

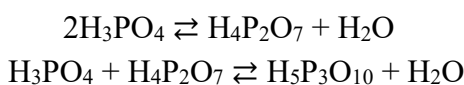


At concentrations higher than 85%, where the molar ratio of H<sub>3</sub>PO<sub>4</sub>/H<sub>2</sub>O > 1, self-dissociation of the acid occurs:

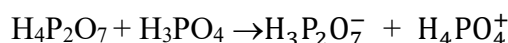


The H<sub>4</sub>PO<sub>4</sub><sup>+</sup> has a  $pK_a = -3$ , a value of that for the strong sulfuric acid.

The behavior of acid hydration and dehydration is of particular importance as water is generated in the fuel cell and the acid-water composition changes the conductivity. In an open atmosphere, phosphoric acid dehydrates at elevated temperatures, forming a series of polyphosphoric acids such as pyro- or diphosphoric (H<sub>4</sub>P<sub>2</sub>O<sub>7</sub>), triphosphoric (H<sub>5</sub>P<sub>3</sub>O<sub>10</sub>) or high polymeric acids:



All the higher acids from condensation are also chemically strong acid and are able to protonate the orthophosphoric acid:



Phosphoric acid is a unique proton conductor where a severe imbalance exists between proton donors and acceptors in the acid molecule, *i.e.*, each acid molecule contains 3 -OH groups as proton donors and only one =O as the acceptor. This so-called hydrogen bond frustration favors the proton conduction via the proton hopping mechanism. In 100% H<sub>3</sub>PO<sub>4</sub> about 96-98% conductivity is achieved by this mechanism. In other words, only a few percent of the charge transport involves the movement of carrying acid molecules [76]. This behavior enables the HT-PEM to operate at above 100 °C with little dependence on the presence of water.

In a phosphoric acid-PBI mixture, for example, the benzimidazole is protonated by the acid:



Compared to water, benzimidazole is a stronger base i.e. proton acceptor, promoting the acid dissociation to a higher degree than in water. In an acid-doped PBI system, the acid distributed in the PBI matrix provides proton conduction and PBI polymers impart mechanical stability to the doped membrane. For the fabrication of acid-doped PBI membrane, two methods have been suggested: 1) polyphosphoric acid (PPA) process (sol-gel process) [60, 77, 78] and 2) post-doping of PBI membranes cast from dimethylacetamide (DMAc) solution [79-83].

### 2.3.2 Direct casting by the PPA process

In this method, PPA is used as a condensation reagent and solvent for the PBI synthesis. After polymerization, the PA-doped PBI membranes can be directly fabricated from the PBI solution in PPA at around 200 °C without isolation of the polymers. Since both PPA and PBI polymers are hygroscopic, the moisture is absorbed from the atmosphere and hydrolyzes the PPA to form PA in situ. The solution temperature also drops from approximately 200 °C to room temperature. The hydrolysis of the solvent from PPA (a good solvent for PBI) to PA (a poor solvent for PBI) combined with the temperature drop induces a transition from the solution state to the gel state of the polymer that produces PBI membranes containing PA. The overall process is represented schematically in Figure 2.5. In this way, acid-doping levels as high as 20-40 mol PA per repeat unit of PBI can be achieved with consequently high conductivity (over 0.2 S cm<sup>-1</sup>) yet acceptable tensile strength (of up to 3.5MPa) [77].

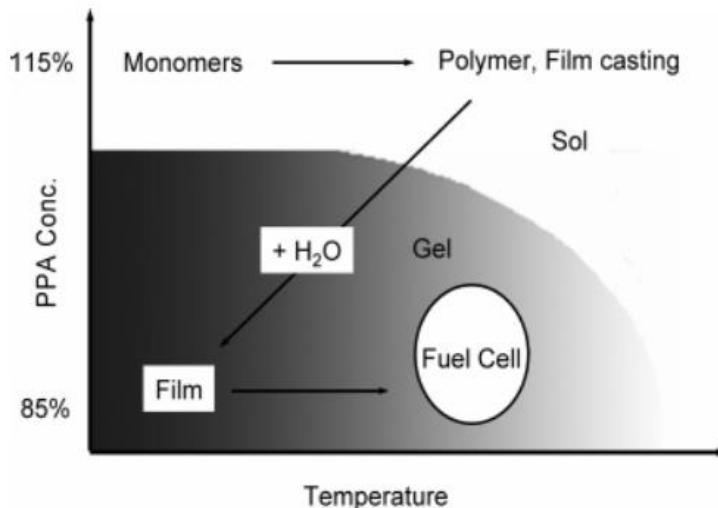


Figure 2.5 State diagram of the PPA process.[77]

### 2.3.3 Post doping of DMAc membranes

In this method, dry PBI membranes are first prepared by casting from a PBI solution in organic solvents and then immersed into an acid solution for acid doping.

A limited number of highly polar aprotic organic solvents are capable of solubilizing the polymer by breaking the relatively strong intermolecular hydrogen bonds present in the dry PBI. These include N,N-dimethylacetamide (DMAc), N,N-dimethylformamide (DMF), N-

methyl-2-pyrrolidone (NMP) and dimethylsulfoxide (DMSO). DMAc is the most widely used organic solvent and is originally chosen in the 1960s as the preferred solvent due to the proper viscosity of the solution for dry-spinning of PBI fibers, as reviewed by Chung [84]. A few weight percents of lithium chloride are often added to the PBI/DMAc solutions in order to facilitate the dissolution and to prevent the polymer from phasing out during storage [85, 86]. PBI membranes can be cast from solutions of different concentrations. After casting onto a glass plate, the majority of the solvent is evaporated in a ventilated oven at temperatures ranging from 60 to 120 °C. The membranes are then washed with hot water in order to remove LiCl and residual solvent, followed by drying at a temperature of up to 190-200 °C.

The cast membranes are then doped with acids to become proton conductive. Various inorganic acids have been investigated such as  $\text{H}_2\text{SO}_4$  [79-83],  $\text{H}_3\text{PO}_4$  [50, 79-81, 87],  $\text{HClO}_4$  [79],  $\text{HNO}_3$  [79],  $\text{HBr}$  [80, 82],  $\text{HCl}$  [79].  $\text{H}_3\text{PO}_4$  is the most widely used dopant for PBI membranes. The acid doping level as a function of the concentration of the phosphoric acid at room temperature is shown in Figure 2.6 [52]. In 85% wt%  $\text{H}_3\text{PO}_4$ , corresponding to molarity of 14.6 mol/L, the acid doping level can reach about 10-11  $\text{H}_3\text{PO}_4$  per polymer repeating unit (PRU).

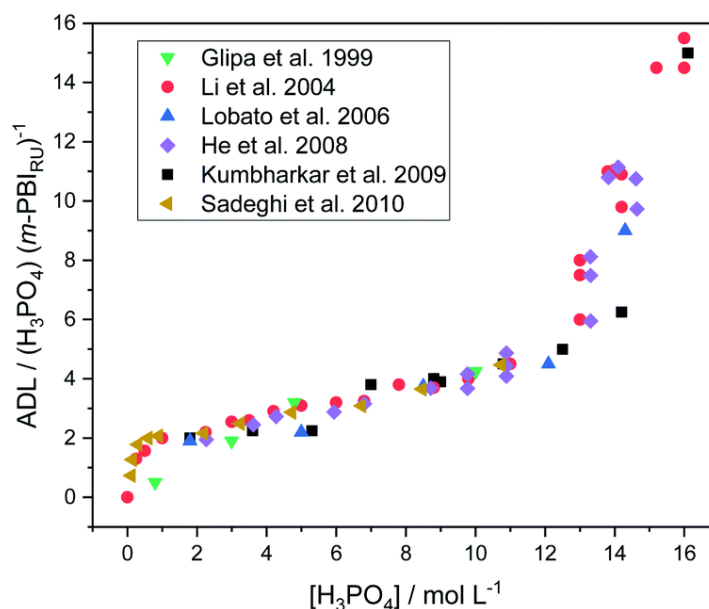


Figure 2.6  $\text{H}_3\text{PO}_4$  sorption isotherm at room temperature for *m*-PBI as a function of  $\text{H}_3\text{PO}_4$  concentration at equilibrium. The acid sorption is normalized as the acid doping level in molar number of  $\text{H}_3\text{PO}_4$  per polymer repeat unit. The figure was adapted from [52] to which the original literature sources for the data points are referred.

Table 2.1 Properties of PBI membranes synthesized by PPA process.

Polymers	Acid doping level (ADL) ( PA per mol PBI repeat unit)	Conductivity (S/cm)	Tensile strength at break (MPa)	Elastic modulus (MPa)	Fuel cell performance	Ref.
m-PBI	32	0.01 (RT), 0.26 (200 °C)	3.5		0.9 W/cm <sup>2</sup> (2.5 A/cm <sup>2</sup> , 160°C)	[77]
m-PBI	49-55			6.6		[88]
<i>p</i> -PBI	27.7	0.25 (160°C)				[89]
2OH-PBI	25.4	0.35 (160°C)				[89]
<i>p</i> -PBI	30-40	0.24 (160°C)				[90]
F <sub>6</sub> -PBI	30-40	0.09 (180°C)	0.8		0.58 V (0.2 A/cm <sup>2</sup> , 160°C)	[91]
2OH-PBI/ <i>p</i> -PBI	19.3-25.4	0.27-0.35(160°C)			0.69 V (0.2 A/cm <sup>2</sup> , 180°C) 0.49 A/cm <sup>2</sup> (0.6 V, 180°C)	[92]
m-PBI/ <i>p</i> -PBI	9.4-30	0.17-0.3 (160°C)				[93]
2OH-PBI, <i>p</i> -PBI, m-PBI, 2,5-py PBI, 3,5-py PBI	7.6-35.6					[94]
s-PBI/ <i>p</i> -PBI	20–40	0.148–0.291 (180°C)	0.528–2.51		0.75V (0.2 A/cm <sup>2</sup> , 180°C)	[95]

Note: The chemical structure of common derivatives of PBI membrane are shown in Table 2.3.

*m*-PBI = poly[2,2'-(*m*-phenylene)-5,5'-(bibenzimidazole)],

*p*-PBI = poly[2,2'-(1,4-phenylene)-5,5'-bibenzimidazole],

2OH-PBI = poly(2,20-(2,5-dihydroxy-1,4-phenylene) 5,50-bibenzimidazole),

F<sub>6</sub>-PBI = fluorinated polybenzimidazole,

2,5-py PBI = 2,5-pyridinedicarboxylic acid polybenzimidazole,

3,5-py PBI = 3,5-pyridinedicarboxylic acid polybenzimidazole, *s*-PBI = sulphonated polybenzimidazole.

## 2.4 Properties of acid doped PBI membranes

### 2.4.1 Proton conductivity

Pristine PBI is reported to possess some proton conductivity. The reported values vary within a range  $2\text{--}8 \times 10^{-4} \text{ S cm}^{-1}$  at relative humidities between 0 and 100% [96]. Some authors observe proton conductivities of two to three orders of magnitude lower [97, 98]. These lower values are generally accepted in literature for non-modified PBI which are too low for any practical use in electrochemical devices. To be applied as an electrolyte, the proton conductivity needs to be enhanced.

When doped with PA, the PA/PBI membranes showed much higher proton conductivity, depending on the temperature, acid content, and relative humidity [49, 99-101]. The conductivity is however lower than that of phosphoric acid itself, either pure or in  $\text{H}_3\text{PO}_4/\text{H}_2\text{O}$  mixtures. The phosphoric acid content of PBI membranes is often expressed as the acid doping level (ADL). It is normally expressed as the mole number of phosphoric acid molecules per mole number of PBI repeating units according to Equation 2.2.

$$ADL = \frac{n_{\text{H}_3\text{PO}_4}}{n_{\text{PBI}_{RU}}} \quad (2.2)$$

In the PA/PBI, the first two molecules of phosphoric acid are associated with the benzimidazole rings, likely via weak ionic interaction. Further acid addition yields free acid which can be more mobile and likely networked through the hydrogen bonding. Though the polymer matrix is present, the proton conductivity mechanism of acid-doped polybenzimidazoles is the same as that of the concentrated phosphoric acid, i.e., by the Grotthius (hopping or structure diffusion) mechanism [99], as shown in Figure 2.7.

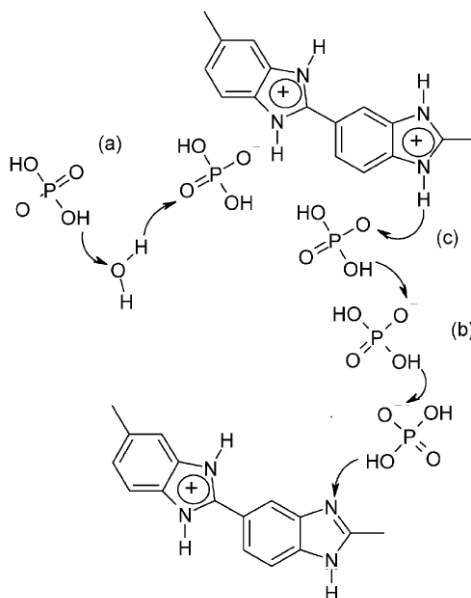


Figure 2.7 Conductivity mechanism of phosphoric acid doped polybenzimidazoles: (a) water-acid proton transfer (b) proton transfer through a phosphoric acid chain and (c) benzimidazole ring-phosphoric acid proton transfer [62].

The conductivity of acid-doped PBI membranes is affected by the acid content. For example, the conductivity of phosphoric acid doped PBI membrane increased from  $0.14 \text{ S cm}^{-1}$  [65] for 11-12  $\text{H}_3\text{PO}_4/\text{PRU}$  to  $0.24 \text{ S cm}^{-1}$  [77] for 32  $\text{H}_3\text{PO}_4/\text{PRU}$ . Figure 2.8 summarizes the conductivities of different types of PBI membranes doped at different acid levels [50, 78]. As a comparison a PFSA membrane (Aquivion<sup>®</sup>S98-09S) is included which shows high conductivity at low temperatures but the conductivity dramatically decreases as the temperature approaches and exceeds  $100 \text{ }^\circ\text{C}$ . The conductivity of the post doped membranes, having an acid doping level of 12, is obtained under a constant water-to-air ratio [102] while the PPA membranes with an acid-doping level of 32, corresponding to 91 wt% phosphoric acid and 9 wt% PBI, exhibit a conductivity as high as  $0.26 \text{ S cm}^{-1}$  at  $200 \text{ }^\circ\text{C}$  under dry conditions. This conductivity is still much lower than that of 100% PA. Apart from the dilution effect by the polymer, it is likely that the H-bond structures present in pure  $\text{H}_3\text{PO}_4$  are broken by the polymer, making proton jumping and perhaps also acid molecule movement more difficult. Similar effects were observed when small molecules such as imidazole and 1-methyl imidazole were introduced into concentrated phosphoric acid instead of water [103].

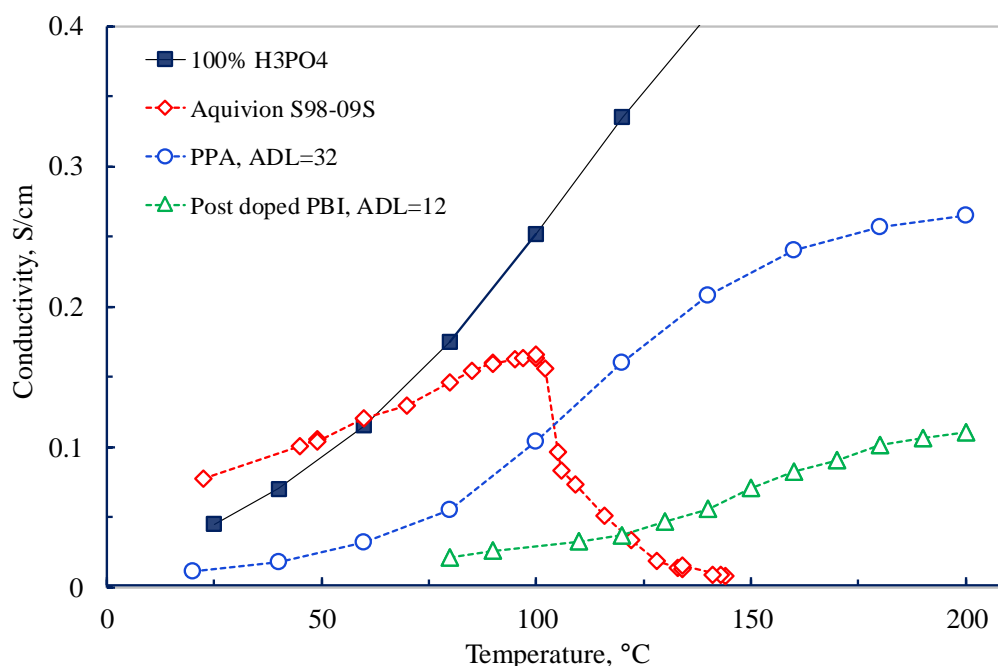


Figure 2.8 Proton conductivity of 100% phosphoric acid, Aquivion S98-09S, and acid doped PBI membranes. The PPA-cast membrane was with an acid doping level of 32 and dry atmosphere; The DMAc-cast membrane was with an acid doping level of 12 and under dry atmosphere; The Aquivion membrane was under 100% relative humidity below  $100 \text{ }^\circ\text{C}$  and under  $P_{\text{H}_2\text{O}}=1 \text{ atm}$  above  $100 \text{ }^\circ\text{C}$  (unpublished work by the DTU Energy group).

#### 2.4.2 Electro-osmotic water drag coefficient

The electro-osmotic drag coefficient is defined as the number of water molecules moved with each proton in the absence of a concentration gradient, a factor reflecting the dependence of the proton conduction on the water molecule carriers. For PFSA membranes, known to have

water mediated proton transport (vehicular) mechanisms, the electro-osmotic drag coefficient of water is reported to be 2.5–3.0  $\text{H}_2\text{O}/\text{H}^+$  for liquid water-equilibrated Nafion membranes at room temperature. When equilibrated with high relative humidity vapour, the drag coefficient was found to be slightly lower. For proton conduction entirely by the Grotthus mechanism, acid doped PBI membranes are reported to a nearly zero electro-osmotic drag coefficient, as proton transport occurs without a net water transport [104].

### 2.4.3 Thermal and oxidative stability

The use of PBI membranes in a fuel cell operating at 200 °C introduced additional concerns of stability when they are in contact with a highly active catalyst and in strongly reducing and oxidizing environments. Therefore, extensive studies have been devoted to investigating the thermal stability of PBI by means of thermogravimetric analysis (TGA) combined with mass spectrometry (MS), the latter technique is for detecting the purge gas released from the TGA [105, 106]. Pristine PBI samples typically have a 10–15% weight loss at temperatures up to 150 °C due to the loss of absorbed water. From 150–500 °C there is little further weight loss showing good stability. Above 500 °C, a significant weight loss occurs when formation of carbon dioxide is detected by the MS showing the polymer decomposition. For the acid-doped PBI samples, weight losses due to dehydration of phosphoric acid and pyrophosphoric acid are also observed. In the presence of platinum catalysts under atmosphere of either nitrogen, 5% hydrogen, or air, Samms et al. [105] observed only weight losses due to water at temperatures below 400 °C.

Chemical stability of membranes is of much concern to the lifetime of PEMFC. The main mechanism of membrane degradation is believed to be due to the radical attack on the hydrogen-containing bonds in the polymer backbone. The hydrogen peroxide, generated as the intermediate of the ORR or chemical product of the permeated hydrogen or oxygen through the membrane within the fuel cell, is decomposed to form highly reactive radicals ( $\cdot\text{OH}$  or/and  $\cdot\text{OOH}$ ) in the presence of transition metal ions, for example, the corrosion product of metallic components of fuel cells. Fenton test is the widely used method to evaluate the stability of PEMs [107]. By being exposed to a 3% hydrogen peroxide solution containing 4 ppm  $\text{Fe}^{2+}$  at 68 °C, for example, PBI membranes have been evaluated by weight loss and visual observation [108–110], as shown in Figure 2.9 [50]. Nafion has better chemical stability with a weight loss of only 1% after the first 20 h of the Fenton test while PBI membranes have a weight loss of about 15%. Gaudiana and Conley [111] reported that the initial stages of oxidative attack to benzimidazoles occur preferentially on the aromatic rings bearing the nitrogen function and subsequently the amine portion of the molecules. This indicates that the weak link is the nitrogen containing heterocyclic and adjacent benzenoid rings. In the Figure 2.9 also showed CrL-PBI with better stability, which will be discussed in Section 2.5.

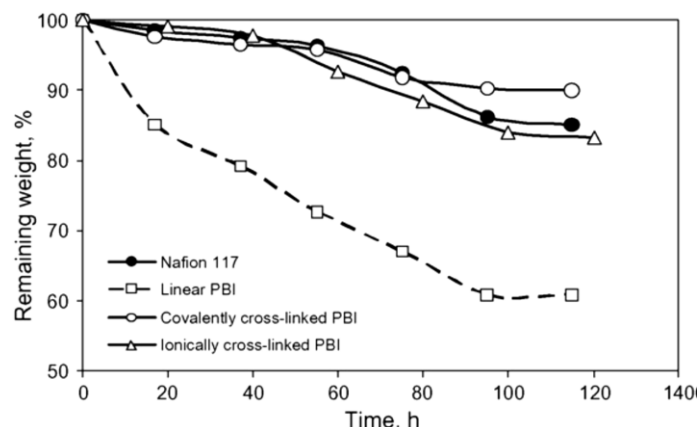


Figure 2.9 Membrane degradation in 3%  $H_2O_2$  containing 4ppm  $Fe^{2+}$  at 68 °C. Solid lines indicate that the samples remained as a whole membrane, whereas dashed lines indicate that samples were broken into small pieces [50]. Data for ionically cross-linked PBI were from [108] and the rest from [110].

#### 2.4.4 Mechanical strength

The strong hydrogen bonding between N and  $-NH-$  groups in PBI is the dominant molecular force, making PBI a mechanically strong membrane. The dry PBI membrane has a very small elongation at break, about 1-3%, and an intermediate tensile strength of about 60-70MPa [50]. In the presence of water or in the humidified atmosphere, this elongation increases to about 7-10% and the tensile strength to 100-160MPa [112].

When doped with the acid, little change of modulus or tensile strength is observed at a low acid doping level ( $<2$ ) [113]. At higher acid-doping levels ( $>2$ ) the free acid is present. The free acid increases the separation for PBI backbones and thus decreases intermolecular forces. The membrane strength is hence decreased particularly at higher temperatures, as shown in Figure 2.10.

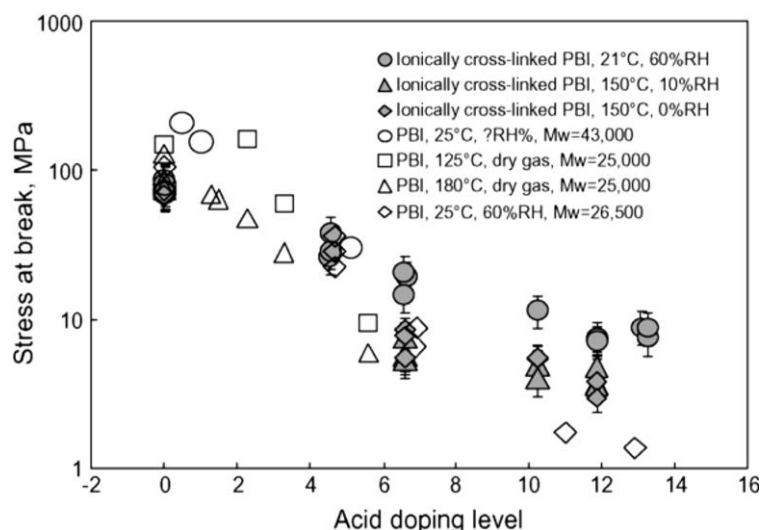


Figure 2.10 Tensile strength of DMac-cast PBI membranes as a function of acid doping level at different temperatures [50]. RH is relative humidity. The tensile strength is with respect to the initial dimensions of samples. Data for ionically cross-linked PBI were from [108]. Data for  $MW = 43,000$  PBI were from [113]. Data for  $MW = 25,000$  PBI were from [114].

The PPA-cast membranes, however, behave differently mechanically. They have been reported to show tensile strengths of 1 to 3.5MPa at acid-doping levels of as high as 20-40 mol phosphoric acid per repeat unit [77, 115].

#### 2.4.5 Gas permeability

As the polymer electrolyte membrane is acting as a separator in a fuel cell, the gas permeability of the polymer is of particular importance. Transport of gases through a dense polymeric membrane is usually described by a solution–diffusion mechanism. In the solution–diffusion model, the permeants dissolve in the membrane material and then diffuse through the membrane driven by a concentration difference.

The gas permeation is generally determined by the gas solubility and diffusivity in the polymer:

$$P = S \times D \quad (2.3)$$

Where  $P$  is the permeability coefficient,  $D$  is the diffusion coefficient, and  $S$  is the solubility coefficient.

The permeability coefficient  $P$ , which is also called “permeability efficient” or simply “permeability”, is generally defined by the expression

$$P = \frac{q \cdot l}{A \cdot \Delta p} \quad (\text{mol cm}^{-1} \text{ s}^{-1} \text{ Pa}^{-1}) \quad (2.4)$$

Where  $q$  ( $\text{mol s}^{-1}$ ) is the mass flux of gas,  $l$  (cm) is the membrane thickness,  $A$  ( $\text{cm}^2$ ) is the area of the membrane for gas diffusion and  $\Delta p$  (Pa) is the pressure difference through the membrane [116].

Several techniques have been explored to measure the gas permeability and gas crossover including the time-lag method, the volumetric method [117-122], the electrochemical oxidation or stripping method [123-125], the micro-disc electrode method [126] and the direct gas detection method using gas chromatography(GC) or mass spectrometry(MS). Of these methods, the electrochemical oxidation or stripping is an in situ method performance in assembled fuel cells and practically easy in operation and will also be used in this work.

At room temperature, the gas permeability of pristine PBI membranes is low, it is reported  $2 \times 10^{-13}$  and  $5 \times 10^{-15} \text{ mol cm}^{-1} \text{ s}^{-1} \text{ bar}^{-1}$  for hydrogen and oxygen, respectively [127]. The gas permeability increases with temperature increased. At temperatures close to the fuel cell operation temperature i.e. 150-180 °C, He et al. [114] reported a permeability of around  $4 \times 10^{-12} \text{ mol cm}^{-1} \text{ s}^{-1} \text{ bar}^{-1}$  for hydrogen. Pesiri et al. [128] reported a similar value ( $2.7 \times 10^{-12} \text{ mol cm}^{-1} \text{ s}^{-1} \text{ bar}^{-1}$ ) at 180 °C.

The above discussion on PBI membrane properties are summarized in Table 2.2.

Table 2.2 Properties of PBI membranes (DMAc-cast) before and after acid doping.

Properties	Pristine PBI	PBI-H <sub>3</sub> PO <sub>4</sub>	Nafion 117
Conductivity (S cm <sup>-1</sup> ) (at 25 °C)	~0	~0.06 (ADL 12, 150 °C) ~0.2 (ADL 22, 150 °C)	>0.1 (80 °C)
Electro-osmotic drag coefficient of water (mol H <sub>2</sub> O/H <sup>+</sup> )	-	~ 0	~3.2
Thermal stability (°C) (decomposition in air, 5 °C/min)	>500	>500	>280
Oxidative degradation (%)	15 (in pieces)	-	-
Weight loss after 18h in 3% H <sub>2</sub> O <sub>2</sub> +4 ppm Fe <sup>2+</sup> at 68 °C	<2 (cross-linked)	-	<1
Tensile strength at break (MPa, RT)	120-160	25	18
Elongation (% , RT)	3	40	120
H <sub>2</sub> permeability (×10 <sup>-12</sup> mol cm <sup>-1</sup> s <sup>-1</sup> bar <sup>-1</sup> )	2.7 [128]/4.3(180 °C)	380 (ADL 5, 180 °C)	20 (25 °C)
O <sub>2</sub> permeability (×10 <sup>-14</sup> mol cm <sup>-1</sup> s <sup>-1</sup> bar <sup>-1</sup> )	10 (180 °C)	90 (ADL 5, 180 °C)	10 (25 °C)

## 2.5 PBI variants and crosslinking

Phosphoric acid doped PBI membrane shows high proton conductivity and excellent thermal stability. However, there are some important issues waiting to further improve. One is the trade-off between proton conductivity and mechanical strength. The high conductivity is achieved with excess doping PA (typical acid doping level of 10-12 mol H<sub>3</sub>PO<sub>4</sub>/RPU which, on the other hand, deteriorates the mechanical strength of the membranes. Another issue is the oxidative stability of PBI membranes [129] – the linear PBI is less stable than PFSA membranes in the Fenton test. The weakest part of the PBI in an oxidative atmosphere is the benzenoid ring bearing the nitrogen function and the amine portion of the molecule. Attack of peroxide radicals on the polymer membranes in fuel cells is a principal degradation mechanism of membranes. Furthermore, the slow leach out of water-soluble phosphoric acid from the membrane may occur [89]. Many efforts are being made to further improve PBI membranes as reviewed [35, 43, 50, 54, 61] including (i) synthesis of PBI with varied structures [130-132] and (ii) crosslinking of membranes [133-135].

### 2.5.1 Synthesis of modified PBI

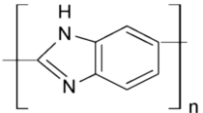
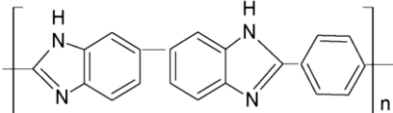
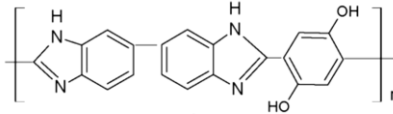
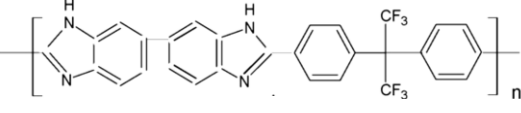
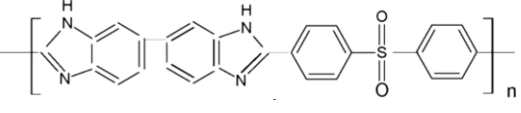
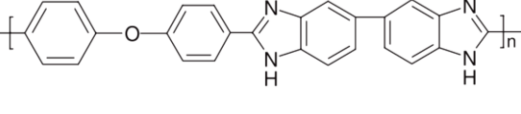
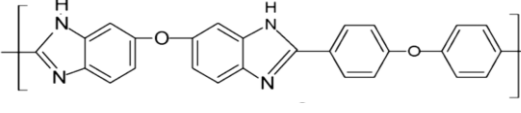
The most widely studied PBI polymer is poly[2,2'-(*m*-phenylene)-5,5'-(bibenzimidazole)] (*m*-PBI). Chemical modification of polybenzimidazole backbone is being made to improve the performance of the polybenzimidazole, including poly(2,2'-(1,4-phenylene)5,5' -bibenzimidazole) (*para*-PBI or *p*-PBI) [136, 137], poly(2,5-benzimidazole) (ABPBI)[130-132], sulphonated PBI (*s*-PBI) [138-140], and so on. Table 2.3 shows the common derivatives of PBI membranes.

The *p*-PBI was first synthesized in the early 1960s [69, 74]. Compared with *m*-PBI, *p*-PBI

bearing the para phenylene structure has better tensile strength and stiffness [136]. The challenge for uses of p-PBI membranes is its extremely poor solubility. It is, in fact, only soluble in strong acids e.g. methanesulfonic acid (MSA) and impossible to process using common organic solvents for membrane casting [137, 141].

The design of polymer structures with additional basic sites is a benefit for improving the acid doping and retention in order to improve the conductivity and long-term stability [142]. ABPBI has a simpler structure than m-PBI without the connecting phenyl rings and therefore a high concentration of the basic sites [143, 144]. It can be polymerized from a single monomer (3,4-diaminobenzoic acid, DABA) in PPA, and can be doped in phosphoric acid. [132].

Table 2.3 Examples of common derivatives of PBI membranes.

Derivatives Names	Structure	Ref.
ABPBI		[131, 132, 143, 144]
p-PBI		[69, 74, 136].
2OH-PBI		[89]
F <sub>6</sub> -PBI		[91, 150]
SO <sub>2</sub> -PBI		[141, 151]
O-PBI		[146, 152, 153]
PBI-OO		[154]

Flexible spacer groups introduced in the polymer backbones may assist to enhance the solubility of the polymers in organic solvents, though most often at expense of lowered thermo-oxidative stability. These variants of PBI structures can be synthesized using a variety of diacids with active groups such as pendant amino, carboxyl, sulfonic acid, hydroxyl, etc. It has been demonstrated the capability of improved acid retention and therefore high proton conductivity with sufficient mechanical strength [92, 145]. Typical examples include polymers containing ether linkages (OPBI) [146], fluoro containing groups [91, 147], pyridine containing

groups [148], sulfone linkages (SO<sub>2</sub>PBI) [147], hydroxyl (2OH-PBI) [62] and their copolymers [141, 149], as listed in Table 2.3.

## 2.5.2 Crosslinking

As previously mentioned, the conductivity of the PA doped membrane generally increases with increasing the acid content, while the tensile strength of the doped membrane decrease with the increasing acid content, thus reducing the long-term mechanical stability of the membrane. This reduction occurs due to increasing polymer chain spacing as PA is absorbed by the membrane. Crosslinking is widely considered to be an effective method for improving the mechanical properties of polymeric systems. It can improve mechanical, dimensional stability and phosphoric acid retention of PBI membranes [50, 109, 135, 155]. However, a highly cross-linked membrane may become brittle, which would affect long-term durability and manufacturing. In addition, crosslinking may also reduce the acid content of the membrane due to the compact structure of the crosslinked polymer. Therefore, the degree of the crosslinking must be balanced based on mechanical stability and conductivity.

### 2.5.2.1 Thermal curing

Thermal curing is a very simple method as it proceeds by heat treatment of PBI membranes without additional reagents. It was found that PBI becomes completely insoluble in all standard solvents after heat treatment at 500 °C [69]. Such thermally cured membranes were studied in fuel cells where the PBI was cured irreversibly by heat treatment at 200-350 °C under argon [134, 156-158]. The behind mechanism is still not clear. One hypothesis is that the reaction proceeds first by hydrolysis of a few imidazole rings by water molecules strongly bound to the diamine and a carboxylic acid and second by Friedel-Crafts reaction of aromatic rings and the carboxylic acids, leading to aromatic ketones [156]. The thermally cured PBI showed better mechanical properties for a given PA doping level, and improved durability in a fuel cell under load cycling between 0 and 600 mA cm<sup>-2</sup>. A potential drawback is that it is kinetically controlled, which may lead to varying crosslinking degrees between batches.

### 2.5.2.2 Ionic crosslinking

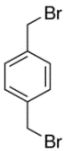
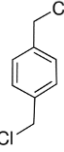
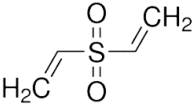
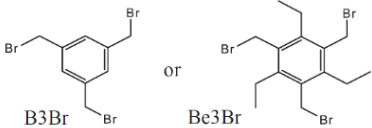
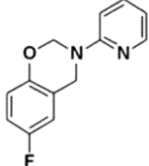
The ionic crosslinking can be accomplished via the Lewis acid-base reaction. The ionically crosslinked blend membrane prepared by mixing PBI (as the basic polymer) with acidic polymers in which the acidic blend component acts as a macromolecular ionic crosslinker for the blend membrane by proton transfer from the acidic group onto the basic imidazole sites of PBI [147, 155]. Kerres and co-workers focused on the development of ionic crosslinked PBI membrane in the past years [135, 155, 159-162]. The PBI is a typical basic polymer, for example, m-PBI, PBIOO and F<sub>6</sub>PBI are always used [135, 155, 159, 163] while the acidic polymers are usually based on sulfonated polymer [135]. It has been shown that the blend membrane exhibits better chemical stabilities than pure PBI membranes as determined by Fenton's test [159]. The proton conductivities of investigated membranes are in a range of up to 0.09 S cm<sup>-1</sup> at typical temperatures around 150 °C [159]. However, the ionically cross-linked

membranes suffer from poor thermal stability as the ionic crosslinking breaks at higher temperatures, resulting in excessive swelling and therefore mechanical instability [155].

### 2.5.2.3 Covalent crosslinking

The crosslinking can be covalent by reaction between the benzimidazole group of PBI and functional groups of crosslinker. Small molecular cross-linking agents are always favoured while polymeric crosslinkers have also been explored. Different cross-linkers include ethylene glycol diglycidyl ether (EGDE) [164], terephthalaldehyde (TPAH) [165], tetracarboxylic dianhydride (TCDA) [166], divinyl sulphone [167, 168],  $\alpha$ -dibromo-p-xylene (DBpX) [169], p-xylylene dichloride [170, 171], dichloromethyl phosphonic acid [109], (Poly)benzoxazine [64, 133, 172-174], among many others. Table 2.4 lists some examples of PBI crosslinkers.

Table 2.4 List of example crosslinkers.

Crosslinker	Chemical structure	Ref.
$\alpha,\alpha'$ -Dibromo-p-xylene (DBpX)		[169]
p-xylylene dichloride		[170, 171]
divinyl sulphone		[167, 168]
1,3,5-tris-(bromomethyl)benzene (B3Br), 1,3,5-tris(bromomethyl)-2,4,6- triethylbenzene (Be3Br)		[175]
(Poly)benzoxazine		[64, 133, 172-174, 176]

Covalently crosslinked membranes tend to be brittle or less flexible particularly under the drying out state. N-H sites are crucial to proton transportation for PA-doped PBI. However, these sites in crosslinked PBI are easily reacted by crosslinker, leading to a decreasing proton conductivity. A series of crosslinked PBI without sacrifice of effective N-H sites have been prepared by using (poly)benzoxazine covalent crosslinker [64, 133, 172-174, 176]. Figure 2.11 shows the possible reaction mechanism between benzimidazole and benzoxazine, the carbons

of the benzene ring can react with methylene group on the oxazine ring upon heating.

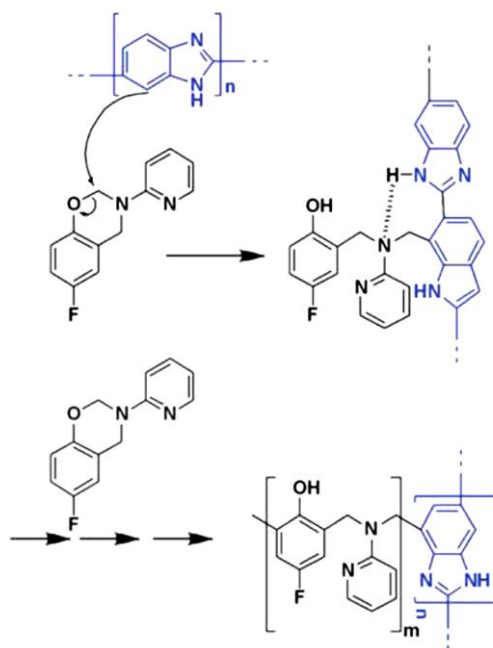


Figure 2.11 Possible reaction mechanism between benzimidazole and benzoxazine [172].

## 2.6 Inorganic-organic composites

Composite membranes are materials made from two or more constituents with significantly different physical or chemical properties. Each individual component remains separate and distinct within the finished structure. The difference between polymer blend and a composite is that the polymer blend is made up of mixing two or more polymers to get a single phase, whereas a composite is made up of a combination of two or more elements resulting in a multiphase, multicomponent system. Typical examples are organic-inorganic composites consisting of a polymer phase and inorganic particle fillers [63, 177, 178]. Other types of composite membranes are made of electrospun fiber based composite [178], and ionic liquids based composite [179, 180], as to be discussed in the next subsections.

### 2.6.1 Types of inorganic fillers

Inorganic-organic composites are the focus of recent attempts to develop proton exchange membranes [50, 63, 177, 181]. Inorganic materials used as fillers in PBI-based composite membranes can be broadly classified into two categories: (i) hygroscopic inorganic particles which impart proton conductivity by their water retention ability, such as  $\text{SiO}_2$  [182-186],  $\text{TiO}_2$  [187-190],  $\text{ZrO}_2$  [191, 192], and clay [193-195], and (ii) inorganic particles which are both hygroscopic and proton conducting, such as phosphate [130, 196, 197], functionalized graphite oxide (GO) [198-203], heteropolyacids [102, 177, 204-206]. In addition, a variety of other inorganic materials have been explored such as  $\text{Fe}_2\text{TiO}_5$  [207], modified silicon carbide [208]. These efforts are summarized in Table 2.5.

Table 2.5 Selected inorganic-organic composite membranes.

Organic phase	Inorganic phase	Details	Ref.
OPBI	Modified SiO <sub>2</sub>	0.181 S cm <sup>-1</sup> at 160 °C	[182]
CrL-PBI	Modified SiO <sub>2</sub>		[184]
PBI	2 wt% TiO <sub>2</sub>	0.13 S cm <sup>-1</sup> at 150 °C, 10% RH, ADL 15.3. 800 mW cm <sup>-2</sup> at 150 °C	[188]
PBI	CaTiO <sub>3</sub>	0.0327 S cm <sup>-1</sup>	[209]
PBI	CsH <sub>5</sub> (PO <sub>4</sub> ) <sub>2</sub> , SiO <sub>2</sub>	0.0648 S cm <sup>-1</sup> at 250 °C	[210]
PBI	KH <sub>5</sub> (PO <sub>4</sub> ) <sub>2</sub> , SiO <sub>2</sub>	0.139 S cm <sup>-1</sup> at 180 °C, OCV 1.01 V, 36 mW cm <sup>-2</sup>	[211]
CrL-OPBI	ZrPA	0.012 S cm <sup>-1</sup> at 140 °C, 0%RH 0.072 S cm <sup>-1</sup> at 140 °C, 100%RH	[196]
PBI	ZrP	0.2 S cm <sup>-1</sup> at 180 C, 0%RH	[197]
CrL-PBI	modified GO	0.0586 S ·cm <sup>-1</sup> at 170 °C	[200]
PBI	modified GO	0.027 S cm <sup>-1</sup> at 140 °C, 0%RH	[198]
PBI	modified GO	0.028 S ·cm <sup>-1</sup> at 170 °C, 0%RH, tensile strength 27.3- 38.5 MPa, RT	[201]
sPBI	modified GO	15 wt % GO, swelling ratio 12.2, Young's modulus 1.70 GPa, 0.006 S ·cm <sup>-1</sup> at 120 °C, RH 10%	[212]
OPBI	GO	0.3 wt % GO, 17% increase in Young's modulus, 33% increase in tensile strength, and 88% increase in toughness.	[213]
PBI	BaCe <sub>0.85</sub> Y <sub>0.15</sub> O <sub>3-δ</sub>	0.092 S cm <sup>-1</sup> at 180 °C under dry conditions	[214]
OPBI	modified SiC	Tensile strength 27.3 to 36.8 MPa, 0.0271 S cm <sup>-1</sup> at 170 °C without humidity	[208]

### 2.6.2 Methods of composite preparation

There are two ways to prepare inorganic/organic composite membranes [181]. In the first approach, inorganic nanofillers are first prepared and then dispersed in polymer solutions, followed by film casting and drying.

This is one of the most convenient and widely practiced approaches to fabricate PBI-based composite membranes. Using this approach, composite membranes with oxides, phosphates and heteropolyacids have been fabricated. For solution casting, good dispersion of inorganic particles can usually be achieved through the modification of particle surfaces and a common

practice for the surface modification of inorganic oxide particles is through the use of silane coupling agents [215]. To further achieve compatibility with PBI matrixes, numerous modifiers with similar polarity, hydrogen bonding or/and dispersive force have been suggested [193].

In the second approach, the precursors are first introduced into the polymer from which inorganic fillers are in situ formed after the membrane casting. As an example, when a membrane is pre-formed as the template, metal ions can usually be introduced through ion exchange – the method is limited by the ion exchange capacity of the host polymer. In the case of PBI-based composites, polymer solutions containing appropriate precursors for inorganic fillers can be cast into membranes. In the subsequent drying or post-treatment, inorganic precursors can further undergo chemical reactions such as sol–gel reactions if alkoxy precursors are used and allow for the homogeneity or good dispersion of in situ formed inorganic fillers inside polymeric matrixes. Using this method, composite membranes with oxide fillers such as SiO<sub>2</sub> from hydrolysis of tetramethoxysilane mixture to cast membranes [185]. Another example is the introduction of metal (Sb, Sn or Fe) chlorides which are eventually converted into phosphate after the membrane doping [130].

### 2.6.3 Composite membranes containing oxides and phosphates

PBI-SiO<sub>2</sub> composites have been widely investigated showing higher conductivity [182, 183]. An interesting finding is that the formation of phosphosilicates within the polymer matrix is benetial for stabilizing the conductivity (ca. 0.04 S cm<sup>-1</sup>) at temperatures of up to 250 °C under an un-humidified atmosphere [58].

Studied the influence of PBI-TiO<sub>2</sub> composites containing 2-16 wt.% TiO<sub>2</sub> have been prepared by Pinar et al [189], exhibiting improved properties such as acid and water absorption capability and proton conductivity. The long-term stability of the 2 wt.% TiO<sub>2</sub> composite PBI membrane was demonstrated in a 150 cm<sup>2</sup> HT-PEM stack cell, which exhibited an irreversible voltage loss of less than 2% after 1100 h continuously operation [190].

The PBI/BaCe<sub>0.85</sub>Y<sub>0.15</sub>O<sub>3-δ</sub> composite membranes were prepared by dispersing BaCe<sub>0.85</sub>Y<sub>0.15</sub>O<sub>3-δ</sub> powder into the PBI solution followed with solution casting. The maximum phosphoric acid adsorption (175%) and protonic conductivity (0.092 S cm<sup>-1</sup> at 180 °C under dry conditions) were observed for all of the PBI nanocomposite membranes containing 5 wt.% of BaCe<sub>0.85</sub>Y<sub>0.15</sub>O<sub>3-δ</sub> in the membrane matrix. The polarization and power density curves were studied at 150 and 180 °C operating temperatures. The power density of about 0.42 W cm<sup>-2</sup> and current density of about 0.84 A cm<sup>-1</sup> at 0.5 V and 180 °C were achieved under dry conditions [214].

### 2.6.4 Composite membranes containing phosphates and heteropolyacids

Phosphates are a big family of salts of orthophosphoric acid and its condensed/polymeric forms. The anions are comprised of pentavalent phosphorus atoms surrounded by (distorted) tetrahedra of four oxygen atoms. Monophosphates or orthophosphates are the biggest group with an isolated anionic entity of PO<sub>4</sub><sup>3-</sup> tetrahedron while condensed phosphates are another containing corner-sharing PO<sub>4</sub> tetrahedra. The conductivity of ZrPA doped cross-linked PBI

can reach  $0.072 \text{ S cm}^{-1}$ ,  $0.025 \text{ S cm}^{-1}$  and  $0.012 \text{ S cm}^{-1}$  at  $140 \text{ }^\circ\text{C}$  at 100% RH, 50% RH, and 0% RH, respectively [196]. Proton conductor ZrPA was chosen as a potential alternate for PA because of its insolubility in water and can avoid leaching. ZrPA has the characteristics that low cost, facile preparation, good thermal stability, and high proton conductivity under high temperature and low humidity. ZrPA shows excellent compatibility with PBI because of its inorganic-organic structure while the compatibility can avoid phase separation. The membrane conductivity of ABPBI was enhanced with metal phosphate (Sb-PA, Sn-PA, Fe-PA) [130]. The enhancement effect is most prominent in Sb-PA, with the maximum conductivity at  $160 \text{ }^\circ\text{C}$ ,  $0.067 \text{ S cm}^{-1}$ . Chen et al. [210] reported a  $\text{CsH}_5(\text{PO}_4)_2/\text{SiO}_2/\text{PBI}$  composite membrane. A molten proton conductor fuel cell equipped with such an electrolyte membrane operating at  $200 \text{ }^\circ\text{C}$  showed an open-circuit voltage of 1.08 V, and a stable output voltage during continuous measurement for 150 h at a constant output current density of  $100 \text{ mA cm}^{-2}$  [210].

Heteropolyacids (HPA), e.g. phosphomolybdic acid ( $\text{H}_3\text{PMo}_{12}\text{O}_{40}$ , PMA) [204], phosphotungstic acid ( $\text{H}_3\text{PW}_{12}\text{O}_{40}$ , PWA) [102], and silicotungstic acid ( $\text{H}_3\text{SiW}_{12}\text{O}_{40}$ , SWA) [102]. These solid acids possess high conductivity and strong acidity and are generally surrounded by a large number of water molecules, making them especially suitable for operation under anhydrous conditions [205]. Initial results indicated that the conductivities of the composite membranes containing 20 and 30 wt% of PWA at  $140 \text{ }^\circ\text{C}$  and that of SiWA at  $200 \text{ }^\circ\text{C}$  were lower than that of pristine PBI membranes under the same conditions [102]. Further doping is necessary. At  $150 \text{ }^\circ\text{C}$ , the conductivity of PA doped 40% SiWA/PBI composite membrane was  $0.177 \text{ S cm}^{-1}$  [177]. In a single cell test, for example, 40 wt% SiWA/PBI exhibits only around 10–15 mV loss in cell potential due to IR drop which is around 75 mV at  $500 \text{ mA cm}^{-2}$  for PBI. CsHPA was used extensively for PEMFC due to its insolubility in water. Typically,  $\text{PBI}/\text{Cs}_{2.5}\text{H}_{0.5}\text{PMo}_{12}\text{O}_{40}/\text{H}_3\text{PO}_4$  composite membrane exhibited high conductivity above  $0.1 \text{ S cm}^{-1}$  at the temperature of  $140\text{--}180 \text{ }^\circ\text{C}$ , and in a fuel cell gave a high power density of  $0.7 \text{ W cm}^2$  (at atmospheric pressure and  $150 \text{ }^\circ\text{C}$  with  $\text{H}_2/\text{O}_2$ ) [206].

### 2.6.5 Composite membranes containing carbon based fillers

PBI composites with carbon-based fillers are of recent interest. Graphene oxide (GO) and functionalized GO have been used as fillers in PBI membranes [198-203]. Graphite oxide has received a great deal of attention because of its single atomic layer structure and functional groups. It has different oxygen-containing functional groups, such as carboxyl, hydroxyl, and epoxy groups. Because of the oxygen-containing functional groups, GO is easy to hydrate. As GO itself is an electronic insulator with differential conductivity, the high proton conductivity of the composite membrane is attributed to the hydrogen bonds in GO [216]. The acidic functional groups such as carboxylic acid and intermolecular hydrogen bonding can even provide additional proton conducting paths [217]. However, the dispersion of GO prepared by the Hummer method is poor in organic solvents such as DMF [218]. To avoid GO aggregates in organic solvents, one of the most effective ways is to graft active groups on the GO surface. The swelling ratios of the PA doped modified-GO/PBI composite membranes are smaller than those of reference PBI, it could be explained by the strong interfacial adhesion between the

fillers and the matrix [198, 212]. Wang et al.[213] reported that the imidazole rings in the polymer chains interacted strongly with the oxygen-containing groups such as the carboxyl groups (non-covalent bonding) and the epoxy groups (covalent bonding) of GO. Compared with pure PBI, the addition of only 0.3 wt % of Go resulted in a 17% increase in Young's modulus, 33% increase in tensile strength, and 88% increase in toughness.

### 2.6.6 PBI composite containing ionic liquids

The incorporation of ionic liquids (ILs) into PEMs has been studied recently. Owing to their temperature stability and high ionic conductivity, ILs have been used to enhance conductivity and thermochemical stability in PBI based membranes [179, 180, 219]. Zhang reported an ionogel incorporated into ABPBI membranes with low phosphoric acid doping levels, the schematic is shown in Figure 2.12 [195]. The natural sepiolite was first acid-treated to obtain one-dimensional silicon nanorods (SNRs) with a large specific surface area and a hierarchical porous structure. The SNRs were then filled with imidazolium IL to prepare IL@SNR ionogels. Analysis of related spectra and thermal behavior verified that the IL molecules were confined in the inner channels of SNRs. The as-prepared IL@SNRs were embedded in the ABPBI to form composite membranes (ABPBI/IL@SNRs) via in situ synthesis. By immobilizing proton conductors, the ABPBI/IL@SNR composite membranes show  $0.048 \text{ S cm}^{-1}$  at  $180^\circ\text{C}$  under 0% RH.

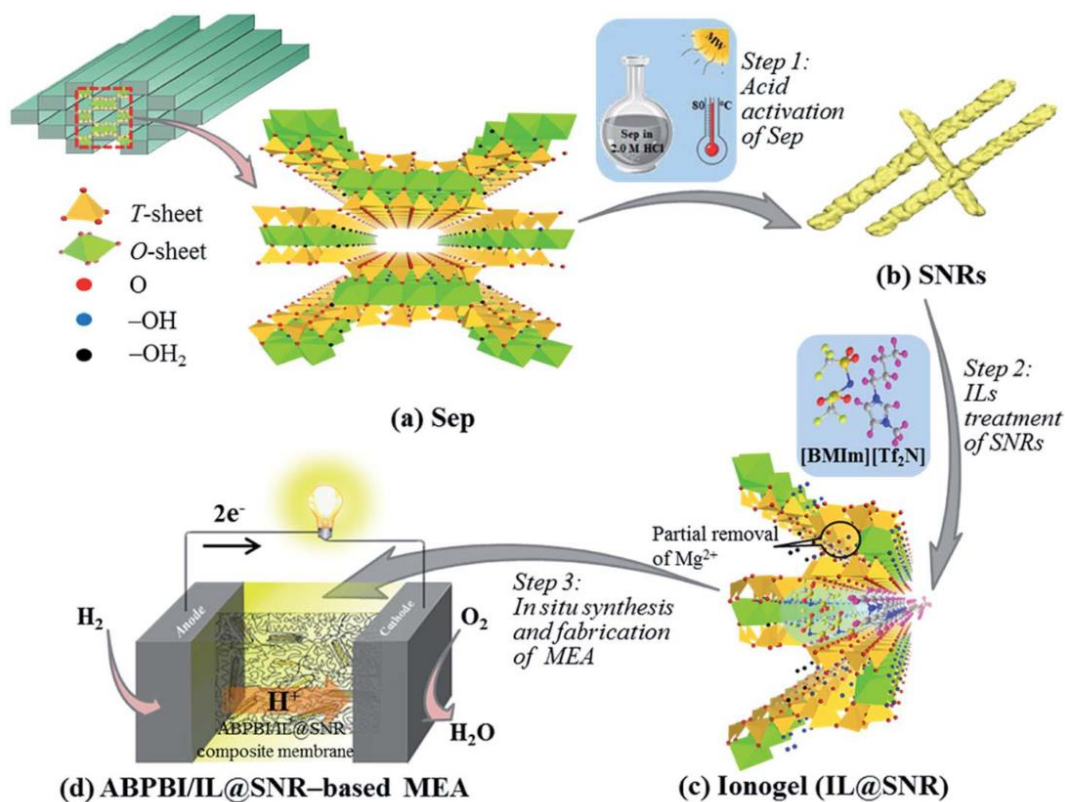


Figure 2.12 Schematic representation of the synthesis of IL@SNR ionogels [via microwave (MW)-assisted acid activation treatment and high-vacuum dryness] upon loading of phosphoric acid and they were subsequently integrated in PEMFCs. (A) Sep; (B) SNRs; (C)

*IL@SNR ionogel; (D) ABPBI/IL@SNR-based MEA [195].*

ILs tend to drain out from the membranes after a long time operation, therefore polymerization of ILs emerges as an alternative in terms of safety, stability, and mechanical properties [183]. Rewar et al. [179] reported a composite membrane with PBI and polymeric ionic liquid (PIL). With the increase in PIL content, the proton conductivity of the composite membranes gradually increased from 0.04 S cm<sup>-1</sup> for PBI to 0.07 S cm<sup>-1</sup> for the composite membrane at 150°C. The maximum power density and current density obtained were 515 mW cm<sup>-2</sup> and 1632 mA cm<sup>-2</sup>. Kallem et al. [180] fabricated hierarchical porous PBI (HPBI) membrane infiltrated with 1H-3-vinylimidazolium bis(trifluoromethanesulfonyl)imide ([HVIm][TFSI]) liquid and divinylbenzene (as a cross-linker), followed by in situ UV polymerization. The polymeric ionic liquid moiety plays the role of a proton conductor, whereas the HPBI microsieve ensures the mechanical resistance of the system. The obtained membranes achieved conductivity values up to 0.085 S cm<sup>-1</sup> at 200 °C under anhydrous conditions and in the absence of mineral acids.

*Table 2.6 Ionic liquids/PBI composite membranes.*

<b>Ionic Liquids</b>	<b>Details</b>	<b>Ref.</b>
[HVIm][TFSI]	0.085 S cm <sup>-1</sup> at 200 °C under anhydrous conditions and in the absence of mineral acids.	[180]
P[DADMA][TFMS]	0.07 S cm <sup>-1</sup> at 150 °C, the maximum power density and current density obtained were 515 mW cm <sup>-2</sup> and 1632 mA cm <sup>-2</sup> .	[179]
1-butyl-3-methylimidazolium (BMIM)-BF <sub>4</sub>	0.094 S cm <sup>-1</sup> at 200 °C under anhydrous conditions.	[219]
1-butyl-3-methylimidazolium bis(trifluoromethanesulfonyl)imide ([BMIm][Tf <sub>2</sub> N])	0.01 S cm <sup>-1</sup> at 40 - 90 °C, 0.048 S cm <sup>-1</sup> at 180 °C, 0% RH. 0.15 W cm <sup>-2</sup> at 80 °C, 0.28 W cm <sup>-2</sup> at 180 °C, 0% RH.	[195]

## 2.7 Electrospun nanofiber based composite membranes

### 2.7.1 Electrospinning technique

In recent years, electrospinning has attracted significant interest for use in preparing nanofiber-based materials due to its good versatility, reproducibility, and scalability [178]. It can be applied to the preparation of catalysts [220], support materials [221, 222], and electrolyte membranes [223] for fuel cells. The number of published research articles on the relative topics has significantly increased in the past ten years (Figure 2.13), and close to 50 % of articles are related to the preparation of membranes.

Electrospinning is a top-down approach to develop one-dimensional (1D) nano-materials starting from molten polymers or polymers solution. The conventional electrospinning set-up consists of three major components: a high voltage (kV) power supply, a spinneret (a syringe

or pipette tip) and a grounded collector (typically a metal plate or a rotating mandrel) (Figure 2.14) [220]. This technology is based on the application of an electric field to a drop of fluid polymer on the tip of a spinneret. As the intensity of the electric field increases, the hemispherical surface of the solution at the tip of the capillary tube elongates to form a conical shape known as the Taylor cone. When the applied electric field reaches a critical value, the repulsive electrical forces overcome the surface tension of the drop. A charged jet of the solution is then ejected from the tip of the Taylor cone and an unstable and rapid whipping of the jet occurs between the tip and the collector leading to the evaporation of the solvent and the formation of solidified continuous, ultra-thin fibers on the collector [220].

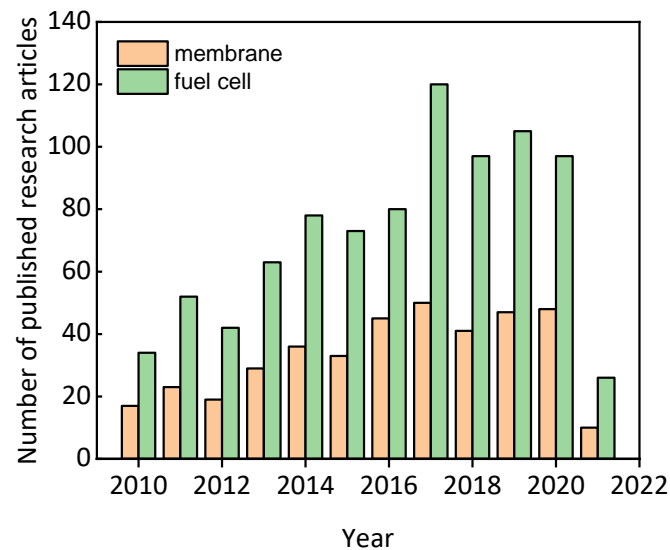


Figure 2.13 Number of research articles concerning electrospun nanofiber applications in fuel cells and electrolyte membranes published between 2010 and 2021 (Web of Science data: topic: Electrospinning + Fuel cell, topic: Electrospinning + Fuel cell + membrane)

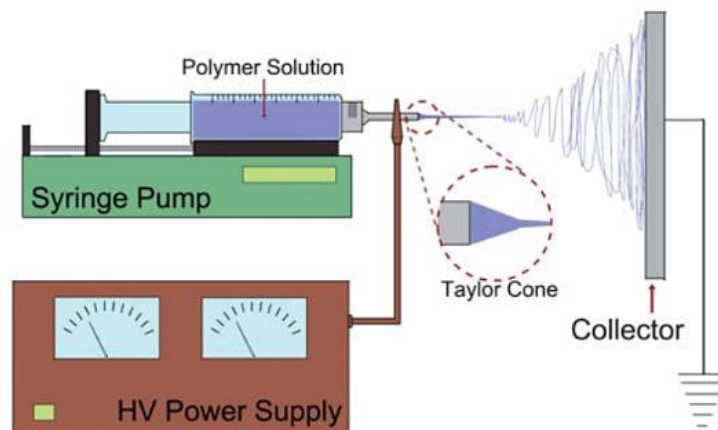


Figure 2.14 Schematic illustration of a typical electrospinning set-up and the Taylor cone [220].

The electrospun nanofiber structure has the advantages of good interconnectivity, high porosity, and large special surface area. The composite membranes containing electrospun nanofibers

and mats show exceptional tensile strength and stiffness because of the polymer chains' orientation enabled by extensional forces during the electrospinning process. Two types of membrane architecture of nanofiber-based PBI composite membrane are shown in Figure 2.15, (i) electrospun PBI nanofiber mats to be used as reinforcement in an ionomeric matrix [149, 224, 225], (ii) electrospun crosslinked or inorganic fibers to be used as nanofillers in PBI-based composite membranes [133, 226].

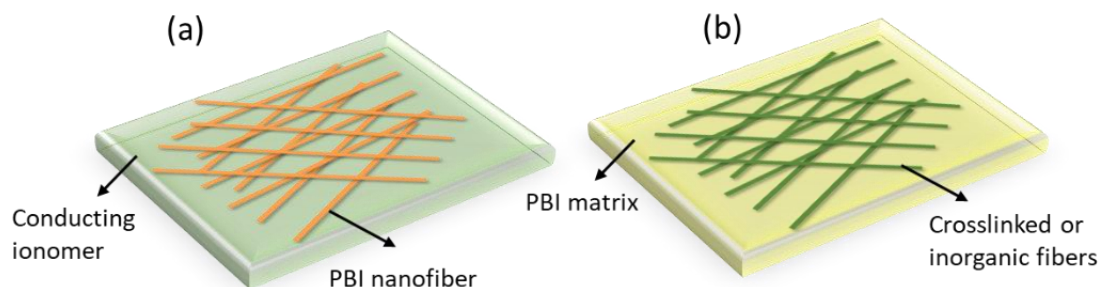


Figure 2.15 Types of membrane architectures based on PBI materials. (a) A proton conducting polymer surrounding an electrospun mat of PBI nanofibers. (b) A crosslinked or inorganic mat embedded in a PBI matrix.

### 2.7.2 PBI nanofiber mat/ionomer matrix

Kim et al. [227] first reported the production of PBI nanofibers via electrospinning from this typical DMAc/PBI system in 1999, they pointed out that PBI molecules are oriented parallel to the fiber axis and the mechanical strength of the nanofiber mat was increased by treatment in sulfuric acid and heat. Penchev[228] reported a new approach for PBI electrospinning from ethanol/KOH solvent system. The obtained yarns are in the centimeter length range and thickness 0.2-1 mm, composed of individually self-bundled nanofibers with average diameter  $281 \pm 74$  nm. In the PBI nanofiber mat/ionomer matrix composite, the PBI fiber mat worked as mechanical support, but the nanofiber shows lower thermal stability than the corresponded dense materials because of the nano effects [149, 224]. Table 2.7 shows the overview of PBI nanofiber mat/ionomer matrix.

### 2.7.3 Crosslinked or inorganic fibers/PBI matrix

There are only a few studies reported on the crosslinked fiber mats/PBI matrix and inorganic fiber mats/PBI matrix. Li et al. [133] reported composite membranes with enhanced mechanical properties as well as higher proton conductivities. The crosslinked PBI nanofibers were prepared from the precursor with crosslinker polybenzoxazine (PBz) by electrospinning process, and then polyelectrolyte composite membranes of PBI and crosslinked mats were prepared by an impregnation process. The modified membranes showed significantly improved mechanical properties, acid uptakes, and dimensional stability upon acid doping. Figure 2.16 presents the stress-strain curves and the proton conductivity of the composite membrane with various wt% of PBz in comparison to the neat PBI membrane. The composite membrane shows a proton conductivity of  $0.17 \text{ S cm}^{-1}$  at  $160^\circ \text{C}$  under anhydrous conditions, which is about 2-fold higher compared to that of the neat PBI membrane.

Table 2.7 Overview of PBI nanofiber mat/ionomer matrix.

Electrospun materials	Solution	Matrix materials	Details	$\sigma$ (S cm <sup>-1</sup> )	power density (mW cm <sup>-2</sup> )	Ref.
PBI	-	Nafion	Phytic acid doped PBI fibers impregnated with Nafion, the composite thickness is about 15 $\mu$ m	0.003 (80°C, 40%RH)	About 240 (60°C, 40%RH)	[225]
PVFP/PBI	PVFP/PBI +DMAC/acetone	Nafion	The thickness of electrospun PVFP/PBI mat is about 13-15 $\mu$ m	0.13 (70°C, 95%RH)	106.2 (methanol/O <sub>2</sub> , 90°C)	[224]
PBI	DMAc+20wt%PBI +4wtLiCl%	-	Non-wovens followed by sulfuric acid and heat treatment	-	-	[227]
PBI	DMAc+LiCl +10-15wt%PBI	-	The mean fiber diameter of PBI mat is about 170nm, 2-fold increase in mean fiber diameter after immersion in phosphoric acid for 72h.	0.123(RT)	-	[229]
SO <sub>2</sub> -OPBI	DMSO+ SO <sub>2</sub> -OPBI	-	Fiber diameter ~500nm, tensile stress 5.96 MPa, elongation modulus 27.3 MPa.	0.0667(160°C)	232 mW cm <sup>-2</sup> (dense membrane, 160°C)	[149]
PBI	DMAc+10-30wt%PBI (Mw 27200) +10-25wt%SiO <sub>2</sub>	-	Non-wovens obtained by electrospinning PBI solution with SiO <sub>2</sub> nanoparticles followed by hot pressing treatment	-	-	[230]

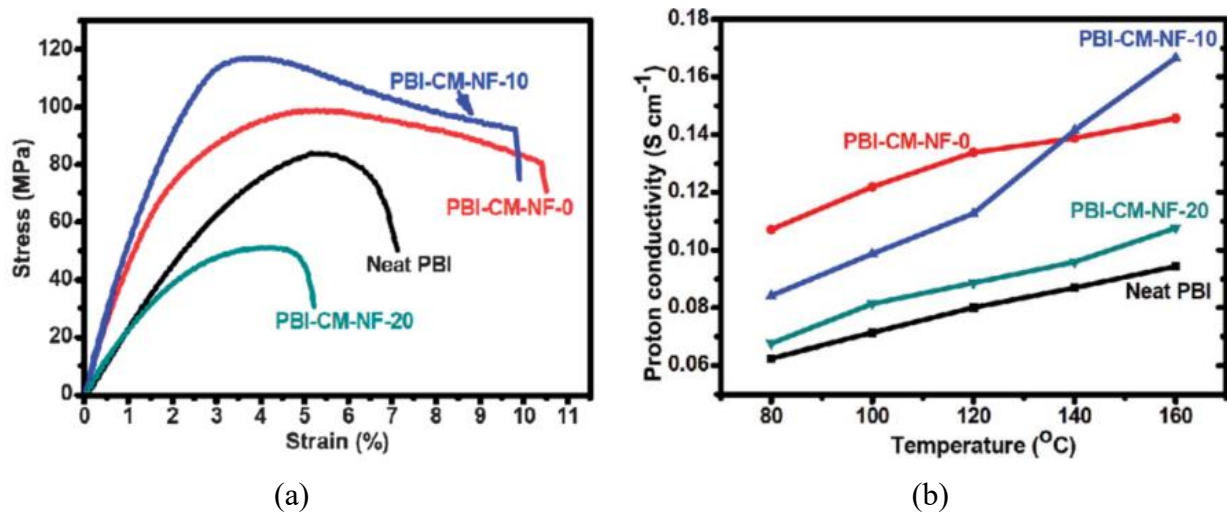


Figure 2.16 (a) Stress-strain curves; (b) Temperature-dependent proton conductivity of nanofiber-reinforced PBI composite membranes (PBI-CM-NF- $X$ ), where CM stands for composite, NF for nanofiber, and  $X=0, 10$ , and  $20$  for the weight fraction of PBz in the polymeric nanofibers [133].

Table 2.8 Overview of proton conducting membranes of crosslinked electrospun polymer mat/ionomer or inert matrix.

Electrospun materials	Solution	Matrix materials	Details	$\sigma$ (S cm <sup>-1</sup> )	power density	Ref.
PBI/PBz	DMAc +25wt%PBI +0-20wt%PBz	PBI	PBI was impregnated into the crosslinked PBI/PBz nanofiber mats	0.170 (160 °C)	670 mW cm <sup>-2</sup>	[133]
Modified SiO <sub>2</sub> fibers	TEOS+Ethanol +HCl	PBI	PBI was impregnated into electrospun silica nanofiber mats.	0.004 (200 °C)	-	[226]

## 2.8 Challenges of PBI membranes

### 2.8.1 Acid loss and inventory in MEAs

Acid loss is one of the most important issues connected to the long-term durability of the PBI based on fuel cells. The loss of the acid out of the fuel cell is dominated by the evaporation mechanism. The extrapolated acid vapor pressure to the fuel cell operational temperatures provides a guideline of the acid evaporation rate. As seen from Figure 2.17 the phosphoric acid vapor pressure is estimated to be 0.7 ppm at 160 °C. At this temperature for a current density

of  $0.2 \text{ A cm}^{-2}$  and an air stoichiometry of  $\lambda_{\text{Air}} = 2$ , the acid loss rate caused by the acid-saturated cathode air flow is about  $6 \mu\text{g m}^{-2} \text{ s}^{-1}$  or  $2 \mu\text{g cm}^{-2} \text{ h}^{-1}$  [54]. Measurements in PBI cells [231], showed an acid loss rate below  $1 \mu\text{g m}^{-2} \text{ s}^{-1}$  or  $0.4 \mu\text{g cm}^{-2} \text{ h}^{-1}$ .

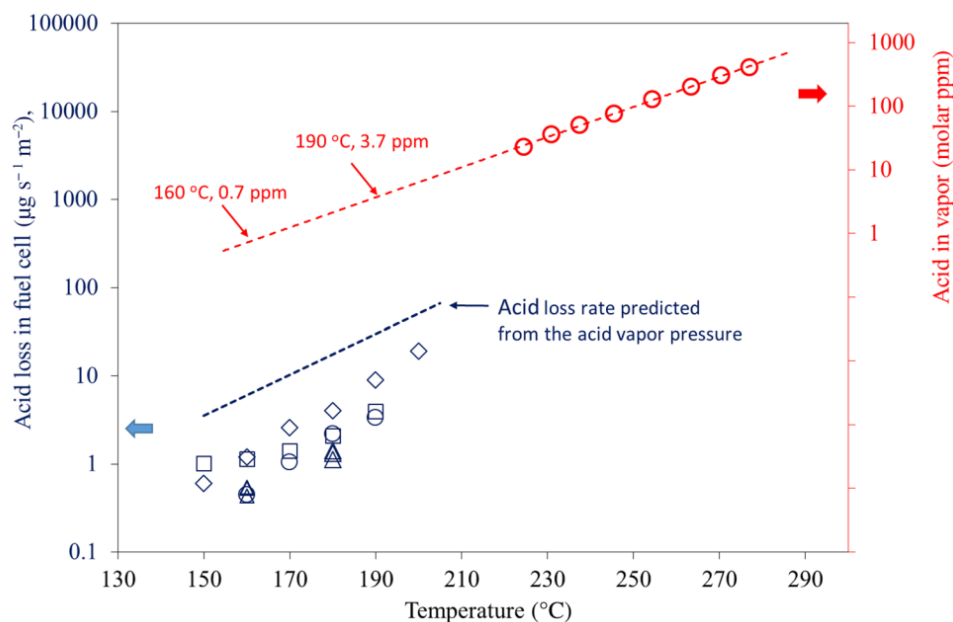


Figure 2.17 Estimations and measurements of acid loss carried by gas flow and the extrapolation of acid vapor pressure [54].

For a typical  $40 \mu\text{m}$  thick dry PBI membrane, the specific mass is estimated to be  $10 \text{ mg PBI/cm}^2$ . At an acid doping level of  $11 \text{ mol H}_3\text{PO}_4/\text{PRU}$ , the specific loading of phosphoric acid is  $36 \text{ mg H}_3\text{PO}_4/\text{cm}^2$ . This is the total inventory of the acid in the membrane. Assuming that 50% acid loss from the membrane will result in the death of the fuel cell, the above acid loss rate indicates that this acid inventory is just sufficient to reach the targeted lifetime of 50,000 hours. Operation at high current densities, temperatures or air stoichiometries, the acid loss will always be a critical issue.

### 2.8.2 Importance of the membrane thickness

With high molecular weight polymers e.g. higher than  $60,000 \text{ g/mol}$ , strong and robust membranes can be obtained from the DMAc solution casting. Such membranes can be doped to an acid doping level around  $11 \text{ mol H}_3\text{PO}_4$ . At this doping level, the PBI membranes possess a typical conductivity of  $0.05 - 0.08 \text{ S cm}^{-1}$  at  $150\text{-}160 \text{ }^\circ\text{C}$  without atmospheric humidification. Figure 2.18 shows the dependence of the conductivity on the acid doping level at  $120 \text{ }^\circ\text{C}$  [52], which is slightly lower than at  $160 \text{ }^\circ\text{C}$ . Though scattered due to small variations in experimental conditions and experimental uncertainties in the reported acid contents, a clear trend is seen that the conductivity increases dramatically by 5-6 orders of magnitude when the acid doping level is increased from about 1 to 4-6. Increasing the acid doping level from 4-5 to 10-11 the conductivity increases by roughly another two orders of the magnitude. Any further increase in the acid doping level above 11, however, does not lead to significant enhancement of the conductivity.

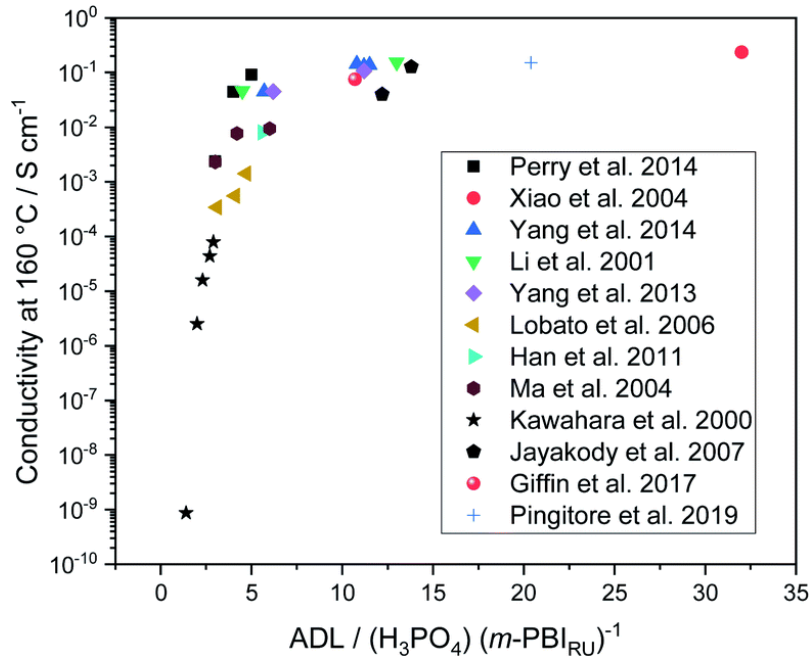


Figure 2.18 Conductivity data for phosphoric acid doped *m*-PBI prepared by casting from DMAc. The data were recorded at 120 °C without humidification and are compiled by D. Aili et al [52], to which the original literature sources of data points are referred.

In fuel cells the performance is, however, depending on the ratio of the membrane thickness to the conductivity, which is called the area specific resistance (ASR):

$$ASR (\Omega \cdot cm^2) = \frac{Thickness \text{ cm}}{Conductivity \text{ S/cm}^2} = \frac{Voltage \text{ V}}{Current \text{ density S/cm}^2} \quad (2.5)$$

This hints that better fuel cell performance can be achieved by reducing the membrane thickness, of course, without too much compromise of the mechanical strength and gas permeability.

For a typical PBI membrane with a thickness of 80  $\mu\text{m}$  (wet or after doping) and acid doping level of 11 mol  $\text{H}_3\text{PO}_4/\text{PRU}$  corresponding to a proton conductivity of  $0.08 \text{ S cm}^{-1}$  at 160 °C, the ASR is estimated to be  $0.1 \Omega \cdot \text{cm}^2$ . The ASR can be translated into a voltage loss of 100 mV at a current density of  $1 \text{ A cm}^{-2}$ .

For LT-PEMFCs, the Gore-select® membranes are widely used which are reinforced with thin PTFE porous fiber sheet and have a characteristic thickness between 5-30  $\mu\text{m}$ . Compared with standard Nafion 117 membranes, which have a thickness of 200  $\mu\text{m}$  and a conductivity of  $0.14 \text{ S cm}^{-1}$ , the Gore-select® membranes have lower conductivity ( $0.05 \text{ S cm}^{-1}$ ). At a typical thickness of 10-20  $\mu\text{m}$ , the ASR of the Gore-select® membranes is as low as  $0.02\text{-}0.04 \Omega \cdot \text{cm}^2$ , much smaller than that ( $0.14 \Omega \cdot \text{cm}^2$ ) of the Nafion 117 membranes. At the same current density of  $1 \text{ A cm}^{-2}$  the Gore-select® membrane would display an Ohmic loss of 20-40 mV.

## 2.9 Approaches and scope of the thesis

As outlined in this chapter, one of the major issues in PEMFC is the relatively large ohmic resistance primarily due to the thick PBI membranes used. Better fuel cell performance can be achieved by reducing the membrane thickness, but this also comes with challenges of 1) reduced mechanical stability, 2) increased crossover of reactants, among which the later may result in formation of additional hydrogen peroxide and hence exaggerated oxidative degradation of the polymer, 3) decreased acid inventory. The focus of the present project is to explore the possibility to reduce the membrane thickness without too much compromise of the mechanical strength and gas permeability by development of PBI composites.

The strategy of the project is to prepare the electrospun PBI fiber mats, which after crosslinking are insoluble or less swollen in organic solvents or doping acid. The PBI fiber mats are then used as reinforcement of PBI membranes. The reinforcement fiber mat and the bulk membrane are made of the same polymer to improve the compatibility of the two phases.

The thesis is structured as follows. The most frequently recurring experimental methods and techniques are described in **Chapter 3** while the experimental details for specific tasks and the corresponding results are presented in **Chapters 4-7**.

In **Chapter 4**, thin PBI membranes with thicknesses from 10 to 40 (standard)  $\mu\text{m}$  are first benchmarked in association with development of characterization protocols and techniques. **Chapter 5** reports preparation of PBI fibers and fiber mats by electrospinning. Composite membranes reinforced by the fiber mats are presented in **Chapter 6**. Conclusions and outlook are given in **Chapter 7**.



# CHAPTER 3

## Experimental

---

This chapter gives an overview and a basic introduction of the most commonly used experimental methods and material characterization techniques in this project.

### 3.1 Preparation of membranes

The polymer for membrane casting in this project is supplied by the early Danish Power Systems ApS (DPS, now Blue World Technologies). The polymer has an average molecular weight of 58000, determined by the viscosity measurement in concentrated sulfuric acid using the empirical Mark–Houwink constants  $K = 1.94 \times 10^{-4} \text{ dL g}^{-1}$  and  $\alpha = 0.791$  [129]. Membranes with varied dry thickness of 40, 20, and 10  $\mu\text{m}$  were obtained from 8.6 wt%, 4.3%, and 2.5% PBI solution in DMAc, respectively. 60 ml of each solution was poured onto a rectangle glass plate with confined area of 41 cm x 26 cm and dried in an oven by slow heating to 120 °C. The obtained solid membrane was then washed with hot (ca. 90 °C) water for about 30 min, followed by further drying at 120 °C for 2 hours.

For the thermal curing membranes, the heat treatments were conducted in a tube furnace at temperatures ranging from 350 °C to 430 °C under argon atmosphere. During the heat treatment, argon was continuously purged through the tube with a flow rate of 80 mL/min.

To prepare the crosslinked membranes, the crosslinker DBpX was added in PBI solution with a cross-linker degree of 15%. The post-treatment of the membrane was carried at 280 °C for 10 min.

### 3.2 Preparation of fiber reinforced composite membranes

Two electrospinning equipment were used in this project. A needle-based electrospinning machines (Linari, Linari Nanotech) was used for preparing small scale fibers. While Nanospider™ (Elmarco), a commercial nozzle-less electrospinning equipment, was used for preparing large size mats with different thickness.

#### 3.2.1 Electrospun fiber preparation

The PBI precursor solution for electrospinning was prepared by dissolving dry PBI powder and lithium chloride (LiCl) in DMAc at a bath temperature controlled at 145 °C for 18 h with a refluxing condenser. The concentration of PBI polymer in the precursor solution is in a range of 10-15 wt.%. Afterwards, the PBI solution was cooled down to room temperature and

transferred to a syringe with a stainless steel needle, the diameter of the needle is 0.8 mm. The syringe was set on a pump to control the solution flow rate during electrospinning. A drum collector covered by aluminium foil or brown paper was used to collect the nanofibers. The roll speed was kept constant at 100 rpm, and the distance between the collector edge and needle tip ranged from 8 to 12 cm. The applied voltage between the needle and the collector was kept at 25-40 kV, the electrical bias potential was supplied by electrospinning device Linari. The collected nanofiber mat was dried at 200 °C for 2 hours to remove the residual solvent.

### 3.2.2 Upscale of electrospun mats

The upscales PBI mats were prepared on a laboratory scale machine Nanospider™ (Elmarco) [232, 233]. As in the needle design, the principle of fiber drawing is based on the forces generated by an electrostatic field. However, instead of using needles, the fibers are formed by applying the voltage to a cylindrical electrode having part of its circumference immersed in the polymer solution (Figure 3.1). As the electrode rotates, a thin layer of polymer solution is carried on its surface and exposed to the high-voltage electric field between the electrode and counter-electrode. As in the case of the basic electrospinning, Taylor cones are formed from the polymer solution; then as the electric field forces strengthen, nanofiber jets are drawn toward the counter electrode and deposited on a collection substrate such as a fabric.



*Figure 3.1 Nozzle-less electrospinning [232].*

The PBI mats were prepared with diluted S26 solution. Commercial S26 solution (containing 26.2 wt% of PBI powder, 72.3 wt% DMAc, and 1.5 wt% LiCl) was purchased from PBI Products Inc (Charlotte, North Carolina). The electrospinning solutions were diluted to 13% with DMAc, stirred magnetically at 70 °C overnight to ensure homogeneity. For the spinning process [234, 235], the distance between the emitter and collector was set to 180 mm; the voltage was set to 45-55 kV, carriage velocity was 100 mm s<sup>-1</sup>, the collector carrier velocity was set at 4-9 mm min<sup>-1</sup> to control the mat thickness. The chamber atmosphere conditions were controlled at 20 %RH and 20 °C.

### 3.2.3 Thermal treatment

The heat treatments were conducted in a tube furnace at temperatures ranging from 390 to

450 °C under an argon atmosphere. The temperature of tube furnace was calibrated before use. The furnace was repeatedly heated to the target temperature and hold for 30 min to reach equilibrium. During the heat treatment, argon was continuously purged through the furnace at a flow rate of about 80 mL min<sup>-1</sup>. The sample was put in a quartz boat. The quartz boat connected with a long stick was placed in a low-temperature zone (120 °C) during heating (Figure 3.2). After the temperature arrived, the quartz boat was moved into the heating zone and hold for 10 min. The boat was then pulled out to the low-temperature zone soon. The sample can be taken out after the furnace cooling down below 100 °C.

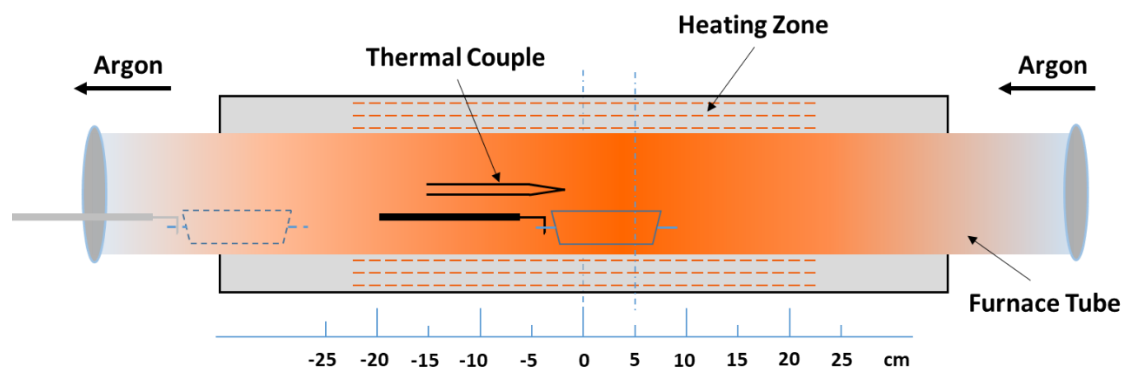


Figure 3.2 Schematic diagram of thermal treatment in Ar atmosphere.

### 3.2.4 Crosslinked fibers

To obtain the crosslinked fiber, the electrospinning solution with crosslinker was prepared. Firstly, the crosslinker DBpX was dissolved in DMAc and then mixed with PBI solution at room temperature. The crosslinking degree is 10%, as assuming a complete reaction for each mole of the crosslink agent with 2 equiv of imidazole ring. The crosslinker fiber was produced in the Nanospider, the voltage was set to 45kV, other conditions are the same as preparing pure PBI fibers. The collected PBI fiber mats containing DBpX were then heat-treated to activate the crosslinking at 280 °C for 10 min under ambient atmosphere.

### 3.2.5 Fabrication of composite membranes

For further composite fabrication, the cured or crosslinked PBI nanofiber mat was dry at 120 °C for 1h to remove the moisture first. The mat was placed in a clean petri dish and wetted with ethanol. After removing the air bubbles between the mat and glass, the mat was fixed with four heavy stainless (Figure 3.3). 5wt% PBI solution was then poured into the petri dish. The amount of the PBI was calculated according to the expected thickness of the final membrane. The heating process for solvent evaporation is the same as described in Section 3.1.

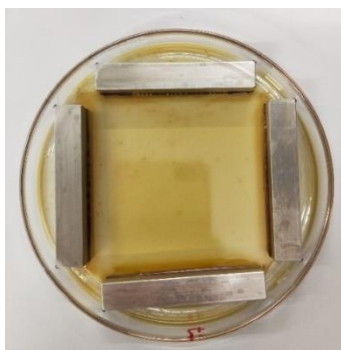


Figure 3.3 Mat edge fixed with metal sticks during the composite casting process.

### 3.3 Thermogravimetric Analyses

Thermogravimetric Analyses (TGA) were used to evaluate the composition and thermal behavior of PBI membranes and composite membranes. Studies were conducted with 10-15 mg samples, in the temperature range from 25-1000 °C with a heating rate of 5 °C min<sup>-1</sup> under air atmosphere.

### 3.4 Scanning electron microscope

Scanning electron microscope (SEM) is an instrument that provides a wide variety of information from the sample surface, it can show the microstructure of samples down to the nm scale. Information such as morphology, size, topography, and others are made possible through the use of this technique. The interaction of electron and sample results in various radiation forms such as secondary electrons (SE), diffracted backscattered electrons (BSE), cathodoluminescence (CL), auger electrons and X-ray (Figure 3.4).

The most commonly used detectors in this work are In-lens detector and SE2 detector (secondary electron detector). In-lens detectors mostly collect SE1 secondary electrons, which carry the highest spatial resolution information. SE2 detector provides an SEM topography image of the sample surface with a large depth of field.

In this project, Zeiss-Merlin field emission SEM was used to characterize the morphology, porosity, and dimension of electrospun fibers and composite membranes.

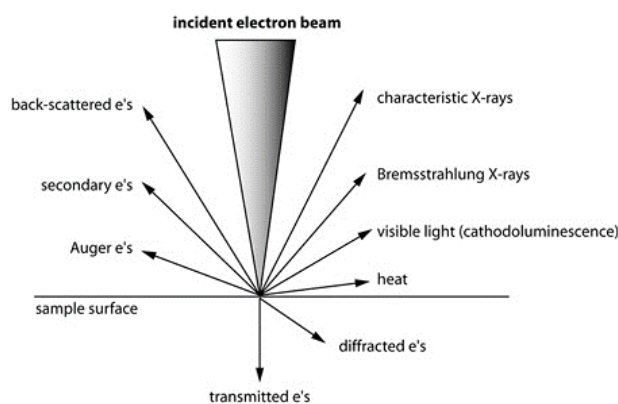


Figure 3.4 Types of interactions between electrons and a sample [236].

### 3.5 Acid doping and swellings

Typical doping of PBI membranes is carried out by submerging the samples in 85 wt% PA aqueous solution at room temperature for a couple of days. For some membrane samples such as crosslinked, thermal cured, and composite membranes, higher doping temperatures are used in order to achieve higher acid doping levels. After doping the samples are taken out of the acid solution and surface acid is gently wiped off. The acid doping extent of the membranes is usually characterized by the acid doping level (*ADL*) which is defined as the molar number of PA molecules per mole of polymer repeat unit:

$$ADL = \frac{W_a - W_b}{W_b} \cdot \frac{M_{PA}}{M_{PBI}} \quad (\text{mol } H_3PO_4/PRU) \quad (3.1)$$

Where  $W_b$  and  $W_a$  are the membrane weight before and after the acid doping,  $M_{PA}$  and  $M_{PBI}$  are the molar mass of phosphoric acid and PBI, respectively. Accordingly, area swelling (*AS*) and volume swelling (*VS*) of the doped membranes are determined based on the dimensional changes of membranes before and after acid doping as expressed as:

$$AS(\%) = \frac{A_a - A_b}{A_b} \cdot 100 \quad (3.2)$$

$$VS(\%) = \frac{V_a - V_b}{V_b} \cdot 100 \quad (3.3)$$

Where  $A_b$ ,  $A_a$ ,  $V_b$ ,  $V_a$  are the area and volume of the membrane before and after acid doping, respectively.

### 3.6 Mechanical strength

A modified universal materials testing machine (Testometric Micro 350) was used to measure the tensile properties of membranes. Tests were operated in a metallic chamber with a temperature controller. The grip was separated at a rate of 10 mm/min. Grip separation and axial force are recorded as a function of time. The stress-strain curves were recorded. The engineering tensile stress ( $\sigma$ ) and the tensile strain ( $\varepsilon$ ) were calculated according to Equations 3.7 and 3.8, respectively.

$$\sigma = \frac{F}{A} \quad (3.4)$$

$$\varepsilon = \frac{\Delta L}{L_0} \times 100\% \quad (3.5)$$

Where  $F$  is the force in Newton,  $A$  is the cross-sectional area of the sample,  $\Delta L$  is the linear dimension change of the sample and  $L_0$  is the initial sample length.

Young's modulus  $E$ , which is also known as modulus of elasticity, is defined as the ratio between tensile stress and tensile strain of a material during its elastic deformation, as Equation 3.9.

$$E = \frac{\sigma}{\varepsilon} \quad (3.6)$$

The reported mechanical data were determined from the average values of 3-4 samples and the reported errors are the standard deviations.

## 3.7 Fuel cell test

### 3.7.1 21 cm<sup>2</sup> cell

**Test setup.** Cells with an active size of 21 cm<sup>2</sup> are used for tests at Danish Power System (DPS, today Blue World Technologies) using the in-house built test stations. The cell temperature is controlled by electric heaters and reactants are supplied by gas inlet tubes controlled by flow meters. The test cell hardware consists of an anode and a cathode endplate. The anode endplate has three channels for inlet of water, fuel, and outlet of excess fuel separately, while the cathode endplate has two channels for inlet of air and outlet of exhaust air together with product water. The set-up is controlled using a program written in LabView. Electrochemical tests are performed with BioLogic electrochemical workstations coupled with a potentiostat (SP-50/150, Bio-Logic). The fuel cell control is conducted by setting test conditions (current, gas flows, temperature etc.) and recording the monitored system variables in a time-series text file. The cell is kept at a regulated temperature of 160 °C. During the single-cell testing, dry hydrogen and air are fed to the anode and cathode at 0.1 MPa without pre-humidification.

**MEA fabrication.** Gas diffusion electrodes are prepared from PtCo/C catalysts, with a catalyst loading of 0.9 mg Pt/cm<sup>2</sup>, provided by DPS. The MEAs are prepared by sandwiching the doped membranes between two pieces of gas diffusion electrodes and hot-pressed at 100 °C under a pressure of 0.06 t/cm<sup>2</sup> (of the electrode) for 3 min. For typical MEAs, the size of the acid-doped membrane is 8\*8 cm<sup>2</sup> and the active area of electrodes is 5\*5 cm<sup>2</sup>. To reinforce the membrane two pieces of protective polysulfide films of 8\*8 cm<sup>2</sup> size, with an opening of 21 cm<sup>2</sup> active area in the middle, are placed between the electrodes and the membrane.

**Assembly.** The single cell is assembled from an MEA, 2 PTFE gaskets with a thickness of 150 µm, 2 graphite flow plates with gas channels, and 2 aluminium endplates. The cell was tightened with 2 N on 8 bolts. The assembled cell is first checked with leakage. The cell is filled with pressurized air to a relative pressure of 100 mBar and then closes the cell. If the pressure release rate is larger than 3 mBar/sec the cell should be reassembled otherwise the cell passes the leakage test.

**Recording polarization curves.** The polarization curve (I-V curve) measurements are carried out to evaluate the cell performance typically in a temperature range of 120°C-200 °C. For the present project most of the I-V curves are recorded at 160 °C with a constant stoichiometry of 1.5 for hydrogen and 2.5 for air, which means for each current step the gas flow rates are accordingly adjusted, as shown in Table 3.1. The voltage data are recorded by varying current from low to high values. The gas flow rates are varying to the corresponding current as followed.

**Start-up procedure.** After assembling the cell is connected to the fuel cell test house with tubes and wires. The cell is first heated to 120°C, then both fuel and air flows are started with flow rates corresponding to  $\lambda_{H_2} / \lambda_{Air} = 1.5/2.5$  for current density of 0.4 A cm<sup>-2</sup>. After checking the OCV (above 900 mV) the cell is further heated to the measuring temperature e.g. 160 °C. A constant current e.g. 8.4 A is then applied and the V-t data are recorded with sampling

frequency of every 60 sec. Polarization curves are recorded at specified time points.

*Table 3.1 H<sub>2</sub> and air flow rate for measurements of I-V curves at fixed stoichiometries.*

<b>Current density</b> <b>A cm<sup>-2</sup></b>	<b>Current (active area 21 cm<sup>2</sup>)</b> <b>A</b>	<b>H<sub>2</sub> flow (<math>\lambda_{H_2}=1.5</math>)</b> <b>ml min<sup>-1</sup></b>	<b>Air flow (<math>\lambda_{Air}=2.5</math>)</b> <b>ml min<sup>-1</sup></b>
0	0	0	0
0.01	0.21	2.4	9.5
0.02	0.42	4.8	19
0.03	0.63	7.2	28.5
0.05	1.05	12	47.5
0.08	1.68	19.2	76
0.1	2.1	24	95
0.2	4.2	48	190
0.3	6.3	72	285
0.4	8.4	96	380
0.5	10.5	120	475
0.6	12.6	144	570
0.8	16.8	192	760
0.9	18.9	216	855
1	21	240	950

### 3.7.2 1 cm<sup>2</sup> cell

Some membranes are prepared on small sizes and the fuel cell tests are hence conducted with 1 cm<sup>2</sup> cells. The cell assembling procedure is the same as described above. The MEA is not pre-hot pressed but directly assembled in the fuel cell hardware tightening to standard compression of 1.5 N on 4 bolts. The cell is prechecked by electrochemical impedance spectroscopy (EIS) to see if the ohmic resistance of the cell at room temperature is less than 1000 m $\Omega$ . The cell is then heated to the desired temperature e.g. 160 °C under no gas feed or current drawing. As soon as the temperature reaches 160°C, hydrogen at 30 ml/min and air at 100 ml/min are supplied to the anode and cathode, respectively. These flow rates are fixed during the following measurements, which means the I-V curves are recorded with varying stoichiometries. All electrochemical measurements are made using Potentiostats (VersaSTAT 4). The cell is activated with a constant current density of 0.2 A/cm<sup>2</sup> while the cell voltage is recorded with a sampling rate of every 60 s. The I-V data are recorded at specific times from linear scan voltammetry (LSV) with a scan range from -0.9 V to 0 V (vs. OCV) at a scan rate of 0.002 Vs<sup>-1</sup>.

### 3.7.3 Electrochemical impedance spectroscopy

The resistance of fuel cells is evaluated by EIS. Impedance can be defined as a complex resistance [237]. Impedance data is measured by recording the response by applying a small excitation. If a sinusoidal potential signal

$$E(t) = E_0 \sin(\omega t) \quad (3.7)$$

is applied as excitation, the response to this potential will be a current response:

$$I(t) = I_0 \sin(\omega t + \varphi) \quad (3.8)$$

Therefore, analogous to Ohm's Law, the impedance is defined as the complex number  $Z$  with the expression:

$$Z = \frac{E(t)}{I(t)} = \frac{E_0 \sin(\omega t)}{I_0 \sin(\omega t + \varphi)} \quad (3.9)$$

Based on Euler's relationship:

$$\exp(j\varphi) = \cos\varphi + j\sin\varphi \quad (3.10)$$

$Z$  can be further defined as the expression:

$$Z = Z_0 \exp(j\varphi) = Z_0(\cos\varphi + j\sin\varphi) = Z_R + jZ_{Im} \quad (3.11)$$

where  $Z_R$  is the real part and  $Z_{Im}$  is the imaginary part.  $j$  is defined as  $j^2 = -1$ .

Presentation of impedance spectra is usually done in a Nyquist plot, which puts the real impedance on the X-axis and the negative imaginary counterpart in the Y-axis.

A typical Nyquist plot of an EIS spectrum for a working HT-PEMFC at 160 °C is shown in Figure 3.5. The long tail coming from the value of  $Z_{Im}$  of the positive value is the inductance coming from the wirings. The plot crosses the real axis (the primary axis) at the lowest value at  $Z_{Im} = 0$ . This intercept gives the series ohmic resistance, typically with the main contribution from the electrolyte resistance  $R_{electrolyte}$ . Other contributions to this value may include resistances of the electrodes, flow plates, and the interfacial contact between the flow plates and electrodes or other parts of the hardware. These contributions of the ohmic resistance are sometimes an issue in determining the through-plane conductivity of the membrane electrolyte, which in the present project is in thickness of 20-80  $\mu\text{m}$ , corresponding to an overall ohmic resistance of 50-200 m $\Omega$ . This contact resistance in fuel cells depends also on clamping pressure, temperature, and surface treatments.

The contact resistance of each pair of flow plates is usually measured before the fuel cell assembling by impedance measurement. For doing so, the cell is assembled as usual but using a Papiex® flexible graphite sheet in place of the MEA to ensure the contact between GDLs and flow plates. The cell was clumped with standard pressure. The measured resistance from this cell assembly includes the bulk resistances of two flow plates and contact resistances between current collectors.

Other resistances from the EIS are illustrated in Figure 3.5 including the anode activation (HOR), cathode activation (ORR), and mass transfer resistances. As the present study is focused on the membrane, no further efforts are made to explore the determination and explanation of these resistances.

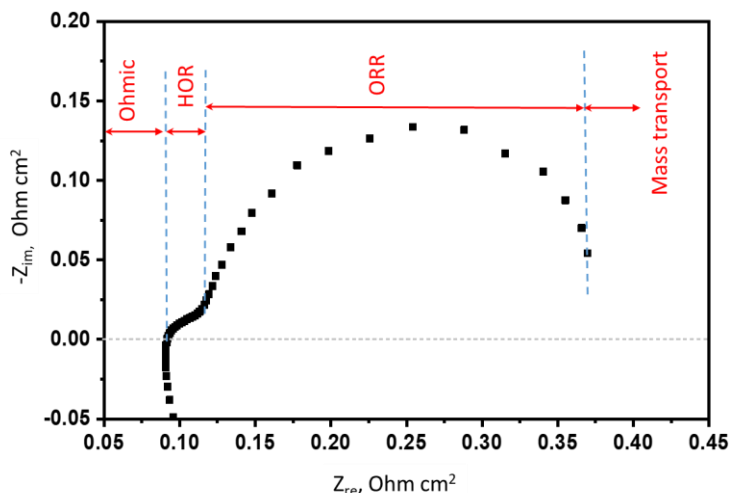


Figure 3.5 Nyquist plot of EIS spectra for a HT-PEMFC operating at 160 °C, current density of 600 mA cm<sup>-2</sup>, active area 1 cm<sup>2</sup>.

### 3.7.4 Hydrogen crossover

Hydrogen crossover through the membrane is determined by an electrochemical method similar to that described in literature [238, 239]. The membrane is assembled in a standard test cell with hydrogen flowing on one side of the membrane and nitrogen on the other. The hydrogen electrode acts as the reference and counter electrode and the nitrogen electrode as the working (and sensor) electrode. Dry H<sub>2</sub> and N<sub>2</sub> are fed without additional humidification under ambient pressure with a flow rate of 30 ml min<sup>-1</sup> and 400 ml min<sup>-1</sup> on the 1 cm<sup>2</sup> cell. The working electrode potential is first swept between 0.1-1.1 V at a rate of 50 mV s<sup>-1</sup> until a stable voltammogram is achieved, typically for 2 hours in order to ensure the removal of trace oxygen. The working electrode potential is finally swept from 0.1 V to 0.4 V at a scan rate of 5 mV s<sup>-1</sup> and hold at 0.4 V for 600-1000 s. The resulting chronoamperometric (i-t) curve shows a stable oxidation current due to hydrogen permeation through the membrane.

The hydrogen permeability is calculated from the oxidation current using the following formula:

$$\kappa = \frac{i \delta}{nF p} \quad (3.12)$$

where  $\kappa$  is the permeability coefficient in mol cm<sup>-1</sup> s<sup>-1</sup> bar<sup>-1</sup>,  $i$  is the measured oxidation current in A cm<sup>-2</sup>,  $n = 2$  is the mole number of electrons involved in oxidation of each mole hydrogen;  $F = 86485$  C/mol e<sup>-</sup> is the Faraday constant;  $\delta$  is the thickness of the membrane in cm;  $p$  is the partial pressure of hydrogen in the feeding stream in bar.



# CHAPTER 4

## Thin membranes

---

### Summary of the chapter

Exploration to use thin membranes in HT-PEMFCs is justified. Membranes in three different thicknesses are prepared, doped and characterized including fuel cell test. At normal acid doping levels the PBI membranes of 10-20  $\mu\text{m}$  are mechanically strong for MEA fabrication. Good fuel cell performance is achieved due to the reduced ohmic resistance and the loss of open circuit voltage due to the fuel crossover does not seem a critical issue. The low acid content of thin membranes is limiting the performance and likely durability of fuel cells using the conventional MEA fabrication method. Extra acid is suggested to add to the catalyst layer, which is however not evaluated in the work.

### 4.1 Introduction

PBI membranes are fabricated in two methods 1) direct casting of a polymer solution in polyphosphoric acid [115] and 2) post-doping of a pre-cast PBI membrane in a phosphoric solution [49]. The present thesis focuses on the second type of acid-doped PBI membrane.

It has long been rationalized that, high fuel cell performance can be achieved by optimizing the ratio of membrane thickness ( $\delta$ , cm) and ionic conductivity ( $\sigma$ ,  $\text{S cm}^{-1}$ ) i.e. the area specific resistance ASR ( $\Omega\text{cm}^2$ ). In other words, with a constant or slightly lower conductivity, a thinner membrane will exhibit lower ASR and therefore better fuel cell performance. A critical issue for thinner membranes is the weak mechanical strength which can be improved by, for example, porous PTFE reinforcement, as demonstrated by the commercial Gore-select<sup>®</sup>) membranes, as listed in Table 4.1.

The PA-doped PBI membrane is also listed in the table with varied molecular weight (33-97 kDa) and acid doping levels (6.4-11.5) at a specified temperature of 130 °C. The doping acid creates proton conductivity, but at the same time, it softens the polymer membrane making the membrane difficult to handle and less durable during the fuel cell operation. Compared to PFSA membranes, PA-doped PBI membranes are mechanically weak. As a result, acid-doped PBI membranes of 80-100  $\mu\text{m}$  thickness, as prepared from dry membranes of 40-50  $\mu\text{m}$  thickness are typically used for the post doped membranes. The thickness is even larger for the direct cast membranes. The use of thick membranes is mainly responsible for the large ohmic loss and poor power performance of HT-MEA.

Table 4.1 A set of parameters of Nafion, Nafion/PTFE composite and PA-doped PBI membranes at specified temperatures

Membrane	Thickness $\mu\text{m}$	Conductivity $\text{S cm}^{-1}$	ASR $\Omega \text{ cm}^2$	Tensile strength $\text{MPa}$	Ref.
Nafion-117 (25°C,100%RH)	200	0.14	0.143	15.9	[240]
Nafion-211 (60°C,100%RH)	25	0.09	0.028	21.3	[240]
Nafion/PTFE (25°C,100%RH)	20	0.05	0.040	32.5	[240]
Nafion/PTFE (60°C,100%RH)	14	0.06	0.023	34.1	[240]
PBI-PA (33kDa, ADL6.4, 130°C)	100	0.045 (140°C)	0.222	3.6	[150]
PBI-PA (33kDa, ADL11.5, 130°C)	100	0.11 (140°C)	0.091	0.6	[150]
PBI-PA (78-94kDa, ADL10.9, 130°C)	100	0.115	0.087	7.2	[65]

For PBI membranes, high molecular weight polymers have been synthesized through these years [52]. At the same time, higher acid doping levels have been steadily increased from 5-6 for the early year low molecular weight PBI [112] to the current trend of 10-12 for high MW polymers [54]. As a result of the increasing ADL, the membrane conductivity has increased from 0.05 to about  $0.10 \text{ S cm}^{-1}$ . The high ADL is inevitably accompanied by a decrease of mechanical strength of the membranes, though this has been significantly compromised by use of high MW polymers. Other measures to achieve the trade-off between proton conductivity and mechanical strength including polymer blends [135], polymer composites [63], crosslinked copolymers [159, 241].

Early attempts were made to develop PBI-PFTE composite using porous PFTE fiber substrates impregnated with PFSA as coupling agent. Lin et al. [242] reported thin membranes of 17-22  $\mu\text{m}$  with improved mechanical properties, however, fuel cells using this type of membranes exhibit open circuit voltages lower than 0.85 V [243], indicating the fuel gas crossover issue of the membranes. Yuk et al. [244] prepared a thin polymer layer supported on a gas diffusion electrode. The authors used a 1:1 blend of PBI and poly(ethylene glycol) (PEG) in a doped thickness of 35  $\mu\text{m}$ , showing an OCV around 1.0 V. Yi et al. [153] synthesized ether-containing PBI-O and cast membranes of 20  $\mu\text{m}$  thick. After doping in phosphoric acid at 120°C, an ADL of around 11 was achieved while the membrane thickness was increased to 40  $\mu\text{m}$ . The fuel cell showed an OCV of above 1.0 V for about 100 hours.

It is interesting to notice that thinner PBI membranes have been suggested for use in the vanadium redox flow battery (VRFB) [245]. The VRFB is a device that is structurally similar to fuel cells but operating aqueous solutions containing vanadium salts of different oxidation states, instead of hydrogen and air. The electrolyte separator is an ion-conducting membrane allowing for passage of proton, sulfate and other ions. Nafion membranes are widely used due to the high oxidative stability and proton conductivity, but they suffer from high vanadium cation permeability. PBI-based membranes are also suggested for VRFBs with low vanadium permeability and better performance [246]. Noh et al. [247] investigated PBI membranes of 15,

25 and 35  $\mu\text{m}$  thicknesses showing the beneficial effect of thin membranes on the voltage and current efficiencies.

In this chapter, the thin PBI membranes with thicknesses of 40, 20, and 10  $\mu\text{m}$  are prepared using a high molecular weight PBI (58kDa). The membranes are doped and explored for use in fuel cells.

## 4.2 Experimental

### 4.2.1 Membrane casting

The membrane casting was started from an initial 8.6 wt% PBI solution in DMAc, kindly supplied by Danish Power Systems. The polymer has an average molecular weight of  $M_w = 58000$ , determined by the viscosity measurement, as described elsewhere [129]. The polymer solution was first diluted to concentrations of 4.3%, and 2.5% so that membranes with varied dry thickness of 20 and 10  $\mu\text{m}$ , respectively, would be prepared using the same volume of the solution. 60 ml of each solution was poured onto a rectangle glass plate with confined area of 41 cm x 26 cm and dried in an oven by slow heating to 120 °C. The obtained solid membrane was then washed with hot (ca. 90 °C) water for about 30 min, followed by further drying at 120 °C for 2 hours. A reference membrane with a dry thickness of 40  $\mu\text{m}$  before acid doping was supplied by DPS.

### 4.2.2 Acid doping and tensile strength measurement

Dry membranes were immersed in 85% phosphoric acid at room temperature for at least 24 h. The membranes were then taken out of the acid solution. Excess acid was removed and thus doped membranes were stored in plastic bags and placed in a cabinet with humidity of 21-23%. To vary the acid doping level, phosphoric acid of low concentrations e.g. 70 wt% is used, also at room temperature, to achieve a low acid doping level. To achieve high acid doping levels, the same 85% PA was used but the acid doping temperature was slightly increased to 35 °C-48 °C. The tensile strength was measured using the protocol described in Chapter 3 at room temperature and ambient humidity.

### 4.2.3 MEA fabrication and fuel cell tests

Details on MEA fabrication are given in Section 3.7.1. The major part of the fuel cell test was carried out at Danish Power Systems using cells with active area of 21  $\text{cm}^2$  by following the test procedure described in Chapter 3. In brief, the fuel cell was activated at a constant current density of 0.4  $\text{A cm}^{-2}$  and 160 °C for about 170 hours ( 7 days) before the polarization curves are recorded with dry hydrogen and air at stoichiometries of 1.5 and 2.5, respectively. The I-V curves were obtained at steady state measurements. The voltage was recorded after 2 mins load at the current density of 0, 0.01, 0.02, 0.03, 0.05, 0.08, 0.1, 0.2, 0.3, 0.4, 0.5, 0.6, 0.7, 0.8, 0.9, and 1  $\text{A cm}^{-2}$ .

Part of the fuel cell test was conducted at DTU Energy labs with the 1  $\text{cm}^2$  size cell for

measuring the H<sub>2</sub> crossover and impedance spectra. In brief, the I-V curves were recorded by slow potential scanning of rate 2 mV/s. The hydrogen crossover was determined for membranes of different thicknesses and varied acid doping levels by an electrochemical approach [238, 239]. With flow rates of 30 ml min<sup>-1</sup> for H<sub>2</sub> and 400 ml min<sup>-1</sup> for N<sub>2</sub> the working (the N<sub>2</sub> side) cell was stabilized under cyclic voltammetry between 0.1 and 1.1 V at a rate of 50 mV s<sup>-1</sup> for about 2 hours. The working (N<sub>2</sub> side) electrode potential was then swept from 0.1 V to 0.4 V at a scan rate of 5 mV s<sup>-1</sup> followed by holding at 0.4 V while the resulting current was recorded for a period of 600 s.

## 4.3 Results and discussion

### 4.3.1 Preparation and acid doping of thin membranes

The prepared membranes are in three thicknesses about 40, 20 and 10 μm. Flat and transparent membranes were obtained after drying and washing, see the sample photos in Figure 4.1. It can be seen that the color of membranes is getting darker with the increase of thickness. The obtained pristine membranes are hereafter referred to as PBI-thickness, e.g. PBI-10 means a pristine PBI membrane with a dry thickness around 10 μm before doping, the height gauge measured value is shown in Table 4.2.

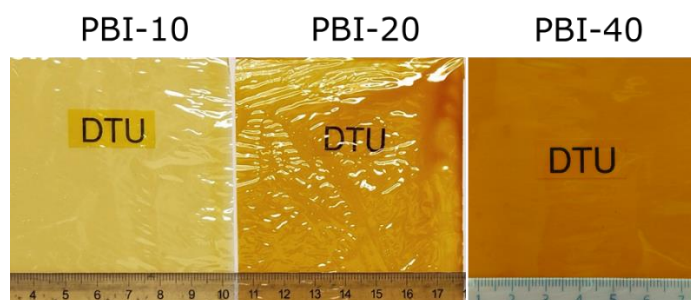
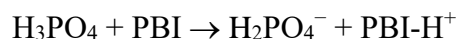


Figure 4.1 Photo of pure membranes.

The membranes were then doped with phosphoric acid at room temperature for a few days to achieve an equilibrium acid doping level (ADL). PBI contains functional basic sites in the imidazole ring in the polymer backbone and hence has a high affinity towards water and acids. By immersing a dry PBI membrane in a phosphoric acid aqueous solution, the acid-base interaction leads to protonation of the polymer:



The acid-base chemistry indicates that 2 molecules of the acid will be bound to the polymer. The acid uptake of the polymer from the doping is, however, higher than an ADL of 2, likely due to the mechanism of physical adsorption. The process has been described by a multilayer adsorption model [248]. Using 85 wt% H<sub>3</sub>PO<sub>4</sub> solution at room temperature, the equilibrium ADL for three membrane samples was about 11.6 - 12.2 mol H<sub>3</sub>PO<sub>4</sub> per polymer repeat unit (PRU), as also listed in Table 4.2. This number is in good agreement with the literature data [249] for polymers of similar molecular weights.

The doping acid results in membrane swelling in all three directions. The thickness swelling of

the membranes is increasing from 100% to 120% when the dry membrane thickness is reduced from 40 to 10  $\mu\text{m}$  while the area swelling of membranes decreased from 51 to 43% (see Table 4.2). The difference in the thickness and area swellings shows the anisotropic nature of the acid swelling and hence the effect of membrane thickness.

This membrane swelling leads to a significant separation of the polymer backbones. As a result, the membrane exhibits a proton conductivity and, at the same time, a decrease in the mechanical strength and an increase in the gas permeability of the acid-doped membranes, as to be discussed below.

*Table 4.2 Summary of acid doping level, swelling, and mechanical data at room temperature.*

<b>Membranes</b>	<b>PBI-40- ADL 12.2</b>	<b>PBI-20- ADL 11.6</b>	<b>PBI-10- ADL 12</b>
Thickness ( $\mu\text{m}$ , dry)	40	18.5	11
Thickness ( $\mu\text{m}$ , doped)	80	40	24
Thickness swelling (%)	100	116.3	120.5
Area swelling (%)	51	50.6	43.3
ADL* (mol $\text{H}_3\text{PO}_4$ /PRU)	12.2	11.6	12
Elongation at break (%)**	121-149	153-166	208-209
Tensile Strength at break (Mpa)**	18.2-24.6	19.3-21.5	28.5-28.6
Young's Modulus (Mpa)**	62.7-65.2	38.1-47.2	30.2-35.4

\* Doped in 85 wt%  $\text{H}_3\text{PO}_4$  at room temperature

\*\* Data obtained from three duplicate samples.

### 4.3.2 Mechanical strength

From the tensile measurements three parameters are obtained: the tensile strength at break, elongation at break and tensile modulus, as indicated in Figure 4.2. In general, the reproducibility of the tensile strength and elongation is poor, depending on how perfect the prepared samples are. The tensile modulus is more reliable with respect to reproducibility.

The tensile strength of a membrane is defined as the ratio of the force to the cross-sectional area of the sample, with a unit of Newton per square meter or pascal (Pa). The tensile modulus, as a ratio of tensile stress to elastic strain (elongation, %), indicates the rigidity of the membrane. Both tensile strength and modulus are relative to the cross-sectional area of the membrane samples. Theoretically both parameters are intrinsic properties of a membrane, the value of which will not change with the membrane thickness. In fact, the number of defects in the sample may change with the sample thickness. In membranes of varied thicknesses from 40 to 20 or 10  $\mu\text{m}$  at the same strain rate, as used in the present work, do result in changes in the tensile strength and modulus. This is observed as seen in Figure 4.2. The results are listed

in Table 4.2. The tensile strength at break of samples are 18.2-24.6 Mpa for PBI-40, 19.3-21.5 MPa for PBI-20, and 28.5-28.6 MPa for PBI-10. The Young's modulus of PBI-40, PBI-20, PBI-10 are 62.7-65.2 MPa, 38.1-47.2 MPa, and 35.4-38.7 MPa, respectively, showing a decrease of Young's modulus with the decrease of sample thickness.

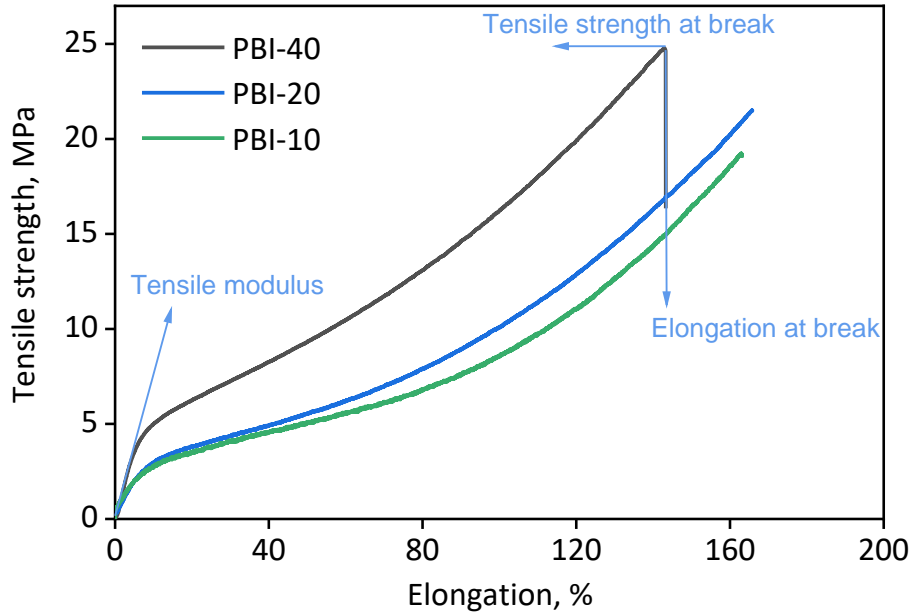


Figure 4.2 Representative stress-strain curves of membranes with different thicknesses at room temperature and atmospheric humidity.

#### 4.3.3 Analysis of I-V data

First of all, the flow plate and contact resistance of the fuel cell hardware was often measured by EIS. The values are in general in a range of 3.0-6.8 mΩ and corrected for individual cells in the measured I-V data.

Before presentation of polarization curves the analytic method is first described in this section. The following equation has been shown to give very good fits to experimentally obtained polarization curves and is thus a simple tool to separate contributions from the ohmic, activation and mass transport losses.

$$E_{Cell} = E_{rev} - h_{ORR} - i\dot{a}R - h_{mt} \quad (4.1)$$

Here  $E_{rev}$  is the reversible cell voltage,  $\sum R$  is the sum of ohmic resistance,  $\eta_{ORR}$  is the cathode activation loss and  $\eta_{mt}$  is the mass transport loss. The ohmic resistance includes the electronic and ionic conducting resistances originating from the electrolyte membrane, electrode substrate and catalyst layer, bipolar plates and leading wires, among which the membrane resistance is the predominant contribution. The anode activation loss, which is often assumed to be negligible, has also ohmic behavior and can in fact be included in the total ohmic resistance. The reversible cell voltage is a function of temperature and pressures of hydrogen and oxygen and can be expressed as [250]:

$$E_{rev} = 1.23 - 0.9 \times 10^{-3}(T - 298) + \frac{2.303 RT}{2F} \log \left[ \frac{P_{H_2} \cdot P_{O_2}^{1/2}}{P_{H_2O}} \right] \quad (4.2)$$

Under standard conditions that  $P_{H_2} = P_{H_2O} = P_{O_2} = 1.0$  atm the standard reversible voltage can be calculated to be 1.108 V at 160 °C. For a practical PBI cell, the feeding dry air has  $P_{O_2} = 0.21$  atm which leads to a voltage of 0.03 V lower. For low-temperature PEMFCs the feeding hydrogen and air are often saturated with water, allowing for calculation of the cell reversible voltage. In PBI-based cells, hydrogen is usually fed without humidification except for the case where reformat hydrogen containing water is used. In the present work the water vapor pressure is unknown and therefore the reversible cell voltage ( $E_{rev}$ ) is poorly defined. In the following analysis an approximate value of  $E_{rev} = 1.1$  V is arbitrarily used for the cell temperature of 160°C.

The cathode overpotential is expressed by the Tafel equation:

$$h_{ORR} = b \log \left( \frac{i}{i_0} \right) = a + b \cdot \log(i) \quad (4.3)$$

where  $b$  is the Tafel slope and  $i^0$  the exchange current density.

The concentration or mass transport overpotential can be expressed as

$$h_{mt} = c \log \left( 1 - \frac{i}{i_L} \right) \quad (4.4)$$

where  $i_L$  is the limiting current density which is difficult to measure and the estimated value may lead to errors in the mass transport overpotential.

Taking equations (4.3 and 4.4) into (4.1) one has

$$E_{Cell} = A - iR - b \log(i - i_x) - c \log \left( 1 - \frac{i}{i_L} \right) \quad (4.5)$$

Here the constant  $A$  is different from the cell open circuit voltage as it has the form of:

$$A = E_{rev} - b \log(i^0) \quad (4.6)$$

Using  $i$ ,  $\log(i)$  and  $\log(1-i/i_L)$  as independent variables, a multiple linear regression will give the estimated values of constant  $A$  (in V), total cell resistance  $R$  (in  $\Omega \cdot \text{cm}^2$ ), Tafel slope  $b$  (in V/dec) and the mass transport coefficient  $c$  (in V).

In the following a PBI cell at 160°C is taken as an example. The membrane of 20  $\mu\text{m}$  thickness has an acid doping level of 13.3 mol  $\text{H}_3\text{PO}_4/\text{PRU}$ . The cells were tested in DTU lab, the hydrogen and air flow kept at 30 ml/min and 100 ml/min during linear scan from -0.9V to 0V (vs. OCV), the scan rate is 0.002  $\text{V s}^{-1}$ .

The limiting current was assumed to be 1.49  $\text{A cm}^{-2}$ . With this limiting current as input, the obtained coefficient for the mass transport loss is 0.038 V, which can be translated to a voltage loss of 16 mV at the current density of 1.0  $\text{A cm}^{-2}$ .

The obtained Tafel slope is 0.101 V/dec, which is typical for PBI-based fuel cells [54]. The measured open circuit voltage is 0.95 V, as also shown in the figure. Compared to the reversible cell voltage of e.g. 1.1 V, there is an OCV loss of 0.15 V. This will be discussed in connection to the hydrogen crossover in Section 4.3.7 but here is attributed to the activation loss. The total activation loss is in all 410 mV at current density of 1.0  $\text{A cm}^{-2}$ .

The total ohmic resistance is 0.149  $\Omega \text{cm}^2$ . The physical meaning of this area specific resistance is the ohmic resistance loss of 0.149 V at current density of 1.0  $\text{A/cm}^2$ . Using the membrane thickness of 40  $\mu\text{m}$ , this resistance corresponds to a conductivity of 0.027  $\text{S/cm}$ , which is

slightly lower than the reported values for the membranes of similar acid doping levels at this temperature [251, 252].

The analytic results are shown in Figure 4.3. In the following sections and other chapters, the measured I-V data are treated in the similar way and parameters of the Tafel slope, total ohmic resistance and mass transport coefficient are presented for comparison.

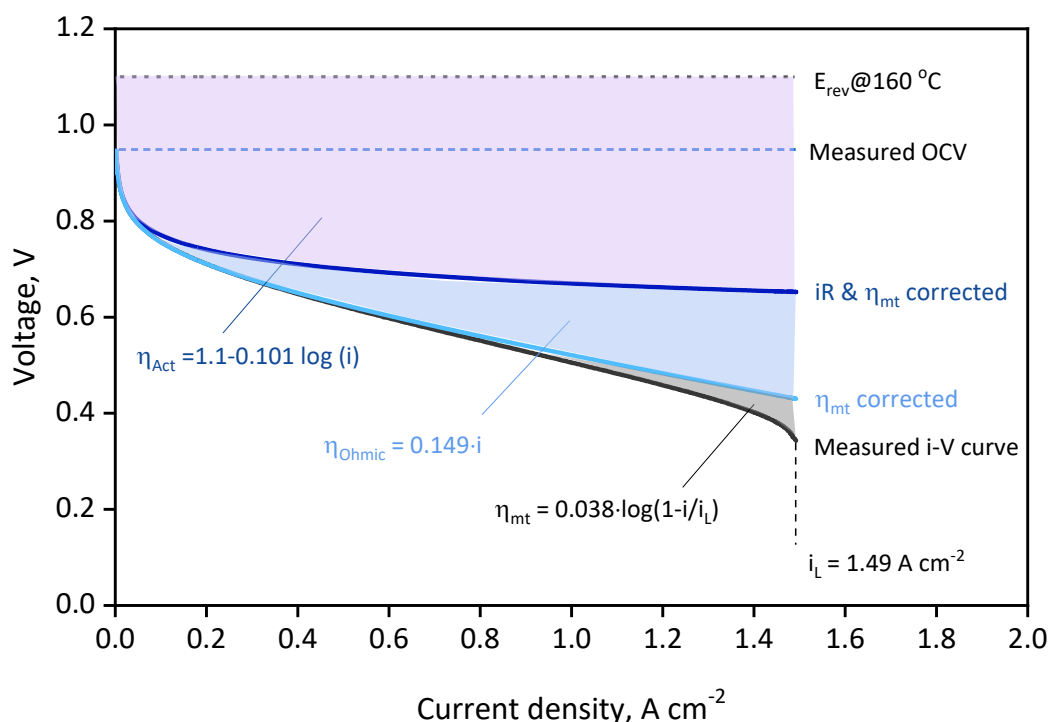


Figure 4.3 Polarization curve of a PBI cell obtained by linear scan voltammetry from  $-0.9V-0V$  (vs. OCV) at scan rate of  $0.002 V s^{-1}$ . Contributions of activation, ohmic and mass transport losses were obtained from the linear regression. The membrane was PBI-20-ADL13.3. The active electrode area was  $1 cm^2$ . The cell was operating at temperature of  $160 ^\circ C$  with  $H_2$   $30 ml min^{-1}$  and Air  $100 ml min^{-1}$ .

#### 4.3.4 Break-in under constant current

The break-in or activation of a PBI fuel cell is the initial period of operation needed to reach a stable performance, ensuring reproducibility and comparability of results [253]. The processes taking place during the break-in are assumed to be the phosphoric acid redistribution within the MEA. As a result, the phosphoric acid originating from the membrane wets the catalyst layer and enhances the electrode kinetics and therefore the fuel cell performance. The typical procedure of the break-in is by galvanostatic operation at a constant temperature and current density of e.g.  $0.2 A cm^{-2}$  for a period of a few hundred hours [254, 255]. The acid is driven into the catalyst layer by the capillary force and therefore depending on the microporous structures of the carbon.

In the present work, the break-in was carried out at  $160 ^\circ C$  and  $0.4 A cm^{-2}$  for 180 hours. A set of the voltage-time curves are shown in Figure 4.4 by following the start-up procedure (DPS)

mentioned in Section 3.8. The initial performance of the three cells was 0.607 V (PBI-40), 0.62 V (PBI-20), and 0.63 V (PBI-10). The noisy signals were due to recording the polarization data. A steady increase of the cell voltage was observed in the first 80 hours, followed by a stable value for all three cells.

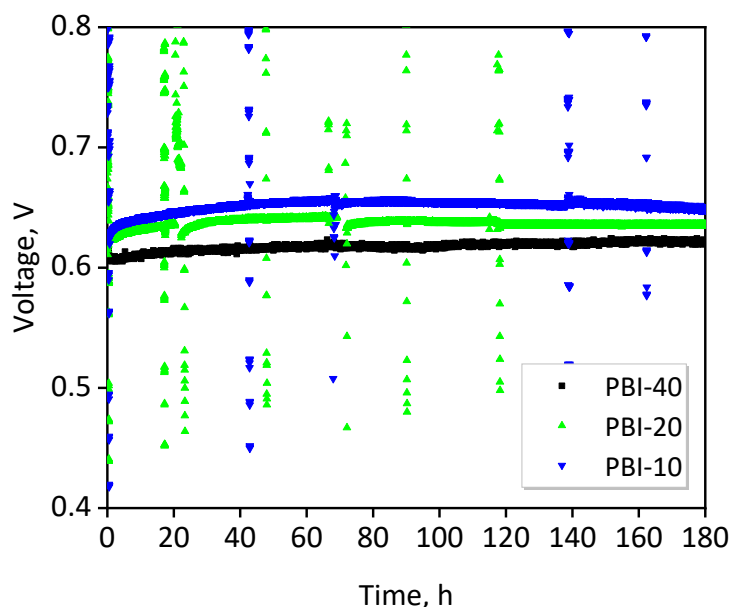


Figure 4.4 Cell voltages as a function of time for MEAs. The cells were operated at 160 °C, current density of 400 mA cm<sup>-2</sup> with ambient pressure hydrogen and air. The stoichiometry was  $\lambda_{\text{H}_2} = 1.5$  and  $\lambda_{\text{Air}} = 2.5$ .

Polarization curves of the MEA to be presented in this chapter were all recorded after that the fuel cells have operated at a constant current load of 400 mA cm<sup>-2</sup> for 168 h (7 day). The I-V polarization results recorded at the first (day 0), second (day 2), sixth (day 6) and seventh (day 7) are shown as symbols in Figure 4.5a. The measurements were made for a PBI cell with a membrane of 10  $\mu\text{m}$  thick at acid doping level of 13.3 mol H<sub>3</sub>PO<sub>4</sub> per polymer repeat unit. The linear regression analysis gives *iR*-free polarization curves as dotted lines, showing a steady improvement in the ORR kinetics during the break-in period as the catalysts are slowly wetted by the adsorbed acid. The small change in the *iR*-free curves from day 6 to day 7 seems denoting the ending of the break-in. As a result of the acid transferring from the membrane to the electrode catalyst layer, the acid content of the membrane decreases, and the cell ohmic resistance is accordingly increasing, as shown in Figure 4.5b. Also indicated in the figure are the fitted area specific resistance, which is increased from 0.043 (day 0) to 0.105  $\Omega$  cm<sup>2</sup> (day 7). Taking the thickness of the doped membrane of 24  $\mu\text{m}$ , these resistances can be translated into the membrane conductivity of 0.056 and 0.023 S cm<sup>-2</sup>. This decrease in conductivity is significant because of the small thickness of the PBI-10 membrane.

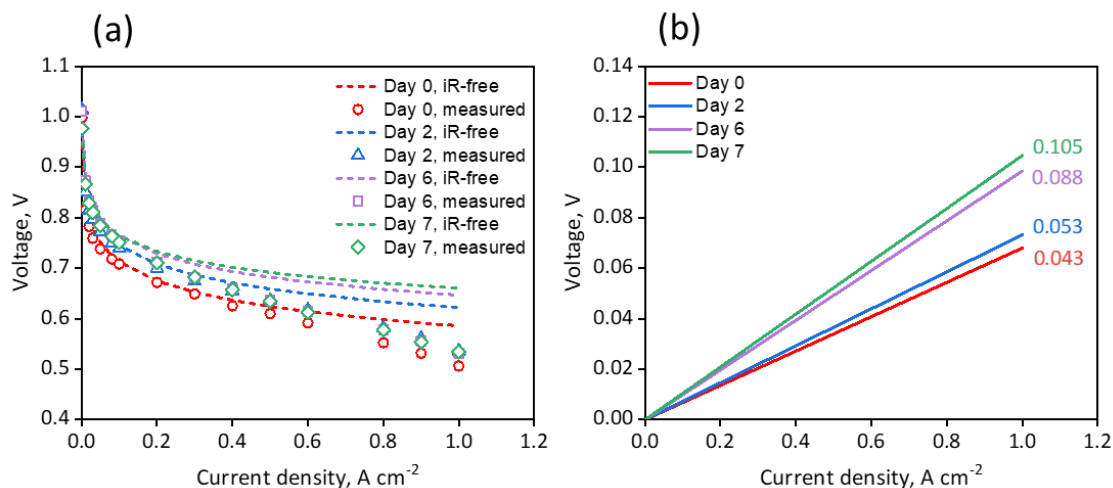


Figure 4.5 (a) Polarization data (symbols) and the *iR*-free fitting curves and (b) the fitted area specific resistance of PBI-10 operating at 160 °C, 1 bara  $H_2$  and air with a gas stoichiometry of  $\lambda_{H_2}/\lambda_{Air} = 1.5/2.5$ . The numbers indicated in (b) are the fitted area specific resistance in  $\Omega\text{ cm}^2$ .

#### 4.3.5 Polarization curves of varied membrane thicknesses

Polarization curves of the MEA based on membranes of different thicknesses are shown in Figure 4.6 (solid lines). The fuel cell performance is often defined by a single point, for example, a cell voltage at a rated current density. The commercial Dapozol<sup>®</sup> MEAs are reported to exhibit a voltage of 0.67 V at 0.2 A  $\text{cm}^{-2}$  when operating under ambient pressure dry hydrogen and air, with a total electrode platinum loading of 1.5 mgPt  $\text{cm}^{-2}$  [256]. The peak power is also used to specify the single cell performance e.g. the commercial Celtec P1000 MEAs was reported to be 0.42 W  $\text{cm}^{-2}$  at 1.1 A  $\text{cm}^{-2}$  [257]. The reference MEA using 40  $\mu\text{m}$  thick PBI membranes at an acid doping level of 12.2 has a performance comparable to those reported in literature, i.e. 0.689 V at 0.2 A  $\text{cm}^{-2}$  and 0.414 W  $\text{cm}^{-2}$  at 1.0 A  $\text{cm}^{-2}$ .

The open circuit voltage of this reference membrane based MEAs is always around 1.0 V. When thinner membranes are used, the OCV is slightly lower (0.96-0.98 V), as seen from Table 4.3, indicating the increased hydrogen crossover through the thinner membranes, as to be shown in Section 4.3.8 (permeability). The overall fuel cell performance is improved, e.g. the voltage at 0.2 A  $\text{cm}^{-2}$  is 0.70 and 0.71 V for the membranes of 20  $\mu\text{m}$  and 10  $\mu\text{m}$  thick membranes, respectively and the corresponding power density at 1 A  $\text{cm}^{-2}$  is increased from 0.414 W  $\text{cm}^{-2}$  (40  $\mu\text{m}$ ) to 500 W  $\text{cm}^{-2}$  (20  $\mu\text{m}$ ) and 525 W  $\text{cm}^{-2}$  (10  $\mu\text{m}$ ).

It should be remarked that in the measured current densities of up to 1.0 A  $\text{cm}^{-2}$  the I-V curves exhibit a small mass transport loss, as discussed above. The linear regression analysis for the ohmic and activation losses gives results as listed in Table 4.3 and presented in Figure 4.6.

When these ohmic resistances are compensated, the obtained *iR*-free polarization curves well coincide for three fuel cells with varied membrane thicknesses. This is not a surprise because the electrodes used are the same for these cells. It seems that the amount of acid transferred from the membrane to the catalyst layer of the electrodes is more or less the same so that the electrode (ORR) performance is identical for these cells.

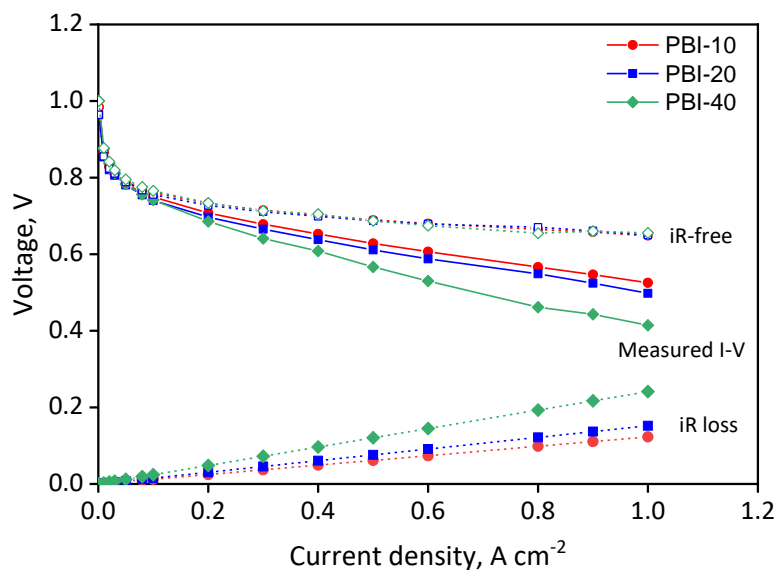


Figure 4.6 Polarization curve at 160 °C and 1 bar  $H_2$  and air on the anode and cathode respectively together with the power curve, gas flow  $\lambda_{H_2}/\lambda_{Air} = 1.5/2.5$ .

Table 4.3 Summary of cell performance at 160 °C with membranes of different thicknesses.

Properties	PBI-40-ADL 12.2	PBI-20-ADL 11.6	PBI-10-ADL12
Thickness ( $\mu\text{m}$ , doped)	80	40	24
Cell voltage (V):			
Open circuit	1.000	0.958	0.977
at 0.2 A/cm <sup>2</sup>	0.686	0.697	0.708
at 0.4 A/cm <sup>2</sup>	0.61	0.64	0.66
Power density (W/cm <sup>2</sup> ):			
at 1.0 A/cm <sup>2</sup>	0.414	0.498	0.525
Area specific resistance ( $\Omega\text{cm}^2$ )	0.225	0.136	0.107
Tafel slope (V/dec)	0.112	0.101	0.102

The total acid content on the MEAs, on the other hand, is depending on the membrane thickness or volume when the acid doping level is nearly the same. It is therefore that the remaining acid content is smaller for thin membranes. This will be further discussed in Section 4.3.6. The area specific resistance of the 40  $\mu\text{m}$  reference cell ( $0.225 \Omega\text{cm}^2$ ) can be translated into the membrane conductivity of  $0.036 \text{ S cm}^{-1}$ . This value is further reduced to 0.029 and  $0.022 \text{ S cm}^{-1}$  for 20  $\mu\text{m}$  and 10  $\mu\text{m}$  thick membranes, indicating the remaining acid doping level is lower for the thin membranes. This will be further discussed in the next section.

#### 4.3.6 Effect of acid inventory

During the fuel cell break-in, phosphoric acid originated from the membrane is transferred to the catalyst layer. Several samples with acid doping level of 6.9-16.5 were prepared, the doping conditions are shown in Table 4.4.

Table 4.4 Properties of PBI-20 with different ADLs

	PBI-20 ADL6.9	PBI-20 ADL11.6	PBI-20 ADL13.3	PBI-20 ADL16.5	PBI-40 ADL11
Doping condition:					
- H <sub>3</sub> PO <sub>4</sub> (wt%)	70	85	85	85	85
- Temperature (°C)	RT	RT	35°C	45°C	RT
- Duration (h)	24	24	24	24	48
Acid doping level (mol H <sub>3</sub> PO <sub>4</sub> /PRU)	6.9	11.6	13.3	16.5	11
Specific mass of membranes(mg/cm <sup>2</sup> )	2.6	2.6	2.6	2.6	5.2
Acid mass in membrane (mgPA/cm <sup>2</sup> )	5.7	9.6	11	13.7	18.2
Ohmic resistance from EIS (Ωcm <sup>2</sup> )	0.309	0.075	0.075	0.062	0.068

Fuel cell tests of these membranes were carried at DTU labs with 1 cm<sup>2</sup> size cell at 160 °C under dry atmosphere for 48h. The conductivity was measured by impedance spectroscopy measurements performed under galvanostatic mode. Figure 4.7 shows the Nyquist plots of PBI-20 membranes with different acid doping levels. The ohmic resistance of the membrane was read from the arc intercept with the real axis and also listed in Table 4.4. The membrane conductivity is closely relative to the acid doping level, with the acid doping level increase from 6.9 to 16.5, an obviously decreasing of Ohmic resistance from 0.309 Ωcm<sup>2</sup> to 0.062 Ωcm<sup>2</sup> was observed, corresponding to the increasing to conductivity.

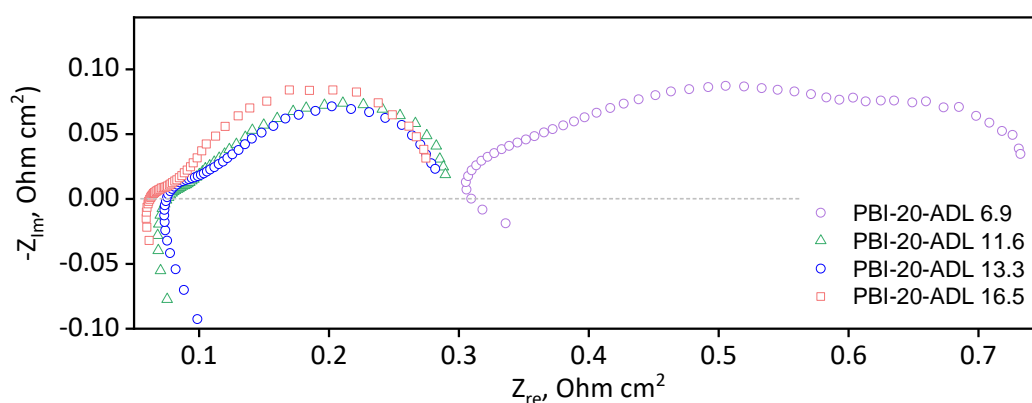


Figure 4.7 Nyquist plots of PBI-20 membrane with different acid doping levels of 6.9, 11.6, 13.3, and 16.5. H<sub>2</sub>/air 30/100, active area 1 cm<sup>2</sup>, electrode 0.9mgPt/C cm<sup>2</sup>.

Studies with varying amounts of initial phosphoric acid in membranes showed that an equilibrium is eventually established with about 13 to 16 mg cm<sup>-2</sup> in the membrane and 3 to 5 mg cm<sup>-2</sup> in the catalyst layers, which depends on the amount of the polymer content in membrane and the thickness of the catalyst layer [258]. The standard PBI-40 membranes at

ADL=11 have an acid content of 18.2 mgPA cm<sup>-2</sup> it is estimated that about 15-20% phosphoric acid is transferred to the catalyst layer. Since the iR-free polarization curves are nearly the same, it is assumed that the amount of the acid transferred to the catalyst layer is very close for those cells using different thickness membranes. It is therefore that the acid remaining in the membrane after break-in would be less for thinner membranes.

This results indicate an issue of the acid inventory when thin membranes are used and MEAs are fabricated without additional acid into the electrodes. More efforts to evaluate the effect of adding extra acid into the electrode structures are however not made in this project due to the limited time.

#### 4.3.7 OCV loss

The measured open circuit voltage of PEMFC is always lower than the reversible cell voltage. There are two major reasons: the hydrogen crossover through the membrane and the electrode irreversibility. The electrode irreversibility concerns oxidation (corrosion) of platinum catalysts in acid. The formed surface oxides are a mixture phase, possibly including PtO<sub>2</sub>, PtO or its hydrated form PtO·H<sub>2</sub>O (Pt(OH)<sub>2</sub>) and therefore display a lower reversible potential than that of the oxygen electrode, though a fixed value is unknown [259].

Any hydrogen crossover through the membrane corresponds to an internal leakage current, in a similar way as the electronic conductivity in solid oxide electrolytes. This leakage current (*i<sub>leak</sub>*) influences the measured current density in the low current range and therefore the cell voltage. In analysis of the cathode kinetics this is taken into account by using an effective current density instead of the as measured current density (*i*) in the analysis:

$$i_{\text{eff}} = i + i_{\text{leak}} \quad (4.7)$$

The overpotential of the cathode can therefore be expressed as

$$\eta_{\text{ORR}} = b \log \left( \frac{i+i_x}{i^0} \right) \quad (4.8)$$

The OCV loss at *i* = 0 due to the hydrogen crossover (*i<sub>x</sub>*) is therefore

$$\Delta E = b \log \left( \frac{i_x}{i^0} \right) \quad (4.9)$$

Taking the Tafel slope of 100 mV/dec for PBI cells, a hydrogen crossover current of a couple of mA/cm<sup>2</sup> may lead to a significant OCV loss because the exchange current density based on the gas diffusion electrode area is very small. Table 4.5 lists the OCV of PBI cells with 40 μm (dry) with ADL 12.2 and 20 μm (dry) with ADL range from 6.9 to 16.5. For all these cells the OCV is quite high though seems slightly higher for PBI-40 (1.00 V) than PBI-20 series (0.97-0.99 V) thin membranes.

Table 4.5 Summary of hydrogen permeability for thin PBI membranes at different acid doping levels.

Properties	PBI-40	PBI-20			
	ADL 12.2	ADL 6.9	ADL 11.6	ADL 13.3	ADL 16.5
OCV (V, fuel cell)	1.000	0.988	0.970	0.990	0.978
Thickness ( $\mu\text{m}$ , doped)	80	35	40	45	46
Crossover current density ( $\text{mA cm}^{-2}$ )	0.186	0.53	0.35	0.31	0.499
H <sub>2</sub> crossover rate ( $\times 10^{-10}$ mol / $\text{cm}^2$ s)	9.64	27.4	18.0	16.0	25.9
Permeability ( $\times 10^{-12}$ mol $\text{cm}^{-1}$ s <sup>-1</sup> bar <sup>-1</sup> )	7.71	9.59	7.19	7.18	11.9

#### 4.3.8 Hydrogen permeability

The hydrogen crossover rate through the membrane is assessed via an electrochemical method at the fuel cell operating temperatures. The test cell with membrane sandwiched between two gas diffusion electrodes was fed with hydrogen on one side and nitrogen on the other. A potentiostat is used to sweep the potential when the working and sensor electrodes are connected to the nitrogen side while the count and reference electrodes are connected to the hydrogen side. The thickness of the acid-doped membrane prior to cell assembly was measured. A widely used protocol was sweeping the potential from 100 mV to 400 mV at a typical scan rate of 2 mV/s. This protocol is modified in the present study. Instead of recording a scanning current at a certain potential, the measurement is based on chronoamperometry and recording a steady current under a constant potential. It starts by scanning the cathode potential from a rest point to 0.4 V at a rate of 20 mV/s followed by keeping a constant potential at 0.4 V. An i-t plot is recorded until a steady state current is obtained, typically for 600-1000 seconds. This is illustrated in Figure 4.8.

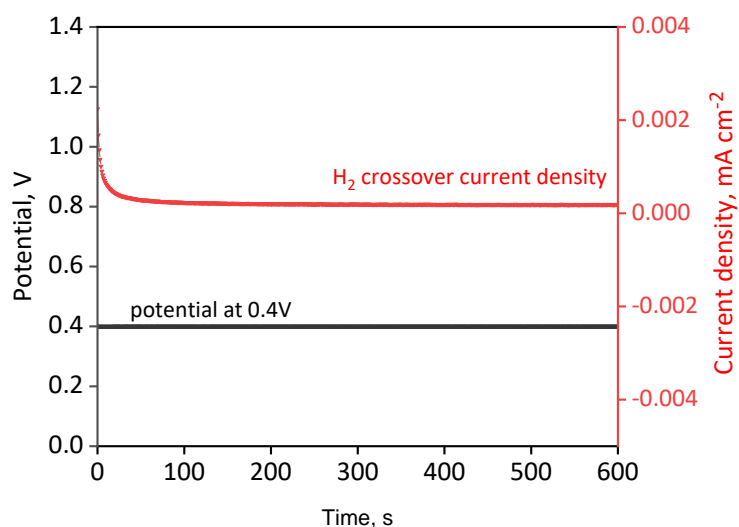


Figure 4.8 Hydrogen crossover current density of membrane. PBI-20, measurements obtained at 160 °C, dry condition.

A set of typical current-time curves under a constant potential of 0.4 V from the hydrogen permeability measurement is shown in Figure 4.9. The membrane is the PBI-20 series doped at varied acid doping levels. The hydrogen crossover rate of the reference PBI-40-ADL11.0 membrane is about 0.5 mA/cm<sup>2</sup>, corresponding to a hydrogen permeation flux of  $9.6 \times 10^{-11}$  mol cm<sup>-2</sup> s<sup>-1</sup>. Taking the membrane thickness of 80 μm into account, this can be translated into the hydrogen permeability of  $7.7 \times 10^{-12}$  mol·cm<sup>-1</sup>·s<sup>-1</sup>·bar<sup>-1</sup>. It should be noted that these values are obtained under dry atmosphere (purging with dry hydrogen and nitrogen at 160°C).

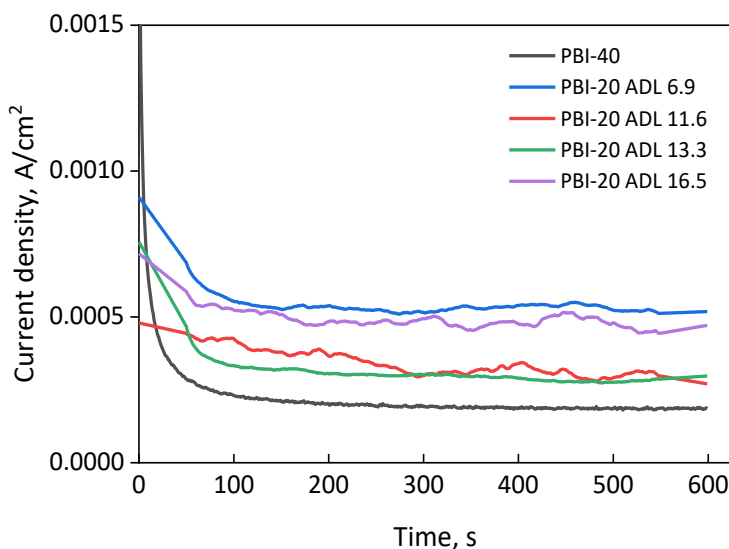


Figure 4.9 Chronoamperograms for the hydrogen permeability measurements at 160 °C. The membranes are PBI-40 and PBI-20 at different acid doping levels as indicated in the figure.

These values are lower than those ( $4.0 \times 10^{-10}$  mol cm<sup>-1</sup> s<sup>-1</sup> bar<sup>-1</sup>) measured by two chamber diffusion cells with a pressure difference of 10 bar at 180 °C [114] but close to the electrochemical measurement ( $6.0 \times 10^{-11}$  mol cm<sup>-1</sup> s<sup>-1</sup> bar<sup>-1</sup>) by Wainright et al [49].

A thin PBI membrane (PBI-20) was doped at different acid doping levels. The measured hydrogen permeability data are listed in Table 4.5. Compared to the reference membrane (PBI-20-ADL11.0), the thin membranes display increased hydrogen crossover, as expected. For the same dry thickness of the membrane, an increase in the acid doping level results in further swelling and hence the separation of the polymer backbone. An increasing trend in the hydrogen crossover is also observed. In terms of the hydrogen permeability by taking the thickness effect into account, the values are all within an order of magnitude, i.e. from 7.2 to  $11.9 \times 10^{-12}$  mol cm<sup>-1</sup> s<sup>-1</sup> bar<sup>-1</sup>. This seems in good agreement with the observed high OCV of these cells, as seen from Table 4.5.

In summary, the hydrogen permeability does not seem to be a critical issue for fuel cells using PBI membranes as thin as 10 μm, though the long-term durability of the membrane and fuel cells needs further evaluation.

### 4.3.9 Thermally cured and covalently crosslinked membranes

The mechanical strength of thin membranes has been of concern and it was assumed that the thin membranes should be mechanically improved by thermal curing and covalently crosslinked.

Crosslinking is an effective approach to improve mechanical stiffness and chemical stability particularly at higher acid doping levels [110]. The benzimidazole groups in PBI are active sites for reactions with bifunctional molecules, for example, alkyl or other organo halides.

Thermal curing is a simple method that does not require additional reagents and can simply proceed through the heating of membranes to temperatures above 300 °C [134]. It is believed that the chemistry proceeds through carboxylic acid groups, which are either present as unreacted end groups or available from the ring opening from thermal degradation, react in a Friedel–Crafts reaction with a phenyl ring [156].

In the present study three thermal cured and crosslinked samples were prepared. The thermal treatment was carried in N<sub>2</sub> at 350 °C for 15 min with a heating profile shown in Figure 4.10. The thermally cured membranes with thickness 10 μm, 20 μm, and 30 μm named PBI-TC-thickness.

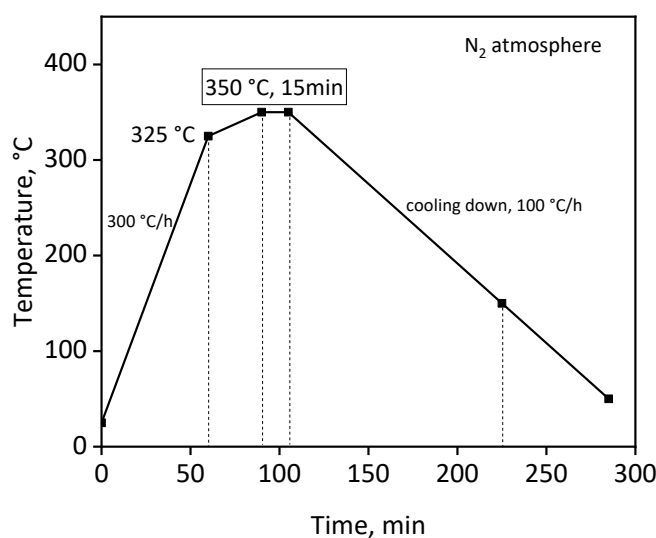


Figure 4.10 Schematic of thermal curing heating process.

In the crosslinking process, DBpX was used as the crosslinker. DBpX was dissolved in a PBI solution and membranes were cast by following the normal procedure ended by drying at 200 °C. The post-treatment of the membrane was carried in N<sub>2</sub> at 280 °C for 10 min. Crosslinked membranes with a thickness of 20 μm and crosslinking degree of 10% and 15% are called PBI-CrL-10-20 and PBI-CrL-15-20, respectively. Figure 4.11 shows photos of thermal cured and crosslinked membranes. The color of membranes became darker after heat treatment.

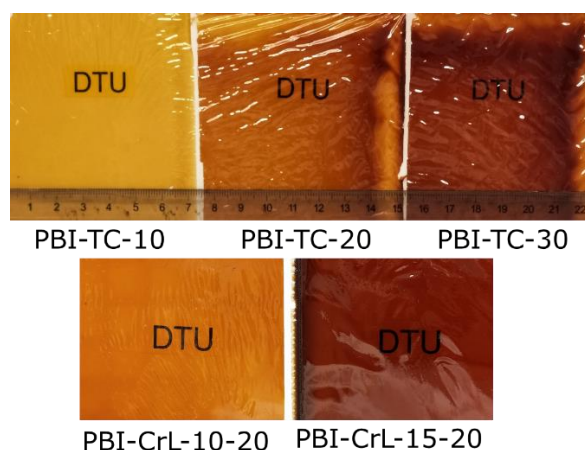


Figure 4.11 Photos of thermal cured (top) and crosslinked (bottom) membranes. The thermal cured membranes are named by PBI-TC-thickness while the crosslinked membranes are named by PBI-CrL-crosslinking degree-thickness.

Phosphoric acid doping was achieved by submerging the membranes in 85%  $H_3PO_4$  at temperatures ranging from room temperature to 150 °C, as shown in Figure 4.12. For pristine PBI membranes at room temperature, a doping level of 11-12 was obtained after 24 hours, as reported above. For the thermal cured and crosslinked membranes, the phosphoric uptake at room temperature after 24 hours immersing in the acid was low, corresponding to an acid doping level of 7.7 - 8.8, lower for the crosslinked and higher for the thermally cured samples. Higher acid doping levels can be achieved by elevating the doping temperatures. Further doping of thermal cured and crosslinked PBI membranes at higher temperatures increases the acid doping level. Doping at 150 °C, for 24 hours the thermal cured and crosslinked membranes can reach an acid doping level of 10.6-11.8, a practical level for fuel cell applications.

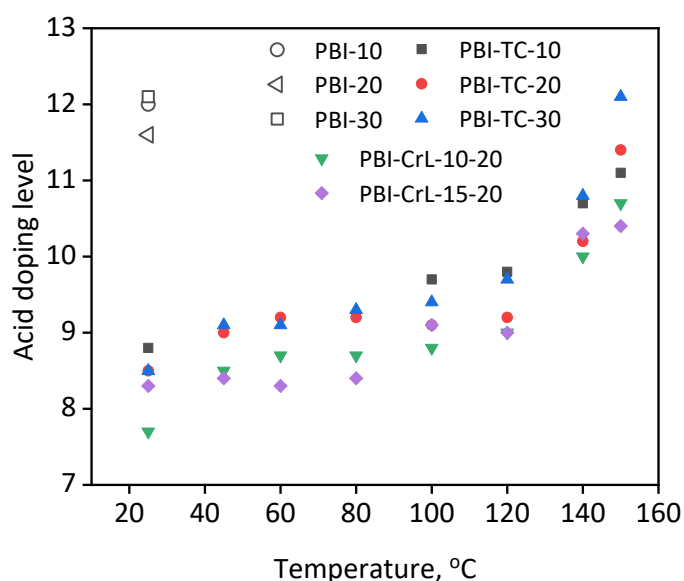


Figure 4.12 Acid doping level of thermal cured and crosslinked membranes at different temperatures.

Table 4.6 Summary of cell performance of thermal cured and crosslinked membranes operated at 160 °C.

	PBI-TC-30	PBI-TC-20	PBI-TC-10	PBI-CrL -10-20	PBI-CrL -15-20
Thickness ( $\mu\text{m}$ , dry)	26.5	21.8	11	21.4	22.2
Thickness ( $\mu\text{m}$ , doped)	46	29	19	40	31
ADL (150 °C)	11.8	10.8	10.8	10.6	10.6
Cell voltage (V):					
Open circuit	0.802	-	0.906	-	0.896
at 0.2 A $\text{cm}^{-2}$	0.681	-	0.681	-	0.697
at 0.4 A $\text{cm}^{-2}$	0.608	-	0.601	-	0.635
Conductivity ( $\text{S cm}^{-1}$ , EIS)	0.028	-	0.015	-	0.018

The heavily doped cured and crosslinked membranes exhibited sufficient mechanical strength for handling, obvious cracks could be seen after hot pressing in MEA preparation. Polarization curves of MEAs with thermal cured membranes and crosslinked membranes were recorded after that the fuel cells have operated at a constant current load of 400 mA  $\text{cm}^{-2}$  for 144 h (6 day). The cell performance were summarized in Table 4.6. The OCV of PBI-TC-30 (0.802 V), PBI-TC-10 (0.906 V) and PBI-CrL-15-20 (0.896 V) is lower than the pristine PBI membranes with the similar thickness. The hydrogen crossover may be caused by the cracks in the membranes after hot pressing. The voltage at 0.4 A  $\text{cm}^{-2}$  were 0.608, 0.601, and 0.635V, respectively. Their conductivity decrease with the decrease of membrane thickness, confirming our previous observation for the thin pristine membranes in Section 4.3.5.

#### 4.4 Conclusions

Membranes of thicknesses from 10 to 40 microns are prepared from the polymer of an average molecular weight of 58 kilodalton. The membranes are doped at varied acid doping levels and evaluated in fuel cell tests. At typical doping levels of 11-12 mol  $\text{H}_3\text{PO}_4/\text{PRU}$ , the membrane showed 100-120% thickness swelling and 43-51% area swelling, with an increase in the thickness swelling and decrease in the area swelling for thinner membranes.

The fuel cell test is activated by a break-in procedure under constant current of 0.4 A  $\text{cm}^{-2}$  for a period of 7 days. During the break-in, part of the acid originated from the membrane is transferred into the catalyst layer. The acid redistribution leads to a steady improvement of the electrode kinetics while the membrane resistance is slowly increasing. For thin membranes the total acid inventory in the membrane is small and a significant increase in the membrane ohmic resistance is observed.

MEAs with thin membranes down to 10  $\mu\text{m}$  show slightly lower open circuit voltages than that for the reference 40  $\mu\text{m}$  but all above 0.97 V. This is in good agreement with the hydrogen permeability measurements, which show the permeability coefficient around  $10^{-12} \text{ mol cm}^{-1} \text{ s}^{-1} \text{ bar}^{-1}$ , corresponding to a crossover current density of  $< 1 \text{ mA cm}^{-2}$ . This value is measured under dry  $\text{H}_2$  and  $\text{N}_2$  atmosphere which might be higher under real fuel cell operating conditions. It seems that the gas crossover of PBI based membranes is not a critical issue for using thinner membranes in fuel cells.

The I-V data from steady state measurements are analyzed by multiple linear regression. All polarizations of membranes of different thicknesses show similar activation losses, which is about 410 mV at  $1.0 \text{ A/cm}^2$ . The Tafel slope is about 0.1 V/dec. The ohmic resistance is decreasing with the membrane thickness, however, not in a simple proportional way since the membrane conductivity is changed.

Assuming that the acid transferred from the membrane to the catalyst layer is fixed, as the  $iR$ -free polarization plots are nearly the same for membranes of varied thicknesses, the acid remaining in the membrane after the break-in period is estimated, showing an acid inventory issue when thin membranes are used.

Addition of extra acid to the catalyst layers is suggested as a solution but without further evaluation in the present work. Instead, attempt is made to dope the thin membranes to high ADLs and an improvement in the fuel cell performance is observed.

In addition, thermal curing and cross-linking are explored as an approach to strengthen the thin membranes. The fuel cell test shows, however, that the combination of small thickness and high rigidity makes the membrane less flexible during the hot-press of MEAs, leading to cracking failures of the membranes.



## CHAPTER 5

# Fabrication of electrospun PBI nanofibers and mats

### Summary of the chapter

PBI nanofibers and mats are prepared by electrospinning from the PBI/DMAc solution. The process parameters are optimized to fabricate well structured nanofiber. The nanofibers and resultant mats are further strengthened by thermal curing and crosslinking, which impart the insolubility of the materials in organic solvents and structure stability in hot phosphoric acid. Finally, the electrospinning process is upscaled to fabricate PBI fiber mats of 50 x 100 cm<sup>2</sup> size, which are used to prepare reinforced PBI composite membranes.

### 5.1 Introduction

Nanostructures, having at least one dimension at the nanoscale, have gained huge interest driven by their unique and fascinating properties over their bulk counterparts [260-262]. Among those existed nanostructures, one-dimensional (1D) nanostructures such as wires, rods, tubes, fibers, and belts are of current interest for their unique applications in mesoscopic physics and nanoscaled devices [262, 263]. In contrast to other nanostructures (e.g., quantum dots, quantum wells), the development of 1D nanostructures was slow in the early years for the difficulties related to the synthesis of those nanostructures with defined morphologies, purities chemical compositions.

Many advanced techniques have been developed for the preparation of 1D nanostructures, including electron-beam or focused-ion-beam writing, lithography, hydrothermal, chemical vapor deposition, electrospinning, solution method, etc. [263]. Among those methods, electrospinning is the simplest approach to fabricate 1D nanostructures with both solid and hollow interiors with continuous length, tunable diameter, aligned direction, and controllable composition [264-266].

The process of electrospinning was firstly patented by J. F. Gooley in 1900 [267]. Further development toward commercialization was made by Anton Formals [268] in 1934 for the generation of textile yarns. In 1936, C. L. Norton described in a patent [269] the melt electrospinning. Before the early 1990s, more than 30 US patents on electrospinning have been issued. Since the early 1990s, Reneker and co-workers revived the electrospinning technique for the generation of one-dimensional (1D) polymer nanostructures, and the electrospinning technique has since then been a subject of wide research [264, 265].

Despite the simplicity of the electrospinning setup (Figure 2.14), the electrospinning mechanisms are rather complicated. During the electrospinning process, electric field force acts on a polymer solution or melt to form the electrospun jet. The solidified fibers can be achieved by stretching the electrified jet for the electrostatic repulsions between the surface charges and

the evaporation of the solvent [178, 270]. Various theories such as Taylor Cone theory [271], bending instability theory [272], electrically forced jet-stability theory [273, 274], and others [275, 276] have been developed. Those theories not only provide a better understanding of the mechanisms of the electrospinning process but also endow scientists with the good ability to design novel setups for the further control of electrospun nanostructure performances. Prompted by those theories, electrospun precursor materials have been extended from polymer nanofibers to polymer/inorganic hybrid nanofibers, and inorganic nanofibers with the diameter range from microscale down to nanoscale [277, 278]. Additionally, by modification of electrospun setups, individual nanofibers, aligned nanofibers, and patterned nanofibers have also been achieved.

### 5.1.1 Basic setup and working parameters

The conventional electrospinning setup consists of three major components: a high voltage (kV) power supply, a spinneret (a syringe or pipette tip), and a grounded collector (typically a metal plate or a rotating mandrel) [220]. The syringe is to host the polymer solution. As a high voltage applied, the drop of polymer solution at the tip of the syringe is polarized and the induced charges distribute on the surface. Under the influence of a strong electrostatic field, the charged polymer is accelerated toward the collector. In other words, within the electrospinning process, the role of the electrostatic forces is to supplement or replace the conventional mechanical forces (e.g., hydrostatic, pneumatic) used to form the jet and to reduce the size of the fiber, hence termed as “electrohydrodynamic jetting.” The collector, usually, is a good electric conductor for the neutralization of the charge carried by nanofibers. However, airborne ions from the corona discharges can also neutralize the charge on the nanofibers in some degree, resulting in that the nanofibers can be collected on isolated collectors or even on the surface of liquid. The morphology and diameter of the electrospun nanofibers, in particular, depend on various parameters that can be divided into 3 groups: polymer solution properties (solution viscosity, solution concentration, polymer molecular weight, etc), processing conditions (applied voltage, volume flow rate, etc), and ambient conditions (temperature, humidity, etc) [270].

### 5.1.2 Applications

These unique properties of electrospinning nanofibers afford the multi-functional and diverse applications, including nanofiber reinforcement, filtration, electronic devices, biomedical field, fuel cells, etc. In fuel cells, electrospun materials can be applied to the preparation of catalysts [220], support materials [221, 222], electrolyte membranes [223] and others [279].

For electrolyte membranes, electrospinning is increasingly recognized as a powerful means of introducing unique phase-separated architectures into composite proton exchange membranes [220, 280-283]. Electrospinning can provide uniaxial alignment of the polymer chains within nanofibers, which can result in enhanced mechanical properties [284, 285] or can promote the formation of interconnected channels, which facilitate improvement in proton conductivity [286, 287].

### 5.1.3 Electrospun PBI nanofibers

In 1999, Kim and Reneker [227] first produced continuous PBI nanofibers with a diameter of 160–300 nm by electrospinning a PBI/DMAc solution containing ca. 20wt% PBI and 4wt% LiCl as a stabilizer. The resulting nonwoven PBI fibers were rinsed with a non-solvent (methanol) to remove the residual solvent (DMAc) and LiCl, followed by washing in sulfuric acid (50 wt%) to stabilize the fibers against shrinkage during the following heat treatment and

to increase the mechanical strength. The electrospun nanofibers have random orientations, but along the fiber axis, the polymer chains are highly oriented. Compared with the solution cast membranes, the fibers have much better tearing and tensile properties [288].

In recent years, nonwoven electrospun PBI nanofiber mats have been explored as electrolyte membranes for high-temperature PEMFCs [133, 289-291]. Two types of membrane architectures of PBI nanofiber-based composite membranes have been attempted (i) using the electrospun PBI nanofiber mat as the porous substrate into to which phosphoric acid is filled; 2) using the PBI nanofibers as reinforcement of another PBI matrix phase to form composite membranes that are going to be acid doped.

On the surface of nanoscaled fibers the polymer chains can be chemically more reactive and thermally less stable. The phenomenon is called the nano-effect.[149, 224] The work by Muthuraja et al. [149] was based on porous sulfone (SO<sub>2</sub>) modified PBI and the pores of the fiber mat was filled or doped with phosphoric acid. When doped with phosphoric acid the PBI fibers have been shown to possess high surface proton conductivity along the fiber direction [290]. This conductivity is of little use in composite membranes where a high through-plane conductivity in the membrane thickness direction is desired.

Also, as a result of the nano-effect, PBI nanofibers can easily be soluble or swollen in solvents such as DMAc or phosphoric acid. This means that the nanofibers are poor in chemical and mechanical stability during the impregnation process for the preparation of PBI nanofiber reinforced PBI membranes. Jahangiri et al. [229] found that the acid doping caused significant swelling and a 2-fold increase in the mean fiber diameter.

To overcome this problem, the PBI nanofibers should be crosslinked. Li et al. [133] used polybenzoxazine (PBz) to crosslink the electrospun PBI nanofibers. PBz is a bicyclic heterocyclic polymer containing oxygen and nitrogen atoms as active sites for crosslinking. Membranes prepared from the PBI-PBz copolymers exhibited enhanced proton conductivity, mechanical properties, and fuel cell performance.

In the present work, the prepared porous PBI nanofiber mats are either thermal cured or covalently crosslinked and used as reinforcement in PBI matrixes. It is essentially a two-phase composite system, and the crosslinked reinforcement fibers are mechanically rigid while the polymer matrix is swollen and conductive after acid doping.

## 5.2 Experimental

Two electrospinning equipments were used in this project. For lab-scale fiber preparation, a Linari Engineering electrospinner was used, which is a needle base setup. The commercial electrospinning equipment Elmarco Nanospider, a nuzzle-less equipment, was used to prepare large-scale PBI nanofiber mats with different thicknesses.

### 5.2.1 Fiber preparation by Linari electrospinninger

With the systematic investigation of operational parameters such as the composition, applied voltage, collect distance, flow rate, and collector substrate, a selected combination was used to produce nanofibers, as shown in Table 5.1. The PBI polymer powder has an average molecular weight of 45 kDa provided by Danish Power Systems. The PBI precursor solution (10.7-15 wt.% ) was prepared by dissolving dry PBI powder and lithium chloride (LiCl) in DMAc at a bath temperature controlled at 150 °C for 18 h with a refluxing condenser. Afterwards, the PBI solution was cooled down to room temperature and transferred to a syringe with a stainless steel needle. The diameter of the needle is 0.8 mm. An electrical bias potential range from 25-

40 kV was applied between the needle and the grounded rounding drum covered with aluminium foil or brown paper, the collect distance was placed 8-13 cm. A syringe pump was used to maintain a solution flow rate of 0.4-1.2 ml/h during electrospinning. The collected nanofiber mat was then dried at 200 °C for 2 hours in air.

### 5.2.2 Upscaled fiber preparation by Nanospider electrospinninger

To upscale the production of PBI nanofiber mat, we used the Nanospider (Elmarco) electrospinning setup with diluted commercial S26 PBI solution. The commercial S26 PBI solution was purchased from PBI Performance Products Inc. The polymer has an inherent viscosity of 0.46 dL/g, corresponding to an average molecular weight of ca. 18 kDa. The solution contains 26.2 wt% PBI, 72.3 wt% DMAc and 1.5 wt% LiCl. The electrospinning solution was obtained by diluting the S26 solution to 13% with DMAc, stirred magnetically at 70 °C overnight to ensure the solution homogeneity. For the spinning process [234, 235], the distance between the emitter and collector was set to 18 cm; the voltage was set to 55 kV, the carriage velocity was 100 mm/s, the collector carrier velocity was set at 4-9 mm/min to control the mat thickness. The chamber temperature and humidity were controlled with NS Air Conditioning Unit (Elmarco).

### 5.2.3 Thermal curing of fiber mats

The obtained PBI fiber mats were heat-treated in a tube furnace at temperatures ranging from 390 to 450 °C under an argon atmosphere. The temperature of the tube furnace was calibrated before use. The furnace was repeatedly heated to the target temperature and held for 30 min to reach equilibrium. During the heat curing, argon was continuously purged through the furnace at a flow rate of about 80 mL/min. The sample was put in a quartz boat. The boat was initially placed in the low-temperature zone (120 °C) during the furnace heating. After the set temperature was reached the mat sample in the quartz boat was moved to the central heating zone with uniform temperature and hold for 10 min. The sample boat was then pulled out to the low-temperature zone immediately. The process of moving the sample into and out of the central heating zone is called a cycle. The mat curing was in general treated by 1-3 cycles. The samples were finally taken out after the furnace was cooled to room temperature. Standard PBI membranes were treated in parallel as the reference sample.

### 5.2.4 Covalent crosslinking of fiber mats

To obtain the crosslinked fibers, the polymer solution for electrospinning was prepared by adding a crosslinker. The crosslinker dibromo-p-xylene (DBpX) was first dissolved in DMAc at room temperature and then mixed with the PBI solution by magnetic stirring at room temperature for 1 hour. The weight ratio of DBpX /PBI was 8.57wt%, corresponding to a crosslinking degree of 10%, as assuming a complete reaction for each mole of the crosslink agent with 2 equiv of imidazole ring [110]. The fiber mats containing DBpX crosslinker were prepared using the Nanospider setup with the voltage set to 45 kV while other parameters being the same as preparing pure PBI fibers. The collected PBI fiber mats containing DBpX were then heat-treated to activate the crosslinking at 280 °C for 10 min under ambient atmosphere.

### 5.2.5 Solubility and swelling test

The thermally cured and covalently crosslinked fiber samples were evaluated by the solubility and swelling tests. The solubility test was carried out in hot DMAc. The pre-weighed dry mat samples were immersed in the DMAc at 80 °C. After a certain period of time, the mat samples were collected, washed with water, and dried at 180 °C for 2h, followed by comparing the weight change.

Table 5.1 Summary of experiments for PBI nanofiber preparation under various solution and electrospinning parameters.

Name	Solution	Electrospinning conditions				Electrospinning products		
		Voltage (kV)	Flow rate (ml h <sup>-1</sup> )	Collector distance (cm)	Collector substrate	Morphology	Fiber diameter (nm)	
A1 *	10.7% PBI (45 kDa) +1% LiCl	40	0.4	10	Al foil	droplets	-	
A2 *	15% PBI (45 kDa)	40	0.5	9	Al foil	droplets and beads	-	
A3 *	15% PBI (45 kDa) +1% LiCl	40	0.4	9	Al foil	fibers and beads #	-	
A4	15% PBI (45 kDa) +1% LiCl	1	40	0.4	10	Al foil	fibers#	217±79
		2	30	0.4	10	Al foil	fibers	225±90
		3	25	0.4	10	Al foil	fibers	231±93
A5	14% PBI (48 kDa)	1	40	0.45	10	Al foil	fibers	172±75
		2	40	0.8	10	Al foil	fibers	232±97
		3	40	1.2	10	Al foil	fibers	252±113
		4	40	0.8	13	Al foil	fibers	236±100
		5	40	1.2	13	Al foil	fibers	251±105
		6	40	0.45	8	Brown paper §	fibers	198±91
		7	40	0.45	9	Brown paper	fibers	211±90
		8	40	0.45	10	Brown paper	fibers	286±127
A6	14% PBI (48 kDa) + 0.5% LiCl	40	0.45	8	Brown paper	fibers	202±88	
A7	14% PBI (48 kDa) +1% LiCl	40	0.45	8	Brown paper	fibers	200±82	
A8	15%PBI (48 kDa) +1% LiCl	40	0.45	8	Brown paper	fibers	198±75	

\* Experiments A1-A3 were later found that the used PBI solutions were not homogeneous by mistake. Rest PBI solutions were prepared at 150°C overnight.

# The morphology of products is described as with *droplets or beads* when the number of beads (< 1µm) is more than ca. 50 pieces/10000 µm<sup>2</sup>. Products with the number of beads less than 50 pieces/10000 mm<sup>2</sup> are described as *fibers* without further specifications

§ The brown paper is a paper product with special organosilicone surface coating supplied by KHASK LTD.

The swelling test of the mat samples was conducted by immersing the samples in hot phosphoric acid (85wt% at 80°C). The area and average fiber diameter, after a certain period of the immersion, were examined using scanning electron microscopy (SEM, Zeiss microscopy). The diameter of the fibers was estimated from the microscopic images using ImageJ software.

### 5.2.6 ATR-FTIR characterization

Attenuated Total Reflectance Fourier Transform Infrared (ATR-FTIR) spectroscopy was conducted using a Perkin Elmer Spectrum One FTIR spectrometer equipped with a universal ATR sampling accessory. The membrane samples were pre-dried at 200 °C for 2 h before the spectra were recorded [134].

## 5.3 Results and discussion

Experiments for the preparation of PBI fibers by electrospinning under a variety of parameters are summarized in Table 5.1. The investigated parameters are divided into two groups: polymer solution properties (polymer molecular weight, concentration, and addition of a phase stabilizer LiCl) and processing conditions (applied voltage, volume flow rate, collector distance and substrate materials). The temperature and relative humidity(RH) of the spinning chamber were controlled at 20 °C and 17-23%RH, respectively.

### 5.3.1 Solution parameters

#### 5.3.1.1 Concentration

The concentration of polymer solutions plays an important role in fiber formation during the electrospinning process. The concentration changes the solution viscosity. If the concentration is too low, the polymer solution jet breaks up into droplets. As a result, the formation of beads is often observed in fibers [292]. Anandhan et al. [293] studied five PBI concentrations from 8 to 16 %, and Jahangiri et al. [229] studied the concentration range from 10 to 15%. They found that no PBI fibers but only beads, droplets, and cups were formed at low concentrations. In low concentration solutions, the polymeric chains seem to be in an imbalance to withstand the electrostatic forces acting on a charged jet, which is hence broken up into smaller charged entities. Under the influence of the solution surface tension, droplets or beads are formed in order to minimize the surface area. At sufficiently higher concentrations, the breaking up of the charged jet is prevented, and smooth fibers can be formed. High concentrations are often accompanied by the high solution viscosity, which might lead to the formation of larger diameter fibers, though an absolute correlation has never been established. Too high concentrations may also prohibit fiber formation due to the too high viscosity. As a compromise, uniform and defect-free PBI fibers along with a small number of beads can be produced at solution concentrations of 10 and 15 %.

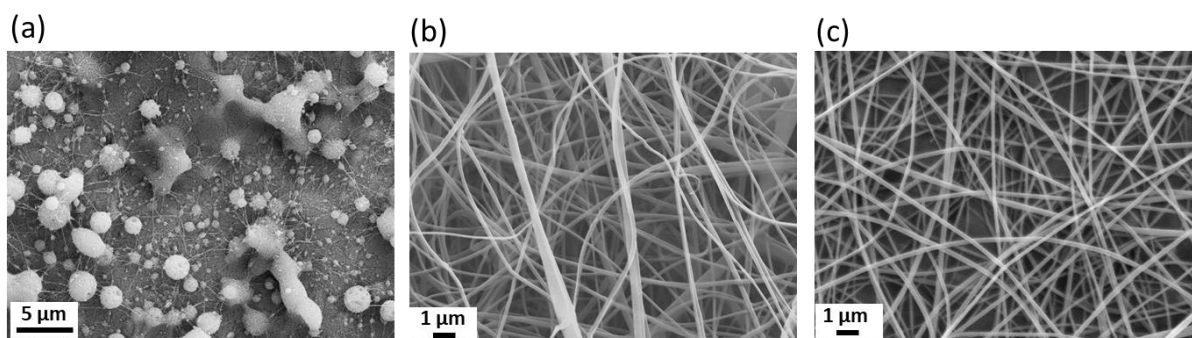


Figure 5.1 SEM images of samples obtained from solution, (a) A1, 10.7%, 40 kV, 0.4 ml h<sup>-1</sup>, 10 cm, Al foil, (b) A7, 14%, 40 kV, 0.45 ml h<sup>-1</sup>, 8 cm, brown paper, (c) A4-1, 15%, 40 kV, 0.4 ml h<sup>-1</sup>, 10 cm, Al foil.

In the present study, good fibers with a varied number of beads are obtained with polymer concentrations of around 15 wt%. With such polymer solutions, other parameters can vary to a certain extent resulting in limited changes in the morphology and fiber diameter of the electrospinning products. These include the small change of polymer molecular weights from 45 to 48 kDa, of the spinning voltage from 25 to 40 kV, the pumping rate of the polymer solution from 0.4 to 1.2 ml/h as well as the collector substrate and distance. Figure 5.1 shows selected examples of the obtained products where the particles in sample A1 were most likely due to the inhomogeneous polymer solution by mistake.

### 5.3.1.2 Molecular weight and LiCl content

Yang et al.[65] studied PBI membranes prepared from polymers of molecular weights from 30 to 94 kDa and showed enhanced chemical stability, reduced acid swelling, and improved mechanical strength of PBI membranes with high molecular weights. For the electrospinning experiments, two batches of the polymer were used with a molecular weight of 45 and 48 kDa, respectively. This small molecular weight difference is not sufficient to conclude any effect on the PBI nanofiber morphology. In fact, no difference is observed in this study.

It is known that PBI may precipitate from DMAc solutions upon storing. This phenomenon can be prevented by the addition of a phase stabilizer, LiCl [294]. It has been described that PBI and LiCl form complexes in DMAc solution where lithium ions interact with the polar DMAc solvent and chloride ions protonate the amine of the imidazole ring [85]. As a result, addition of LiCl promotes the dissolution of PBI. Although the presence of LiCl increases the PBI solubility and stability of the DMAc solution, the mechanical properties of the membrane are reduced [295]. Another effect of the LiCl addition is the increase of the PBI solution viscosity. Lin et al.[296] observed that with increasing LiCl content, the solution viscosity dramatically decreases, showing a minimum at a molar ratio of [LiCl]/[benzimidazole] of 8.0. In terms of electrospinning, if the solution is absolutely insulating or the electrostatic force cannot overcome the surface tension, no fibers can be produced. If some salt is added to the solution, the problem can be overcome due to the enhancement of the conductivity of the solution, which is a factor determining the spinning current and fiber diameter [297, 298]. In the present work, the variation of the LiCl content is from zero (A5) to 0.5 wt% (relative to the total weight of

the solution, the same below, A6) and 1.0 wt% (A7 and A8). Within this narrow yet practical range of the LiCl addition, little effect is observed on the morphology of the PBI nanofiber produced, as shown in Figure 5.2 and Figure 5.3.

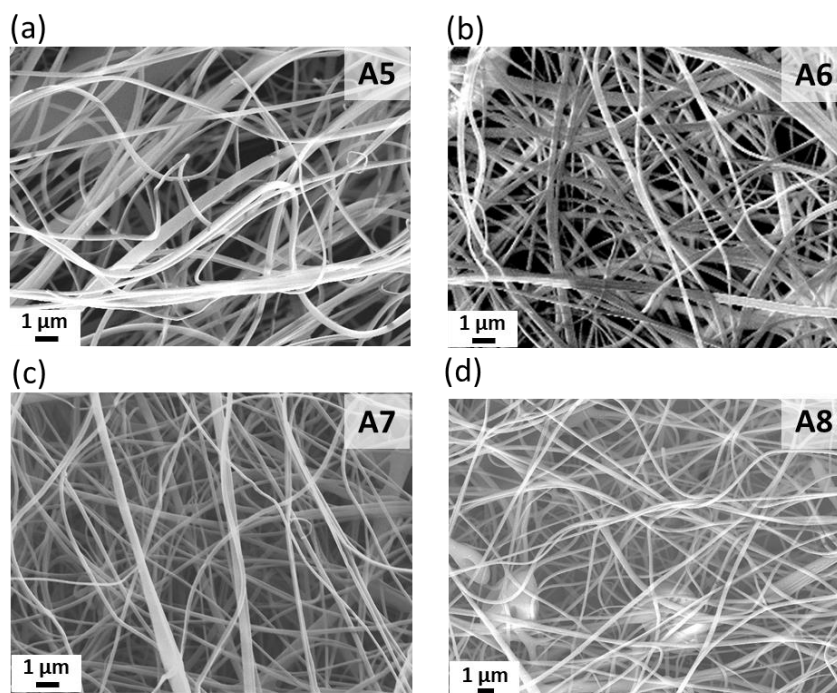


Figure 5.2 SEM images of samples obtained from solution (a)A5, 0% LiCl, 14% PBI, (b)A6, 0.5% LiCl, 14% PBI, (c)A7, 1.0% LiCl, 14% PBI and (d)A8, 1.0% LiCl, 15% PBI. These samples were obtained at a voltage of 40 kV and the flow rate is  $0.45 \text{ ml h}^{-1}$ , the brown paper was used as the collector substrate.

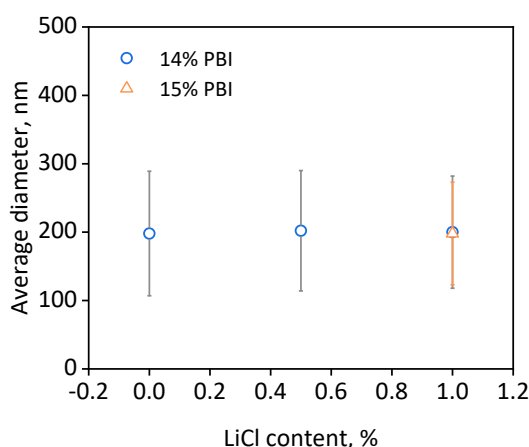


Figure 5.3 The average fiber diameter as a function of the LiCl content in the polymer solutions.

### 5.3.2 Processing parameters

#### 5.3.2.1 Voltage

Within the electrospinning process, the applied voltage is a crucial factor. Only when the

applied voltage is higher than a threshold value can the charged jets ejected from the Taylor Cone occur. The effect of the applied voltages on the diameter of electrospun fibers is somehow controversial. It is generally reported that the average diameter of fibers tends to decrease with increasing applied voltage since the electrostatic repulsive force on the fluid jet is increasing and therefore favors the formation of thinner and uniform fibers [299]. The narrowing of the fiber diameter distribution has also been reported [300]. Anandhan et al. [293] observed, however, an increase in the average fiber diameter increases as the applied voltage was increased from 15 kV to 20 kV while further increase in the applied voltage led to a decrease in the average diameter of PBI fibers. Usually, PBI nanofibers could be obtained at the voltage 15 – 25 kV in the needle-based spinning system [227, 229]. Jahangiri et al. [229] have attempted to electrospin at relatively low voltages from 12-15 kV using diluted PBI S26 solutions (with an average Mw of about 18 kDa containing 1.5% LiCl) and observed that the high spinning voltage (18 kV) caused a wider fiber diameter distribution.

In the present study, the applied voltage ranges from 25 to 40 kV. As seen in Table 5.1, the diameter of fibers is  $231\pm 93$ ,  $225\pm 90$ , and  $217\pm 79$  nm for the applied voltage of 25, 30, and 40 kV, respectively. Figure 5.4 shows the variation of the average fiber diameter as a function of the applied voltage. It is seen from Figure 5.4d that slightly thinner PBI nanofibers and narrower diameter distribution are obtained at higher voltage, though the variation is not significant.

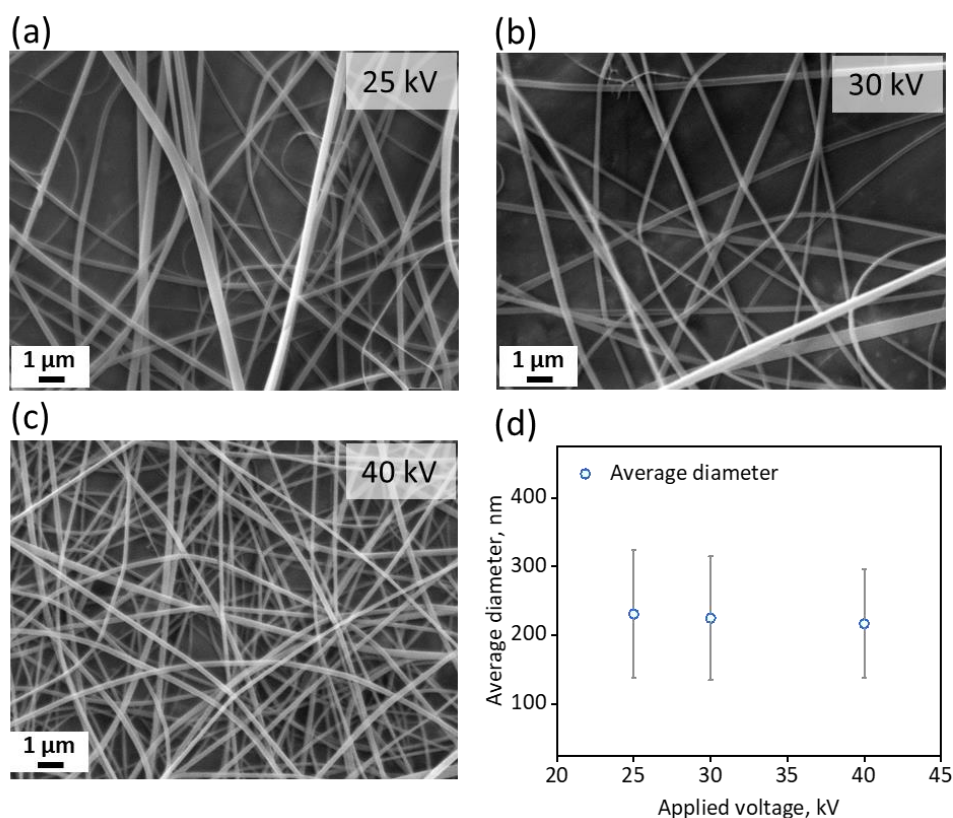


Figure 5.4 SEM images of electrospun PBI nanofibers obtained from solution A4 at a voltage of (a) 25 kV, (b) 30 kV, and (c) 40 kV, the flow rate is  $0.4 \text{ ml h}^{-1}$ , Al foil was used as the collector substrate with a distance of 10 cm. (d) the average fiber diameter as a function of the applied voltage.

## 5.3.2.2 Collector distance and solution flow rate

It has been proven that the distance between the collector and the tip of the syringe can affect the fiber diameter and morphologies [300, 301]. If the distance is too short, the fiber will not have enough time to solidify before reaching the collector. On the other hand, if the distance is too long, bead fiber may be obtained. An optimal distance of the electrospun fiber is a function of the evaporation rate i.e. depending on the polymer concentration, solution flow rate, and chamber temperature and humidity. In the present work, the chamber temperature and humidity are controllable in the setup 20 °C, 17-23% RH. Figure 5.5 shows the fiber collected at the distance of 10 and 13 cm. In this range, only slight changes are observed, for example, the average diameter of fiber change from 232 nm (Figure 5.5a, 10cm) to 236 nm (Figure 5.5c, 13 cm) at the flow rate of 0.8 ml h<sup>-1</sup>, from 252 nm (Figure 5.5b, 10cm) to 251 nm (Figure 5.5d, 13 cm) at the flow rate of 1.2 ml h<sup>-1</sup>.

It was known that increasing the feeding rate decreased the charge density, whereas intense charge density leads to jet bending instabilities, which caused the formation of and thicker fibers with high variance in fiber diameter. Besides, when the feeding rate is higher, solvent molecules cannot be fully evaporated, resulting in formation of beads [300]. It is obvious that the fiber diameter change from 232 (Figure 5.5a, 0.8 ml h<sup>-1</sup>) and 236 nm (Figure 5.5c, 0.8 ml h<sup>-1</sup>) to 252 nm (Figure 5.5b, 1.2 ml h<sup>-1</sup>) and 251 nm (Figure 5.5d, 1.2 ml h<sup>-1</sup>).

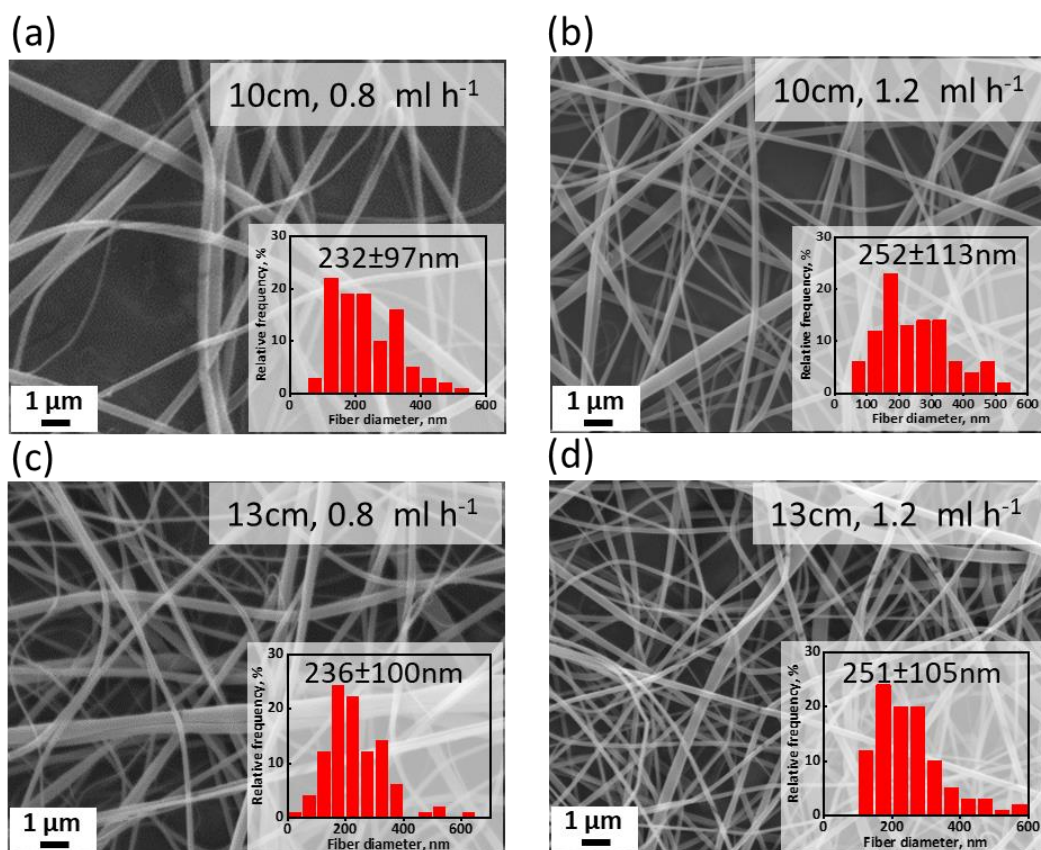


Figure 5.5 SEM images of electrospun fibers obtained from solution A5-14%PBI at different collect distances and flow rates, the electrospinning voltage was 40 kV. Insets are the diameter distribution.

### 5.3.2.3 Collecting substrates

Usually, a conductive substrate is used to collect the charged fibers. Aluminum foil is a common used substrate, but it is difficult to peel the large piece off, especially the thin fiber mats with thickness less than 10  $\mu\text{m}$  [270]. With the need for fibers transferring, brown paper, a special paper product with organosilicone surface coating, was used in this work. It can be seen from Figure 5.6, the fiber collected with paper substrate shows a larger diameter and wider diameter distribution (Figure 5.6c,  $286\pm 127$  nm) than that collected with Al foil (Figure 5.6d,  $172\pm 75$  nm) at the same applied voltage and collector distance. The paper is non-conductive, the electric field between the needle and collector is affected by the non-conductive paper, resulting in some changes [302, 303]. With decreasing of the distance, the diameters and diameter distributions appear different. The diameter of fibers collected at 8 and 9 cm is  $198\pm 91$  and  $211\pm 90$ , respectively.

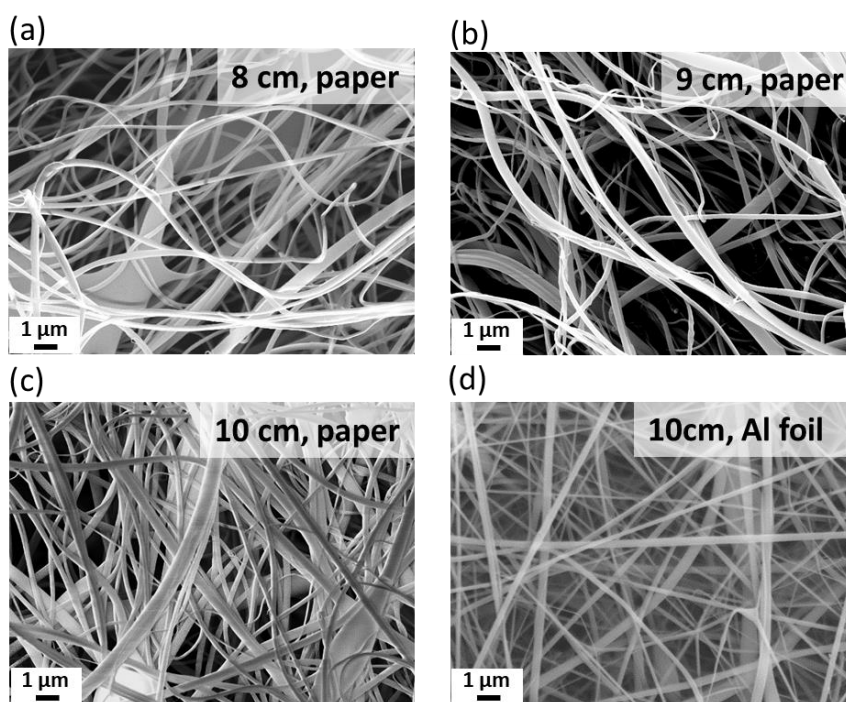


Figure 5.6 SEM images of samples obtained from solution A5, (a)(b)(c) brown paper; and (d) Aluminum foil were used as collector substrate. The voltage is 40kV and the flow rate is  $0.45\text{ml h}^{-1}$ .

Considering the morphology, the fiber diameter and distribution, and ease of tearing off from the substrate, a set of parameters are selected to prepare the fibers for the followed treatment: A8 solution (15% PBI, 1%LiCl), voltage 40 kV, collecting distance 8 cm, flow rate 0.45 ml/h, using the brown paper as the collector, The SEM images of the sample is shown in Figure 5.2d. A photo of the collected electrospun fibers are shown in Figure 5.7.

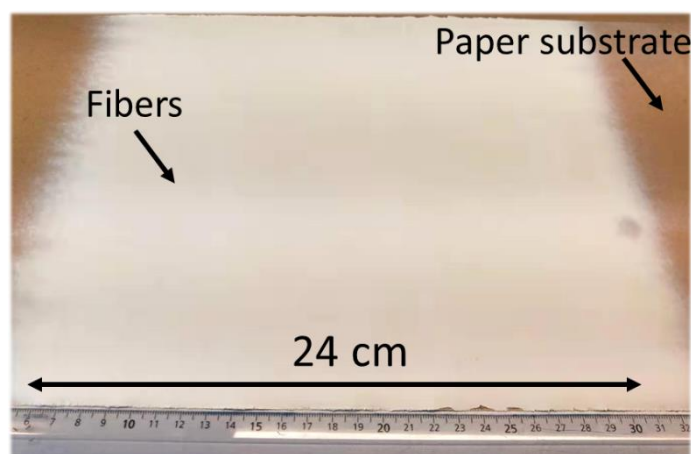


Figure 5.7 Photo of PBI fibers collected with brown paper. A8 solution (15% PBI, 1%LiCl), collected with 40 kV, at a collected distance of 8 cm, flow rate of 0.45 ml/h.

### 5.3.3 Summary and characterization of PBI fiber mats

Based on the test results described above, a set of electrospinning conditions are chosen for the preparation of a large batch mat samples, as listed in Table 5.2. After spinning all samples are dried at 200 °C for 2 hours in air, called *Mat* or pristine *Mat*. The *Mat* sample was further treated by thermal curing at varied temperatures in argon for 10 minutes. Some treatments were repeated 1, 2 or 3 times (cycles) of the 10 minute period. The samples listed in Table 5.2 are named as, for example, Mat-TC420-1C, meaning that the *Mat* was thermally cured at 420 °C for 10 minutes by one cycle. These heat-treatment conditions are selected for the later upscaled samples.

Table 5.2 Summary of prepared PBI fiber mat samples for further characterization

Samples	Electrospinning conditions	Post-treatment conditions	Note
(Pristine) Mat	48 kDa; 15wt%+1%LiCl 40 kV; 8 cm; 0.45 ml/h Paper	200°C drying 2 hr *	
Mat-TC390-1C		Thermal curing, Ar, 390°C, 10 min	
Mat-TC390-2C		Thermal curing, Ar, 390°C, 2x10 min	
Mat-TC390-3C		Thermal curing, Ar, 390°C, 3x10 min	
Mat-TC405-1C		Thermal curing, Ar, 405°C, 10 min	
Mat-TC420-1C		Thermal curing, Ar, 420°C, 10 min	Upscaling
Mat-TC420-2C		Thermal curing, Ar, 420°C, 2x10 min	
Mat-TC435-1C		Thermal curing, Ar, 435°C, 10 min	
Mat-TC450-1C		Thermal curing, Ar, 450°C, 10 min	
Mat-CrL10	18 kDa; 13wt%+0.75%LiCl 45 kV; 18 cm; 0.45 ml/h; Paper Crosslinker: DBpX; Degree: 10%;	Crosslinking at 280°C for 10 min, air	

\* This sample is also called the pristine fiber mat. Other mat samples have all been treated under this drying condition before treated in Ar.

Another mat sample (Mat-CrL10) was prepared by electrospinning from the low molecular weight polymer (18 kDa) containing DBpX (crosslinking degree of 10%). The spinning conditions are listed in Table 5.2 (Mat-CrL10). The mat sample was, after drying at 200 °C for 2 hours, further heated at 280 °C for 10 minutes to activate the crosslinking.

These samples are characterized TGA, FTIR, solubility test in DMAc, and swelling test in hot phosphoric acid, as to be presented below.

### 5.3.4 Crosslinking chemistry and thermogravimetric analysis

The imidazole group of PBI is reactive and can be used for polymer modification and crosslinking. DBpX, among many crosslinkers as listed in Chapter 2, can crosslink PBI via an amide-type linkage at the imidazole group, as shown in Figure 5.8a. Assuming a complete reaction for each mole of the cross-linking agent with two equivalents of amine hydrogen in PBI at 280 °C for 10 minutes, the cross-linking degrees of 10% is defined according to the amount of DBpX added into the PBI solution.

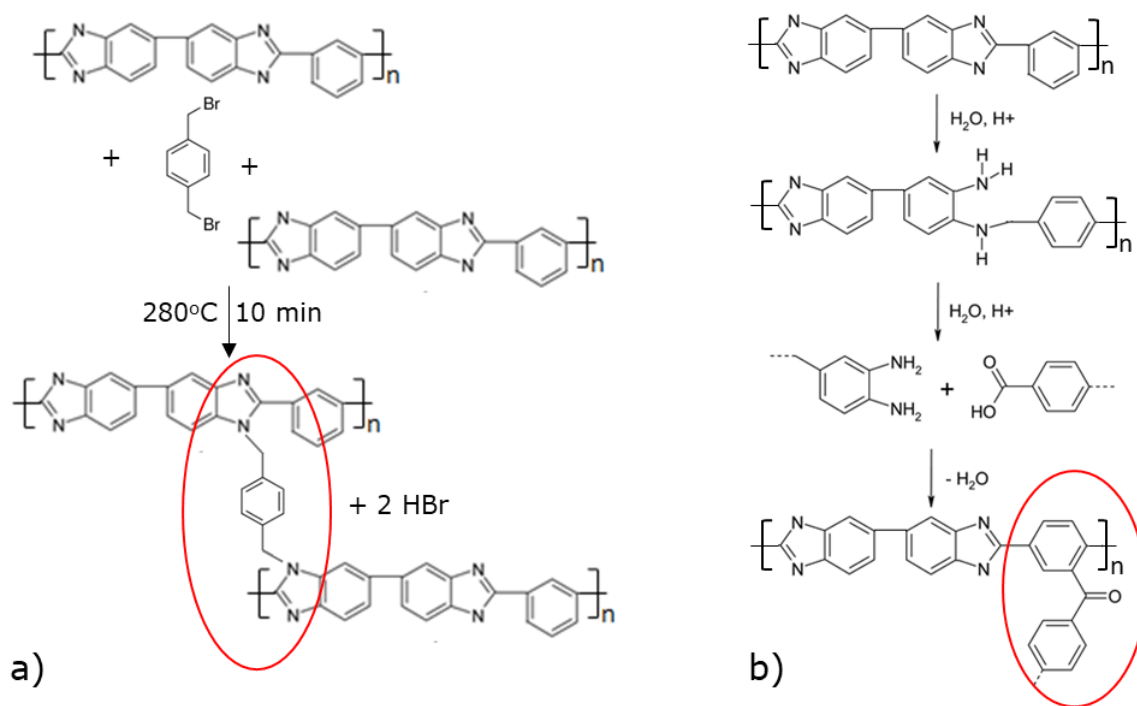


Figure 5.8 Chemistry of PBI crosslinking by (a) DBpX and (b) thermally curing treatment.

The mechanism for crosslinking by thermal curing is not clear. Joseph et al.[156] suggested that the hydrolysis of PBI occurs by the bound water molecules. The opening of the imidazole ring leads to formation of diamine and carboxylic acid term groups, as shown in Figure 5.8b. The carboxylic acid, from the polymer chain end or the hydrolytic degradation of imidazole ring, may react with the aromatic ring through a Friedel-Crafts reaction, forming aromatic ketones as the linkage of the cross-linking [156]. A balance of the thermal degradation and the thermal curing crosslinking should be considered by selecting the curing temperature and duration.

The thermally cured mats were investigated by TGA, as shown in Figure 5.9a. The samples were pre-dried at 200 °C for 2h. The thermograms were recorded at a heating rate of 5 °C min<sup>-1</sup>. The solvent residuals and absorbed moisture completely evaporated before 250 °C. The weight at 250 °C was set to 100%. The onset temperature of the weight loss was 436, 440, 449 °C for the pristine PBI mat and samples that have been thermally cured at 390 °C (Mat-TC390-1C) and 420 °C (Mat-TC420-1C). The weight loss of three samples from 350 to 450 °C was found to be 28.7%, 12.6%, and 7.1% respectively. These numbers observed for the PBI nanofibers are quite large. For PBI membrane samples, only 0.7% weight loss was reported in the temperature range of 350-450 °C while no weight loss for the thermally cured membranes was observed [134]. The PBI in form of nanofibers shows lower thermal stability than the corresponded dense materials because of the nano effects [149]. The DTA data was showed in Figure 5.9b, where the exothermic peaks of the pristine PBI mat, the cured Mat-TC390-1C and Mat-TC420-1C were centred at 453, 457, and 477 °C, respectively.

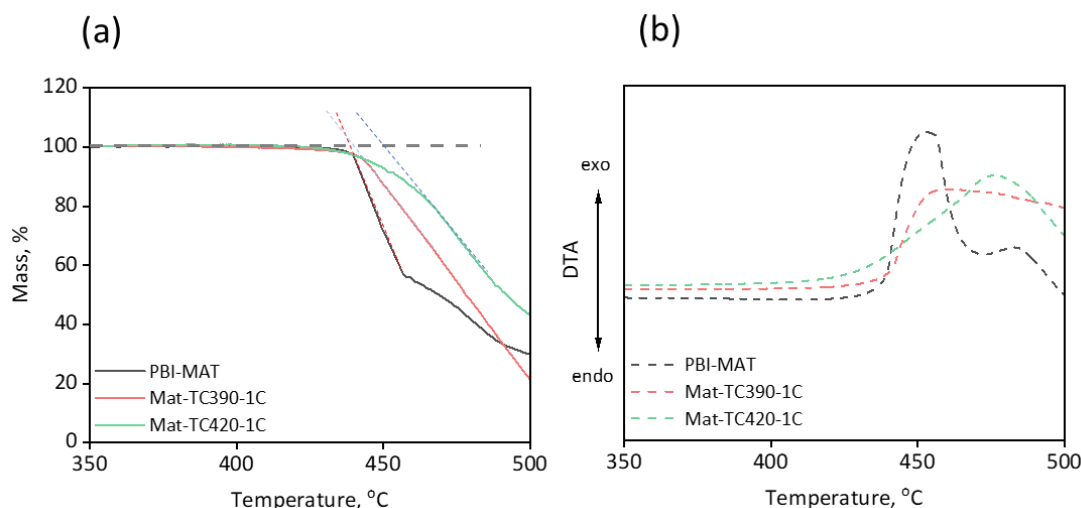


Figure 5.9 (a) TGA and (b) DTA data of the pristine PBI mat, the mats that had been cured at 390 °C for 10 min (Mat-TC390-1C), and cured 420 °C for 10 min (Mat-TC420-1C).

### 5.3.5 ATR-FTIR characterization of thermally cured membranes

Figure 5.10 shows ATR-FTIR spectra of the pristine and cured membranes treated at temperatures ranging from 390 to 450 °C under argon atmosphere. For the pristine sample, the appearance of the FTIR spectrum is in good agreement with those reported in the previous study [129, 134]. Especially, two major absorption bands centred around 1540 and 1640 cm<sup>-1</sup> that have previously been assigned to stretching modes of C=C and C=N bonds in the aromatic backbone, respectively, are all observed.

For samples that were treated at 390 °C for 1-3 cycles (10 minutes each), no obvious variation in the FTIR spectra was observed on the membrane samples (Figure 5.10a). Those membranes that had been treated under different temperatures from 390 to 435 °C (Figure 5.10b) showed invisible changes of the FTIR spectra in comparison with that of the pristine sample. The

sample thermally cured at 450 °C, however, showed noticeable variation in the visual appearance of the spectra (Figure 5.10b), possibly indicating severe oxidation of the polymer backbone.

It is noted that the thermal curing was carried out under an argon atmosphere. The literature data obtained under air at 350 °C showed the broadening of the absorbance bands in the 1000–1800  $\text{cm}^{-1}$  of the spectrum range, accompanied by the polymer oxidation, resulting in ultimate chain scission and molecular weight decrease [304]. In the following thermal curing of the PBI fibers the temperature has therefore been set to be below 420 °C.

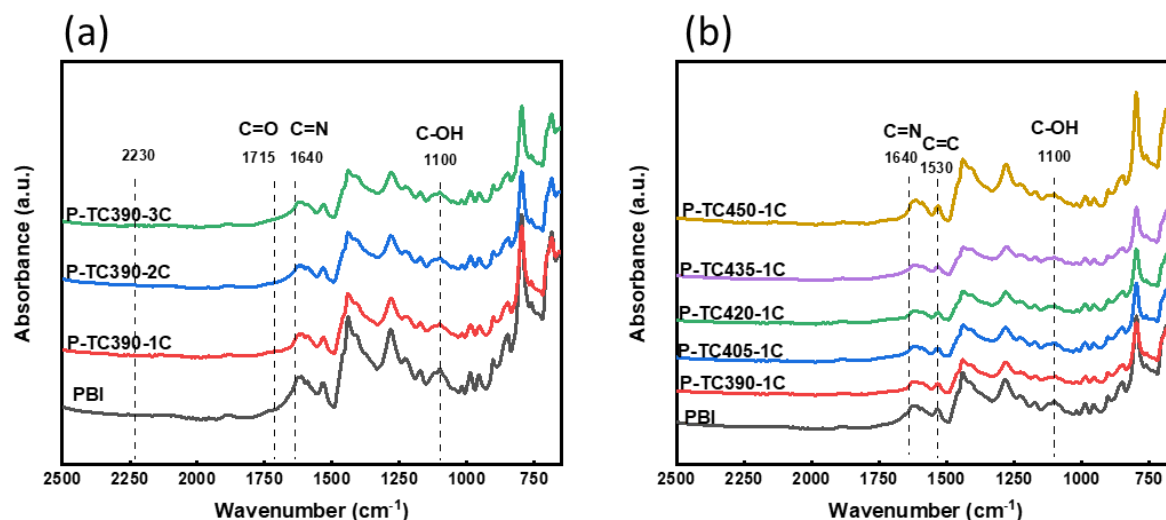


Figure 5.10 ATR-FTIR spectra of (a) pristine membrane and thermal cured membranes at 390 °C for 1-3 times 10 minutes and (b) thermal cured membranes at 390- 450 °C for 10 minutes.

### 5.3.6 Solubility of thermally cured and covalently crosslinked fibers in DMAc

The solubility of PBI in organic solvents is a measure of polymer crosslinking. It has been reported after thermal curing at temperatures of 350–500 °C that the polymer solubility in hot DMAc is significantly decreased, which was attributed to a dramatic increase of molecular weight.

In the study of fiber curing, a dense PBI membrane was also included as a reference for comparison. Both PBI fiber mats and membranes were treated under varying temperatures from 390 to 450 °C or thermal cycling for 1 to 3 times (cycles). The insolubility of cured fiber mats and membranes was evaluated by immersing them in DMAc at 80 °C. The results are shown in Figure 5.11 (fiber mat) and Figure 5.12 (membranes). As expected, the pristine PBI fiber and membrane were dissolved completely in less than 20 minutes. The pristine fiber is dissolved even faster, i.e. after 1 min. This is apparently due to the larger surface area of nanostructures, the so-called nanoscale effect.

In contrast, undissolved masses of all the thermal cured fibers and membranes were still above 95% after 24 h, showing significantly reduced solubility. For the thermally cured fibers, the

solubility is decreased with the increase of the heat-treatment temperature. The sample treated at the highest temperature of 450 °C showed the largest undissolved mass of 97 % after 24 h (Figure 5.11). When the cured cycle number is increased, the undissolved mass increases also. For thermally cured membranes, for example, the sample treated at 390 °C for 3 cycles showed the lowest solubility and was almost completely insoluble (Figure 5.11). The solubility of crosslinked fibers can be seen in the inset of Figure 5.11 i.e. the undissolved mass is up to 96% after 24 h This is consistent with previously reported result [110]. The insolubility of the crosslinked fibers in hot DMAc makes it possible to use them in followed casting process.

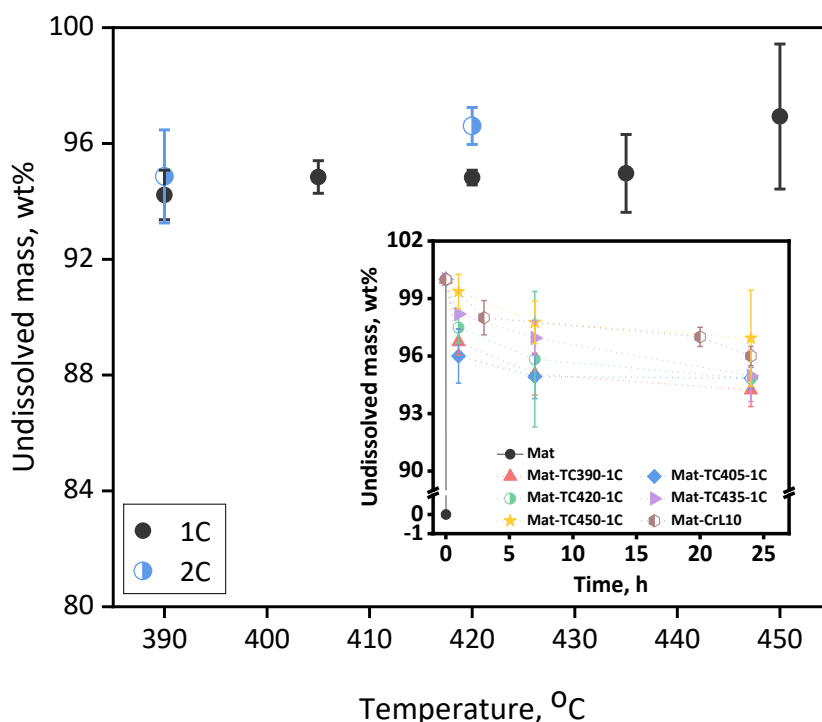


Figure 5.11 Solubility of thermally cured fibers and covalently crosslinked fibers in DMAc at 80 °C. Fibers were thermally cured at 390-450 °C for 10 min (1 or 2 cycles), the fiber with crosslinker was treated at 280 °C for 10 min.

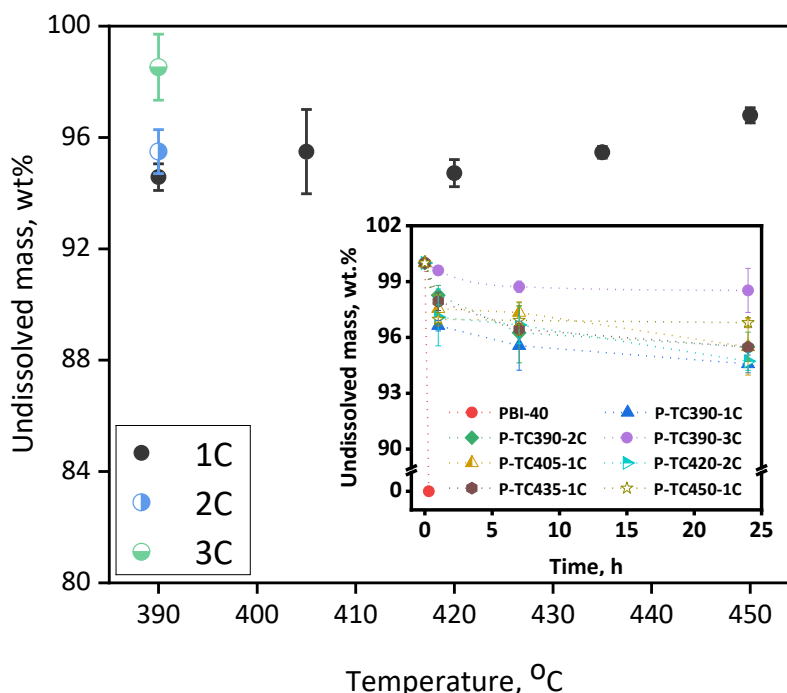


Figure 5.12 Solubility of thermally cured PBI membranes in DMAc at 80 °C.

### 5.3.7 Swelling of thermal cured fiber mats in PA

#### 5.3.7.1 Area swelling

Typically, the dense membrane is swollen after being doped in phosphoric acid. The swelling in three directions can be calculated from the measured length, width, and thickness changes of the sample. The swelling of the aforementioned electrospun fibers was investigated in phosphoric acid at 80 °C. In Figure 5.13, the Y-axis is the mat area swelling defined as the area change on the basis of dry may area before the acid immersion:

$$AS(\%) = \frac{A_a - A_b}{A_b} \cdot 100$$

Where  $A_a$  and  $A_b$  are the areas of mat samples after and before the acid immersion. A negative swelling of the mat means that the mat shrinks. It should be noted that the moment when the fiber mat was fully immersed in phosphoric acid was taken as  $t = 0$  h (Figure 5.13 inset).

For the pristine fiber mat and covalently crosslinked fiber mat, an obvious shrinkage was observed as soon as the samples were immersed in the hot phosphoric acid. After 20 h immersion, the mats shrank to 78% and 73% of their original dry areas, i.e. exhibiting a mat swelling of -22 and -27%. This is an indication of the collapse of the mat structure in the hot acid.

The thermal curing treatment had a significant influence on the swelling/shrinking behavior of the mat. For the fiber mat treated at 375 to 405 °C, the mat shrinkage in the area is decreasing as the thermal curing temperature increases. The mat samples are able to maintain their geometry in hot phosphoric acid, with the area swelling approaching zero.

Further increase in the thermal curing temperature to 420 °C and above, the mats showed a slightly positive (up to 5%) area swelling, implying a rigid structure of the porous fiber mat. It is most likely that the fibers have formed linkages at the contact points of fibers, which are also stable in hot phosphoric acid.

Generally, the area swelling of PBI dense membranes is around 50-70% after doping in 85 wt% phosphoric acid at room temperature. The PBI fiber mat displayed much less area swelling than that of the dense membrane, apparently due to the fact that the high porosity of the mat can accommodate the doping acid.

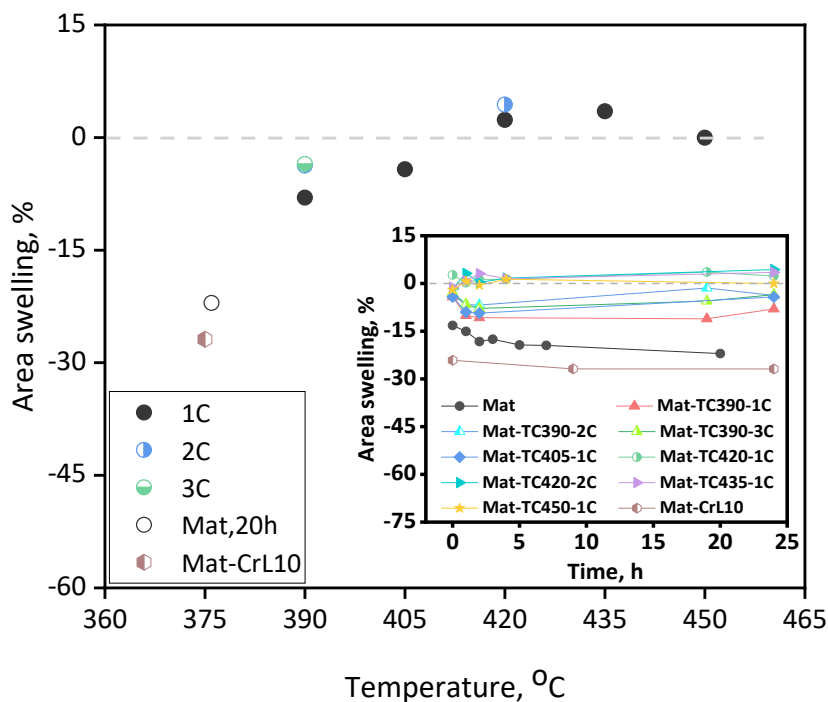


Figure 5.13 Area swelling of PBI fiber mats after immersion in phosphoric acid at 80 °C for 24 hours. Specifications of the mat sample names are given in Table 5.2.

### 5.3.7.2 Fiber diameter swelling

As the mat samples are porous and often not sufficiently rigid, the measurements of the thickness swelling of the mat samples are difficult and in most cases in larger errors. Therefore, in the following, the swelling in the fiber diameter was evaluated by SEM.

Figure 5.14 shows SEM images of the PBI nanofibers after being immersed in phosphoric acid at 80°C for 24 hours. The microstructure of the pristine fibers and the fibers cured at 390 °C (TC-390-1C), and 405 °C (TC405-1C) was found to totally collapsed after the acid immersion (Figure 5.14 a-c).

For the fibers cured at higher temperatures e.g. 420, 435, and 450°C, the microstructural stability in hot phosphoric acid is much better, as shown in Figure 5.14 d-f, where the fibers still can be recognized clearly. Figure 5.14 g-i shows the diameter distribution of fibers measured for the three samples shown in Figure 5.14 d-f, respectively. The fiber average diameters are found to be 352 nm, 334 nm, and 234 nm for the fibers treated at 420 °C, 435 °C,

and 450°C, corresponding to swelling of 77.8%, 68.7%, and 18.2% based on the average diameter 198 nm of pristine fibers. An interconnected network is formed in the single fiber during the thermal curing, which limits the expansion of the nanofiber after acid doping. Therefore, the cured fibers show better rigidity. Fibers treated at higher temperatures exhibit less swelling in area and diameter at the same time.

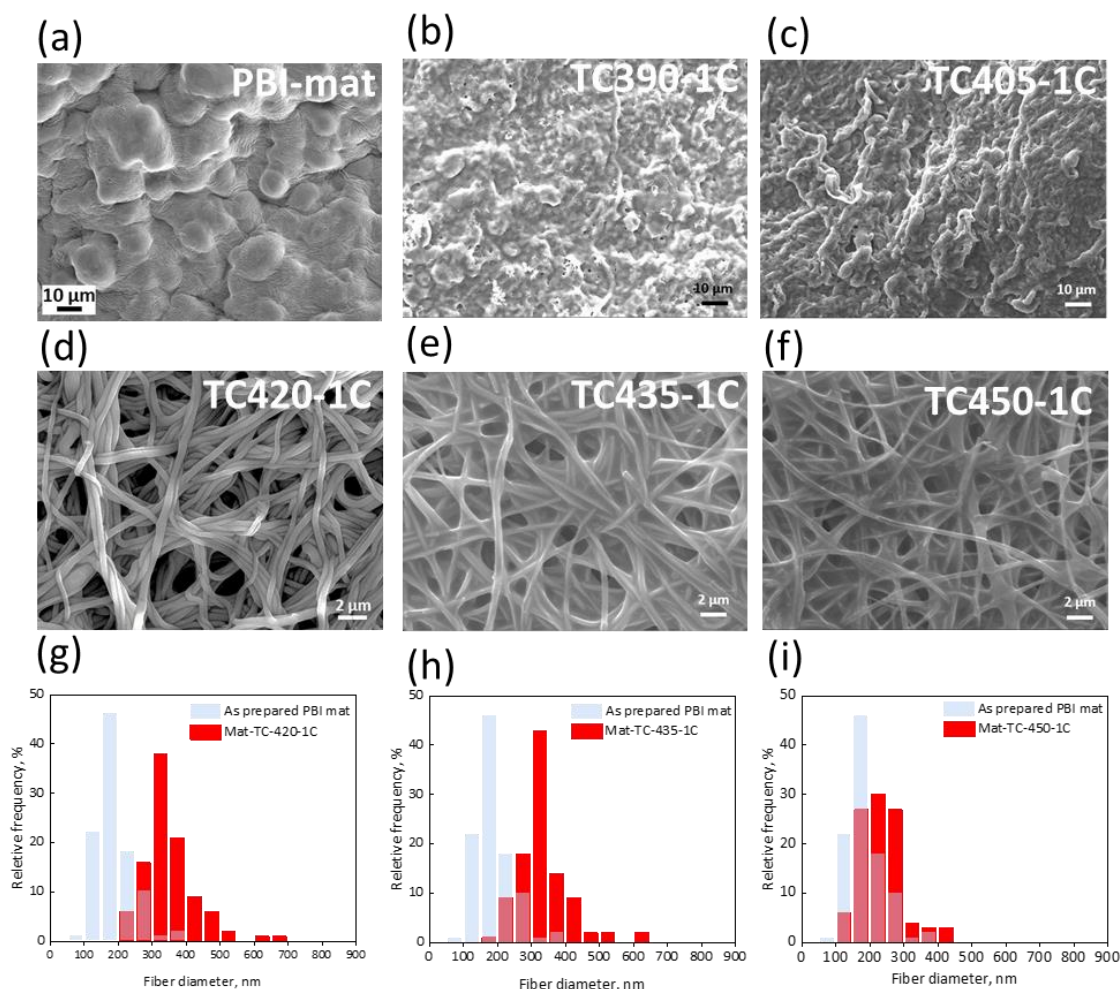


Figure 5.14 SEM images (a-f) of thermally cured fibers in 80 °C PA for 24h and fiber diameter distributions of as prepared and thermmly cured fibers at 420 (g), 435 (h) and 450°C (i).

### 5.3.8 Upscaled electrospinning

An electrospinning setup, Nanospider, was used to fabricate the PBI mats in larger sizes. The chamber atmosphere conditions were controlled at 20 °C and 20% relative humidity (RH). The spinner can fabricate mats on substrates of 50 cm width while the collector carrier can be controlled at a velocity of 4-9 mm/min. With this machine mat samples with a maximum length of 36-54 cm can be fabricated in 1 h. The presence of residual charges on the mat may reduce the speed of the electrospinning jet as it is close to the collector. Thus the later fibers may be laid down at reduced speed [305]. The pictures of obtained mats are shown in Figure 5.15. The

size of the obtained nanofiber mats was cut to the range of 23 cm x 12 cm. The mat is flat, uniform, and opaque.

Table 5.3 Summary of solution and electrospinning parameters for upscaled PBI nanofibers.

Name	Polymer solution	Mat sample name	Electrospinning conditions					Thickness ( $\mu\text{m}$ )
			Voltage (kV)	Carriage velocity* ( $\text{mm s}^{-1}$ )	Collector distance (mm)	Collector substrate	Collector carrier velocity** ( $\text{mm min}^{-1}$ )	
B1	13% PBI	Mat-10	55	100	180	Brown paper	4	10
		Mat-20	55	100	180	Brown paper	6	15
		Mat-30	55	100	180	Brown paper	9	20
B2	13% PBI 10% CrL	Mat-CrL10	45	100	180	Brown paper	4	10

\* Carriage velocity: In the nozzle-less electrospinning equipment, the solution carriage moves to determine how much solution is sprayed per unit time, which corresponds to the flow rate in the needle-based equipment.

\*\* Collector carrier velocity: The substrate used for collection moves under the drive of the roller to realize the continuous collection. The moving speed determines the amount of collection per unit area. The slower the moving speed, the more collected per unit area.

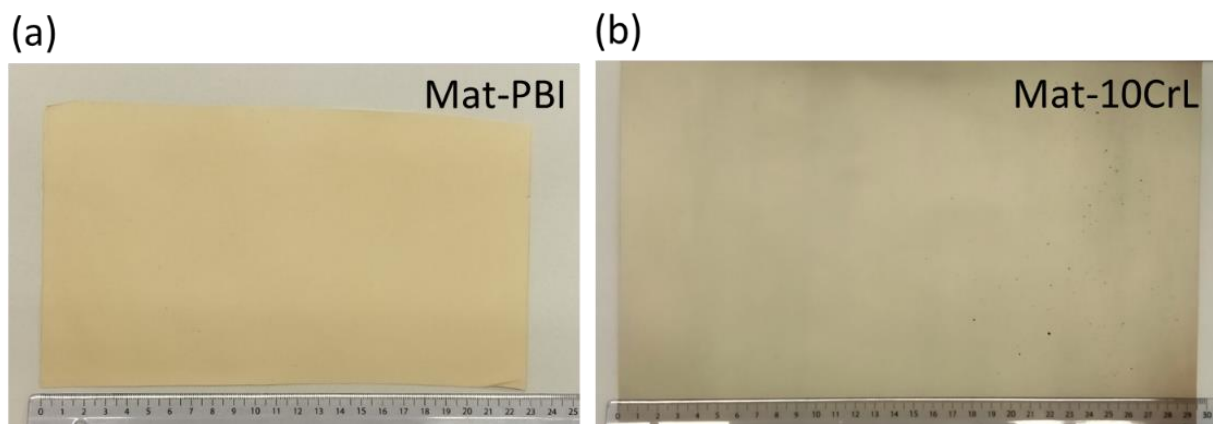


Figure 5.15 Photos of PBI fiber mats prepared using Nanospider, (a) pure PBI in 23 cm x 12 cm size, (b) PBI containing crosslinker in 29 cm x 15 cm.

### 5.3.9 Morphology characterization of upscaled PBI fiber mats

The final PBI fiber mats are prepared in 50 cm x 100 cm for composite membranes. The mat samples are examined by SEM. The surface SEM images of the PBI fiber mat reveal that the mats consist of individual, not merged fibers (Figure 5.16), having an average diameter of  $126 \pm 30$  nm. The thickness of the prepared PBI nanofiber mats was in the range of 10-30  $\mu\text{m}$ , as measured by thickness gauge. The SEM images of the cross section of the 10 and 30  $\mu\text{m}$  thick mats are shown in Figure 5.16, indicating the thickness consistency with the gauge value. As

listed in Table 5.4, the density and porosity of mats were estimated from the weight and dimensions. The porosity of mats is about 80-84% while the area specific mass of the mats is 0.20, 0.39, 0.81 mg cm<sup>-2</sup> for the 10, 20 and 30 μm thick mats, respectively.

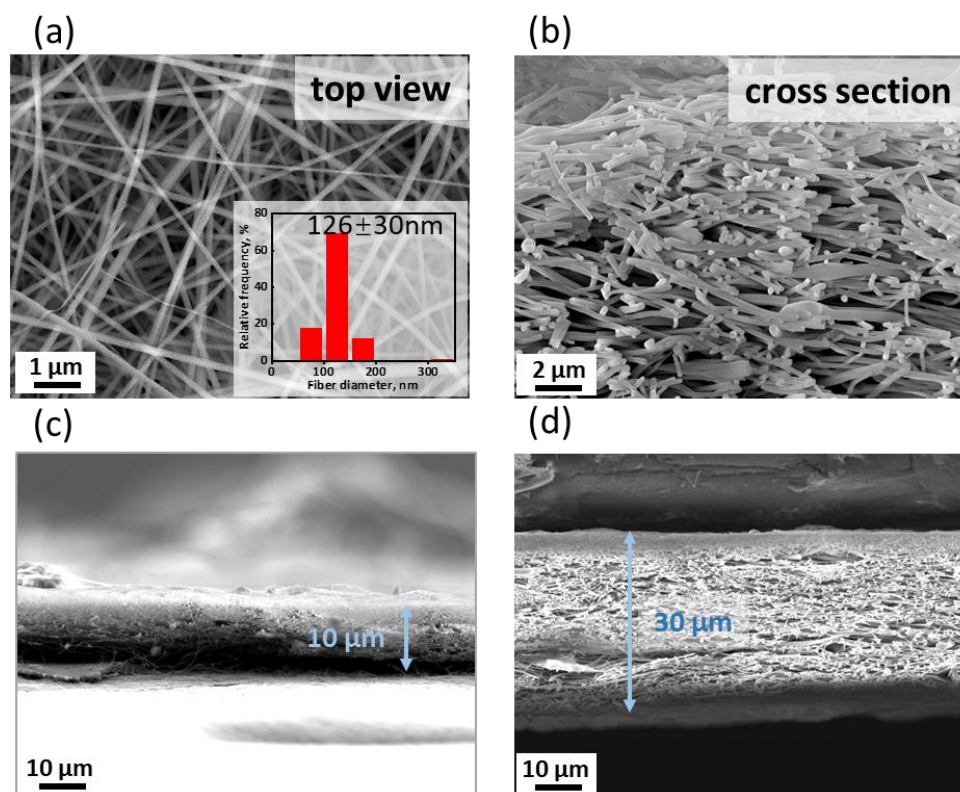


Figure 5.16 SEM images of electrospun PBI fiber mats (a) top view, (b) cross section, (c) cross section of 10 μm thick mats, (d) cross section of 30 μm thick mats.

Table 5.4 Estimated properties of PBI nanofiber mats

Sample names	Thickness (gauge, μm)	Thickness (SEM, μm)	Apparent density (g cm <sup>-3</sup> )	Porosity* (%)	Area density (g m <sup>-2</sup> )
Mat-10	9	10	0.23	82.7	2.0
Mat-20	19	-	0.20	84.3	3.9
Mat-30	31	30	0.26	79.9	8.1
Mat-10CrL	6	-	0.32	75.5	1.9

\* The porosity is estimated using the formula:  $P = 1 - \frac{\text{Weight}_{\text{mat}}/\text{volume}_{\text{mat}}}{\text{Density}_{\text{PBI}}}$  where the theoretical density of PBI is 1.3 g cm<sup>-3</sup>

## 5.4 Conclusions

Electrospinning is an facile technology to fabricate one-dimensional nanostructure materials for energy storage and conversion applications. As reinforcement for polymer electrolyte

membranes, nanofibers of aromatic heterocyclic PBI are prepared from organic solution in DMAc.

Solution and operational parameters are investigated to optimize the process including polymer concentration and additive (LiCl), spinning voltage, solution flow rate, collector substrate and location etc. The polymer concentration, as an easy way to tailor the solution viscosity, plays an important role to obtain fibers without formation of particles and beads. High spinning voltages seem to reduce the average fiber diameter and its distribution. The polymer molecular and LiCl content have been varied in a limited range and showed weak influence on the spinning product. Both conductive (e.g. aluminum foil) and non-conductive (silicone coating paper) substrates can collect the nanofibers by adjusting the distance between the collector and the syringe tip. The diameter of PBI fibers varies from 200 to 300 nanometers after drying at 200 °C for 2 hours, which are easily soluble in hot DMAc or swollen in hot phosphoric acid.

The fibers are further strengthened by thermal curing or covalent crosslinking. The thermal curing of PBI nanofibers is optimized in the temperature range from 405 to 435 °C for a duration of 10 minutes. A mixture of PBI containing 10% crosslinker (DBpX) has been successfully electrospun. The nanofibers are then crosslinked by heat-treatment at 280°C for 10 minutes in air. Both thermally cured and covalently crosslinked PBI fibers have shown very low solubility (<5%) in DMAc at 80 °C. In 85% phosphoric acid also at 80 °C the PBI fiber mats exhibit superstructure stability and swelling resistance.

Finally, a batch of PBI fiber mats are prepared in thickness of 10 to 30  $\mu\text{m}$  and of the size of up to 50 $\times$ 100  $\text{cm}^2$ . The mats have an apparent density of 0.2-0.3  $\text{g cm}^{-3}$  with an estimated porosity of 75-84%. The mats are ready for the preparation of reinforced PBI composite membranes.

# CHAPTER 6

## Composite membranes

---

### Summary of the chapter

Composite membranes reinforced by thermally cured and crosslinked PBI fiber mats are prepared. The membranes are further doped in phosphoric acid, showing anisotropic thickness and area swelling with slightly improved tensile strengths. The fuel cell tests showed improved i-V performance with high open circuit voltages, little changed hydrogen crossover and reduced ohmic resistance. The acid inventory issue in thinner membranes is identified.

## 6.1 Introduction

### 6.1.1 Thin membranes for LT- and HT-PEMFCs

In PEMFCs, a thin and robust membrane is desirable to reduce the area specific resistance. One challenge for thin membranes is the reduced mechanical strength, especially under swelling and at the fuel cell operating temperature. Another concern is the permeability of reactant gases, as already discussed in Chapter 4.

At the same time the low temperature proton exchange membrane based on perfluorosulfonic acids e.g. Nafion® the membrane has a function to allow fast water diffusion from the cathode to the anode side. A thinner membrane facilitates water management and helps to maintain the water content balance, which is essential to achieve high proton conductivity.

For acid doped PBI membranes, recent studies have shown that phosphoric acid anions ( $\text{H}_2\text{PO}_4^-$ ) migrates from the cathode to the anode through the membrane driven by the passage of current under fuel cell operation. The acid anions have a transference number of up to 4%, meaning that about 4% of the total current is carried through by the anions while the rest by protons. The migration of  $\text{H}_2\text{PO}_4^-$  results in parasitic movement of phosphoric acid, which is balanced by the back diffusion of the acid from the anode to the cathode [306]. Compared to aqueous phosphoric acid solution, the transference number of acid anions is similar but the back diffusion coefficient of the acid through PBI membranes is about one order of magnitude lower, indicating that the acid distribution through the membrane thickness is more unbalanced particularly under operation with high current densities [307]. This phenomenon is believed to be relative to the acid retention and eventual loss and therefore an issue for the long-term

lifetime of the fuel cells. A thinner PBI membrane should be effective to eliminate the acid concentration difference during fuel cell operation.

### 6.1.2 PTFE-PFSA composite membranes

In 1990s, W.L. Gore & Associates commercialized composite membranes (Gore-select®) using thin PTFE porous sheets impregnated with PFSA ionomer from both sides. Today very thin membranes of 5 - 20  $\mu\text{m}$  thick are commercially available. A set of data of Gore-select® membranes in comparison with Nafion 117 are compiled in Table 1.4 [42]. They have in general lower conductivity than Nafion®. However, by taking the thickness into account, the reinforced membranes have a significantly lower area specific resistance (ASR).

In these thin composite membranes, the porous PTFE supporting film provides mechanical strength while the Nafion ionomer provides proton conducting paths. To prepare Nafion/PTFE composite membranes, the porous PTFE film with a typical thickness of 10-20  $\mu\text{m}$  is impregnated with a 5 wt% Nafion dispersion mixed with some surfactant which helps in the dispersion of Nafion polymer chains in solutions [308]. The impregnated membranes are dried and annealed at 120-130 °C and then swollen in distilled water. The swollen membranes are immersed in isopropanol to dissolve the surfactant. Since PTFE and Nafion backbone have the same chemical structure, the Nafion backbone is compatible with the PTFE support, and the composite membranes exhibited good interface bonding between Nafion and PTFE. Therefore, no delamination between the Nafion ionomer and PTFE support occurs during the use in fuel cells. Another effect of the compatible PFSA fiber and Nafion ionomer is the resultant dense membranes which in fuel cells show low gas permeability and hence long lifetime.

The PFSA phase is highly ionic while the PTFE phase is highly dielectric, as pointed by Banerjee et al. [309]. The compatibility between these two phases is not perfect. As a result, the PTFE reinforced PFSA membranes have lower proton conductivity than predicted from the inert polymer volume fraction. The phase compatibility is a general issue for the fabrication of inorganic-organic composite membranes [223].

### 6.1.3 PTFE-PBI composite membranes

Only a few studies have been made on fiber-reinforced PBI membranes. Similar to PTFE/Nafion composites, PTFE/PBI composite membranes can be prepared by impregnation of the porous PTFE support mat with a PBI solution, followed by solvent evaporation. The porous PTFE and PBI are however poorly compatible. A common practice to improve the compatibility is to pretreat the PTFE before impregnation in order to achieve a good bonding interface between PTFE and PBI. Two methods of pretreatment have been developed i.e. by chemical activation [310] or coupling agents [242]. The chemical activation of the porous PTFE mat involves treatment in strong acid ( $\text{H}_2\text{SO}_4$ ), base (KOH) or/and  $\text{H}_2\text{O}_2$ . The typical coupling agent for the PTFE mat is the PFSA ionomer e.g. Nafion i.e. by immersing the porous PTFE mat in a Nafion solution to form a Nafion coating layer on the PTFE fiber surface. The Nafion surface coating is, on one hand, compatible with the PTFE mat while the terminal sulfonic acid ( $-\text{SO}_3\text{H}$ ) groups, on the other hand, interact with the imidazole groups of PBI.

Composite membranes using these pre-treated PTFE mats have been prepared by solution casting or dipping. Significantly improved mechanical strength has been reported so that the composite membranes can be as thin as 12-16  $\mu\text{m}$  [243]. Fuel cell tests based on these composite membranes, however, show relatively low OCV and limited durability, apparently suffering from poor compatibility of the reinforcement fiber phase and the polymer matrix phase.

In the present work, the prepared porous PBI nanofiber mats are either thermally cured or covalently crosslinked and used as reinforcement in PBI matrixes. It is essentially a two phase composite system, the crosslinked reinforcement fibers are mechanically rigid while the polymer matrix is swollen and conductive after acid doping.

## 6.2 Experimental

### 6.2.1 Fabrication of composite membranes

The fabrication of nanofiber-reinforced composite membranes is illustrated in Figure 6.1. PBI nanofiber mats were first prepared by electrospinning and crosslinked by either thermal curing at 420  $^{\circ}\text{C}$  for 10 min or covalent bonding using DBpX with a crosslinking degree of 10% at 280 $^{\circ}\text{C}$  for 10 min. The details about the processes of electrospinning and crosslinking have been described in Chapter 5.



Figure 6.1 Schematic illustration of the fabrication of the fiber-reinforced PBI composite membranes.

The collected mats were then dried at 120  $^{\circ}\text{C}$  for 1 h before use in order to remove any moisture absorbed during the storage. The dry PBI fiber mats are used for the PBI solution casting. The casting process of the fiber mat reinforced composite membranes is similar to that of the normal PBI membrane casting, as described in Chapter 4. A mat was first fixed with four stainless sticks on a petri dish that was previously wetted with ethanol. Care should be taken to remove tinny air bubbles, if any, between the mat and glass substrate to ensure that the mat was firmly stuck on the glass. A small flow of compressed air was sometimes applied to accelerate the

ethanol evaporation until the mat was dry. 5 wt% PBI solution in DMAc was then poured into the petri dish. The amount of the PBI was calculated according to the expected thickness of the final membrane. The heating process for the solvent evaporation is the same as described in Chapter 4, i.e. by slowly heating to 120 °C. The casted membranes were washed with hot water and further dried at 200 °C for 1 hour.

### 6.2.2 Redissolution of composite membranes

For testing the insolubility of the crosslinked PBI fiber mats after the composite membranes were prepared, an attempt was made to re-dissolve the composite membrane in hot DMAc. The dissolution was made by immersing the pre-weighed membrane sample in DMAc 80 °C for 2 hours. The residue sample was then taken out of DMAc, dried at 200 °C for 2 hours followed by re-weighing. The re-dissolution and drying process was repeated several times.

### 6.2.3 Acid doping and tensile strength measurement

The size, thickness, and weight of composite membranes were first measured. The membrane samples were then immersed in 85% phosphoric acid at room temperature for at least 24 h. The doping samples are kept in the acid solution at room temperature until use. The tensile strength was measured using the protocol described in Chapter 3 at room temperature and ambient atmosphere.

### 6.2.4 MEA, fuel cell test, and H<sub>2</sub> crossover measurement

The fuel cell test of composite membranes was carried out using fuel cells of 1 cm<sup>2</sup> active size. The gas diffusion electrodes were provided by Danish Power Systems with a catalyst loading of 0.9 mg Pt/cm<sup>2</sup>. The MEA is not pre-hot pressed but directly assembled in the fuel cell hardware and tightened to a standard compression of 1.5 N on 4 bolts. The detailed test procedure was described in Chapter 3. In brief, the cell was activated at a constant current density of 0.2 A/cm<sup>2</sup> and 160 °C for about 2 days before the polarization curves were recorded. I-V curves were recorded by potential scan from -0.9 V to 0 V (vs. OCV) at a scan rate of 0.002 V/s at 160 °C with H<sub>2</sub> and air at flow rates of 30 and 100 ml min<sup>-1</sup>.

Hydrogen crossover and impedance spectra measurements followed the procedures described in Chapter 4.

## 6.3 Results and discussion

### 6.3.1 Composite membrane casting

A series of composite membranes were prepared with reinforced mats. Two types of PBI mats were used: One is thermal cured at 420 °C for 10 min with the mat thickness of 10, 20, and 30 μm, respectively, and the other is covalently crosslinked using DBpX at 280 °C for 10 min, with a crosslinking degree of 10% and thicknesses of 10 μm. The obtained composite membrane samples are named Com-TC-mat thickness-membrane thickness and Com-CrL-mat thickness-membrane thickness, as listed in Table 6.1. For comparison, the PBI-20 membrane was also prepared.

As mentioned in Chapter 5, the electrospun mats are opaque. After casting, the obtained composites membranes appear transparent (Figure 6.2), indicating homogeneity of the membranes.

From the measured mass and dimension (size and thickness) of the composite membranes, the apparent density of the membranes is estimated, which is in a rough range of 1.1-1.2 g cm<sup>-3</sup>. For pure PBI membrane (PBI-20) this is estimated to be about 1.14 g cm<sup>-3</sup>. Zhao et al. [311] suggested a model for calculating the van der Waals (molecule) volume of organic compounds based on the radii of constituting atoms and the covalent bond distance between atoms. Using this method Li et al. [147] estimated the molar volume of PBI to be 164 cm<sup>3</sup>/mol. Compared this value with the theoretical density of PBI of 1.33 g/cm<sup>3</sup>, which corresponds to a molar volume of 232 cm<sup>3</sup>/mol, the porosity of pure PBI membranes was estimated to about 30%. This is much higher than the value (12%) estimated by the present work using the following formula:

$$\text{Membrane porosity (\%)} = \left(1 - \frac{\text{Apparent density}_{\text{composite}}}{\text{Density}_{\text{dense PBI}}}\right) \times 100 \quad (6.1)$$

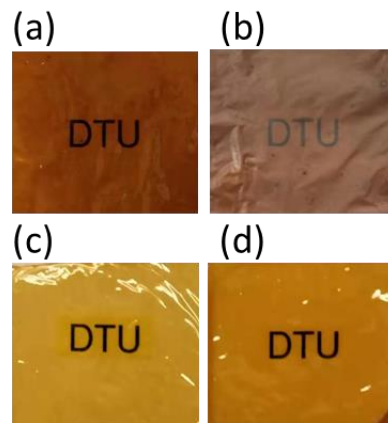


Figure 6.2 Photos of composite membranes (a) Com-TC-20-20, (b) Com-TC-30-30, (c) Com-CrL-10-10, and (d) Com-CrL-10-20.

Similarly from the apparent density of the samples, the porosity of composite membranes is estimated to be in a range from 9-15 % for composite membranes, as listed in Table 6.1. These values seem to indicate the homogeneous and dense layers of the composites, likely due to the good compatibility of the reinforcing fibers and the bulk polymer matrix.

Table 6.1 Summary of composite membrane samples and estimated properties.

Samples	Mats		Composite membranes				
	Mat type	Mat area specific mass (gm <sup>2</sup> )	Dry thickness (μm)	Apparent density (gcm <sup>-3</sup> )	Porosity (%)	Area specific mass (gm <sup>-2</sup> )	Mat content (wt%)
Com-TC-10-20	Mat-TC-10	2.0	20	1.17	10	23	9
Com-TC-20-20	Mat-TC-20	3.9	21	1.13	13	24	16
Com-CrL-10-10	Mat-CrL-10	1.9	11	1.14	12	13	15
Com-CrL-10-20	Mat-CrL-10	1.9	25	1.18	9	30	6
PBI-20	-	-	18.5	1.14	12	21	0

### 6.3.2 Mat content and residue after redissolution test

Based on the area specific mass of the composite membranes and the fiber mats, the solid content of the mat can be estimated using the following formula:

$$\text{Mat content (\%)} = \frac{\text{Area specific mas}_{\text{Mat}}}{\text{Area specific mass}_{\text{Composite}}} \times 100\% \quad (6.2)$$

The results are in the range of 6-25 wt% depending on the thickness of the reinforcing mat and the thickness of the composite membranes, as seen from Table 6.1.

To assess the stability of the PBI fiber mat in the composite membranes, an attempt was made to re-dissolve the composite membranes in DMAc at 80 °C. The pristine PBI membrane is completely dissolved in hot DMAc after a few minutes. It was expected that after immersing the composite membranes in DMAc at 80 °C the PBI matrix phase would be removed while the cross-linked PBI fiber mat remained as residue, which can be calculated as follows:

$$\text{Residue (\%)} = \text{Remaining mass} / \text{Initial mass} \times 100\% \quad (6.3)$$

where the remaining and initial masses of the composite membranes were taken after being dried at 180 °C for 2 h before test and after the re-dissolution test.

The residue of the composite membranes was, however, found to be 38-55% of the initial mass on the composite membranes after 2 hours. This is further decreased only slightly after 4 and 6 hours, even after 24 hours. It seems that a fast dissolution of only part of the PBI matrix occurred within the first 2 hours, after which only a few more percent of the polymer matrix could be dissolved during the prolonged test. Compared to the initial fiber mat content of 6-25 wt%, it is surprising that a significant amount of the PBI matrix phase (17-35%) survived the test after 24 hours.

Table 6.2 Results of the re-dissolution test of the composite membranes in hot DMAc.

Samples	Residue of the membrane (matrix) in DMAc at 80 °C, %			
	2 h	4 h	6 h	24 h
Com-TC-10-20	43.4 (38)	43.4(38)	41.0 (35)	41.0 (35)
Com-TC-20-20	49.1 (40)	34.8(22)	33.3 (21)	30.3 (17)
Com-CrL-10-10	51.8 (43)	35.0 (24)	32.5 (21)	32.5 (21)
Com-CrL-10-20	54.7 (52)	39.5 (36)	39.5 (36)	39.5 (36)

Figure 6.3 shows photos of the composite membranes before and after being immersed in DMAc at 80 °C for 24 h. It is seen that the membranes were still in integral pieces but in lighter colors, showing the decreased thickness. The phenomenon of the insolubility of the PBI matrix in hot DMAc is not understood but interesting. A possibility could be that the surface of the nanofibers initialized some bonding between the fiber mat and the polymer matrix.

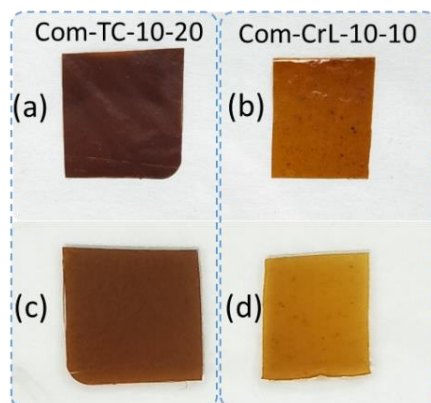


Figure 6.3 Photos of composite samples containing thermal cured (a and c) and covalently crosslinked (b and d) fiber mat immersion before (a and c) and after being immersed in DMAc 80 °C for 24 h.

### 6.3.3 Acid swelling of composite membranes

For determining the dimension change of composite membranes before and after being doped with phosphoric acid, the area and thickness of the composite membrane samples were measured. After doping in 85%  $H_3PO_4$  at room temperature for one week, the reached ADL was 11.2 for PBI-40 (standard PBI of thickness 40  $\mu m$ ), 10.3 for Com-TC420 (composite membranes with mat cured at 420 °C) and 9.6 for Com-TC435 (composite membrane with mat cured at 435 °C). The corresponding total volume swelling for three membranes was 224%, 181%, and 167%, respectively.

These results are shown in Figure 6.4a where the dashed lines through the 0-0 point indicate the trends of the volume swelling increase with the acid doping level. The slope of the lines is the specific volume swelling per molar unit of the doping acid (vol%/mol  $H_3PO_4$ ), which is found to be 20% for the reference PBI, which is consistent with that previously reported [114]. Li et al. collected a large number of the acid swelling data for PBI membranes through years and found a slope of 19 for the volume swelling-acid doping level curve [147]. At a doping level of 11 mol  $H_3PO_4$  per PRU, this value responds to a volume swelling of 209%, close to the present result, showing the significant separation of the polymer backbones when the doping acid is embedded.

The slopes for the two composite membranes are slightly lower, around 17%, indicating the restriction of the PBI fiber mat. Further analysis of the data is shown in Figure 6.4b for area and 6.4c for thickness. The presence of the reinforcement fiber mat limits the area swelling, showing a specific swelling slope of 3.5% (Com-TC420) and 1.9% (Com-TC435), smaller than that of 6.8% for the pristine PBI membrane. On the contrary, the thickness swelling of the two composite membranes is significantly larger. The specific thickness swelling is found to be 12.7 % (Com-TC420) and 10.1% (Com-TC435), compared to 7.3% for the pristine PBI membrane (Figure 6.4c).

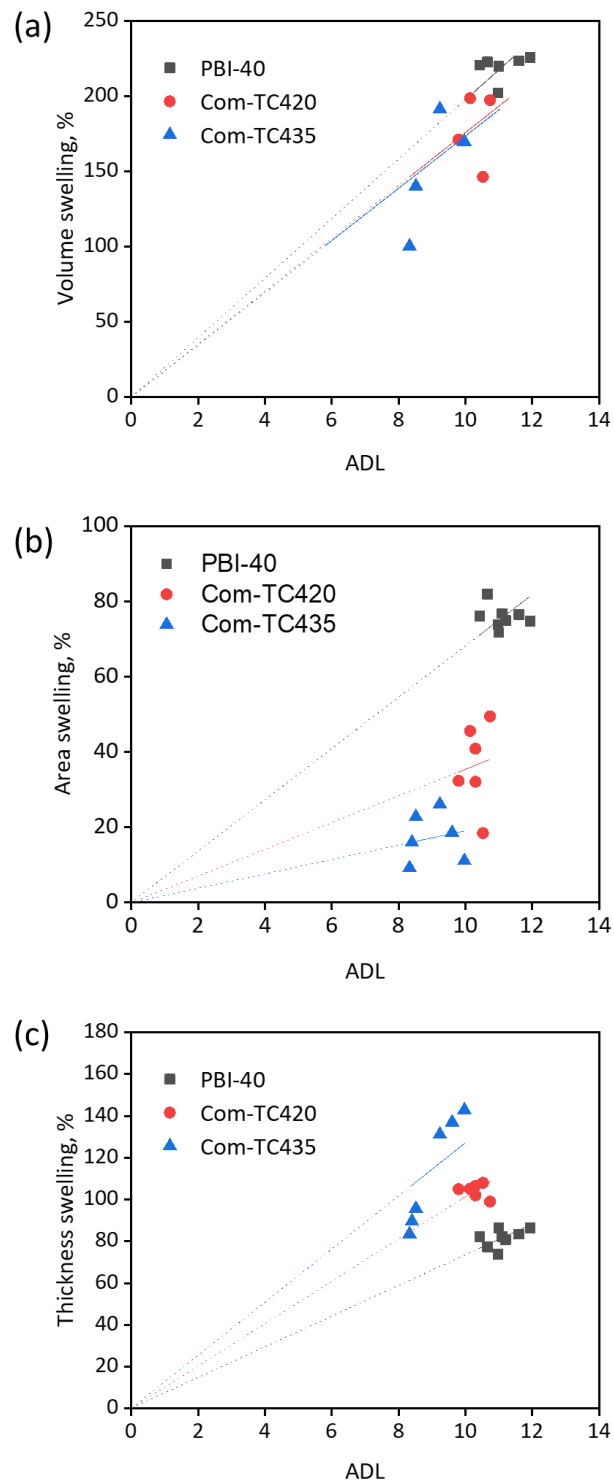


Figure 6.4 Volume (a), area (b), and thickness (c) swelling of PBI reference and composite membranes at different acid doping level.

This anisotropic swelling phenomenon is illustrated in Figure 6.5. As discussed in Chapter 5, the as-prepared fiber mat shrank significantly when immersed in hot acid, indicating the collapse of the mat structure. Thermal curing made the mat rigid and reduced the mat shrinkage.

At thermal curing temperatures of 420°C and higher, the mat structure showed little collapse but a slight swelling after being immersed in hot acid. The swelling behavior of the fiber mat during the acid doping is responsible for the anisotropy of the composite membranes, i.e. considerably reduced area swelling. On the thickness direction, the mat consists of randomly compiled fibers with a large portion of open pores and less fiber-fiber interaction. As a result, there is easy fiber-fiber sliding during the swelling [312]. From the mechanical or dimensional stability of MEAs during the fuel cell assembling and operation, particularly with thermal and load cycling, this anisotropic swelling of the composite membranes should be beneficial to stabilize the interfacial contact between electrode and membranes and hence the fuel cell long-term stability.

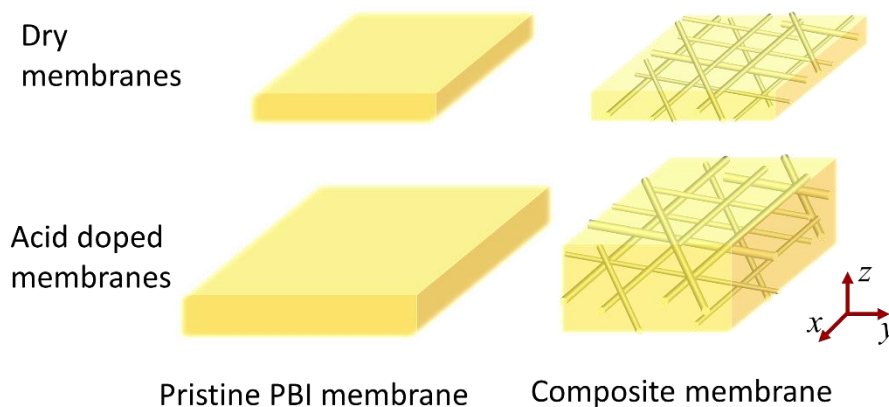


Figure 6.5 Illustration of anisotropic swelling of PBI reference and composite membranes.

#### 6.3.4 Mechanical strength

The mechanical properties of the composite membranes after PA doping were investigated by recording stress–strain curves at room temperature and ambient humidity. A set of typical curves are presented in Figure 6.6. From the stress–strain curves the tensile strength at break and Young's modulus are read and summarized in Table 6.3, together with a set of ADL and swelling data for both the PBI reference and composite membranes.

The tensile strength of the composite membranes is lower than those of the pure PBI at similar ADLs around 11. This is obviously caused by the reduction of the elongation at break due to the rigidity of the composite membranes. The Young's modulus of the composite membranes at ADL around 11 is in a range of 48.3–49.7 MPa, very much similar to the pristine PBI membrane with the same thickness.

The observation that limited improvement in the tensile strength and elastic modulus for the PBI fiber mat reinforced composite membranes does not seem very surprising by consideration of the moderate Young's modulus e.g. 11.2 MPa reported for PBI fibers of 729.9 nm diameter [313]. As loosely arranged nanofibers with a limited degree of the fiber-fiber interaction, the load-carrying capability of such mats is very low, resulting in weak load transfer from fiber to fiber when subjected to any in-plane external loading [314, 315]. In other words, the individual

fibers of the mat respond to external loads nearly independently [316, 317]. An attempt was made by Zholobko et al. [312] to heat and press the PBI fiber mat at 200 °C and found that the heating and compressive stressing can improve the mechanical properties of fiber mats by enhancing the fiber interaction and fusion. The obtained nanofiber mats showed Young's modulus of as high as 61 MPa under dry conditions, however, with a significant reduction in the size of pores and voids between fibers.

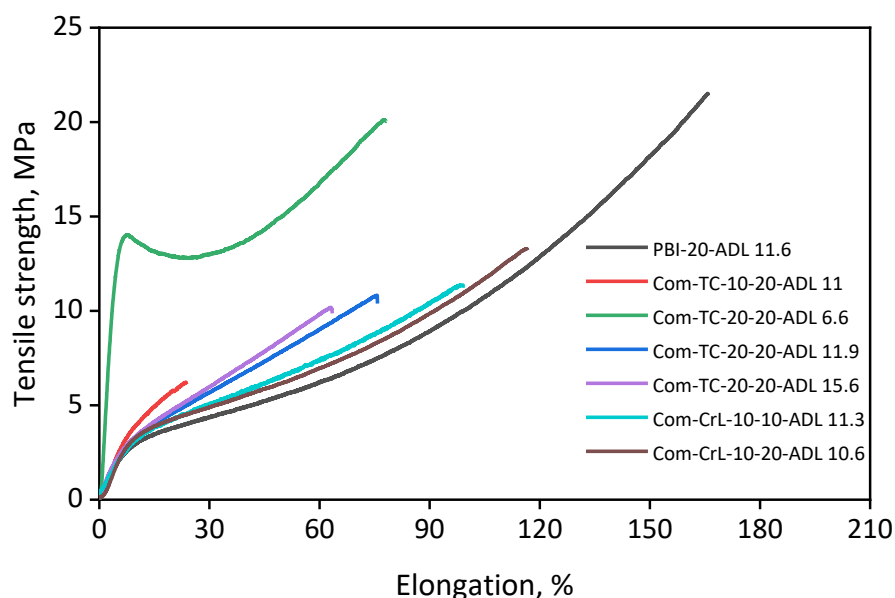


Figure 6.6 Typical stress-strain curves for PBI and fiber mat reinforced composite membranes at ambient temperature and relative humidity.

Table 6.3 Summary of the thickness, acid doping level, area swelling, and the mechanical data of doped composite membranes.

Composite membranes	Thickness swelling (%)	Area swelling (%)	ADL (mol PA/PRU)	Tensile Strength at break, MPa*	Young's Modulus, MPa*
PBI-20-ADL11.6	116.3	50.6	11.6	21.5	47.2
Com-TC-10-20-ADL 11	135	41	11	6.2	49.7
Com-TC-20-20-ADL 6.6	89.4	22.7	6.6	20.1	327.4
Com-TC-20-20-ADL 11.9	147	41	11.9	10.8	48.3
Com-TC-20-20-ADL 15.6	143	46.6	15.6	10.2	45.7
Com-CrL-10-20-ADL 10.6	140	44	10.6	13.3	39.4
PBI-10-ADL 12	120.5	43.3	12	28.5	35.4
Com-CrL-10-10-ADL 11.3	142	42.5	11.3	11.4	38.5

\* Typical data obtained from three duplicate samples.

### 6.3.5 Open circuit voltage and hydrogen crossover

The OCVs of fuel cells with PBI reference and composite membranes are listed in Table 6.4. All cells exhibit high OCVs of 0.95-1.00 V though the thickness of the membranes in their acid doped form varies from 26 to 80  $\mu\text{m}$ . This seems indicating that the hydrogen crossover through the doped PBI membranes is not a critical issue.

The hydrogen crossover was measured by chronoamperometry i.e. by recording a current-time curve under a constant potential of 0.4 V. The principle of the measurements has already been discussed and typical current-time curves are presented in Chapter 4 for pure PBI membranes with different thicknesses. A set of the hydrogen crossover current density data are also listed in Table 6.4 for PBI membranes with thickness of 40 and 80  $\mu\text{m}$ , which are 0.19 and 0.35  $\text{mA cm}^{-2}$ , respectively. These crossover currents can be translated into the hydrogen crossover rate of 10 and 18  $\times 10^{-10} \text{ mol cm}^{-2}\text{s}^{-1}$ . Taking the membrane thickness into account, the hydrogen permeability is obtained as  $7 \times 10^{-12} \text{ mol}\cdot\text{cm}^{-1}\cdot\text{s}^{-1}\cdot\text{bar}^{-1}$  for the two membranes.

*Table 6.4 Summary of fuel cell open circuit voltages and H<sub>2</sub> crossover for PBI composite membranes. The measurements were made at 160 °C under dry atmosphere (N<sub>2</sub> and H<sub>2</sub> on each side).*

Samples	Thickness ( $\mu\text{m}$ , doped)	OCV (V)	H <sub>2</sub> crossover measurement		
			Crossover current ( $\text{mA cm}^{-2}$ )	Crossover Rate ( $10^{-10} \text{ mol cm}^{-2}\text{s}^{-1}$ )	Permeability ( $10^{-12} \text{ mol cm}^{-1}\text{s}^{-1}\text{bar}^{-1}$ )
PBI-40-ADL11.0	80	1.000	0.19	9.6	7.7
PBI-20-ADL11.6	40	0.970	0.35	18.0	7.2
Com-TC-10-20-ADL11.0	45	0.99	0.39	20.2	9.1
Com-TC-20-20-ADL11.9	56	0.95	0.97	50.2	28.1
Com-TC-20-20-ADL15.6	57	0.984	1.37	70.7	40.3
Com-CrL-10-10-ADL11.3	26	0.98	0.43	22.3	5.4
Com-CrL-10-20-ADL10.6	59	1.00	0.20	10.2	6.0

The hydrogen crossover was measured by chronoamperometry i.e. by recording a current-time curve under a constant potential of 0.4 V. The principle of the measurements has already been discussed and typical current-time curves are presented in Chapter 4 for pure PBI membranes with different thicknesses. A set of the hydrogen crossover current density data are also listed in Table 6.4 for PBI membranes with thickness of 40 and 80  $\mu\text{m}$ , which are 0.19 and 0.35  $\text{mA cm}^{-2}$ , respectively. These crossover currents can be translated into the hydrogen crossover rate of 10 and 18  $\times 10^{-10} \text{ mol cm}^{-2}\text{s}^{-1}$ . Taking the membrane thickness into account, the hydrogen permeability is obtained as  $7 \times 10^{-12} \text{ mol}\cdot\text{cm}^{-1}\cdot\text{s}^{-1}\cdot\text{bar}^{-1}$  for the two membranes.

For composite membranes of smaller thicknesses, the open circuit voltage of the fuel cells is also quite high, all above 0.95 V, very comparable with pure PBI membranes. The hydrogen crossover current densities of these composite membranes seem slightly higher than those of pure PBI membranes but all are within the same order of magnitude. When the composite membrane thickness is taken into account, the obtained hydrogen permeability coefficients are somehow higher while some samples (Com-CrL-10 membranes) showed very close values to the pure PBI membranes.

For both pure and composite membranes, the correlation of OCV with the hydrogen crossover and membrane thickness is plotted in Figure 6.7. Though very scattering, a correlative trend seems existing, i.e. the OCV increases as the decrease in the hydrogen crossover current or the increase in the membrane thickness. It is more interesting that the pure PBI membranes and PBI composite membranes follow the same trend, indicating the dense structure of the fiber mat reinforced composite membranes, most likely due to the compatibility of the fiber phase and the matrix phase of the same PBI polymer.

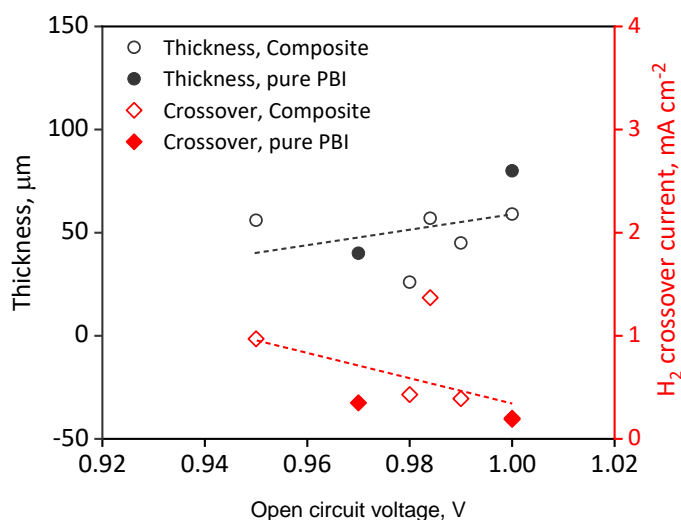


Figure 6.7 Correlation of open circuit voltages with hydrogen crossover current density and thickness of pure and composite membranes

### 6.3.6 Polarization curves

Four composite membranes, three with thermally cured and two with covalently crosslinked PBI fiber mats, were used in preparation MEAs for fuel cell test. After a break-in period of 48 hours at a constant current density of  $200 \text{ mA cm}^{-2}$ , steady state polarization curves were recorded at  $160^\circ\text{C}$  with hydrogen and air, as shown in Figure 6.8. As a single point of the fuel cell performance, the cell voltage of 0.7 V is achieved at  $0.2 \text{ A/cm}^2$ , as listed in Table 6.5.

By linear regression the obtained ohmic resistance losses and  $iR$ -free curves are also shown in Figure 6.8. It is seen that the  $iR$ -free polarization curves obtained for the four MEAs with

different membranes are well coincided, indicating the same activation loss because of the same electrodes. Another important point is that the amount of acid transferred from the membrane to the catalyst layer of the electrodes is also nearly the same, resulting in the identical electrode (ORR) performance.

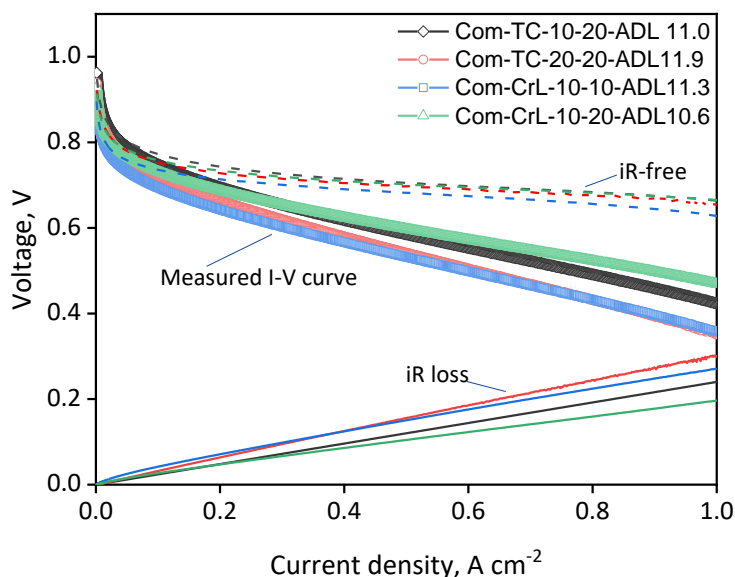


Figure 6.8 Polarization curves (as measured),  $iR$ -free fitting curves and the fitted area specific resistance of fuel cells based on four composite membranes indicated in the figure. Temperature was  $160\text{ }^{\circ}\text{C}$ ,  $\text{H}_2$  and air under ambient pressure were at a fixed flow rate of 30 and  $100\text{ mlmin}^{-1}\text{ cm}^{-1}$ .

Table 6.5 Summary of cell performances of composite membranes with cured mats at  $160\text{ }^{\circ}\text{C}$ .

Properties	Com-TC- 10-20- ADL11.0	Com-TC- 20-20- ADL11.9	Com-TC- 20-20- ADL15.6	Com-CrL- 10-10- ADL 11.3	Com-CrL- 10-20- ADL 10.6
Membrane thickness ( $\mu\text{m}$ , doped)	45	56	57	24	59
Cell voltage (V):					
- Open circuit	0.99	0.95	0.984	0.98	1
- at $0.2\text{ A cm}^{-2}$	0.695	0.677	0.701	0.691	0.698
- at $0.4\text{ A cm}^{-2}$	0.62	0.60	0.633	0.62	0.63
Power density ( $\text{W cm}^{-2}$ ) at $1.0\text{ A cm}^{-2}$	0.42	0.38	0.46	0.44	0.45
Area specific resistance ( $\Omega\text{cm}^2$ )	0.24	0.28	0.21	0.22	0.21
Membrane conductivity ( $\text{S cm}^{-1}$ )	0.019	0.020	0.027	0.027	0.011
Tafel slope (V/dec)	0.100	0.080	0.093	0.100	0.101

The fuel cell performance difference can be attributed to the ohmic losses. There are two factors affecting the ohmic resistance of these four cells: the membrane thickness and the acid content (the actual ADL) in the membranes. The obtained area specific resistance for all four

membranes is in general large, corresponding to a conductivity of about 0.02 S/cm, apparently due to the insufficient acid in the MEAs.

To verify this assumption a test was made by doping the COM-TC-20-20 membrane with a higher ADL of 15.6 mol H<sub>3</sub>PO<sub>4</sub>/PRU. The fuel cell I-V curves are shown in Figure 6.9. An improvement of the fuel cell performance was observed which is attributable to the reduction of the ohmic resistance of the membrane.

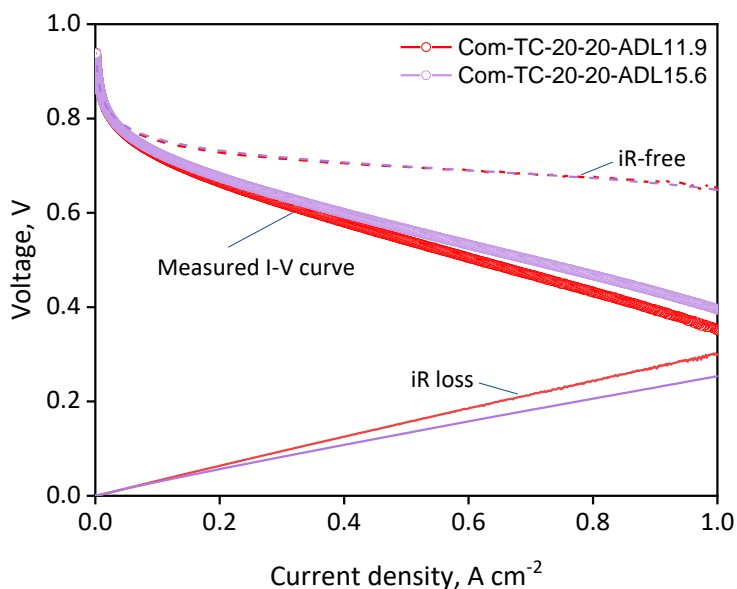


Figure 6.9 I-V curve of composite membranes (Com-TC-20-20) with acid doping levels of 11.9 and 15.6 mol H<sub>3</sub>PO<sub>4</sub>/PRU. Fuel cell test conditions were the same as Figure 6.8.

In summary, the HT-PEMFC performance can be improved by using thinner composite membranes that are reinforced by PBI fiber mats. It seems that the composite membranes are mechanically strong and structurally homogeneous and dense, with acceptable hydrogen crossover. The thin membranes are, however, containing reduced amount of doping acid. When an MEA is assembled, the acid transfers from the membrane to the catalyst layers of both electrodes. As a result, thin membranes have less remaining acid and hence increased ohmic resistance which limits the fuel cell performance. Measures much be taken to increase the total amount of acid in MEAs when thinner composite membranes are used.

## 6.4 Conclusions

A thin and robust membrane is desirable to improve the performance of HT-PEMFCs. Composite membranes with reduced thickness are prepared using PBI fiber mats as reinforcement in the PBI matrix. It is essentially a two phase composite system, the crosslinked reinforcement fibers are mechanically rigid while the polymer matrix is swollen and conductive after acid doping.

The porous PBI nanofiber mats in thickness of 10-30  $\mu\text{m}$  are fabricated by electrospinning followed by either thermal curing or covalent crosslinking. The thermal curing takes place at 420  $^{\circ}\text{C}$  for 10 minutes under an argon atmosphere while the crosslinking is achieved using

DBpX at a crosslinking degree of 10% and heated treated at 280 °C for 10 minutes in ambient atmosphere.

The obtained composite membranes by solution casting have a transparent reddish appearance at 10 μm thickness (both the mat and composite membrane) and darker brown color at 20-30 μm thickness (both the mat and composite membrane). The membranes have similar area specific masses as the reference PBI membranes of similar thicknesses, indicating the homogeneous and dense layer of the composite membranes.

Re-dissolution of the composite membranes shows that about 17-36% bulk PBI matrix remains insoluble in DMAc at 80°C after 24 hours while pristine PBI membranes are completely dissolved after minutes. The phenomenon is not understood, probably due to some bonding between the fiber mat and the polymer matrix.

Doping acid into the membranes causes membrane swelling. For pristine PBI membranes each mol H<sub>3</sub>PO<sub>4</sub> imbedded in the polymer repeat unit leads to 20% of the membrane volume swelling. At an ADL of 11, this corresponds to about a volume increase of 220 %, of which both the area swelling and the thickness swelling are about 80%.

The composite membranes reinforced with porous PBI fiber mats exhibit a slightly low specific acid swelling (17% versus 20% for pristine PBI). The presence of the fiber mat restricts the area swelling and encourages the thickness swelling. Both thermally cured and covalently crosslinked fiber mats behave in the same manner. The increased thickness swelling is attributed to the fact that the mat consists of randomly compiled fibers with minor fiber-fiber interaction and therefore an easy fiber-fiber sliding during the swelling. During the fuel cell assembling and operation with thermal and load changes, this anisotropic swelling of the composite membranes should be beneficial to stabilize the interfacial contact between electrode and membranes. This needs to be verified by the long-term durability test of fuel cells, likely stressed by startup-shutdown cycles.

The composite membranes show reduced tensile strength compared to that of pristine PBI membranes at similar acid doping levels, due to the decrease of the elongation at break of the rigid composite membranes. The elastic modulus of the composite membranes at ADL around 11-12.9 is similar to that of pristine PBI membranes with same thickness, being in a range of 39.4-49.7 MPa.

All composite membranes, though in the doped thickness ranging from 26 to 60 μm compared to 80 μm of the reference pure PBI analogue, exhibit high open circuit voltage of 0.95-1.00 V in H<sub>2</sub>-air fuel cells at 160°C. This seems confirming the dense composite membranes. The hydrogen permeability measurement by electrochemical stripping of the crossover hydrogen shows an oxidation current of around 1 mA cm<sup>-2</sup> for pure and composite membranes, corresponding to a hydrogen permeability coefficient of the 10<sup>-11</sup> mol cm<sup>-1</sup> s<sup>-1</sup> bar<sup>-1</sup> level. It indicates that the hydrogen crossover through the composite membranes in reduced thickness is not a critical issue. A weak correlation of the fuel cell OCV with the hydrogen crossover and membrane thickness is observed for both pure and composite PBI membranes.

Improved fuel cell performance is achieved with the composite membranes in reduced

thickness, reaching 0.7 V at 0.2 A cm<sup>-2</sup> operating with ambient hydrogen and air at 160°C. The expected reduction of the ohmic resistance of the membranes is however not observed. This is because the thinner membranes contain a smaller amount of acid. The acid originating from the membrane is preferably transferred to the catalyst layer of electrodes, which results in similar activation loss at the cathode ORR for cells of different thickness membranes. The remaining acid in thin membranes is hence lower, leading to larger ohmic resistance though the thickness is smaller. This is verified by a test using a higher acid doping level (15.6 mol H<sub>3</sub>PO<sub>4</sub>/PRU). Other approaches to increase the acid inventory in MEAs e.g. by introducing or storing acid in the electrode structure should be further evaluated.

## Conclusions and perspectives

---

### 7.1 Conclusions

Fuel cells have shown potential in future renewable energy system. One of the key components determining the performance of PEMFCs is the electrolyte membrane. The work presented in this thesis has focused on the development of composite membranes for high temperature polymer electrolyte fuel cell. The study is based on the use of electrospun mats to fabricating composite membranes. The acid doping level, swelling, and mechanical strength of mats were characterized, the fuel cell performance and H<sub>2</sub> crossover of the corresponding composite membranes were measured. The experimental studies yielded the following results.

The properties of thin membranes are presented in Chapter 4. Membranes with thicknesses of 10 to 40  $\mu\text{m}$  are prepared by solution casting from the PBI polymer of an average molecular weight of 58 kDa. The membranes are doped at varied acid doping levels and evaluated in fuel cell tests. At typical doping levels of 11-12 mol H<sub>3</sub>PO<sub>4</sub>/PRU, the membrane showed 100-120% thickness swelling and 43-51% area swelling. A thickness effect is observed that the thickness swelling increases while the area swelling decreases when the membrane thickness is reduced.

The fuel cell test is activated by a break-in procedure under constant current of 0.4 A cm<sup>-2</sup> for a period of 7 days. During the break-in, part of the acid originated from the membrane is transferred into the catalyst layer. The acid redistribution leads to a steady improvement of the electrode kinetics while the membrane resistance is slowly increasing. For thin membranes the total acid inventory in the membrane is small and a significant increase in the membrane ohmic resistance is observed.

MEAs with thin membranes down to 10  $\mu\text{m}$  show slightly lower open circuit voltages than that for the reference 40  $\mu\text{m}$  thick membrane but all above 0.97 V. This is in good agreement with the hydrogen crossover measurements, which show the permeability coefficient around 10<sup>-11</sup> mol cm<sup>-1</sup> s<sup>-1</sup> bar<sup>-1</sup>, corresponding to a crossover current density of < 1 mA cm<sup>-2</sup>. It seems that the gas crossover of PBI based membranes is lower than the PFSA analogues and not a critical issue for using thinner membranes in fuel cells.

The I-V data from steady state measurements are analyzed by multiple linear regression. All polarizations of membranes of different thicknesses show similar activation losses, which is about 410 mV at 1.0 A cm<sup>-2</sup>. The Tafel slope is about 0.1 V/dec. The ohmic resistance is decreasing with the membrane thickness, however, not in a simple proportional way since the membrane conductivity is changed.

Assuming that the acid transferred from the membrane to the catalyst layer is fixed, as the *iR*-free polarization plots are nearly the same for membranes of varied thicknesses, the acid remaining in the membrane after the break-in period is estimated, showing an acid inventory issue when thin membranes are used, which seems verified by the test of the same thickness membrane with a higher acid doping level.

Thermal curing and cross-linking as an approach to strengthen the membranes does not seem suiting the thinner membranes which crack during the hot-press of MEAs. Reinforcement of the membranes is attempted using PBI nanofiber mats which are prepared from the polymer solution in DMAc having a fiber diameter of 200 to 300 nanometers.

Solution and operational parameters are investigated to optimize the process including polymer concentration and additive (LiCl), applied voltage, solution flow rate, collector substrate, and location, etc. The polymer concentration and solution viscosity play an important role to obtain fibers. Other parameters investigated include polymer molecular weight (18 to 45 kDa), lithium chloride content (0-1%), %, spinning voltage (25 to 40 kV), and collector as well as its distance. PBI fiber mats in thickness of 10 to 30  $\mu\text{m}$  and the size of up to 50 x100  $\text{cm}^2$  are successfully prepared, having an apparent density of 0.2-0.3  $\text{g cm}^{-3}$  with an estimated high porosity of 75-84%.

The collected pristine nanofibers, after drying at 200  $^{\circ}\text{C}$  for 2 hours, are easily soluble in hot DMAc or collapsed in hot phosphoric acid. Further strengthening of the fiber mats is achieved by thermal curing or covalent crosslinking. The thermal curing of PBI nanofibers is optimized in the temperature range from 405 to 435  $^{\circ}\text{C}$  for a duration of 10 minutes. A mixture of PBI containing 10% crosslinker (dibromo-*p*-xylene) has been successfully electrospun. The nanofibers are then crosslinked by heat treatment at 280  $^{\circ}\text{C}$  for 10 minutes in air. Both thermally cured and covalently crosslinked PBI fibers have shown very low solubility (<5%) in DMAc at 80  $^{\circ}\text{C}$  for 24 h. In 85% phosphoric acid also at 80  $^{\circ}\text{C}$  the PBI fiber mats exhibit superstructure stability and swelling resistance.

The composite membranes reinforced using the PBI fiber mat are prepared by solution casting. The membranes have similar area specific masses as the reference PBI membranes of similar thicknesses, indicating the homogeneous and dense layer of the composite membranes.

Doping acid into the membranes causes the membrane swelling. The composite membranes reinforced with porous PBI fiber mats exhibit a slightly low specific acid swelling compared with pristine PBI reference membranes. The presence of the fiber mat restricts the area swelling and encourages the thickness swelling. The increased thickness swelling is attributed to the fact that the mat consists of randomly compiled fibers with minor fiber-fiber interaction and therefore an easy fiber-fiber sliding during the swelling.

The composite membranes show however reduced tensile strength compared to that of pure PBI membranes at similar acid doping levels, due to the decrease of the elongation at break of the rigid composite membranes. The elastic modulus of the composite membranes at ADL around 11 is slightly improved, being in a range of 48.3-49.7 MPa.

All composite membranes, though in the doped thickness ranging from 26 to 60  $\mu\text{m}$  compared

to 80  $\mu\text{m}$  of the reference pure PBI analogue, exhibit high open circuit voltage of 0.95-1.00 V in  $\text{H}_2$ -air fuel cells at 160  $^\circ\text{C}$ . This seems confirming the dense composite membranes. The hydrogen permeability measurement by electrochemical stripping of the hydrogen shows a crossover current of around 1  $\text{mA cm}^{-2}$  for pure and composite membranes, corresponding to a hydrogen permeability coefficient of the  $10^{-11} \text{ mol cm}^{-1} \text{ s}^{-1} \text{ bar}^{-1}$  level.

Improved fuel cell performance is achieved with the composite membranes in reduced thickness, reaching 0.7 V (compared to 0.67 V for pristine PBI membranes of 40  $\mu\text{m}$  thick) at 0.2  $\text{A cm}^{-2}$  operating with ambient hydrogen and air at 160 $^\circ\text{C}$ . The expected reduction of the ohmic resistance of the membranes is however not observed. This is because the thinner membranes contain a smaller amount of acid. The acid originating from the membrane is preferably transferred to the catalyst layer of electrodes, which results in similar activation loss at the cathode ORR for cells of different thickness membranes. The remaining acid in thin membranes is hence lower, leading to larger ohmic resistance though the thickness is smaller.

## 7.2 Perspectives

The concept of using thinner membranes by means of fiber mat reinforcement is proofed showing the phase compatibility and membrane compactness. The concerns of high hydrogen permeability and hence lower open circuit voltage of fuel cells seem of little relevance, however, the expected improvement of the mechanical strength of the composite membranes is not observed. In addition, the acid inventory issue in MEAs using thinner membranes is raised. Due to the limited time of the project, evaluation of the long-term stability and durability of the composite membranes has not been performed. This is critical in connection to the acid inventory issue. The technical and economic feasibility of the PBI fiber mat reinforcement cannot be assessed without the knowledge of long-term durability. The following is my considerations and suggestions for the near future work on this subject:

1. The durability test should be prioritized, which can be conducted through membrane-focused accelerated stressing test using, for example, high current density load or with thermal load cycling.
2. The acid is preferably adsorbed in the catalyst layer, resulting in a low acid content in thin membranes. Further increase in the acid doping level should be carefully assessed by consideration of membrane mechanical stability and gas crossover. Storage of extra acid to the catalyst layers, particularly on the anode side, might be a solution deserving exploration.
3. Another strategy is to store the acid in a composite membrane with a multilayer structure. Preliminary work has been done jointly with other researchers in the group, showing promising results. The work will be published separately.



# Bibliography

---

- [1] W. Nicholson, Account of the new electrical or galvanic apparatus of Sig. Alex. Volta, and experiments performed with the same. *Journal of natural philosophy, chemistry and the arts*, 1800, **4**, 179-191.
- [2] W.R. Grove, On voltaic series and the combination of gases by platinum. *Philosophical Magazine Series 3*, 1839, **14**(86-87), 127-130.
- [3] C.F. Schœnbein, On the voltaic polarization of certain solid and fluid substances. *The London, Edinburgh, and Dublin Philosophical Magazine and Journal of Science*, 1838, **14**(85), 43-45.
- [4] L. Mond, C. Langer, V. A new form of gas battery. *Proceedings of the Royal Society of London*, 1889, **46**(280-285), 296-304.
- [5] F.T. Bacon, Fuel cells, past, present and future. *Electrochimica Acta*, 1969, **14**(7), 569-585.
- [6] F.T. Bacon, T. Fry, Review Lecture-The development and practical application of fuel cells. *Proceedings of the Royal Society of London. A. Mathematical and Physical Sciences*, 1973, **334**(1599), 427-452.
- [7] P. Howard, C. Greenhill, Ballard PEM fuel cell powered ZEV bus, SAE Technical Paper, 1993.
- [8] E4tech, The Fuel Cell Industry Review 2020. 2020.
- [9] J.D. Larminie, Andrew, Fuel Cell systems Explained, 2003.
- [10] A.B. Stambouli, E. Traversa, Fuel cells, an alternative to standard sources of energy. *Renew Sust Energ Rev*, 2002, **6**(3), 295-304.
- [11] Z. Sun, B.C. Lin, F. Yan, Anion-Exchange Membranes for Alkaline Fuel-Cell Applications: The Effects of Cations. *Chemsuschem*, 2018, **11**(1), 58-70.
- [12] G. Couture, A. Alaaeddine, F. Boschet, B. Ameduri, Polymeric materials as anion-exchange membranes for alkaline fuel cells. *Progress in Polymer Science*, 2011, **36**(11), 1521-1557.
- [13] N.J. Cherepy, R. Krueger, K.J. Fiet, A.F. Jankowski, J.F. Cooper, Direct conversion of carbon fuels in a molten carbonate fuel cell. *J Electrochem Soc*, 2005, **152**(1), A80-A87.
- [14] A.L. Dicks, Molten carbonate fuel cells. *Current Opinion in Solid State and Materials Science*, 2004, **8**(5), 379-383.
- [15] M.A. Laguna-Bercero, Recent advances in high temperature electrolysis using solid oxide fuel cells: A review. *J Power Sources*, 2012, **203**, 4-16.
- [16] E.D. Wachsman, K.T. Lee, Lowering the temperature of solid oxide fuel cells. *Science*, 2011, **334**(6058), 935-9.
- [17] A. Afif, N. Radenahmad, Q. Cheok, S. Shams, J.H. Kim, A.K. Azad, Ammonia-fed fuel cells: a comprehensive review. *Renew Sust Energ Rev*, 2016, **60**, 822-835.
- [18] M. Boder, R. Dittmeyer, Catalytic modification of conventional SOFC anodes with a view to reducing their activity for direct internal reforming of natural gas. *J Power Sources*, 2006, **155**(1), 13-22.
- [19] J. Ahrenfeldt, T.P. Thomsen, U. Henriksen, L.R. Clausen, Biomass gasification cogeneration – A review of state of the art technology and near future perspectives. *Applied Thermal Engineering*, 2013, **50**(2), 1407-1417.
- [20] Y. Jiang, A.V. Virkar, A high performance, anode-supported solid oxide fuel cell operating on direct alcohol. *J Electrochem Soc*, 2001, **148**(7), A706-A709.

## Bibliography

---

- [21] E4tech, The Fuel Cell Industry Review 2019. 2019.
- [22] Y. Wang, K.S. Chen, J. Mishler, S.C. Cho, X.C. Adroher, A review of polymer electrolyte membrane fuel cells: Technology, applications, and needs on fundamental research. *Applied Energy*, 2011, **88**(4), 981-1007.
- [23] J.-H. Wee, Applications of proton exchange membrane fuel cell systems. *Renew Sust Energ Rev*, 2007, **11**(8), 1720-1738.
- [24] A. Bazylak, Liquid water visualization in PEM fuel cells: A review. *International Journal of Hydrogen Energy*, 2009, **34**(9), 3845-3857.
- [25] R.E. Rosli, A.B. Sulong, W.R.W. Daud, M.A. Zulkifley, T. Husaini, M.I. Rosli, E.H. Majlan, M.A. Haque, A review of high-temperature proton exchange membrane fuel cell (HT-PEMFC) system. *International Journal of Hydrogen Energy*, 2017, **42**(14), 9293-9314.
- [26] R. Othman, A.L. Dicks, Z. Zhu, Non precious metal catalysts for the PEM fuel cell cathode. *International journal of hydrogen energy*, 2012, **37**(1), 357-372.
- [27] A. Hermann, T. Chaudhuri, P. Spagnol, Bipolar plates for PEM fuel cells: A review. *International journal of hydrogen Energy*, 2005, **30**(12), 1297-1302.
- [28] D.J. Kim, M.J. Jo, S.Y. Nam, A review of polymer–nanocomposite electrolyte membranes for fuel cell application. *Journal of Industrial and Engineering Chemistry*, 2015, **21**, 36-52.
- [29] S. Banerjee, D.E. Curtin, Nafion® perfluorinated membranes in fuel cells. *Journal of Fluorine Chemistry*, 2004, **125**(8), 1211-1216.
- [30] S. Litster, G. McLean, PEM fuel cell electrodes. *J Power Sources*, 2004, **130**(1-2), 61-76.
- [31] J. Xie, D.L. Wood, K.L. More, P. Atanassov, R.L. Borup, Microstructural changes of membrane electrode assemblies during PEFC durability testing at high humidity conditions. *J Electrochem Soc*, 2005, **152**(5), A1011-A1020.
- [32] L. Chong, J. Wen, J. Kubal, F.G. Sen, J. Zou, J. Greeley, M. Chan, H. Barkholtz, W. Ding, D.J. Liu, Ultralow-loading platinum-cobalt fuel cell catalysts derived from imidazolate frameworks. *Science*, 2018, **362**(6420), 1276-1281.
- [33] W. Grubb, L. Niedrach, Batteries with Solid Ion-Exchange Membrane Electrolytes II. Low-Temperature Hydrogen-Oxygen Fuel Cells. *J Electrochem Soc*, 1960, **107**(2), 131-135.
- [34] W.G. Grot, Perfluorinated ion exchange polymers and their use in research and industry. *Macromolecular Symposia*, 1994, **82**(1), 161-172.
- [35] Q.F. Li, R.H. He, J.O. Jensen, N.J. Bjerrum, Approaches and recent development of polymer electrolyte membranes for fuel cells operating above 100 degrees C. *Chemistry of Materials*, 2003, **15**(26), 4896-4915.
- [36] H. Zhang, P.K. Shen, Recent Development of Polymer Electrolyte Membranes for Fuel Cells. *Chemical Reviews*, 2012, **112**(5), 2780-2832.
- [37] A. Kraysberg, Y. Ein-Eli, Review of Advanced Materials for Proton Exchange Membrane Fuel Cells. *Energy & Fuels*, 2014, **28**(12), 7303-7330.
- [38] K.D. Kreuer, On the complexity of proton conduction phenomena. *Solid State Ionics*, 2000, **136**, 149-160.
- [39] A. Kusoglu, A.Z. Weber, New Insights into Perfluorinated Sulfonic-Acid Ionomers. *Chem Rev*, 2017, **117**(3), 987-1104.
- [40] T.E. Springer, T.A. Zawodzinski, S. Gottesfeld, Polymer electrolyte fuel cell model. *J Electrochem Soc*, 1991, **138**(8), 2334-2342.
- [41] A. Ghielmi, P. Vaccarono, C. Troglia, V. Arcella, Proton exchange membranes based on the short-side-chain perfluorinated ionomer. *J Power Sources*, 2005, **145**(2), 108-115.

## Bibliography

---

- [42] M. Nakao, M. Yoshitake, Handbook of Fuel Cells: Fundamentals, Technology and Applications, ed. W. Vielstich, HA Gasteiger and A. Lamm, John Wiley & Sons, Ltd, England, 2003.
- [43] S. Bose, T. Kuila, X.L.N. Thi, N.H. Kim, K.T. Lau, J.H. Lee, Polymer membranes for high temperature proton exchange membrane fuel cell: Recent advances and challenges. *Progress in Polymer Science*, 2011, **36**(6), 813-843.
- [44] A. Chandan, M. Hattenberger, A. El-Kharouf, S.F. Du, A. Dhir, V. Self, B.G. Pollet, A. Ingram, W. Bujalski, High temperature (HT) polymer electrolyte membrane fuel cells (PEMFC) - A review. *J Power Sources*, 2013, **231**, 264-278.
- [45] H. Xu, Y. Song, H.R. Kunz, J.M. Fenton, Operation of PEM fuel cells at 120–150°C to improve CO tolerance. *J Power Sources*, 2006, **159**(2), 979-986.
- [46] M. Boaventura, H. Sander, K.A. Friedrich, A. Mendes, The influence of CO on the current density distribution of high temperature polymer electrolyte membrane fuel cells. *Electrochimica Acta*, 2011, **56**(25), 9467-9475.
- [47] K. Oh, H. Ju, Temperature dependence of CO poisoning in high-temperature proton exchange membrane fuel cells with phosphoric acid-doped polybenzimidazole membranes. *International Journal of Hydrogen Energy*, 2015, **40**(24), 7743-7753.
- [48] C. Pan, R.H. He, Q.F. Li, J.O. Jensen, N.J. Bjerrum, H.A. Hjølmand, A.B. Jensen, Integration of high temperature PEM fuel cells with a methanol reformer. *J Power Sources*, 2005, **145**(2), 392-398.
- [49] J.S. Wainright, J.T. Wang, D. Weng, R.F. Savinell, M. Litt, Acid-Doped Polybenzimidazoles - a New Polymer Electrolyte. *J Electrochem Soc*, 1995, **142**(7), L121-L123.
- [50] Q.F. Li, J.O. Jensen, R.F. Savinell, N.J. Bjerrum, High temperature proton exchange membranes based on polybenzimidazoles for fuel cells. *Progress in Polymer Science*, 2009, **34**(5), 449-477.
- [51] S. Subianto, Recent advances in polybenzimidazole/phosphoric acid membranes for high-temperature fuel cells. *Polymer International*, 2014, **63**(7), 1134-1144.
- [52] D. Aili, J. Yang, K. Jankova, D. Henkensmeier, Q. Li, From polybenzimidazoles to polybenzimidazoliums and polybenzimidazolides. *J Mater Chem A*, 2020, **8**(26), 12854-12886.
- [53] J. Zhang, D. Aili, S. Lu, Q. Li, S.P. Jiang, Advancement toward Polymer Electrolyte Membrane Fuel Cells at Elevated Temperatures. *Research (Wash D C)*, 2020, **2020**, 9089405.
- [54] D. Aili, D. Henkensmeier, S. Martin, B. Singh, Y. Hu, J.O. Jensen, L.N. Cleemann, Q.F. Li, Polybenzimidazole-Based High-Temperature Polymer Electrolyte Membrane Fuel Cells: New Insights and Recent Progress. *Electrochemical Energy Reviews*, 2020, **3**(4), 793-845.
- [55] C. Yang, P. Costamagna, S. Srinivasan, J. Benziger, A.B. Bocarsly, Approaches and technical challenges to high temperature operation of proton exchange membrane fuel cells. *J Power Sources*, 2001, **103**(1), 1-9.
- [56] S.M. Haile, D.A. Boysen, C.R. Chisholm, R.B. Merle, Solid acids as fuel cell electrolytes. *Nature*, 2001, **410**(6831), 910-3.
- [57] K. Genzaki, P. Heo, M. Sano, T. Hibino, Proton Conductivity and Solid Acidity of Mg-, In-, and Al-Doped SnP<sub>2</sub>O<sub>7</sub>. *J Electrochem Soc*, 2009, **156**(7), B806.
- [58] Y. Cheng, J. Zhang, S. Lu, H. Kuang, J. Bradley, R. De Marco, D. Aili, Q. Li, C.Q. Cui, S.P. Jiang, High CO tolerance of new SiO<sub>2</sub> doped phosphoric acid/polybenzimidazole polymer electrolyte membrane fuel cells at high temperatures of 200–250 °C. *International Journal of Hydrogen Energy*, 2018, **43**(49), 22487-22499.
- [59] A. Kalathil, A. Raghavan, B. Kandasubramanian, Polymer Fuel Cell Based on Polybenzimidazole Membrane: A Review. *Polymer-Plastics Technology and Materials*, 2018, **58**(5), 465-497.
- [60] J. Mader, L. Xiao, T.J. Schmidt, B.C. Benicewicz, Polybenzimidazole/Acid Complexes as High-Temperature

## Bibliography

---

- Membranes, in: G.G. Scherer (Ed.), Fuel cells II2008, pp. 63-124.
- [61] A.A. Tahir, I.N.H.M. Amin, Advancement in Phosphoric Acid Doped Polybenzimidazole Membrane for High Temperature PEM Fuel Cells: A Review. *Journal of Applied Membrane Science & Technology*, 2018, **23**(1).
- [62] J.A. Asensio, E.M. Sanchez, P. Gomez-Romero, Proton-conducting membranes based on benzimidazole polymers for high-temperature PEM fuel cells. A chemical quest. *Chem Soc Rev*, 2010, **39**(8), 3210-39.
- [63] X. Sun, S.C. Simonsen, T. Norby, A. Chatzitakis, Composite Membranes for High Temperature PEM Fuel Cells and Electrolysers: A Critical Review. *Membranes*, 2019, **9**(7), 83.
- [64] V. Vijayakumar, K. Kim, S.Y. Nam, Recent Advances in Polybenzimidazole (PBI)-based Polymer Electrolyte Membranes for High Temperature Fuel Cell Applications. *Applied Chemistry for Engineering*, 2019, **30**(6), 643-651.
- [65] J.S. Yang, L.N. Cleemann, T. Steenberg, C. Terkelsen, Q.F. Li, J.O. Jensen, H.A. Hjuler, N.J. Bjerrum, R.H. He, High Molecular Weight Polybenzimidazole Membranes for High Temperature PEMFC. *Fuel Cells*, 2014, **14**(1), 7-15.
- [66] E. Quartarone, S. Angioni, P. Mustarelli, Polymer and Composite Membranes for Proton-Conducting, High-Temperature Fuel Cells: A Critical Review. *Materials (Basel)*, 2017, **10**(7).
- [67] S.S. Araya, F. Zhou, V. Liso, S.L. Sahlin, J.R. Vang, S. Thomas, X. Gao, C. Jeppesen, S.K. Kær, A comprehensive review of PBI-based high temperature PEM fuel cells. *International Journal of Hydrogen Energy*, 2016, **41**(46), 21310-21344.
- [68] B.K. Clark, R.I. Maxwell, Polybenzimidazoles, Google Patents, 1959.
- [69] H. Vogel, C.S. Marvel, Polybenzimidazoles, New Thermally Stable Polymers. *J Polym Sci*, 1961, **50**(154), 511-&.
- [70] E.W. Neuse, Aromatic polybenzimidazoles. Syntheses, properties, and applications, Synthesis and Degradation Rheology and Extrusion, Springer1982, pp. 1-42.
- [71] E.-W. Choe, Catalysts for the preparation of polybenzimidazoles. *Journal of Applied Polymer Science*, 1994, **53**(5), 497-506.
- [72] E.W. Choe, Single-stage melt polymerization process for the production of high molecular weight polybenzimidazole, Google Patents, 1982.
- [73] Q. Li, D. Aili, H.A. Hjuler, J.O. Jensen, High Temperature Polymer Electrolyte Membrane Fuel Cells, 2009.
- [74] Y. Iwakura, K. Uno, Y. Imai, Polyphenylenebenzimidazoles. *Journal of Polymer Science Part A: General Papers*, 1964, **2**(6), 2605-2615.
- [75] J. Lobato, P. Cañizares, M.A. Rodrigo, J.J. Linares, G. Manjavacas, Synthesis and characterisation of poly[2,2-(m-phenylene)-5,5-benzimidazole] as polymer electrolyte membrane for high temperature PEMFCs. *Journal of Membrane Science*, 2006, **280**(1-2), 351-362.
- [76] T. Dippel, K. Kreuer, J. Lassegues, D. Rodriguez, Proton conductivity in fused phosphoric acid; A <sup>1</sup>H/<sup>31</sup>P PFG-NMR and QNS study. *Solid State Ionics*, 1993, **61**(1-3), 41-46.
- [77] L.X. Xiao, H.F. Zhang, E. Scanlon, L.S. Ramanathan, E.W. Choe, D. Rogers, T. Apple, B.C. Benicewicz, High-temperature polybenzimidazole fuel cell membranes via a sol-gel process. *Chemistry of Materials*, 2005, **17**(21), 5328-5333.
- [78] L. Xiao, H. Zhang, T. Jana, E. Scanlon, R. Chen, E.W. Choe, L.S. Ramanathan, S. Yu, B.C. Benicewicz, Synthesis and Characterization of Pyridine-Based Polybenzimidazoles for High Temperature Polymer Electrolyte Membrane Fuel Cell Applications. *Fuel Cells*, 2005, **5**(2), 287-295.

## Bibliography

---

- [79] B. Xing, O. Savadogo, The effect of acid doping on the conductivity of polybenzimidazole (PBI). *J New Mat Elect Syst*, 1999, **2**(2), 95-101.
- [80] R. Bouchet, Proton conduction in acid doped polybenzimidazole. *Solid State Ionics*, 1999, **118**(3-4), 287-299.
- [81] X. Glipa, B. Bonnet, B. Mula, D.J. Jones, J. Rozière, Investigation of the conduction properties of phosphoric and sulfuric acid doped polybenzimidazole. *J Mater Chem*, 1999, **9**(12), 3045-3049.
- [82] M. Kawahara, J. Morita, M. Rikukawa, K. Sanui, N. Ogata, Synthesis and proton conductivity of thermally stable polymer electrolyte: poly(benzimidazole) complexes with strong acid molecules. *Electrochimica Acta*, 2000, **45**(8-9), 1395-1398.
- [83] H. Pu, W.H. Meyer, G. Wegner, Proton transport in polybenzimidazole blended with H<sub>3</sub>PO<sub>4</sub> or H<sub>2</sub>SO<sub>4</sub>. *Journal of Polymer Science Part B: Polymer Physics*, 2002, **40**(7), 663-669.
- [84] T.-S. Chung, A critical review of polybenzimidazoles: Historical development and future R&D. *J Macromol Sci R M C*, 1997, **C37**(2), 277-301.
- [85] T.R. Hanley, T.E. Helminiak, C.L. Benner, Expansion of aromatic heterocyclic polymers in salt solution. *Journal of Applied Polymer Science*, 1978, **22**(10), 2965-2978.
- [86] Andreas., Development of proton conducting polybenzimidazole membranes, DTU energy, Technical University of Denmark, Denmark, 2018.
- [87] J.P. Melchior, G. Majer, K.D. Kreuer, Why do proton conducting polybenzimidazole phosphoric acid membranes perform well in high-temperature PEM fuel cells? *Phys Chem Chem Phys*, 2016, **19**(1), 601-612.
- [88] A. Kirkebaek, D. Aili, D. Henkensmeier, J.O. Jensen, Q.F. Li, Gel Electrolytes of Covalent Network Polybenzimidazole and Phosphoric Acid by Direct Casting. *Macromolecular Materials and Engineering*, 2017, **302**(12).
- [89] S. Yu, L. Xiao, B.C. Benicewicz, Durability Studies of PBI-based High Temperature PEMFCs. *Fuel Cells*, 2008, **8**(3-4), 165-174.
- [90] S. Yu, H. Zhang, L. Xiao, E.W. Choe, B.C. Benicewicz, Synthesis of Poly (2,2'-(1,4-phenylene) 5,5'-bibenzimidazole) (para-PBI) and Phosphoric Acid Doped Membrane for Fuel Cells. *Fuel Cells*, 2009, **9**(4), 318-324.
- [91] G. Qian, B.C. Benicewicz, Synthesis and characterization of high molecular weight hexafluoroisopropylidene-containing polybenzimidazole for high-temperature polymer electrolyte membrane fuel cells. *Journal of Polymer Science Part A: Polymer Chemistry*, 2009, **47**(16), 4064-4073.
- [92] S. Yu, B.C. Benicewicz, Synthesis and Properties of Functionalized Polybenzimidazoles for High-Temperature PEMFCs. *Macromolecules*, 2009, **42**(22), 8640-8648.
- [93] A.T. Pingitore, F. Huang, G. Qian, B.C. Benicewicz, Durable High Polymer Content m/p-Polybenzimidazole Membranes for Extended Lifetime Electrochemical Devices. *ACS Applied Energy Materials*, 2019, **2**(3), 1720-1726.
- [94] X. Chen, G. Qian, M.A. Molle, B.C. Benicewicz, H.J. Ploehn, High temperature creep behavior of phosphoric acid-polybenzimidazole gel membranes. *Journal of Polymer Science Part B: Polymer Physics*, 2015, **53**(21), 1527-1538.
- [95] J.A. Mader, B.C. Benicewicz, Synthesis and Properties of Random Copolymers of Functionalised Polybenzimidazoles for High Temperature Fuel Cells. *Fuel Cells*, 2011, **11**(2), 212-221.
- [96] D. Hoel, E. Grunwald, High protonic conduction of polybenzimidazole films. *The Journal of Physical Chemistry*, 1977, **81**(22), 2135-2136.
- [97] E. Powers, G. Serad, High performance polymers: their origin and development. *Elsevier Science, New York*,

## Bibliography

---

- 1986.
- [98] S.M. Aharoni, M.H. Litt, Synthesis and some properties of poly-(2, 5-trimethylene benzimidazole) and poly-(2, 5-trimethylene benzimidazole hydrochloride). *Journal of Polymer Science: Polymer Chemistry Edition*, 1974, **12**(3), 639-650.
- [99] Y.L. Ma, J.S. Wainright, M.H. Litt, R.F. Savinell, Conductivity of PBI membranes for high-temperature polymer electrolyte fuel cells. *J Electrochem Soc*, 2004, **151**(1), A8-A16.
- [100] N.N. Greenwood, A. Thompson, The mechanism of electrical conduction in fused phosphoric and trideuterophosphoric acids. *Journal of the Chemical Society (Resumed)*, 1959, 3485.
- [101] N.N. Greenwood, A. Thompson, Anomalous conduction in phosphoric acid hemihydrate,  $2\text{H}_3\text{PO}_4 \cdot \text{H}_2\text{O}$ . *Journal of the Chemical Society (Resumed)*, 1959, 3864.
- [102] R.H. He, Q.F. Li, G. Xiao, N.J. Bjerrum, Proton conductivity of phosphoric acid doped polybenzimidazole and its composites with inorganic proton conductors. *Journal of Membrane Science*, 2003, **226**(1-2), 169-184.
- [103] A. Schechter, R.F. Savinell, Imidazole and 1-methyl imidazole in phosphoric acid doped polybenzimidazole, electrolyte for fuel cells. *Solid State Ionics*, 2002, **147**(1-2), 181-187.
- [104] D. Weng, J. Wainright, U. Landau, R. Savinell, Electro-osmotic drag coefficient of water and methanol in polymer electrolytes at elevated temperatures. *J Electrochem Soc*, 1996, **143**(4), 1260.
- [105] S.R. Samms, S. Wasmus, R.F. Savinell, Thermal stability of proton conducting acid doped polybenzimidazole in simulated fuel cell environments. *J Electrochem Soc*, 1996, **143**(4), 1225-1232.
- [106] M. Jaffe, M.I. Haider, J. Mencil, J. Rafalko, Thermal characterization of high performance PBI and 6F polymers and their alloys. *Polymer Engineering & Science*, 1992, **32**(17), 1236-1241.
- [107] A. LaConti, M. Hamdan, R. McDonald, Mechanisms of membrane degradation. *Handbook of fuel cells*, 2010.
- [108] Q. Li, J.O. Jensen, C. Pan, V. Bandur, M.S. Nilsson, F. Schönberger, A. Chromik, M. Hein, T. Häring, J. Kerres, N.J. Bjerrum, Partially Fluorinated Aarylene Polyethers and their Ternary Blends with PBI and  $\text{H}_3\text{PO}_4$ . Part II. Characterisation and Fuel Cell Tests of the Ternary Membranes. *Fuel Cells*, 2008, **8**(3-4), 188-199.
- [109] P. Noyé, Q. Li, C. Pan, N.J. Bjerrum, Cross-linked polybenzimidazole membranes for high temperature proton exchange membrane fuel cells with dichloromethyl phosphinic acid as a cross-linker. *Polym Advan Technol*, 2008, **19**(9), 1270-1275.
- [110] Q. Li, C. Pan, J.O. Jensen, P. Noyé, N.J. Bjerrum, Cross-Linked Polybenzimidazole Membranes for Fuel Cells. *Chemistry of Materials*, 2007, **19**(3), 350-352.
- [111] R.A. Gaudiana, R.T. Conley, Weak-link versus active carbon degradation routes in the oxidation of aromatic heterocyclic systems. *Journal of Polymer Science Part B: Polymer Letters*, 1969, **7**(11), 793-801.
- [112] Q. Li, R. He, J.O. Jensen, N.J. Bjerrum, PBI-Based Polymer Membranes for High Temperature Fuel Cells - Preparation, Characterization and Fuel Cell Demonstration. *Fuel Cells*, 2004, **4**(3), 147-159.
- [113] M. Litt, R. Ameri, Y. Wang, R. Savinell, J. Wainwright, Polybenzimidazoles/phosphoric acid solid polymer electrolytes: mechanical and electrical properties. *MRS Online Proceedings Library Archive*, 1998, **548**.
- [114] R.H. He, Q.F. Li, A. Bach, J.O. Jensen, N.J. Bjerrum, Physicochemical properties of phosphoric acid doped polybenzimidazole membranes for fuel cells. *Journal of Membrane Science*, 2006, **277**(1-2), 38-45.
- [115] L. Xiao, H. Zhang, T. Jana, E. Scanlon, R. Chen, E.W. Choe, L. Ramanathan, S. Yu, B. Benicewicz, Synthesis and characterization of pyridine-based polybenzimidazoles for high temperature polymer electrolyte membrane fuel cell applications. *Fuel Cells*, 2005, **5**(2), 287-295.

## Bibliography

---

- [116] S.A. Stern, The “barrer” permeability unit. *Journal of Polymer Science Part A-2: Polymer Physics*, 1968, **6**(11), 1933-1934.
- [117] J. Sanchez-Lainez, B. Zornoza, S. Friebe, J. Caro, S. Cao, A. Sabetghadam, B. Seoane, J. Gascon, F. Kapteijn, C. Le Guillouzer, G. Clet, M. Daturi, C. Tellez, J. Coronas, Influence of ZIF-8 particle size in the performance of polybenzimidazole mixed matrix membranes for pre-combustion CO<sub>2</sub> capture and its validation through interlaboratory test. *Journal of Membrane Science*, 2016, **515**, 45-53.
- [118] A. Eguizábal, J. Lemus, M. Urbiztondo, O. Garrido, J. Soler, J.A. Blazquez, M.P. Pina, Novel hybrid membranes based on polybenzimidazole and ETS-10 titanosilicate type material for high temperature proton exchange membrane fuel cells: A comprehensive study on dense and porous systems. *J Power Sources*, 2011, **196**(21), 8994-9007.
- [119] H. Zamora, P. Canizares, M.A. Rodrigo, J. Lobato, Improving of Micro Porous Layer based on Advanced Carbon Materials for High Temperature Proton Exchange Membrane Fuel Cell Electrodes. *Fuel Cells*, 2015, **15**(2), 375-383.
- [120] J. Lobato, P. Canizares, M.A. Rodrigo, D. Ubeda, F.J. Pinar, J.J. Linares, Optimisation of the Microporous Layer for a Polybenzimidazole-Based High Temperature PEMFC - Effect of Carbon Content. *Fuel Cells*, 2010, **10**(5), 770-777.
- [121] J. Lobato, P. Cañizares, M.A. Rodrigo, C.-G. Piuleac, S. Curteanu, J.J. Linares, Direct and inverse neural networks modelling applied to study the influence of the gas diffusion layer properties on PBI-based PEM fuel cells. *International Journal of Hydrogen Energy*, 2010, **35**(15), 7889-7897.
- [122] J. Lobato, P. Canizares, M.A. Rodrigo, C. Ruiz-Lopez, J.J. Linares, Influence of the Teflon loading in the gas diffusion layer of PBI-based PEM fuel cells. *Journal of Applied Electrochemistry*, 2008, **38**(6), 793-802.
- [123] K.D. Baik, B.K. Hong, M.S. Kim, Effects of operating parameters on hydrogen crossover rate through Nafion (R) membranes in polymer electrolyte membrane fuel cells. *Renew Energ*, 2013, **57**, 234-239.
- [124] K.D. Baik, B.K. Hong, M.S. Kim, Novel technique for measuring oxygen crossover through the membrane in polymer electrolyte membrane fuel cells. *International Journal of Hydrogen Energy*, 2013, **38**(21), 8927-8933.
- [125] X.-Z. Yuan, S. Zhang, H. Wang, J. Wu, J.C. Sun, R. Hiesgen, K.A. Friedrich, M. Schulze, A. Haug, Degradation of a polymer exchange membrane fuel cell stack with Nafion® membranes of different thicknesses: Part I. In situ diagnosis. *J Power Sources*, 2010, **195**(22), 7594-7599.
- [126] P. Gode, G. Lindbergh, G. Sundholm, In-situ measurements of gas permeability in fuel cell membranes using a cylindrical microelectrode. *Journal of Electroanalytical Chemistry*, 2002, **518**(2), 115-122.
- [127] S.C. Kumbharkar, P.B. Karadkar, U.K. Kharul, Enhancement of gas permeation properties of polybenzimidazoles by systematic structure architecture. *Journal of membrane science*, 2006, **286**(1-2), 161-169.
- [128] D.R. Pesiri, B. Jorgensen, R.C. Dye, Thermal optimization of polybenzimidazole meniscus membranes for the separation of hydrogen, methane, and carbon dioxide. *Journal of Membrane Science*, 2003, **218**(1-2), 11-18.
- [129] J.H. Liao, Q.F. Li, H.C. Rudbeck, J.O. Jensen, A. Chromik, N.J. Bjerrum, J. Kerres, W. Xing, Oxidative Degradation of Polybenzimidazole Membranes as Electrolytes for High Temperature Proton Exchange Membrane Fuel Cells. *Fuel Cells*, 2011, **11**(6), 745-755.
- [130] Y.-C. Chiang, D.-S. Tsai, Y.-H. Liu, C.-W. Chiang, PEM fuel cells of poly(2,5-benzimidazole) ABPBI membrane electrolytes doped with phosphoric acid and metal phosphates. *Materials Chemistry and Physics*,

- 2018, **216**, 485-490.
- [131] F. Viva, N. Heredia, S.P. Palmbaum, L. Diaz, J. De Diego, M. Lozano, M. Bruno, H. Corti, Spray-Casting ABPBI Membranes for High Temperature PEM Fuel Cells. *J Electrochem Soc*, 2017, **164**(7), F866-F872.
- [132] R. Rath, P. Kumar, L. Unnikrishnan, S. Mohanty, S.K. Nayak, Current Scenario of Poly (2,5-Benzimidazole) (ABPBI) as Prospective PEM for Application in HT-PEMFC. *Polymer Reviews*, 2019, 1-51.
- [133] H.-Y. Li, Y.-L. Liu, Polyelectrolyte composite membranes of polybenzimidazole and crosslinked polybenzimidazole-polybenzoxazine electrospun nanofibers for proton exchange membrane fuel cells. *J Mater Chem A*, 2013, **1**(4), 1171-1178.
- [134] D. Aili, L.N. Cleemann, Q.F. Li, J.O. Jensen, E. Christensen, N.J. Bjerrum, Thermal curing of PBI membranes for high temperature PEM fuel cells. *J Mater Chem*, 2012, **22**(12), 5444-5453.
- [135] F. Mack, K. Aniol, C. Ellwein, J. Kerres, R. Zeis, Novel phosphoric acid-doped PBI-blends as membranes for high-temperature PEM fuel cells. *J Mater Chem A*, 2015, **3**(20), 10864-10874.
- [136] R.F. Kovar, F. Arnold, Para-ordered polybenzimidazole. *Journal of Polymer Science: Polymer Chemistry Edition*, 1976, **14**(11), 2807-2817.
- [137] T.-H. Kim, T.-W. Lim, J.-C. Lee, High-temperature fuel cell membranes based on mechanically stable para-ordered polybenzimidazole prepared by direct casting. *J Power Sources*, 2007, **172**(1), 172-179.
- [138] B. Zhao, L. Cheng, Y. Bei, S. Wang, J. Cui, H. Zhu, X. Li, Q. Zhu, Grafted polybenzimidazole copolymers bearing polyhedral oligosilsesquioxane pendant moieties. *European Polymer Journal*, 2017, **94**, 99-110.
- [139] A.R. Kim, M. Vinothkannan, D.J. Yoo, Sulfonated-fluorinated copolymer blending membranes containing SPEEK for use as the electrolyte in polymer electrolyte fuel cells (PEFC). *International Journal of Hydrogen Energy*, 2017, **42**(7), 4349-4365.
- [140] M. Cui, Z. Zhang, T. Yuan, H. Yang, L. Wu, E. Bakangura, T. Xu, Proton-conducting membranes based on side-chain-type sulfonated poly(ether ketone/ether benzimidazole)s via one-pot condensation. *Journal of Membrane Science*, 2014, **465**, 100-106.
- [141] J. Yang, Q. Li, L.N. Cleemann, C. Xu, J.O. Jensen, C. Pan, N.J. Bjerrum, R. He, Synthesis and properties of poly(aryl sulfone benzimidazole) and its copolymers for high temperature membrane electrolytes for fuel cells. *J Mater Chem*, 2012, **22**(22), 11185.
- [142] J. Jouanneau, R. Mercier, L. Gonon, G. Gebel, Synthesis of Sulfonated Polybenzimidazoles from Functionalized Monomers: Preparation of Ionic Conducting Membranes. *Macromolecules*, 2007, **40**(4), 983-990.
- [143] J.A. Asensio, S. Borrós, P. Gómez-Romero, Polymer Electrolyte Fuel Cells Based on Phosphoric Acid-Impregnated Poly(2,5-benzimidazole) Membranes. *J Electrochem Soc*, 2004, **151**(2), A304.
- [144] J.A. Asensio, P. Gómez-Romero, Recent Developments on Proton Conducting Poly(2,5-benzimidazole) (ABPBI) Membranes for High Temperature Polymer Electrolyte Membrane Fuel Cells. *Fuel Cells*, 2005, **5**(3), 336-343.
- [145] J. Yang, Y. Xu, L. Zhou, Q. Che, R. He, Q. Li, Hydroxyl pyridine containing polybenzimidazole membranes for proton exchange membrane fuel cells. *Journal of Membrane Science*, 2013, **446**, 318-325.
- [146] T.-H. Kim, S.-K. Kim, T.-W. Lim, J.-C. Lee, Synthesis and properties of poly(aryl ether benzimidazole) copolymers for high-temperature fuel cell membranes. *Journal of Membrane Science*, 2008, **323**(2), 362-370.
- [147] Q.F. Li, H.C. Rudbeck, A. Chromik, J.O. Jensen, C. Pan, T. Steenberg, M. Calverley, N.J. Bjerrum, J. Kerres, Properties, degradation and high temperature fuel cell test of different types of PBI and PBI blend membranes. *Journal of Membrane Science*, 2010, **347**(1-2), 260-270.

## Bibliography

---

- [148] M.R. Berber, N. Nakashima, Bipyridine-based polybenzimidazole membranes with outstanding hydrogen fuel cell performance at high temperature and non-humidifying conditions. *Journal of Membrane Science*, 2019, **591**, 117354.
- [149] P. Muthuraja, S. Prakash, V.M. Shanmugam, P. Manisankar, Stable nanofibrous poly(aryl sulfone ether benzimidazole) membrane with high conductivity for high temperature PEM fuel cells. *Solid State Ionics*, 2018, **317**, 201-209.
- [150] J. Yang, Q. Li, L.N. Cleemann, J.O. Jensen, C. Pan, N.J. Bjerrum, R. He, Crosslinked Hexafluoropropylidene Polybenzimidazole Membranes with Chloromethyl Polysulfone for Fuel Cell Applications. *Advanced Energy Materials*, 2013, **3**(5), 622-630.
- [151] J. Yang, D. Aili, Q. Li, L.N. Cleemann, J.O. Jensen, N.J. Bjerrum, R. He, Covalently cross-linked sulfone polybenzimidazole membranes with poly(vinylbenzyl chloride) for fuel cell applications. *ChemSusChem*, 2013, **6**(2), 275-82.
- [152] H. Dai, H. Zhang, H. Zhong, H. Jin, X. Li, S. Xiao, Z. Mai, Properties of Polymer Electrolyte Membranes Based on Poly(Aryl Ether Benzimidazole) and Sulphonated Poly(Aryl Ether Benzimidazole) for High Temperature PEMFCs. *Fuel Cells*, 2010, **10**(5), 754-761.
- [153] J. Li, X. Li, Y. Zhao, W. Lu, Z. Shao, B. Yi, High-temperature proton-exchange-membrane fuel cells using an ether-containing polybenzimidazole membrane as electrolyte. *ChemSusChem*, 2012, **5**(5), 896-900.
- [154] J. Hu, J. Luo, P. Wagner, O. Conrad, C. Agert, Anhydrous proton conducting membranes based on electron-deficient nanoparticles/PBI-OO/PFSA composites for high-temperature PEMFC. *Electrochem Commun*, 2009, **11**(12), 2324-2327.
- [155] J.A. Kerres, Blended and Cross-Linked Ionomer Membranes for Application in Membrane Fuel Cells. *Fuel Cells*, 2005, **5**(2), 230-247.
- [156] D. Joseph, N.N. Krishnan, D. Henkensmeier, J.H. Jang, S.H. Choi, H.-J. Kim, J. Han, S.W. Nam, Thermal crosslinking of PBI/sulfonated polysulfone based blend membranes. *J Mater Chem A*, 2017, **5**(1), 409-417.
- [157] T. Søndergaard, L.N. Cleemann, H. Becker, D. Aili, T. Steenberg, H.A. Hjuler, L. Seerup, Q. Li, J.O. Jensen, Long-term durability of HT-PEM fuel cells based on thermally cross-linked polybenzimidazole. *J Power Sources*, 2017, **342**, 570-578.
- [158] T. Ossiander, M. Perchthaler, C. Heinzl, C. Scheu, Influence of thermal post-curing on the degradation of a cross-linked polybenzimidazole-based membrane for high temperature polymer electrolyte membrane fuel cells. *J Power Sources*, 2014, **267**, 323-328.
- [159] J. Kerres, V. Atanasov, Cross-linked PBI-based high-temperature membranes: Stability, conductivity and fuel cell performance. *International Journal of Hydrogen Energy*, 2015, **40**(42), 14723-14735.
- [160] G.A. Giffin, S. Galbiati, M. Walter, K. Aniol, C. Ellwein, J. Kerres, R. Zeis, Interplay between structure and properties in acid-base blend PBI-based membranes for HT-PEM fuel cells. *Journal of Membrane Science*, 2017, **535**, 122-131.
- [161] J. Kerres, F. Schönberger, A. Chromik, T. Häring, Q. Li, J.O. Jensen, C. Pan, P. Noyé, N.J. Bjerrum, Partially Fluorinated Arylene Polyethers and Their Ternary Blend Membranes with PBI and H<sub>3</sub>PO<sub>4</sub>. Part I. Synthesis and Characterisation of Polymers and Binary Blend Membranes. *Fuel Cells*, 2008, **8**(3-4), 175-187.
- [162] J. Kerres, W. Zhang, A. Ullrich, C.M. Tang, M. Hein, V. Gogel, T. Frey, L. Jorissen, Synthesis and characterization of polyaryl blend membranes having different composition, different covalent and/or ionic cross-linking density, and their application to DMFC. *Desalination*, 2002, **147**(1-3), 173-178.
- [163] J.A. Kerres, A. Katzfuß, A. Chromik, V. Atanasov, Sulfonated poly(styrene)s-PBIOO® blend membranes:

## Bibliography

---

- Thermo-oxidative stability and conductivity. *Journal of Applied Polymer Science*, 2014, **131**(4).
- [164] T. Yamamoto, Method for producing bridged polymer membrane and fuel cell, Google Patents, 2004.
- [165] H. Xu, K. Chen, X. Guo, J. Fang, J. Yin, Synthesis of hyperbranched polybenzimidazoles and their membrane formation. *Journal of membrane science*, 2007, **288**(1-2), 255-260.
- [166] M.B. Sheratte, Linear and cross-linked polybenzimidazoles, Google Patents, 1979.
- [167] M.J. Sansone, Crosslinking of polybenzimidazole polymer with divinyl sulfone, Google Patents, 1987.
- [168] D. Aili, Q. Li, E. Christensen, J.O. Jensen, N.J. Bjerrum, Crosslinking of polybenzimidazole membranes by divinylsulfone post-treatment for high-temperature proton exchange membrane fuel cell applications. *Polymer International*, 2011, **60**(8), 1201-1207.
- [169] I.B. Valtcheva, P. Marchetti, A.G. Livingston, Crosslinked polybenzimidazole membranes for organic solvent nanofiltration (OSN): Analysis of crosslinking reaction mechanism and effects of reaction parameters. *Journal of Membrane Science*, 2015, **493**, 568-579.
- [170] K.Y. Wang, Y. Xiao, T.-S. Chung, Chemically modified polybenzimidazole nanofiltration membrane for the separation of electrolytes and cephalixin. *Chemical Engineering Science*, 2006, **61**(17), 5807-5817.
- [171] K.Y. Wang, Q. Yang, T.S. Chung, R. Rajagopalan, Enhanced forward osmosis from chemically modified polybenzimidazole (PBI) nanofiltration hollow fiber membranes with a thin wall. *Chemical Engineering Science*, 2009, **64**(7), 1577-1584.
- [172] S.-K. Kim, T. Ko, S.-W. Choi, J.O. Park, K.-H. Kim, C. Pak, H. Chang, J.-C. Lee, Durable cross-linked copolymer membranes based on poly(benzoxazine) and poly(2,5-benzimidazole) for use in fuel cells at elevated temperatures. *J Mater Chem*, 2012, **22**(15), 7194.
- [173] C. Liu, X. Wang, Y.M. Li, S.H. Zhang, J.Y. Wang, X.G. Jian, Novel cross-linked membranes based on polybenzoxazine and polybenzimidazole containing 4-phenyl phthalazinone moiety for high-temperature proton exchange membrane. *Journal of Polymer Research*, 2017, **24**(2).
- [174] L. Wang, Z. Liu, Y. Liu, L. Wang, Crosslinked polybenzimidazole containing branching structure with no sacrifice of effective N-H sites: Towards high-performance high-temperature proton exchange membranes for fuel cells. *Journal of Membrane Science*, 2019, **583**, 110-117.
- [175] J. Yang, H. Jiang, L. Gao, J. Wang, Y. Xu, R. He, Fabrication of crosslinked polybenzimidazole membranes by trifunctional crosslinkers for high temperature proton exchange membrane fuel cells. *International Journal of Hydrogen Energy*, 2018, **43**(6), 3299-3307.
- [176] S.-K. Kim, S.-W. Choi, W.S. Jeon, J.O. Park, T. Ko, H. Chang, J.-C. Lee, Cross-Linked Benzoxazine–Benzimidazole Copolymer Electrolyte Membranes for Fuel Cells at Elevated Temperature. *Macromolecules*, 2012, **45**(3), 1438-1446.
- [177] E. Abouzari-lotf, M.M. Nasef, M. Zakeri, A. Ahmad, A. Ripin, Composite membranes based on heteropolyacids and their applications in fuel cells, *Organic-Inorganic Composite Polymer Electrolyte Membranes*, Springer 2017, pp. 99-131.
- [178] P. Kallem, N. Yanar, H. Choi, Nanofiber-Based Proton Exchange Membranes: Development of Aligned Electrospun Nanofibers for Polymer Electrolyte Fuel Cell Applications. *ACS Sustainable Chemistry & Engineering*, 2018, **7**(2), 1808-1825.
- [179] A.S. Rewar, H.D. Chaudhari, R. Illathvalappil, K. Sreekumar, U.K. Kharul, New approach of blending polymeric ionic liquid with polybenzimidazole (PBI) for enhancing physical and electrochemical properties. *J Mater Chem A*, 2014, **2**(35), 14449-14458.
- [180] P. Kallem, M. Drobek, A. Jube, E.J. Vriezokolk, R. Mallada, M.P. Pina, Hierarchical Porous

## Bibliography

---

- Polybenzimidazole Microsieves: An Efficient Architecture for Anhydrous Proton Transport via Polyionic Liquids. *Acs Applied Materials & Interfaces*, 2017, **9**(17), 14844-14857.
- [181] D. J. Jones, J. Roziere, Inorganic/organic composite membranes, in: Wolf Vielstich, Hubert A. Gasteiger, A. Lamm (Eds.), *Handbook of Fuel Cells-Fundamentals, Technology and Applications*, Wiley 2003, pp. 447-455.
- [182] S. Singha, T. Jana, Structure and properties of polybenzimidazole/silica nanocomposite electrolyte membrane: influence of organic/inorganic interface. *ACS Appl Mater Interfaces*, 2014, **6**(23), 21286-96.
- [183] S. Maity, S. Singha, T. Jana, Low acid leaching PEM for fuel cell based on polybenzimidazole nanocomposites with protic ionic liquid modified silica. *Polymer*, 2015, **66**, 76-85.
- [184] X. Li, H. Ma, P. Wang, Z. Liu, J. Peng, W. Hu, Z. Jiang, B. Liu, Construction of High-Performance, High-Temperature Proton Exchange Membranes through Incorporating SiO<sub>2</sub> Nanoparticles into Novel Cross-linked Polybenzimidazole Networks. *ACS applied materials & interfaces*, 2019, **11**(34), 30735-30746.
- [185] A. Lysova, A. Yaroslavtsev, New Proton-Conducting Membranes Based on Phosphorylated Polybenzimidazole and Silica. *Inorganic Materials*, 2019, **55**(5), 470-476.
- [186] A.A. Lysova, I.I. Ponomarev, A.B. Yaroslavtsev, Effect of the nature of functional groups grafted on the surface of silica nanoparticles on properties of the hybrid proton-conductive membranes based on N-phosphorylated polybenzimidazole. *Mendeleev Communications*, 2019, **29**(4), 403-404.
- [187] J. Lobato, P. Cañizares, M.A. Rodrigo, D. Úbeda, F.J. Pinar, Enhancement of the fuel cell performance of a high temperature proton exchange membrane fuel cell running with titanium composite polybenzimidazole-based membranes. *J Power Sources*, 2011, **196**(20), 8265-8271.
- [188] J. Lobato, P. Cañizares, M.A. Rodrigo, D. Úbeda, F.J. Pinar, A novel titanium PBI-based composite membrane for high temperature PEMFCs. *Journal of membrane science*, 2011, **369**(1-2), 105-111.
- [189] F.J. Pinar, P. Cañizares, M.A. Rodrigo, D. Úbeda, J. Lobato, Titanium composite PBI-based membranes for high temperature polymer electrolyte membrane fuel cells. Effect on titanium dioxide amount. *RSC advances*, 2012, **2**(4), 1547-1556.
- [190] F.J. Pinar, P. Cañizares, M.A. Rodrigo, D. Úbeda, J. Lobato, Long-term testing of a high-temperature proton exchange membrane fuel cell short stack operated with improved polybenzimidazole-based composite membranes. *J Power Sources*, 2015, **274**, 177-185.
- [191] M.M. Nasef, T. Fujigaya, E. Abouzari-Lotf, N. Nakashima, Electrospinning of poly(vinylpyrrolidone) template for formation of ZrO<sub>2</sub> nanoclusters for enhancing properties of composite proton conducting membranes. *International Journal of Polymeric Materials and Polymeric Biomaterials*, 2017, **66**(6), 289-298.
- [192] V. Di Noto, J. Rivetti, F. Bertasi, E. Negro, K. Vezzù, S. Lavina, Nanocomposite Membranes Based on PBI and ZrO<sub>2</sub> for HTPEMFCs, Meeting Abstracts, The Electrochemical Society, 2014, pp. 1017-1017.
- [193] D. Plackett, A. Siu, Q.F. Li, C. Pan, J.O. Jensen, S.F. Nielsen, A.A. Permyakova, N.J. Bjerrum, High-temperature proton exchange membranes based on polybenzimidazole and clay composites for fuel cells. *Journal of Membrane Science*, 2011, **383**(1-2), 78-87.
- [194] X. Zhang, Q. Liu, L. Xia, D. Huang, X. Fu, R. Zhang, S. Hu, F. Zhao, X. Li, X. Bao, Poly (2, 5-benzimidazole)/sulfonated sepiolite composite membranes with low phosphoric acid doping levels for PEMFC applications in a wide temperature range. *Journal of membrane science*, 2019, **574**, 282-298.
- [195] X. Zhang, X. Fu, S. Yang, Y. Zhang, R. Zhang, S. Hu, X. Bao, F. Zhao, X. Li, Q. Liu, Design of sepiolite-supported ionogel-embedded composite membranes without proton carrier wastage for wide-temperature-range operation of proton exchange membrane fuel cells. *J Mater Chem A*, 2019, **7**(25), 15288-15301.

## Bibliography

---

- [196] Y. Lv, Z. Li, M. Song, P. Sun, X. Yin, S. Wang, Preparation and properties of ZrPA doped CMPSU cross-linked PBI based high temperature and low humidity proton exchange membranes. *Reactive and Functional Polymers*, 2019, **137**, 57-70.
- [197] Y. Özdemir, N. Üregen, Y. Devrim, Polybenzimidazole based nanocomposite membranes with enhanced proton conductivity for high temperature PEM fuel cells. *International Journal of Hydrogen Energy*, 2017, **42**(4), 2648-2657.
- [198] C. Xue, J. Zou, Z. Sun, F. Wang, K. Han, H. Zhu, Graphite oxide/functionalized graphene oxide and polybenzimidazole composite membranes for high temperature proton exchange membrane fuel cells. *International Journal of Hydrogen Energy*, 2014, **39**(15), 7931-7939.
- [199] N. Üregen, K. Pehlivanoglu, Y. Özdemir, Y. Devrim, Development of polybenzimidazole/graphene oxide composite membranes for high temperature PEM fuel cells. *International Journal of Hydrogen Energy*, 2017, **42**(4), 2636-2647.
- [200] Y. Cai, Z. Yue, X. Teng, S. Xu, Phosphoric Acid Doped Crosslinked Polybenzimidazole/Modified Graphene Oxide Composite Membranes for High Temperature Proton Exchange Membrane Applications. *J Electrochem Soc*, 2018, **165**(11), F914-F920.
- [201] Y. Cai, Z. Yue, S. Xu, A novel polybenzimidazole composite modified by sulfonated graphene oxide for high temperature proton exchange membrane fuel cells in anhydrous atmosphere. *Journal of Applied Polymer Science*, 2017, **134**(25).
- [202] Y. Cai, Z. Yue, X. Teng, S. Xu, Radiation grafting graphene oxide reinforced polybenzimidazole membrane with a sandwich structure for high temperature proton exchange membrane fuel cells in anhydrous atmosphere. *European Polymer Journal*, 2018, **103**, 207-213.
- [203] Y.M. Deng, G. Wang, M.M. Fei, X. Huang, J.G. Cheng, X.T. Liu, L. Xing, K. Scott, C.X. Xu, A polybenzimidazole/graphite oxide based three layer membrane for intermediate temperature polymer electrolyte membrane fuel cells. *Rsc Advances*, 2016, **6**(76), 72224-72229.
- [204] P. Gómez-Romero, J.A. Asensio, S. Borrós, Hybrid proton-conducting membranes for polymer electrolyte fuel cells: phosphomolybdic acid doped poly (2, 5-benzimidazole)—(ABPBI-H<sub>3</sub>PMo<sub>12</sub>O<sub>40</sub>). *Electrochimica Acta*, 2005, **50**(24), 4715-4720.
- [205] K. Scott, C. Xu, X. Wu, Intermediate temperature proton-conducting membrane electrolytes for fuel cells. *Wiley Interdisciplinary Reviews: Energy and Environment*, 2014, **3**(1), 24-41.
- [206] M.-Q. Li, Z.-G. Shao, K. Scott, A high conductivity Cs<sub>2.5</sub>H<sub>0.5</sub>PMo<sub>12</sub>O<sub>40</sub>/polybenzimidazole (PBI)/H<sub>3</sub>PO<sub>4</sub> composite membrane for proton-exchange membrane fuel cells operating at high temperature. *J Power Sources*, 2008, **183**(1), 69-75.
- [207] M. Moradi, A. Moheb, M. Javanbakht, K. Hooshyari, Experimental study and modeling of proton conductivity of phosphoric acid doped PBI-Fe<sub>2</sub>TiO<sub>5</sub> nanocomposite membranes for using in high temperature proton exchange membrane fuel cell (HT-PEMFC). *International Journal of Hydrogen Energy*, 2016, **41**(4), 2896-2910.
- [208] Y. Cai, Z. Yue, Q. Jiang, S. Xu, Modified silicon carbide whisker reinforced polybenzimidazole used for high temperature proton exchange membrane. *Journal of energy chemistry*, 2018, **27**(3), 820-825.
- [209] P. Muthuraja, S. Prakash, V.M. Shanmugam, S. Radhakrishnan, P. Manisankar, Novel perovskite structured calcium titanate-PBI composite membranes for high-temperature PEM fuel cells: Synthesis and characterizations. *International Journal of Hydrogen Energy*, 2018, **43**(9), 4763-4772.
- [210] X.J. Chen, Y.C. Zhang, P. Ribeiorinha, H.B. Li, X.Y. Kong, M. Boaventura, A proton conductor electrolyte

## Bibliography

---

- based on molten  $\text{CsH}_5(\text{PO}_4)_2$  for intermediate-temperature fuel cells. *Rsc Advances*, 2018, **8**(10), 5225-5232.
- [211] L. Liu, H. Li, X. Chen, X. Lei, Electrolyte Membranes Based on Molten  $\text{KH}_5(\text{PO}_4)_2$  for Intermediate Temperature Fuel Cells. *Fuel Cells*, 2019.
- [212] M.A. Imran, G. He, X. Wu, X. Yan, T. Li, A.S. Khan, Fabrication and characterization of sulfonated polybenzimidazole/sulfonated imidized graphene oxide hybrid membranes for high temperature proton exchange membrane fuel cells. *Journal of Applied Polymer Science*, 2019, **136**(34), 47892.
- [213] Y. Wang, Z. Shi, J. Fang, H. Xu, J. Yin, Graphene oxide/polybenzimidazole composites fabricated by a solvent-exchange method. *Carbon*, 2011, **49**(4), 1199-1207.
- [214] J. Salehi Artimani, M. Ardjmand, M. Enhessari, M. Javanbakht, Polybenzimidazole/ $\text{BaCe}_{0.85}\text{Y}_{0.15}\text{O}_{3.5}$  nanocomposites with enhanced proton conductivity for high-temperature PEMFC application. *Canadian Journal of Chemistry*, 2019, **97**(7), 520-528.
- [215] J. Lin, J.A. Siddiqui, R.M. Ottenbrite, Surface modification of inorganic oxide particles with silane coupling agent and organic dyes. *Polym Advan Technol*, 2001, **12**(5), 285-292.
- [216] C. Xu, Y. Cao, R. Kumar, X. Wu, X. Wang, K. Scott, A polybenzimidazole/sulfonated graphite oxide composite membrane for high temperature polymer electrolyte membrane fuel cells. *J Mater Chem*, 2011, **21**(30), 11359.
- [217] K. Hinokuma, M. Ata, Fullerene proton conductors. *Chemical physics letters*, 2001, **341**(5-6), 442-446.
- [218] N.D. Luong, U. Hippi, J.T. Korhonen, A.J. Soininen, J. Ruokolainen, L.-S. Johansson, J.-D. Nam, J. Seppälä, Enhanced mechanical and electrical properties of polyimide film by graphene sheets via in situ polymerization. *Polymer*, 2011, **52**(23), 5237-5242.
- [219] J. Escorihuela, A. Garcia-Bernabe, A. Montero, O. Sahuquillo, E. Gimenez, V. Compan, Ionic Liquid Composite Polybenzimidazol Membranes for High Temperature PEMFC Applications. *Polymers*, 2019, **11**(4).
- [220] S. Cavaliere, S. Subianto, I. Savych, D.J. Jones, J. Rozière, Electrospinning: designed architectures for energy conversion and storage devices. *Energ Environ Sci*, 2011, **4**(12), 4761.
- [221] R. Padmavathi, D. Sangeetha, Synthesis and characterization of electrospun carbon nanofiber supported Pt catalyst for fuel cells. *Electrochimica Acta*, 2013, **112**, 1-13.
- [222] I. Savych, J.B. d'Arbigny, S. Subianto, S. Cavaliere, D.J. Jones, J. Roziere, On the effect of non-carbon nanostructured supports on the stability of Pt nanoparticles during voltage cycling: A study of  $\text{TiO}_2$  nanofibres. *J Power Sources*, 2014, **257**, 147-155.
- [223] R. Sood, S. Cavaliere, D.J. Jones, J. Roziere, Electrospun nanofibre composite polymer electrolyte fuel cell and electrolysis membranes. *Nano Energy*, 2016, **26**, 729-745.
- [224] S.H. Wang, H.L. Lin, Poly (vinylidene fluoride-co-hexafluoropropylene)/polybenzimidazole blend nanofiber supported Nafion membranes for direct methanol fuel cells. *J Power Sources*, 2014, **257**, 254-263.
- [225] M. Tanaka, Y. Takeda, T. Wakiya, Y. Wakamoto, K. Harigaya, T. Ito, T. Tarao, H. Kawakami, Acid-doped polymer nanofiber framework: Three-dimensional proton conductive network for high-performance fuel cells. *J Power Sources*, 2017, **342**, 125-134.
- [226] J. Escorihuela, A. Garcia-Bernabe, A. Montero, A. Andrio, O. Sahuquillo, E. Gimenez, V. Compan, Proton Conductivity through Polybenzimidazole Composite Membranes Containing Silica Nanofiber Mats. *Polymers*, 2019, **11**(7).
- [227] J.-S. Kim, D.H. Reneker, Polybenzimidazole nanofiber produced by electrospinning. *Polymer Engineering & Science*, 1999, **39**(5), 849-854.
- [228] H. Penchev, F. Ublekov, D. Budurova, V. Sinigersky, Novel electrospun polybenzimidazole fibers and yarns

## Bibliography

---

- from ethanol/potassium hydroxide solution. *Materials Letters*, 2017, **187**, 89-93.
- [229] S. Jahangiri, I. Aravi, L.I. Sanli, Y.Z. Menceloglu, E. Ozden-Yenigun, Fabrication and optimization of proton conductive polybenzimidazole electrospun nanofiber membranes. *Polym Advan Technol*, 2018, **29**(1), 594-602.
- [230] T. von Graberg, A. Thomas, A. Greiner, M. Antonietti, J. Weber, Electrospun Silica-Polybenzimidazole Nanocomposite Fibers. *Macromolecular Materials and Engineering*, 2008, **293**(10), 815-819.
- [231] T. Søndergaard, L.N. Cleemann, H. Becker, T. Steenberg, H.A. Hjuler, L. Seerup, Q. Li, J.O. Jensen, Long-term durability of PBI-based HT-PEM fuel cells: effect of operating parameters. *J Electrochem Soc*, 2018, **165**(6), F3053.
- [232] S. Petrik, M. Maly, Production Nozzle-Less Electrospinning Nanofiber Technology. *MRS Proceedings*, 2011, **1240**.
- [233] Jirsak; Oldrich , Sanetnik; Filip, Lukas; David, Kotek; Vaclav , Martinova; Lenka, C. Jiri, Method of nanofibres production from a polymer solution using electrostatic spinning and a device for carrying out the method, Technicka Universita V Liberci, United States, 2009.
- [234] K.M. Skupov, I.I. Ponomarev, D.Y. Razorenov, V.G. Zhigalina, O.M. Zhigalina, I.I. Ponomarev, Y.A. Volkova, Y.M. Volfkovich, V.E. Sosenkin, Carbon Nanofiber Paper Electrodes Based on Heterocyclic Polymers for High Temperature Polymer Electrolyte Membrane Fuel Cell. *Macromolecular Symposia*, 2017, **375**(1), 1600188.
- [235] K.M. Skupov, I.I. Ponomarev, Y.M. Volfkovich, V.E. Sosenkin, I.I. Ponomarev, Y.A. Volkova, D.Y. Razorenov, A.G. Buyanovskaya, V.N. Talanova, Porous structure optimization of electrospun carbon materials. *Russian Chemical Bulletin*, 2020, **69**(6), 1106-1113.
- [236] D. Henry, Electron-sample interactions, *Geochemical Instrumentation and Analysis*, 2012.
- [237] J. Zeng, S.P. Jiang, L. Li, High Temperature Proton Exchange Membranes Based on Various Heteropoly Acids(HPW, HSiW, HPMo or HSiMo) Functionalized Silica Nanocomposites with Tunable Mesoporous Structure and Superior Proton Conductivity for Fuel Cells. 2011, 1603-1613.
- [238] K. Neyerlin, A. Singh, D. Chu, Kinetic characterization of a Pt-Ni/C catalyst with a phosphoric acid doped PBI membrane in a proton exchange membrane fuel cell. *J Power Sources*, 2008, **176**(1), 112-117.
- [239] J.O. Park, K. Kwon, M.D. Cho, S.G. Hong, T.Y. Kim, D.Y. Yoo, Role of Binders in High Temperature PEMFC Electrode. *J Electrochem Soc*, 2011, **158**(6), B675.
- [240] T.L. Yu, Polybenzimidazole/Porous Poly (tetrafluoro ethylene) Composite Membranes, High Temperature Polymer Electrolyte Membrane Fuel Cells, Springer2016, pp. 251-273.
- [241] M.F. Song, X.W. Lu, Z.F. Li, G.H. Liu, X.Y. Yin, Y.X. Wang, Compatible ionic crosslinking composite membranes based on SPEEK and PBI for high temperature proton exchange membranes. *International Journal of Hydrogen Energy*, 2016, **41**(28), 12069-12081.
- [242] H.-L. Lin, T.L. Yu, W.-K. Chang, C.-P. Cheng, C.-R. Hu, G.-B. Jung, Preparation of a low proton resistance PBI/PTFE composite membrane. *J Power Sources*, 2007, **164**(2), 481-487.
- [243] H.-L. Lin, J.-R. Huang, Y.-T. Chen, P.-H. Su, T.L. Yu, S.-H. Chan, Polybenzimidazole/poly(tetrafluoro ethylene) composite membranes for high temperature proton exchange membrane fuel cells. *Journal of Polymer Research*, 2012, **19**(5), 9875.
- [244] S. Yuk, D.H. Lee, S. Choi, G. Doo, D.W. Lee, H.T. Kim, An electrode-supported fabrication of thin polybenzimidazole membrane-based polymer electrolyte membrane fuel cell. *Electrochimica Acta*, 2018, **270**, 402-408.

## Bibliography

---

- [245] B. Schwenzer, J. Zhang, S. Kim, L. Li, J. Liu, Z. Yang, Membrane development for vanadium redox flow batteries. *ChemSusChem*, 2011, **4**(10), 1388-1406.
- [246] X. Zhou, T. Zhao, L. An, L. Wei, C. Zhang, The use of polybenzimidazole membranes in vanadium redox flow batteries leading to increased coulombic efficiency and cycling performance. *Electrochimica Acta*, 2015, **153**, 492-498.
- [247] C. Noh, M. Jung, D. Henkensmeier, S.W. Nam, Y. Kwon, Vanadium redox flow batteries using meta-polybenzimidazole-based membranes of different thicknesses. *ACS applied materials & interfaces*, 2017, **9**(42), 36799-36809.
- [248] C. Korte, F. Conti, J. Wackerl, P. Dams, A. Majerus, W. Lehnert, Uptake of protic electrolytes by polybenzimidazole-type polymers: absorption isotherms and electrolyte/polymer interactions. *Journal of applied electrochemistry*, 2015, **45**(8), 857-871.
- [249] Q.F. Li, R.H. He, R.W. Berg, H.A. Hjuler, N.J. Bjerrum, Water uptake and acid doping of polybenzimidazoles as electrolyte membranes for fuel cells. *Solid State Ionics*, 2004, **168**(1-2), 177-185.
- [250] D.M. Bernardi, M.W. Verbrugge, A mathematical model of the solid-polymer-electrolyte fuel cell. *J Electrochem Soc*, 1992, **139**(9), 2477.
- [251] R. He, Proton conducting membranes, Department of Chemistry, The Royal Veterinary and Agricultural University, Denmark, 2004.
- [252] R. He, Q. Che, B. Sun, The acid doping behavior of polybenzimidazole membranes in phosphoric acid for proton exchange membrane fuel cells. *Fibers and Polymers*, 2009, **9**(6), 679-684.
- [253] S. Thomas, S.S. Araya, J.R. Vang, S.K. Kær, Investigating different break-in procedures for reformed methanol high temperature proton exchange membrane fuel cells. *International Journal of Hydrogen Energy*, 2018, **43**(31), 14691-14700.
- [254] S. Galbiati, A. Baricci, A. Casalegno, G. Carcassola, R. Marchesi, On the activation of polybenzimidazole-based membrane electrode assemblies doped with phosphoric acid. *International Journal of Hydrogen Energy*, 2012, **37**(19), 14475-14481.
- [255] M. Boaventura, A. Mendes, Activation procedures characterization of MEA based on phosphoric acid doped PBI membranes. *International Journal of Hydrogen Energy*, 2010, **35**(20), 11649-11660.
- [256] R. Kerr, H. García, M. Rastedt, P. Wagner, S. Alfaro, M. Romero, C. Terkelsen, T. Steenberg, H. Hjuler, Lifetime and degradation of high temperature PEM membrane electrode assemblies. *international journal of hydrogen energy*, 2015, **40**(46), 16860-16866.
- [257] U. Reimer, B. Schumacher, W. Lehnert, Accelerated degradation of high-temperature polymer electrolyte fuel cells: discussion and empirical modeling. *J Electrochem Soc*, 2014, **162**(1), F153.
- [258] K. Kwon, T.Y. Kim, D.Y. Yoo, S.-G. Hong, J.O. Park, Maximization of high-temperature proton exchange membrane fuel cell performance with the optimum distribution of phosphoric acid. *J Power Sources*, 2009, **188**(2), 463-467.
- [259] M. Devanathan, Z. Stachurski, The mechanism of hydrogen evolution on iron in acid solutions by determination of permeation rates. *J Electrochem Soc*, 1964, **111**(5), 619.
- [260] P. Alivisatos, P.F. Barbara, A.W. Castleman, J. Chang, D.A. Dixon, M.L. Klein, G.L. McLendon, J.S. Miller, M.A. Ratner, P.J. Rossky, From molecules to materials: Current trends and future directions. *Advanced Materials*, 1998, **10**(16), 1297-1336.
- [261] G.A. Ozin, Nanochemistry: synthesis in diminishing dimensions. *Advanced Materials*, 1992, **4**(10), 612-649.

## Bibliography

---

- [262] Y. Xia, P. Yang, Y. Sun, Y. Wu, B. Mayers, B. Gates, Y. Yin, F. Kim, H. Yan, One-dimensional nanostructures: synthesis, characterization, and applications. *Advanced materials*, 2003, **15**(5), 353-389.
- [263] Z.L. Wang, Characterizing the structure and properties of individual wire-like nanoentities. *Advanced Materials*, 2000, **12**(17), 1295-1298.
- [264] J. Doshi, D.H. Reneker, Electrospinning process and applications of electrospun fibers. *Journal of electrostatics*, 1995, **35**(2-3), 151-160.
- [265] D.H. Reneker, I. Chun, Nanometre diameter fibres of polymer, produced by electrospinning. *Nanotechnology*, 1996, **7**(3), 216.
- [266] G. Srinivasan, D.H. Reneker, Structure and morphology of small diameter electrospun aramid fibers. *Polymer international*, 1995, **36**(2), 195-201.
- [267] N. Tucker, K. Hofman, H. Razzaq, A History of Electrospinning 1600–1995. *GB-06385*, 1900.
- [268] A. Formhals, Process and apparatus for preparing artificial threads. US Patent: 1975504, vol, 1934, p. 7.
- [269] C.L. Norton, Method of and Apparatus for producing fibrous or filamentary material, U.S, 1936.
- [270] Z. Li, C. Wang, Effects of working parameters on electrospinning, One-dimensional nanostructures, Springer2013, pp. 15-28.
- [271] A.L. Yarin, S. Koombhongse, D.H. Reneker, Taylor cone and jetting from liquid droplets in electrospinning of nanofibers. *Journal of applied physics*, 2001, **90**(9), 4836-4846.
- [272] D.H. Reneker, A.L. Yarin, H. Fong, S. Koombhongse, Bending instability of electrically charged liquid jets of polymer solutions in electrospinning. *Journal of Applied physics*, 2000, **87**(9), 4531-4547.
- [273] M.M. Hohman, M. Shin, G. Rutledge, M.P. Brenner, Electrospinning and electrically forced jets. I. Stability theory. *Physics of fluids*, 2001, **13**(8), 2201-2220.
- [274] M.M. Hohman, M. Shin, G. Rutledge, M.P. Brenner, Electrospinning and electrically forced jets. II. Applications. *Physics of fluids*, 2001, **13**(8), 2221-2236.
- [275] J. Feng, Stretching of a straight electrically charged viscoelastic jet. *Journal of Non-Newtonian Fluid Mechanics*, 2003, **116**(1), 55-70.
- [276] Y. Shin, M. Hohman, M. Brenner, G. Rutledge, Experimental characterization of electrospinning: the electrically forced jet and instabilities. *Polymer*, 2001, **42**(25), 09955-09967.
- [277] P. Costamagna, C. Sanna, A. Campodonico, E.M. Sala, R. Sazinas, P. Holtappels, Electrochemical Impedance Spectroscopy of Electrospun  $\text{La}_{0.6}\text{Sr}_{0.4}\text{Co}_{0.2}\text{Fe}_{0.8}\text{O}_{3-\delta}$  Nanorod Cathodes for Intermediate Temperature - Solid Oxide Fuel Cells. *Fuel Cells*, 2019, **19**(4), 472-483.
- [278] A. Enrico, W.J. Zhang, M.L. Traulsen, E.M. Sala, P. Costamagna, P. Holtappels,  $\text{La}_{0.6}\text{Sr}_{0.4}\text{Co}_{0.2}\text{Fe}_{0.8}\text{O}_{3-\delta}$  nanofiber cathode for intermediate-temperature solid oxide fuel cells by water-based sol-gel electrospinning: Synthesis and electrochemical behaviour. *Journal of the European Ceramic Society*, 2018, **38**(7), 2677-2686.
- [279] M. Krifa, C. Prichard, Nanotechnology in textile and apparel research – an overview of technologies and processes. *The Journal of The Textile Institute*, 2020, **111**(12), 1778-1793.
- [280] D. Li, Y. Xia, Electrospinning of nanofibers: reinventing the wheel? *Advanced materials*, 2004, **16**(14), 1151-1170.
- [281] Z.-M. Huang, Y.Z. Zhang, M. Kotaki, S. Ramakrishna, A review on polymer nanofibers by electrospinning and their applications in nanocomposites. *Composites Science and Technology*, 2003, **63**(15), 2223-2253.
- [282] V. Thavasi, G. Singh, S. Ramakrishna, Electrospun nanofibers in energy and environmental applications. *Energ Environ Sci*, 2008, **1**(2), 205-221.
- [283] S. Peng, L. Li, J.K.Y. Lee, L. Tian, M. Srinivasan, S. Adams, S. Ramakrishna, Electrospun carbon nanofibers

## Bibliography

---

- and their hybrid composites as advanced materials for energy conversion and storage. *Nano Energy*, 2016, **22**, 361-395.
- [284] M.V. Kakade, S. Givens, K. Gardner, K.H. Lee, D.B. Chase, J.F. Rabolt, Electric field induced orientation of polymer chains in macroscopically aligned electrospun polymer nanofibers. *J Am Chem Soc*, 2007, **129**(10), 2777-2782.
- [285] S.F. Fennessey, R.J. Farris, Fabrication of aligned and molecularly oriented electrospun polyacrylonitrile nanofibers and the mechanical behavior of their twisted yarns. *Polymer*, 2004, **45**(12), 4217-4225.
- [286] T. Tamura, H. Kawakami, Aligned electrospun nanofiber composite membranes for fuel cell electrolytes. *Nano letters*, 2010, **10**(4), 1324-8.
- [287] C. Pan, H. Wu, C. Wang, B. Wang, L. Zhang, Z. Cheng, P. Hu, W. Pan, Z. Zhou, X. Yang, Nanowire-based high-performance “micro fuel cells”: one nanowire, one fuel cell. *Advanced Materials*, 2008, **20**(9), 1644-1648.
- [288] J. Yao, C. Bastiaansen, T. Peijs, High Strength and High Modulus Electrospun Nanofibers. *Fibers*, 2014, **2**(2), 158-186.
- [289] J. Weber, K.D. Kreuer, J. Maier, A. Thomas, Proton Conductivity Enhancement by Nanostructural Control of Poly(benzimidazole)-Phosphoric Acid Adducts. *Advanced Materials*, 2008, **20**(13), 2595-2598.
- [290] T. Ibaraki, M. Tanaka, H. Kawakami, Fast surface proton conduction on acid-doped polymer nanofibers in polymer electrolyte composite membranes. *Electrochimica Acta*, 2019, **296**, 1042-1048.
- [291] Z. Zhou, O. Zholobko, X.-F. Wu, T. Aulich, J. Thakare, J. Hurley, Polybenzimidazole-Based Polymer Electrolyte Membranes for High-Temperature Fuel Cells: Current Status and Prospects. *Energies*, 2020, **14**(1), 135.
- [292] X. Zong, K. Kim, D. Fang, S. Ran, B.S. Hsiao, B. Chu, Structure and process relationship of electrospun bioabsorbable nanofiber membranes. *Polymer*, 2002, **43**(16), 4403-4412.
- [293] S. Anandhan, K. Ponprapakaran, T. Senthil, G. George, Parametric study of manufacturing ultrafine polybenzimidazole fibers by electrospinning. *International Journal of Plastics Technology*, 2012, **16**(2), 101-116.
- [294] C.B. Shogbon, J.-L. Brousseau, H. Zhang, B.C. Benicewicz, Y.A. Akpalu, Determination of the molecular parameters and studies of the chain conformation of polybenzimidazole in DMAc/LiCl. *Macromolecules*, 2006, **39**(26), 9409-9418.
- [295] X. Li, R.P. Singh, K.W. Dudeck, K.A. Berchtold, B.C. Benicewicz, Influence of polybenzimidazole main chain structure on H<sub>2</sub>/CO<sub>2</sub> separation at elevated temperatures. *Journal of Membrane Science*, 2014, **461**, 59-68.
- [296] H.-L. Lin, Y.-C. Chen, C.-C. Li, C.-P. Cheng, T.L. Yu, Preparation of PBI/PTFE composite membranes from PBI in N, N'-dimethyl acetamide solutions with various concentrations of LiCl. *J Power Sources*, 2008, **181**(2), 228-236.
- [297] H. Fong, I. Chun, D.H. Reneker, Beaded nanofibers formed during electrospinning. *Polymer*, 1999, **40**(16), 4585-4592.
- [298] X.-H. Qin, Y.-Q. Wan, J.-H. He, J. Zhang, J.-Y. Yu, S.-Y. Wang, Effect of LiCl on electrospinning of PAN polymer solution: theoretical analysis and experimental verification. *Polymer*, 2004, **45**(18), 6409-6413.
- [299] S. Gu, J. Ren, G. Vancso, Process optimization and empirical modeling for electrospun polyacrylonitrile (PAN) nanofiber precursor of carbon nanofibers. *European polymer journal*, 2005, **41**(11), 2559-2568.
- [300] X. Yuan, Y. Zhang, C. Dong, J. Sheng, Morphology of ultrafine polysulfone fibers prepared by

## Bibliography

---

- electrospinning. *Polymer international*, 2004, **53**(11), 1704-1710.
- [301] C.S. Ki, D.H. Baek, K.D. Gang, K.H. Lee, I.C. Um, Y.H. Park, Characterization of gelatin nanofiber prepared from gelatin–formic acid solution. *Polymer*, 2005, **46**(14), 5094-5102.
- [302] J.L. Storck, T. Grothe, A. Mamun, L. Sabantina, M. Klocker, T. Blachowicz, A. Ehrmann, Orientation of Electrospun Magnetic Nanofibers Near Conductive Areas. *Materials (Basel)*, 2019, **13**(1).
- [303] C. Hellert, J.L. Storck, T. Grothe, B. Kaltschmidt, A. Hütten, A. Ehrmann, Positioning and Aligning Electrospun PAN Fibers by Conductive and Dielectric Substrate Patterns. *Macromolecular Symposia*, 2021, **395**(1), 2000213.
- [304] P. Musto, F. Karasz, W. MacKnight, Fourier transform infra-red spectroscopy on the thermo-oxidative degradation of polybenzimidazole and of a polybenzimidazole/polyetherimide blend. *Polymer*, 1993, **34**(14), 2934-2945.
- [305] W.E. Teo, S. Ramakrishna, A review on electrospinning design and nanofibre assemblies. *Nanotechnology*, 2006, **17**(14), R89-R106.
- [306] H. Becker, L.N. Cleemann, D. Aili, J.O. Jensen, Q. Li, Probing phosphoric acid redistribution and anion migration in polybenzimidazole membranes. *Electrochem Commun*, 2017, **82**, 21-24.
- [307] H. Becker, U. Reimer, D. Aili, L.N. Cleemann, J.O. Jensen, W. Lehnert, Q. Li, Determination of anion transference number and phosphoric acid diffusion coefficient in high temperature polymer electrolyte membranes. *J Electrochem Soc*, 2018, **165**(10), F863.
- [308] H.-L. Lin, T.L. Yu, L.-N. Huang, L.-C. Chen, K.-S. Shen, G.-B. Jung, Nafion/PTFE composite membranes for direct methanol fuel cell applications. *J Power Sources*, 2005, **150**, 11-19.
- [309] K. Ohno, Y. Kawashima, Super-Rayleigh Slopes in Transmission Spectra of Exoplanets Generated by Photochemical Haze. *The Astrophysical Journal Letters*, 2020, **895**(2), L47.
- [310] M. Li, K. Scott, A polymer electrolyte membrane for high temperature fuel cells to fit vehicle applications. *Electrochimica Acta*, 2010, **55**(6), 2123-2128.
- [311] Y.H. Zhao, M.H. Abraham, A.M. Zissimos, Fast calculation of van der Waals volume as a sum of atomic and bond contributions and its application to drug compounds. *The Journal of organic chemistry*, 2003, **68**(19), 7368-7373.
- [312] O. Zhlobko, X.F. Wu, Z. Zhou, T. Aulich, J. Thakare, J. Hurley, A comparative experimental study of the hygroscopic and mechanical behaviors of electrospun nanofiber membranes and solution-cast films of polybenzimidazole. *Journal of Applied Polymer Science*, 2020, **137**(39), 49639.
- [313] S.J. Cho, H. Choi, J.H. Youk, Evaluation of PBI Nanofiber Membranes as a High-temperature Resistance Separator for Lithium-ion Batteries. *Fibers and Polymers*, 2020, **21**(5), 993-998.
- [314] M. Gardel, J.H. Shin, F. MacKintosh, L. Mahadevan, P. Matsudaira, D.A. Weitz, Elastic behavior of cross-linked and bundled actin networks. *Science*, 2004, **304**(5675), 1301-1305.
- [315] X.-F. Wu, Y.A. Dzenis, Elasticity of planar fiber networks. *Journal of Applied Physics*, 2005, **98**(9), 093501.
- [316] F. Chen, X. Peng, T. Li, S. Chen, X.-F. Wu, D.H. Reneker, H. Hou, Mechanical characterization of single high-strength electrospun polyimide nanofibres. *Journal of Physics D: Applied Physics*, 2008, **41**(2), 025308.
- [317] X.-F. Wu, Y.Y. Kostogorova-Beller, A.V. Goponenko, H. Hou, Y.A. Dzenis, Rippling of polymer nanofibers. *Phys Rev E*, 2008, **78**(6), 061804.